The CFD assisted design and experimental testing of a wingsail with high lift devices

DANIEL W. ATKINS

THE RESEARCH INSTITUTE FOR DESIGN
MANUFACTURE AND MARKETING
UNIVERSITY OF SALFORD, SALFORD, UK

Submitted in Partial Fulfilment of the Requirements
of the Degree of Doctor of Philosophy

APRIL 1996

CONTAINS DISKETTE

UNABLE TO COPY

CONTACT UNIVERSITY

IF YOU WISH TO SEE

THIS MATERIAL

ABSTRACT

A wingsail is a solid symmetrical aerofoil section which creates thrust in the same manner as a conventional sail. Wingsails may either be used as a sole power unit, e.g. for a yacht or catamaran, or as an auxiliary power unit on a larger craft, e.g. fishing vessels, cargo ships or passenger liners. To augment the thrust created by the wingsail, high lift devices are employed to increase both the maximum lift and the stall incidence of the aerofoil. A wingsail must be symmetrical and capable of creating an equal lift force with the flow approaching the leading edge from either side of the wing centreline, i.e. the wingsail surface must act as either the upper, or lower pressure surface.

Initial experimental work proved that using a symmetrical slat as a leading edge high lift device both delayed the separation of flow over the wingsail upper surface and increased the effective camber of the aerofoil. To increase the thrust created still further, this leading edge high lift device was combined with a trailing edge high lift device, a symmetrical single slotted flap.

Due to the large number of possible model configurations, a commercially available CFD package was introduced to assist with the design. A series of validation tests comparing the CFD with published and experimental results showed a qualitative agreement with these results. However, the CFD predictions were not sufficiently accurate to be used quantitatively.

The computationally designed triple element model was tested experimentally. Lift, drag, pitching moment and pressure distribution measurements were taken from the model. The results of this testing showed that the triple element wingsail increased the plain wing C_{Lmax} by 68% and the stall incidence by between 4° and 6°. The final triple element wingsail design also increased the thrust of a plain wingsail over the whole operating region. Thrust was increased by up to 83% at the wind angles where a wingsail is most efficient. The results also proved that a commercially available CFD package can be used as an effective and time saving tool for wingsail design.

CHAPTER 1 - INTRODUCTION

CHAPTER 2 - WINGSAIL THEORY

CHAPTER 3 - LITERATURE SURVEY

CHAPTER 4 - TESTING CONSIDERATIONS

CHAPTER 9 - RESULTS AND DISCUSSION

Chapter 1

INTRODUCTION

1.1 Introduction

Wingsails are solid aerofoil sections (usually symmetrical) which create thrust (via combined lift and drag components) in the same manner as a conventional soft sail. Wingsails have many applications, all of which can be split into two groups:

i) Sole Power Unit (SPU), used on yachts or catamarans.

ii) Auxiliary Power Unit (APU), used on larger powered craft e.g. Cargo Ships, Passenger Liners or Fishing Vessels.

In the APU application, wingsails are normally controlled by microprocessor (often linked directly to the engine control unit). There are two reasons for microprocessor control. Firstly, to enable wingsails to be economic, they should not require additional crew to operate them and they should also be maintenance free. Secondly, load cells fitted to the wingsail measure the thrust created and de-power the engines accordingly, allowing the vessel to maintain a constant speed and course (aiding navigation).

During the late 70's and early 80's the cost of crude oil rose sharply. As a result of this, the U.S. Maritime Administration (MARAD) commissioned a report entitled 'Wind propulsion for the ships of the American merchant marine'. This report tested seven 'Wind Assist' devices and scored each on:

i) Economic viability

ii) Simplicity

iii) Rugged reliability

iv) Remote operation from the bridge

v) No additional crew requirements

vi) Design and installation within shipping regulations

vii) No interference with cargo handling

The main findings of this report, based on $20 per barrel Arabian crude were:

" A properly engineered automated sailing rig requires no additional manning and is an economically advantageous propulsion system, when used in conjunction with conventional screw propulsion. Of the hardware alternatives examined, Wingsails offer the greatest potential for simplicity, reliability and cost effective performance."

The MARAD report, compiled by Bergeson [1] considered seven of the best wind power units available at the time of writing. There are many types of wind power unit, most of which fall into a 'family' of devices. The main families of wind power units are described in the following section.

1.2 Types of Wind Power Units

There are many types of SPU/APU, they fall into three categories:

a) Soft Sails

These are conventional sails as we know them and operate by placing a two dimensional camber line at incidence to a flow. In the APU situation, these sails can often reduce in area by 'furling' inside the mast. ($C_{Lmax} \approx 1.6$)

b) Wingsails*

These are solid symmetrical aerofoil sections. As plain symmetrical sections cannot create particularly high lift coefficients, most Wingsails have a flap arrangement of some sort (either plain or

slotted). Wingsails can be arranged singly, in tandem or in bi-plane or trike arrangements, the latter two configurations being known as 'wingsets'. (Plain flapped NACA 0018 wingsail, $C_{Lmax} \approx 2.0$)

c) Mechanical Devices

These devices all require some form of power source to manipulate the boundary layer around the propulsion device. Mechanical devices are usually capable of achieving very high lift coefficients. (Flettner Rotor, $C_{Lmax} \approx 10$)

* Wingsails should not be confused with 'solid square sails' or 'rigid sails' which unfold and create thrust solely by drag when the vessel is travelling in a downwind direction.

1.2.1 Soft/Rigid Sails

i) Gaff Rig

Commonly seen powering small fishing vessels, this is one of the most efficient sailing rigs. The Gaff rig is frequently chosen for use on small fishing vessels (the mast/gaff may also be used for other operations e.g. deck crane etc.).

ii) Square rig

The Square rig, shown in **Figure 1:1a**, is the oldest form of rig. Typically used on large vessels, this arrangement allows the highest density of sail to be rigged for a given area. Square rigs are efficient downwind , but must be furled when travelling upwind since this creates a large drag. ($C_{Lmax} \approx 1.0$)

iii) Bermudan rig

The Bermudan rig is shown in **Figure 1:1b**. Most commonly used to propel pure sailing vessels, dinghies/cruisers etc. The Bermudan rig is not, in fact, the most aerodynamic sail-plan since it tends to have a very poor lift distribution. This distribution is, however, very

structurally desirable, making masts and rigging easy to construct. ($C_{Lmax} \approx 1.8$)

iv) Cat rig

The Cat rig, shown in **Figure 1:1c**, is the sail-assist designer's version of the Bermudan rig. Identical in shape, this rig can be fully controlled by a microprocessor. The soft-sail rig is supported by a mast which can rotate independently of the boom, thus reducing or enlarging the sail area, known as furling. The mast will also rotate, setting the leading edge for maximum efficiency. Controls alter the angle of the boom and adjust the sail camber and twist.

The boom is adjusted by a unique arrangement of hydraulic cylinders, which are all contained within the deck area of the system. The adaptability of this arrangement allows rapid installation of the sail power unit.

v) Ljungstrom rig

The main disadvantage with Bermudan and cat rigs is that, whilst being superior in upwind performance to the square and gaff rigs, they lose performance downwind, when drag becomes thrust. The Ljungstrom rig, designed in 1934, can overcome this loss of thrust. In this rig, there are two sails. When sailing up/across the wind, the sails appear as a single profile. When sailing downwind, however, the two sails separate and effectively double the planform area, thus doubling the available downwind thrust. There is, however, a disadvantage to this since there is the need for a traveller. The traveller is mounted behind the rig and separates the two sails, thus occupying a large volume of deckspace.

vi) Rigid sail (Dynarig)

This is a solid square rig, with the capability to fold mechanically instead of furl. As with the soft square rig, this sail is efficient when

sailing downwind although it is less efficient when sailing upwind. Unfortunately, due to the mechanical opening/closing nature of this sail, it carries the mast and hydraulics on the high pressure side of the sail. This, combined with a low aspect ratio normally around 0.8, leads to a very high induced drag penalty when sailing upwind. These were the first solid sails to be used on commercial vessels.

1.2.2 Wingsail

Figure 1:1d shows a wingsail, a symmetrical aerofoil section capable of rotating about a spanwise vertical axis. The wing can rotate 360° about a point on the chord length (usually the aerodynamic centre). Wing control systems are usually hydraulic. Either the wing and flap are set to the desired incidence by a microcomputer or the wing is allowed to behave passively. With the passive control system, control inputs are made to the tail vane. Hydraulic actuators create a tail incidence which, due to the tail moment arm, creates the main wingsail angle of attack. Chordwise frames transmit loads from the flaps into the structure and thus the main spar, which is often designed to lie on the axis of rotation.

The style of the wingsail depends greatly upon its intended use. Large vessels are relatively unaffected by any rolling moment created by the wingsail, whereas, for pure sailing vessels, the maximum rolling moment often constrains the sail size. Wingsails can easily be constructed with enough stiffness to allow constant chord over the span (height), these constant chord sections may then be fitted with endplates to maximise the lift created at the tip (head) and reduce drag from induced vortices. The constant chord wingsail is often employed on large vessels, where several devices are used and the simplicity of the wingsail is often essential. Tapered wingsails are used more frequently on pure sailing vessels e.g. C-Class catamarans and on 'Yellow Pages', the wind-powered speed record challenger. Tapered wingsails are designed to create a close to optimum loading distribution (elliptic), thus reducing induced drag and lowering the wingsail centre of effort. The centre of effort of a sail is similar to the two dimensional definition of aerodynamic

centre, but involves the span of the wingsail also. Centre of effort is defined as: the single point at which the total thrust can be considered to act; if a single force and moment were applied at this point it would create the same resultant forces and moments as the resolved total thrust distribution.

i) Single Wingsails

These are, as the description states, just single aerofoils. They can be either:

i) Plain aerofoil section
ii) Aerofoil with plain flap
iii) Aerofoil with single-slotted flap
iv) Aerofoil with double-slotted flap
v) Aerofoil with variable 'nose' camber

ii) Tandem devices

Developed from single aerofoils with large flap/chord ratios, at first glance these look very similar to flapped aerofoils. Tandem devices are actually two plain aerofoils - often of identical section arranged in a row and operating at slightly off set incidences.

iii) Wingsets

Designed primarily for structural purposes, the wingset can increase the lift characteristics of the whole device whilst not incurring a size penalty. Wingsets are either arranged in bi-plane or tri-plane fashion in order to take advantage of the benefits of having aerofoils in close proximity with each other.

1.2.3 Mechanical Devices

i) Flettner rotor

The Flettner rotor is shown in **Figure 1:1e**, this device relies on the well documented Magnus effect. The Flettner rotor gains its name from the German designer Anton Flettner. Flettner, credited as the first designer of the wingsail/set, then became obsessed with rotating boundary layer devices. The Flettner rotor is a rotating cylinder in a streamflow. The air on one side of the cylinder is accelerated, whilst on the other side of the cylinder the air is retarded. Due to viscous friction between the cylinder and the air, a pressure gradient is created. The Magnus effect can be increased by the use of endplates to prevent the high pressure flow from leaking to the low pressure side and thus reducing the effectiveness of the rotor. It should be noted, however, that force can only be created in a direction perpendicular to the streamflow. To create a force acting in the opposing direction, required whilst sailing upwind, the direction of spin of the cylinder must be reversed. Rotors create a very high drag especially when travelling upwind, 0 to 40°.

ii) Horizontal axis turbine

These devices, shown in **Figure 1:1f**, look very similar to the horizontal turbines which are used in terrestrial power generation. The difference is that terrestrial wind power devices use the turbine to generate electrical power, whereas the nautical version uses the turbine through complex gearing to power the vessel directly. Although, for the terrestrial power generation purpose, a great deal of work has been done on horizontal axis turbines, the sail assist application of the device has never taken off. The most advantageous characteristic of this, the horizontal, and the vertical axis turbine is their ability to power a craft sailing directly into the wind. Horizontal turbines do have a major disadvantage (besides cost), which is that the size of device required, and so the deck/air space required, is rather prohibitive.

iii) Vertical axis turbine

An excellent use for this device, as suggested by K.J. England and P. Beardwood [2] would be to power the Flettner rotor. This would eliminate the need for a power source, other than the wind, to spin the cylinder.

iv) Turbosail

A wingsail with a high thickness/chord ratio and mechanically blown boundary layer control. The French-designed Turbosail is an elliptical section, with a thin trailing edge flap. The surface of the sail is aspirated, the low pressure air being 'blown' to provide delayed boundary layer separation. On the high pressure side, the boundary layer is held attached by suction. As with a standard wingsail, either surface must act as the high or low pressure surface and so the boundary layer control is reversed with the aerodynamic forces. As with the rotor, end plates are also used to increase efficiency.

1.3 Performance Comparison

Bergeson [1] discussed the point that lift and drag coefficients do not fully explain the performance of sailing rigs. However, their sail areas must be taken into account in order to determine the actual propulsive power developed. **Figure 1:2** contains lift and drag curves for the Wingsail, Cat rig, Turbosail and Flettner rotor. These four curves have been factored by a non-dimensional quantity 'SA/3000 ft^2', where SA = Sail Area. The sail areas are non-dimensionalised by 3000ft^2 because that is a typical size for a conventional (non-powered) rig. This figure clearly shows the advantage of a wingsail over the alternative wind power devices.

1.4 Benefits of Sail Assist

More than fifteen years ago, in 1980, the world's first sail assisted commercial vessel, the tanker Shin-Aitoku-Maru, was completed. This vessel, although only operating with a crude folding solid square sail, attained notable fuel efficiency. The sail control on the vessel was totally automated, and linked to a complex management system controlling the lean burning engine and variable pitch propeller.

It was found from the trials of this vessel that sail assist is more than just a way of improving fuel economy. It also helps to reduce rolling, pitching, yawing and endows the ships with excellent course keeping ability. As a result of this, vessels are capable of operating in rough conditions and have a higher rate of utilisation. Figures from the Shin-Aitoku-Maru suggest a fuel saving of as much as 20-30% on some routes, along with a 20-30% reduction in rolling. Unfortunately, soon after the success of the Shin-Aitoku-Maru, a vessel fitted with a similar wingsail malfunctioned in a Japanese harbour during high winds. The vessel broke free of its moorings and was blown across the harbour, damaging other vessels and seriously damaging the harbour. This incident discredited wingsail safety and ended the wingsail technology development programme.

1.5 Required Characteristics for a Wingsail

The following chapter, 'Wingsail Aerodynamics', describes the aerodynamic characteristics required to optimise wingsail performance. The required characteristics are rather different from those need for aircraft design since the force resolution is dependent upon the direction of the airflow (wind) relative to the vessel. Probably the most important restriction upon wingsail design is the necessity for a symmetrical wing section, to enable the vessel to sail with the wind coming from either port or starboard.

CHAPTER 3 - LITERATURE SURVEY

c = Wing Chord

i_t = Tail Setting Angle

l_t = Tail Moment Arm

L_t = Tail Lift Force

L_w = Wing Lift Force

M_w = Wing Pitching Moment

U = Freestream Wind Speed

α = Wind Angle

ϵ = Downwash Angle

λ_c = Aerodynamic Pivot Distance

Chapter 2

WINGSAIL THEORY

2.1 Apparent Wind Direction

Apparent wind velocity, V_A, is the result of adding the vessel velocity V_S and the true wind velocity V_T, vectorially. **Figure 2:1a** shows a vessel, sailing a course of 90° to the true wind V_T, at a vessel velocity V_S. The apparent wind V_A, acting on the vessel, has a magnitude and direction equal to the resultant of V_T and V_S. **Figures 2:1 'b'** and **'c'** show the same vessel, with the true wind V_T remaining at the same angle and velocity. Vessel velocity V_S is increased to give V_S/V_T ratios of 2 & 3 respectively; the effect of this ratio change is shown in the table included in **Figure 2:1**. Here, β is the angle of the apparent wind and V_A is the magnitude. All sails, including wingsails, are set with the apparent wind velocity as the speed and direction of the airflow.

2.2 Wingsail Aerodynamics

For the purposes of discussion, we can divide sail requirements into two points of sailing:

i) Upwind and close reaching

ii) Downwind and broad reaching.

Some of the requirements of upwind and downwind sailing will be discussed here. The primary criterion is to maximise available driving force, or thrust, for any given sail configuration.

2.2.1 Upwind and Close Reaching

Aerodynamic requirements for sailing upwind and close reaching are basically the same. These points of sailing are characterised by having the apparent wind at a small angle β to the course of the boat, β being defined in **Figure 2:1**. We might consider β = 30 degrees typical for this point of sailing. It can be seen from **Figure 2:2a**, that the resultant force, *R*, is nearly at right angles to the course, so there is only a small thrust force, *T*, compared to the rather large heeling force, *H*. The resultant *R* is composed of an aerodynamic lift force, *L*, normal to the wingsail and drag force, *D*, acting along the wingsail centreline, in the direction of the airflow. Inspection of the diagram indicates that optimising *L/D* will both increase available thrust and reduce heeling force. The sail setting angle, α, will therefore be the optimum L/D configuration for the aerofoil.

2.2.2 Downwind and Broad Reaching

Boats which sail directly downwind, relying solely on aerodynamic drag to produce thrust, are limited to about half the speed of the wind. This is because, as the boat sails faster, the apparent wind over the sails is reduced. Since the driving force is reduced at a rate proportional to the square of the apparent wind velocity and the hull resistance typically increases at a rate between the square and cube of the boat speed, it becomes very difficult to obtain any significant gains sailing straight before the wind.

However, no theoretical limit to speed exists for boats which sail downwind, using both lift and drag forces in the normal manner, or 'broad reach'. This may involve the boat taking a course up to 30° either side of the direct downwind course required and proceeding in a course best described as a zig-zag. Under such conditions, a boat sails a course to allow the most efficient wingsail setting, which is when the apparent wind is coming from around 90-140°, as shown in **Figure 2:2b**. This condition is then the same as broad reaching and is an important concern in wingsail design.

Sailing downwind is conceptually much simpler than the upwind problem. Sail drag is of secondary importance, as it acts either normal to the course of the boat, or as a thrust, while the lift force acting in the direction of required thrust is of primary importance. Since an unstalled sail can produce more than twice the lift coefficient of a stalled sail, the downwind problem is basically one of designing a sail that will produce the highest possible lift before stall.

2.3 Summary of Design Criteria

A vessel travelling upwind, with the wind coming from +/-40° to +/-90°, requires optimum lift/drag ratio from the aerofoil to create maximum thrust.

A vessel travelling downwind, with the wind coming from +/-90° to +/-180°, requires maximum lift to create maximum thrust. However, when two lift configurations create a similar lift at similar incidence, the lower drag case (i.e. higher lift/drag ratio) is normally preferable due to the reduction in heeling moment created.

To arrive at the most efficient wingsail, one of these optimisations must be given priority. As a result, the downwind design optimisation was chosen. There are two reasons for this:

i) Wingsails are at their most efficient at angles between 90-140°. Therefore, maximum wingsail performance is obtained if thrust is maximised in this wind range. However, as stated in the downwind optimisation, the lift/drag ratio of similar lift configurations at similar incidences should be used as the deciding factor.

ii) The downwind configuration covers a greater percentage of wind direction. A wingsail, or any sail, is very rarely used for sailing at an angle of less than 30°, even with a high lift/drag ratio, since a prohibitive amount of heeling force is created, for a small thrust.

2.4 Wind-Assist versus Pure Sail Power

Spaans [7] studied the effects of wind assist versus pure sail power and pure engine power, during a study on weather patterns in shipping routes. Spaans shows the simplified propulsion force vectors for a pure sailing vessel, an engine driven ship and a wind-assisted ship, see **Figures 2:3 a-c**.

Figure 2:3a shows a pure sailing case. Thrust from the sails is the component of the resultant vector R (the result of aerodynamic lift L and drag D) resolved in the direction of the vessel. R divides into the propulsive thrust vector T_w and the heeling vector H_w. The heeling force steadies the ship and makes the vessel roll towards the lee side smoothly, but with substantial heel.

Figure 2:3b shows a pure engine powered vessel. T_e is the propeller thrust, the steady effect of heeling force being absent. The lack of a constant side force actually deteriorates the vessel's stability, particularly in rough seas, where the sail has the effect of acting as a damper.

Figure 2:3c shows an engine and sail system. The forward thrust T_t is now composed of the aerodynamic thrust T_w and engine thrust T_e. This addition in thrust also provides additional ship speed, or efficiency, by allowing propeller pitch to be reduced. The heeling force from the sail system H_w causes only moderate heel, but still gives the ship a steadying effect.

2.5 Benefits of High Lift Devices

To optimise all-round wingsail performance, the maximum thrust is required from the given wingsail area whilst maintaining a reasonable maximum L/D ratio. To accomplish this, high lift devices are used to alter the geometry of the aerofoil section and improve thrust characteristics.

C_{Lmax} can be increased in one of two ways, either by increasing lift at the present incidence, or by delaying the onset of stall thus increasing C_{Lmax} at stall. Obviously achieving both increased lift and delayed stall is the optimum solution.

Increased lift can be achieved by an increase in aerofoil camber, whereas delaying stall relies on preventing flow separation over the aerofoil. There are two main points of separation for flow around a wing:

i) Leading edge separation, where flow separates from the nose, or upstream edge of the aerofoil.

ii) Trailing edge separation, where the flow separates from the downstream edge of the aerofoil.

A leading edge stall is a poor characteristic for a wingsail because this leads to a sudden loss of lift at stall. Stall characteristics are described in **Chapter 4**.

Leading edge slats are small aerofoils located upstream of the leading edge of the main wing. The purpose of a leading edge slat is to assist the flow in turning around the leading edge of the wing, the point of maximum curvature. Delaying separation from the leading edge will delay the onset of stall and increase the maximum angle of attack for the aerofoil. Leading edge slats also increase the effective camber of the aerofoil.

Slotted flaps derive their effectiveness from increasing the effective camber of the aerofoil section as a whole. The slot created by the flap ducts high energy air from the lower surface of the wing to the upper surface of the flap. This higher energy air delays separation of flow over the flap, allowing greater flap angles and thus greater lift force to be achieved. Increasing the angle of the flap also increases the effective camber of the aerofoil section.

CHAPTER 3 - LITERATURE SURVEY

c = Wing Chord

i_t = Tail Setting Angle

l_t = Tail Moment Arm

L_t = Tail Lift Force

L_w = Wing Lift Force

M_w = Wing Pitching Moment

U = Freestream Wind Speed

α = Wind Angle

ϵ = Downwash Angle

λ_c = Aerodynamic Pivot Distance

Chapter 3

LITERATURE SURVEY

3.1 Literature Survey

The greatest amount of research into windship technology appears to have been done in the late 70's and early 80's, when the oil market was volatile. Wind power research seems to have peaked around 1985, when most of the leading sail-assist designers met at *Windtech '85'*, the international symposium on windship technology. [Proceedings published in the *'Journal of Wind Engineering and Industrial Aerodynamics'* Vol. 19/20 (1985)].

Research into this subject falls into a number of categories:

i) Aerodynamics - The analysis of how wingsails operate and, from this analysis, further design recommendations.

ii) Wingsail dynamics - A logical progression from aerodynamics, the analysis of wingsails subject to constantly changing operating conditions caused by fluctuating wind velocities, directions and ship motion effects.

iii) Applications - Designers see the application of wind-assist or wind power in different ways. There are four main areas:

a) On large commercial vessels, as a means of saving fuel and reducing toxic and noise pollution.

b) The more rugged wind-assist devices could be used in the propulsion of vessels for the third world countries, where fuel is expensive and hard to come by.

c) In a retro-fit application, for wind power on ageing vessels (typically fishing vessels). With age, power plants on most vessels become less and less effective. A cost effective alternative to re-fitting a new engine is to fit a sail-assist device, thus relieving work load from the engine.

d) Finally, on private yachts and multihulls, as a sole power unit.

iv) Wind routeing - Naturally, there are some trade routes which favour the use of a wind powered vessel more than others. As a result of this, various organisations have set up in the business of wind routeing sailing vessels and wind assisted ships. These companies make very attractive claims about time savings which can be made by following their routes. As a result, much research has been done into the effectiveness of wind routeing.

v) Economics - A combination of all of the above factors must be taken into account when considering the economics of fitting a ship propulsion device. The size of the vessel must be considered, then the type, cost and size of device must be considered with respect to the route, vessel usage and need for meterological assistance. The economics of wind-assistance is definitely not an exact science. To assess the length of payback time for the cost of fitting a wingsail,

many assumptions must be made. Obviously it is wise to underestimate slightly the effectiveness of a device, in the knowledge that the wingsail is unlikely to underperform. Unfortunately, ship and boat owners also tend to underestimate this estimate, in order to calculate the likely payback time of fitting a wingsail device. The effect of this often makes the economic analysis of these devices seem less attractive.

3.2 Aerodynamics

3.2.1 Force Resolution

J. Otto Scherer [3] wrote an excellent and frequently referenced paper entitled 'The Aerodynamics of high performance wingsails', which describes wingsail force resolution. The paper defines the essential qualities required when designing a wingsail and the trade offs/considerations that must be made. Although this report is written for wingsails used in the sole power application, particularly racing yachts/catamarans, by discussing optimisation for all points of sail the conclusions become generic.

3.2.2 Drop Nose Study

There has only been one study on the effects of leading edge devices on wingsails. This paper, entitled 'A reversible asymmetry rigid aerofoil' was written by Kenneth Abel [4] at Oxford University. The study was undertaken to determine if the drop nose asymmetric aerofoil effect would be practical for use with a wingsail. The experimental results were obtained in order to answer two questions:

i) Would an aerofoil profile suitable for dropnose asymmetry show behaviour similar to that of well characterised aircraft aerofoils?

ii) Could windtunnel tests confirm the superiority of rigid aerofoils over soft sails?

The study involved modifying a single plain aerofoil section with t/c ratio of 20%. In standard configuration, this aerofoil has a relatively low stall incidence. For this reason, it would not perform well on a sail assist vessel. Therefore the drop nose asymmetry is used to increase maximum lift and stall angle.

Experiments were performed on small models (just 7″ wall to wall span), and therefore results are only qualitatively correct. Abel answers in the affirmative to both of his questions. He makes several interesting and important conclusions, the first being that a properly designed and engineered wingsail, when at zero incidence, creates so little drag, compared with the structure found normally on the deck of a ship, that the wingsail need never be reefed (reduced in size - due to foul weather).

The following table, **Table 3:1**, compares the form resistance of several shapes. These shapes might occur on a fully reefed sailing vessel, or one at anchor. In each case, the force exerted by a constant wind velocity on a 6.14m (20 ft) vertical length of each shape is tabulated. The shapes are; an 205mm (8″) diameter mast, an aerofoil of 205mm (8″) thickness and a 4.8mm (3/16″) diameter stay or halyard. (The aerofoil is considered at 0° incidence).

WIND VELOCITY (ms^{-1})	WIND FORCE (N) (All shapes 6.14m vertical height)		
	8″ DIA. MAST	8″ THICK AEROFOIL	3/16″ WIRE
0.51	0.011	0.001	0.0002
1.03	0.043	0.004	0.001
2.06	0.169	0.018	0.005
4.12	0.674	0.072	0.019
8.23	2.70	0.290	0.078
16.46	10.8	1.16	0.312
32.92	43.16	4.63	1.25

TABLE 3:1 - Wind Force Comparison

It can be seen, that under storm conditions (windspeed >20 ms^{-1}) the aerofoil will produce no more resistive force than the round mast under pleasurable $10ms^{-1}$ sailing conditions. It should also be noted that a single 4.8mm (3/16″) wire (similar to that used in standard mast rigging arrangements) will create 1/4 of the resistive force of the plain aerofoil section.

These values clearly demonstrate how a properly designed and engineered wingsail (without the need for external wires or stays) when at zero incidence, creates so little drag, compared with the bare structure found normally on the deck of a ship (mast, stays, halyards etc.) that it need never be reefed (reduced in size to reduce drag).

Abel also carries out an investigation into the effect of the bi-plane arrangement of aerofoils. The effects of the bi-plane configuration have been recognised for nearly two centuries, but only studied and understood for a few decades. Certain combinations of flow patterns can combine to produce desirable flow patterns (and hence pressure distributions) that could otherwise not be obtained. The basis for this is that a second foil, properly positioned, creates conditions which reduce vortex formation and can delay/prevent separation as slotted flaps do. The positive effect of a jib on a yacht mainsail is well known and Abel shows that this effect can be further improved by the use of a flow deflector.

3.3 Wingsail Dynamics

3.3.1 Aerodynamic Loading

The dynamic response to unsteady aerodynamic loads and ship motion effects was investigated by Gordon Firestone [5]. As current wingsails would look far more at home protruding from an aircraft fuselage, rather than a ship's deck, Firestone borrows some tools from aircraft analysis to describe them. Lifting strip theory permits the calculation of unsteady lifts and moments on a three dimensional aerofoil. The aerodynamic forces and moments comprise two dynamic components for a wingsail. There is one more, however, which is ship motion. Although Firestone borrows tools from aircraft analysis to

model aerodynamic effects, tools for simple earthquake analysis are employed to describe the dynamic effects of ship motion upon the wingsail.

The goal of this combined analysis is to provide a quick and inexpensive method to evaluate the stresses in a wingsail mast. At present, this analysis is only correct for a very simplified case. The case considered is for a plain (without flaps) mass balanced wingsail, at constant angle of incidence, heading directly into steady oncoming wind. The analysis allows only for rolling moment, not pitching moment.

With this scenario Firestein finds that wingsail tip (or head) displacement is small. To put this into perspective, for a wingsail (height 27m) operating in a 30 knot wind at 12˚ angle of attack, the tip of the wing is found to displace 0.03m laterally. Clearly the mast design tested here is very stiff. Recommendations are made for further work, particularly in the areas of wind angles other than dead ahead, and an integral program for ship motion and structural analysis is proposed.

3.3.2 Analysis of a Self Trimming Wingsail

A self-trimming wingsail is a device which will automatically align itself to the apparent wind direction, either by the use of a foreplane, or a tailplane. The tailplane/foreplane can then be given a small deflection so as to give the wing a small angle of incidence, and the wing in turn creates a thrust.

The first self-trimming sailboat was apparently made by Fin Utne in Norway during the Second World War (this boat is described in **Appendix A** - 'Wingsail History').

The analysis of a self-trimming wingsail is very similar to the wing - tailplane arrangement of a standard aircraft. Once again, the tools of the aircraft trade are borrowed to analyse wingsail behaviour.

The analysis described below was developed by B.G. Newman and G.I. Fekete [6], at McGill University, Canada.

The general case of a symmetrical wing, shown in **Figure 3:1** is considered. This wing is fitted with a flap and trimmed about a pivot axis by means of an all-moving tail surface, also of symmetrical section. The analysis performed follows the conventional assumptions of aircraft stability; all angles are assumed small, and the contribution to nose-up moment from drag is neglected.

The most important conclusion drawn from this analysis states that the combination of total inertia, tail arm and tail area must not be too small, thus allowing the wingsail to realign itself quickly to a windshift. However, the inertia of the wing itself should be as small as possible to reduce oscillatory effects. An early wingsail powered craft, the Blackburn Aircraft yacht (described in **Appendix A**) was scrapped due to its unstable oscillatory characteristics.

3.4 Wind Routeing

Several papers have been written on this historic subject. Two authors (Blackburn [7] and Spaans [8]) in particular researched wind routeing with regard to sail assisted vessels. The concept of wind routeing for sailing vessels dates back to the 13th Century, the Compasso de Navigare being the first collation of routeing charts known. After WWII, when the collection and processing of meteorological data became computerised, the prediction and development of weather systems improved greatly. Initially wind routeing was aimed at time optimised crossings, but it soon became apparent that fuel saving and damage avoidance priorities made more economic sense. The best technique for routeing powered vessels is to avoid high winds which can cause heavy seas, particularly those coming from dead ahead, without incurring too much added distance.

Wind routeing for wind assisted vessels involves the use of a set of performance curves plotting speed versus either head, beam or following winds and then referring to the basic principles of powered vessels. In 1984, the cost of saving 4hrs on an Atlantic crossing was $5000 (fuel and labour charge). At that time, the cost of purchasing a wind routeing plan for the Atlantic crossing was $200. Wind routeing is becoming increasingly popular.

3.5 Economics

Many authors on wingsail design, and indeed wind propulsion as a whole, have undertaken their own assessments of the future for wind power and particularly wind assist devices. References to the economics of wind assist are made in the following papers [8,29,32,35,44,45]. The following section aims to summarise the often very similar points made in these references.

The whole concept of wind-assist suffers from the total unpredictability of the crude oil market; when a crisis arises, oil prices go up sharply. Although many times in recent history experts have predicted that oil prices will either double or treble, in fact, such prices have remained constant. Three points that should really be considered are:

i) Although oil prices will continue to fluctuate, there is no suggestion that there will ever be any long term decline.

ii) Substantial improvements to hull and engine design, also stimulated by high oil prices, are by no means an alternative to sail-assist; each should complement the other.

iii) The present pause in oil prices provides an excellent opportunity for shipowners to study the subject in depth and select the best system to meet their needs. This preparation would be much more beneficial than the acceptance of the first system that comes along if another oil crisis occurs.

3.5.1 Economic findings

The development of sail-assist devices has been impeded by a deep worldwide depression in the shipping industry. This depression has inhibited capital investment by shipowners. Sail-assist really missed an opportunity to get a foothold in the market in 1980-81. However, world economics are known to behave cyclically, so it is likely that another opportunity will arise again. At that time, wingsail technology will be capable of creating instant savings and a rapid payback.

The previous paragraph does not imply that wingsails are not economic today. Sail-assist has been proven to yield fuel savings on almost any hull form, from barge to catamaran. Properly engineered rigs do not require additional crew, nor on board maintenance, and produce a safe, trouble free source of power. What should be understood is that sail-assist is not solely the answer to achieving fuel savings. Slower shipspeeds, vastly improved diesel engine economics and improved hull forms will also yield significant fuel savings. What should be noted is that all of these developments work in perfect harmony. When a diesel engine is working at its optimum power versus fuel ratio, the vessel will be travelling at the optimum velocity for a wingsail, and savings gained will be greater than those obtained from each device individually.

CHAPTER 4 - TESTING CONSIDERATIONS

AR,A = Aspect Ratio

A′ = Corrected Aspect Ratio

b = Wing Span

B = Working Section Width

c = Total Aerofoil chord

c_f = Flap Chord

c_s = Slat Chord

c_w = Wing Chord

C_D = Drag Coefficient

$C_{D'}$ = AR Corrected Drag Coefficient

C_L = Lift coefficient

C_M = Pitching moment coefficient

C_P = Pressure coefficient

h = Tunnel height

k = Non-Dimensional Buoyancy Coefficient

l = Working Section Length

L = Characteristic Length

p = Pressure

R_e = Reynolds Number

S = Wing Area

V = Velocity of Free Stream

α = Aerodynamic Incidence

α' = AR Corrected Aerodynamic Incidence

Δ_α = Incidence correction factor (in Radians)

ϵ = Blockage coefficient

Λ = Solid blockage tunnel factor

μ = Viscosity of the Fluid

π = Pi

ρ = Mass Density of Fluid

σ = Solid blockage model geometry factor

$_{un}$ = Uncorrected value

Chapter 4

TESTING CONSIDERATIONS

4.1 Types of Stall

Stalling is the process which leads to the loss of lift and rise in drag, caused by flow separation from an aerofoil surface. Separation occurs when the fluid elements moving downstream very close to the surface of the body are placed in an increasing, or adverse, pressure gradient. The motion of these elements is then retarded by both the effect of friction and an increase in pressure, thus reducing velocity. Consequently, at some point, flow may cease to move in the direction of the freestream and reverse in an upstream direction. This reversed-flow phenomena causes flow to separate from the surface of the body and create a large wake of recirculating flow downstream of this separation point. Separation occurs either from a smooth surface (dependent upon pressure gradient in the boundary layer and Reynolds number), or instantaneously from a sharp corner (effectively a large change in pressure gradient).

If a boundary layer on a wingsail is laminar, it will either separate, or become a turbulent boundary layer (this change is referred to as transition), which may subsequently separate. A turbulent boundary layer is thicker and separates less easily than a laminar boundary layer under the influence of an adverse pressure gradient (rise in pressure). There are three main types of stall demonstrated in **Figure 4:1**:

i) Trailing Edge stall

ii) Leading Edge stall

iii) Thin Aerofoil stall

A particular phenomenon that is characteristic of both leading edge and thin aerofoil stall, is that of the laminar separation bubble. A bubble is formed when a boundary layer separates before transition occurs; the shear layer then undergoes transition (bubble transition) and then the turbulent boundary layer reattaches at some point downstream. This reattachment is dependent upon the pressure gradient decreasing and upon the Reynolds number which should not be too low.

4.1.1 Trailing Edge Stall

The trailing edge stall describes the separation of a turbulent boundary layer toward the rear of an aerofoil. The separation point moves steadily forward as the incidence is increased. This progressive movement yields a smooth and continuous variation in lift near the stall. If C_p versus x/c were plotted, the typical pressure distribution for this type of stall would have a rounded suction peak at approximately 10% chord. This low pressure area will increase to a peak near the leading edge with increasing incidence. This type of stall is exhibited by many thicker aerofoil sections (t/c > 15%) at high Reynolds Numbers.

4.1.2 Leading Edge Stall

The leading edge stall occurs as a laminar separation bubble near the leading edge of the aerofoil shortens and bursts suddenly. At low incidence there is a region of laminar flow which separates and reattaches to form a bubble. As incidence rises, the increasing curvature causes the bubble to shorten and the laminar separation point to move forward. This reduces the extent of the laminar flow ahead of the bubble. At some point, the boundary layer fails to reattach and the bubble bursts, creating a sudden loss of lift. Plotting the pressure distribution versus the chord for this type of stall shows increasing peak suction up to C_{Lmax}, followed by a collapse of suction at the point of bursting. This type of stall is exhibited by aerofoil sections 9%> t/c <15%,

at lower Reynolds numbers.

4.1.3 Thin Aerofoil Stall

This type of stall is not really relevant for the aerofoil sections tested in this thesis. Thin aerofoil stall is characterised by a bubble at fairly low incidence which grows into a longer bubble, as opposed to bursting in the leading edge stall case. The bubble will grow until it reaches the trailing edge, where maximum lift is attained. This type of stall occurs for aerofoils with t/c < 10% or at low Reynolds numbers.

4.1.4 Combination Stall

Some families of aerofoils display a combination of leading and trailing edge stalls. This is attributed to the existence of a short bubble over a certain range of Reynolds numbers. The ensuing boundary layer has a tendency to separate at the trailing edge. The stall will either have a slightly rounded lift peak followed by a sudden loss of lift, or a sharper lift peak followed by a not so rapid decrease in lift.

4.2 Stall Type for Wingsails

It is not necessarily the case that aerofoils will exhibit a particular type of stall depending upon their thickness. Stall is affected by all factors dominating the growth of the boundary layer, namely pressure gradient, Reynolds number, free stream turbulence and surface roughness. Incidence variation is essentially a means of altering the pressure gradient, as is altering the camber of the aerofoil section achieved by displacing either the leading or trailing edge flap. Maximum lift for any wing section is achieved in two ways; increasing the camber and by delaying stall, therefore increasing the stall incidence, α. Wingsails have for many years had high lift devices on the trailing edge, to increase the aerofoil camber and, in the case of slotted flaps, to re-energise the airflow on the upper surface. The addition of a leading edge high lift device is an attempt to delay leading edge stall and further increase maximum incidence. Increasing α_{max} is useful in wingsail design, since it allows a wider choice of wingsail setting angles and can reduce the chance of a gust causing stall.

4.3 Reynolds Number Effects

In order to be able to compare directly forces acting on geometrically similar bodies of various sizes at various air speeds, it is customary to express the forces in terms of non-dimensional coefficients. It is well known, however, that some characteristics such as drag and maximum lift coefficients vary with the size of the wing for a given air speed, and for a given size of wing and varying air speed.

The two most important factors neglected in defining force coefficients are effects associated with the compressibility and viscosity of air. At speeds where the pressure variations around the body are small compared with the absolute pressure (i.e. at low Mach number), the effects of compressibility are assumed to be negligible. Therefore only viscous effects are considered independently.

This leaves the factor related to the viscosity of air, the Reynolds number:

$$R_e = \frac{\rho VL}{\mu} \qquad 4:1$$

Here, ρ = the mass density of the fluid, V = the velocity of the free stream, L = the characteristic length, and μ = the viscosity of the fluid. It can be shown that similarity of flow around different bodies is obtained only if the bodies are geometrically similar and if the Reynolds numbers are the same.

4.4 Effects of Scale

4.4.1 Scale Effect on Drag

The variation of drag coefficient cannot be predicted with accuracy, particularly if the separation phenomenon varies with Reynolds number. For bodies of good streamline shape, where separation does not occur, the form drag is approximately independent of the Reynolds number. Drag consists of three parts: form drag, induced drag and skin friction drag. Induced drag depends largely upon 3 dimensional aerodynamic effects such as tip vortices. For a given transition position, the skin friction drag coefficient (due to surface friction) increases as Reynolds number increases. If the boundary layer flow over the model is turbulent right from the leading edge, the

variation in skin friction drag is the equivalent order of magnitude to the skin friction coefficient of a flat plate at zero incidence with equivalent dimensions and surface finish.

4.4.2 Scale Effects on Lift

Jacobs [9] states that the actual variations in the lift curve slope caused by Reynolds number are very small. In general, the effect of increasing Reynolds number on the lift curve will create a more linear slope of increased gradient, and the stall will become more abrupt. If the lift curve is already linear at lower Reynolds numbers, then the linear section will simply be extended at higher α. It follows from this that C_{Lmax}, and the angle at which it occurs, will also be increased.

It is possible to determine the C_{Lmax} at Reynolds numbers below 8.3×10^6 for a large group of NACA aerofoils. Jacobs [9] uses an empirically created chart and carpet graph to achieve this (see **Figures 4:2 a-b**). **Figure 4:2a** classifies the stall type for a NACA 0018 section as E_0. Using the required Reynolds number and the classification E_0, a value of ΔC_{Lmax} can then be obtained (usually negative). The ΔC_{Lmax} given is the difference in C_L between that at a Reynolds number of 8.3×10^6 and the required value. To obtain the difference between Reynolds numbers of 3.2×10^6 and 1.0×10^6, the process must be repeated for both Reynolds number and the difference between the two ΔC_L's used. The results of using Jacobs' method are shown in **Table 4:1**;

AEROFOIL SECTION	NACA 0018
SCALE EFFECTS ON C_{Lmax}	E_O
ΔC_{Lmax} BETWEEN 8.3×10^6 AND 3.2×10^6	-0.15
ΔC_{Lmax} BETWEEN 8.3×10^6 AND 1.0×10^6	-0.38
C_{Lmax} ADJUSTMENT BETWEEN 3.2×10^6 AND 1.0×10^6	-0.23

TABLE 4:1

Therefore using Jacobs' tables, C_{Lmax} is predicted to be 0.23 lower than the NACA value. The NACA published results, experimental results from model

I and Jacobs' predicted values of C_L (after correcting the NACA published results for the plain NACA 0018 section), are shown in **Figure 4:3**. Jacobs' predicted C_L versus α curve shows agreement with the experimental results on stall incidence, but predicts a 13% higher C_{Lmax}.

Unfortunately, although this seemingly simple method is useful for correcting the C_L behaviour of the plain wing, when the high lift devices are attached the method is no longer valid. Although this method is not used for correcting the experimental results, the corrected results for a NACA 0018 wing section are shown here, thus giving an indication of the magnitude of Reynolds number corrections on results.

4.4.3 Scale Effects on Flap Characteristics

Roskam [10] suggests that it is usually justified to expect a little more lift from a full scale flap than is found in a tunnel at low Reynolds number. In a number of fairly typical examples, on aircraft wings, flaps created approximately 0.2 more C_L at full scale, than tunnel results predicted.

4.5 Effects of Aspect Ratio

Aspect Ratio *AR* is defined as the ratio of span squared to the wing area ($AR = b^2/S$), which reduces to the ratio of the span to the chord in the case of a rectangular wing. It has been recognised since windtunnel testing began that the rates of change of C_L with angles of attack were strongly affected by the aspect ratio of the model. Wings of high aspect ratio were observed to have higher lift-curve slopes, and lower drag coefficients at high lift coefficients, than wings of low aspect ratio.

The Lanchester-Prandtl wing theory was developed to convert the observations on wings of a finite aspect ratio to the equivalent two-dimensional flow, or simply to predict the effects of altering the aspect ratio. The aspect ratio correction, developed by Prandtl, taken from Rae and Pope [15], gives the following **Equations 4:2 a-b**. The aspect ratio correction formulae enable the characteristics of a two wings, with differing aspect ratios, to be compared with some accuracy.

$$C_{D'} = C_D + \frac{C_{L^2}}{\Pi}\left(\frac{1}{A'} - \frac{1}{A}\right) \qquad 4:2a$$

$$\alpha' = \alpha + \frac{C_L}{\Pi}\left(\frac{1}{A'} - \frac{1}{A}\right) \qquad 4:2b$$

Figure 4:4 shows the experimental C_L versus α results, for model III, the plain NACA 0018 wing section with an aspect ratio of 4. Prandtl's aspect ratio correction is applied to the model III experimental results, for a range of aspect ratios between 2 and 8. The figure shows, that the incidence at which C_{Lmax} occurs remains almost constant, whereas the value of $dC_L/d\alpha$ increases and decreases, with an increase and decrease in aspect ratio.

4.6 Two Dimensional Windtunnel Testing

As discussed in the **Section 1.2.2**, most modern wingsails are of constant section and often have an endplate at the mast head (wingsail tip). As a result, the aerodynamics of these wingsails are largely two-dimensional; the only deviation occurs if there is no seal between the wingsail foot and the vessel deck.

Two dimensional testing is frequently used for testing alterations to aerofoil sections. Two dimensionality is improved in one of two ways:

i) Sealed endplates can be attached to the tunnel working section, essentially moving the tunnel walls in to the span of a constant chord model; these endplates should be sealed at the wing tips. Force and moment coefficients for this type of testing are normally evaluated by using pressure tappings on the model and tunnel and possibly by a wake survey.

ii) Endplates may also be attached directly to a model. This configuration allows force measurements to be recorded by a balance via model supports.

Note: Terminating flaps short of the wall will produce a pair of shed vortices, which destroy the concept of a two-dimensional wing with a uniform span loading.

4.7 Blockage Corrections

Blockage occurs because the conditions under which a wind tunnel model is tested are different from those in free air. With the exception of ground board testing, there is no difference in having a model still and the airstream moving or vice-versa. The longitudinal pressure gradient usually present in the test section in most cases produces extraneous forces which must be subtracted out.

i) Horizontal Buoyancy - Caused by the tunnel wall boundary layer thickening as it progresses along the test section. This effectively decreases the tunnel cross-section, which therefore creates a static pressure gradient and creates a force which attempts to draw the model downstream.

ii) Solid Blockage - A lateral constraint to the flow pattern around a body. In a closed wind tunnel, solid blockage effectively reduces the cross sectional area in the working section and therefore creates an increase of dynamic pressure, increasing all forces and moments at a given angle of attack.

iii) Wake Blockage - Again a lateral constraint of the flow pattern, but this time due to the model wake. This effect increases with an increase in wake size (drag), and, in a closed section, increases the drag of the model.

4.7.1 Consideration of Model Size

To avoid scaling difficulties when applying tunnel data to reality, it is desirable to test at close to the actual Reynolds number. In a conventional tunnel (i.e. not variable density) this necessitates the use of a large model, which in turn gives rise to blockage. If the maximum frontal area of a model exceeds 15% of the tunnel working section area, the effect of the floor and

ceiling of the tunnel is to constrain the naturally free air. Curvature cannot be neglected and therefore the model acts like one with extra camber.

4.7.2 Buoyancy

Almost all windtunnels with a closed section have a variation in static pressure along the axis of the test section. It follows that the pressure is usually reduced as the flow progresses downstream. Hence there is a tendency for the model to be drawn downstream. Glauert [11] finds that the magnitude of the gradient may be expressed as a non-dimensional factor k defined by:

$$\frac{dp}{dl} = -k\frac{(\rho/2)\,V^2}{B}, \qquad 4:3$$

where l = working section length; p= pressure; B = working section width.

The amount of horizontal buoyancy is usually negligible for wings (as opposed to complete aircraft models). This fact, combined with a very small pressure gradient measured in the tunnel section, leads to this factor being neglected.

4.8 Blockage Corrections Considered

Three sets of blockage correction methods are considered, those published by Rogers [12], Maskell [13] and Thom [14]. All three theories are derived theoretically, as opposed to empirically.

The model considered is tested in four formats, to allow each high lift device to be tested and assessed individually. The following table, **Table 4:2**, shows the percentage tunnel area blockage ratios of the four configurations at two incidences, 0° and 30°.

CONFIGURATION	BLOCKAGE % AT 0°	BLOCKAGE % AT 30°
WING ONLY	2.71	7.53
WING + SLAT	2.71	9.40
WING + FLAP	2.71	12.54
SLAT, WING + FLAP	2.71	14.41

TABLE 4:2

4.8.1 Theory I

Rogers [12] derives solid blockage by representing the aerofoil with a doublet (source and sink of equal strength), and the tunnel walls by an array of doublet images. These doublet images extend above and below the model, spaced at the tunnel height. The additional velocity induced by the images at the model position may then be calculated; this is the velocity increment due to solid blockage. Wake blockage is determined by placing a source of equal strength to the model far downstream. The velocity increment due to wake blockage can then be calculated as that effectively induced by the infinite array of source and sink images. Rogers' blockage theories are only correct for a small blockage ratios < 10%.

4.8.2 Theory II

Maskell's correction [13] is also derived theoretically, although in this case by using a momentum balance. The momentum balance is applied to the flow outside the wake and includes two empirical relationships. Maskell's blockage correction is principally aimed at high blockage ratios and bluff bodies e.g. stalled wings.

4.8.3 Theory III

Thom [14] again uses an infinite row of line sources, each of equal strength. To represent a symmetrical aerofoil, each source is replaced by a series of doublets. Although this blockage theory is derived principally for higher speed flows, a low speed set of equations is also derived.

4.9 Blockage Theory Selection

To assist in selecting the most appropriate blockage correction, all three blockage theories were applied to the uncorrected plain wing data. The results of these calculations are shown in **Figures 4:5 a-c**, which show lift, drag and pitching moment coefficients. The figures include the notation EP-ON, this indicates that the endplates are attached to the model. During the experimental testing stage, the endplates are attached to the model at all times unless otherwise stated.

The table below, **Table 4:3**, summarises the effect of the three blockage theories on the plain wing configuration. As the table shows, Theory II, Maskell's blockage correction, has the highest percentage of wake blockage, and this is related to the uncorrected drag coefficient. Wake blockage is the greatest contributor to the total blockage factor ϵ_{TOT} (where ϵ_{TOT} is the sum of wake and sold blockage) and thus Theory II gives the most pessimistic values for C_L.

WING ONLY (AT C_{Lmax})	THEORY I	THEORY II	THEORY III
C_L CORRECTION	-8.15%	-10.5%	-7.71%
C_D CORRECTION	+1.5%	-1.0%	+1.9%
C_M CORRECTION	-5.3%	-2.5%	-5.0%
% WAKE BLOCKAGE	65%	80%	63%
% SOLID BLOCKAGE	35%	20%	37%
ϵ_{TOT} BLOCKAGE FACTOR	0.0220	0.0357	0.0199

TABLE 4:3

The triple element model has a high blockage ratio (14% at 30° incidence). As a result, Maskell's blockage theory, designed for high blockage ratios and bluff bodies (e.g. stalled wings), is the most appropriate correction. This blockage correction was formulated and verified in a 0.9 x 1.2 m (3′ x 4′) section, similar to one used in this thesis. **Figure 4:6** shows a summary of the Maskell blockage correction on the plain wing.

4.10 Maskell's Blockage Correction

Since Maskell's original paper in 1965, the corrections have been further refined. For increased accuracy, those refinements are described below. The equations used are taken from Rae and Pope [15].

The effect of static pressure gradient associated with the wake and induced drag correction is included (Pankhurst and Holder, 1968). Rae and Pope approximate the equation for use with small ϵ only, by neglecting terms in the order of ϵ^2. As model III has a high solid blockage ratio, terms in the order of ϵ^2 cannot be neglected. In these corrections, the ϵ^2 terms are retained as in Wentz (1979) because of the large magnitude of ϵ.

4.10.1 Solid Blockage

The presence of a model in a test section reduces the area through which air must flow. This creates a negative pressure gradient, which increases the velocity of air as it flows over the model. This increase of velocity is known as solid blockage, ϵ_{SB}. Its effect is a function of the model thickness, thickness distribution and model size (this factor is independent of camber).Solid blockage, ϵ_{SB}, is the product of Λ, the solid blockage tunnel factor and σ, the solid blockage model geometry factor.

$$\Lambda = 1.75\left(\frac{t}{c}\right) + 1.875\left(\frac{t}{c}\right)^2 \qquad 4:4$$

Solid blockage tunnel factor, is derived from the model thickness chord ratio, t/c.

$$\sigma = \frac{\pi^2}{48}\left[\frac{c}{h}\right]^2 \qquad 4:5$$

Solid blockage model geometry factor is derived from the model chord length, c, and the tunnel working section height, h.

$$\epsilon_{SB} = \Lambda\sigma \qquad 4:6$$

4.10.2 Wake Blockage

Any real, body without suction type boundary layer control, will have a wake behind it, and this wake will have a mean velocity lower than the freestream. This wake forms from the boundary layer, either at the trailing edge of the model, or at the flow separation point. According to the law of continuity, the velocity outside the wake in a closed tunnel must be higher than freestream in order that a constant volume of fluid may pass through the test section. The higher velocity in the mainstream has, by Bernoulli's principle, a lowered pressure. Therefore, the wake places the model in a pressure gradient due to the velocity increment through the working section. Wake blockage, ϵ_{WB}, is the principal factor in blockage corrections, where the model has a high drag.

$$\epsilon_{WB} = [\frac{c}{2h}] C_{D_{uncorr}} \qquad 4:7$$

Here, ϵ_{WB} = Wake blockage factor, c = Total wing chord and h = Windtunnel test section height.

4.10.3 Total Blockage

The sum of the solid and wake blockage factors is:

$$\epsilon = \epsilon_{SB} + \epsilon_{WB} \qquad 4:8$$

4.11 Corrections

The total blockage factor ϵ is applied to the force and pressure coefficients as follows:

Corrected Lift:

$$C_L = C_{L_{un}} \frac{(1-\sigma)}{(1+\epsilon)^2} \qquad 4:9$$

Corrected Drag:

$$C_D = C_{D_{un}} \frac{(1 - \Lambda\sigma)}{(1+\epsilon)^2} + \Delta_\alpha C_{L_{un}} \qquad 4:10$$

Corrected Pitching Moment:

$$C_M = C_{M_{un}} \frac{(1 - \frac{\sigma C_L}{4})}{(1+\epsilon)^2} \qquad 4:11$$

Corrected Incidence: (Alpha in Radians)

$$\alpha = \alpha_{un} + \Delta_\alpha$$

$$\Delta_\alpha = \frac{\sigma}{2\pi} [C_{L_{un}} + 4C_{M_{un}}] \qquad 4:12$$

Corrected Velocity:

$$V = V_{un}(1+\epsilon) \qquad 4:13$$

$$C_P = \frac{C_{P_{un}}}{(1+\epsilon)^2}$$

UNLESS OTHERWISE STATED - ALL RESULTS IN THE FOLLOWING CHAPTERS ARE CORRECTED USING THE ABOVE METHOD.

4.12 Preliminary Testing

Two models were constructed, referred to here as model I and model II, in order to test the feasibility of using a symmetrical aerofoil section as a leading edge high lift device.

All three experimental models are NACA four digit wing sections and are therefore defined by the NACA four digit classification system. NACA four digit classification defines the first two digits as the percentage of camber (in the symmetrical case 0%) and the last two as the thickness chord t/c ratio, i.e. a NACA 0018 section has no camber and a maximum thickness of 18% its chord length.

4.13 Model I Design

The objective was to discover if a symmetrical section can function as a leading edge high lift device and augment maximum lift and incidence angle. The function of a symmetrical slat can be seen to be quite different from that of a standard aircraft slat, as shown in **Figure 4:7**. It was also not known if the slat would function with an axis of rotation in line with the wing centreline, and, if so, what degree of overlap it would require over the main wing.

4.13.1 Model Construction

Model I was constructed to assess qualitatively the effect of the slat arrangement shown above. As the geometry of the slat position was the main variable to be investigated, the model was therefore designed to provide as wide a range of configurations as possible.

4.13.2 Slat Design

The slat/wing chord ratio was chosen to be 20%, the same ratio used in standard slat arrangements. The section chosen for the slat also had to satisfy two opposing design criterion:

i) There is a need for structural integrity of both the model and a full scale wing. The section, which operates primarily at high angles of attack, is subject to a large spanwise bending moment. The result of

reducing both the wing chord and thickness ratio would be to reduce the strength of the slat.

ii) In the model design, the slat will be held fixed at the angle of incidence at which it is to be tested. As a result of this configuration, the slat must operate at angles of attack often much greater than the section stall incidence. When operating in this fully stalled condition, the section chosen should have a relatively low drag and therefore, low t/c ratio. The slat section should also have as small a chord length as possible, so as to present the smallest possible frontal area to the airflow.

As a result, it was decided that the slat should be a NACA 0010 wing section, a symmetrical section (necessitated by the design criterion that the slat must operate with flow approaching either surface) with a 10% t/c ratio. The chord length, as stated earlier in this section, was selected to be 20% of the wing chord, giving the normal c_s:c_w ratio of 1:5.

4.13.3 Main Wing Design

The wing section chosen was a NACA 0018 design (a symmetrical section with a t/c ratio of 18%). This was chosen for two reasons:

i) The section has a relatively large radius of curvature at the nose. This characteristic allows flow to stay attached at relatively high incidences. Aerofoils of relatively high thickness are normally used in plain wingsail applications.

ii) The section has a relatively high C_{Lmax} and does not have sudden stalling characteristics.

The span of the model, and so the aspect ratio, were limited by the need to limit the bending moment on the leading edge device. A main wing chord of 200mm was decided upon, and this in turn restricted the slat chord to 40mm

(1:5 ratio).

The standard structural formula for a beam with a uniform distributed load was used to calculate the maximum deflection of the slat. The slat was calculated to have a second moment of area, I = 2.133 x 10^{-10} m^4, and a distributed load, q = 35.43 Nm^{-1}. The formula for calculating maximum deflection y_{max} is shown below, where s = wing span (0.4 m) and E = Young's modulus of aluminum (7 x 10^{10} Nm^{-2}).

$$y_{max} = \frac{5}{384} \quad \frac{qs^4}{EI} \qquad 6:18$$

Displacement, y_{max}, for the slat under maximum loading conditions is less than 1 x 10^{-3} m and maximum bending moment is well within limits for the material. The model design is shown in **Figure 4:8**.

4.13.4 Variable Geometry Design

As stated above, it was necessary to develop some system for positioning the slat in a large number of configurations. It was necessary to provide a series of pivot points for the slat itself and for a number of 'Overlap distances'. Overlap distance is defined as the length by which the slat is overlapping the wing, measured when the slat is at zero incidence. The slat arrangement decided upon is shown in the **Figure 4:9**. This arrangement can be seen to provide 25 different flap pivot positions (not including the actual setting angle of the slat).

4.14 Model II design

The low C_{Lmax} attained by Model I, when compared with published NACA data, was attributed to two factors:

i) A low experimental Reynolds number, compared with NACA published data.

ii) 3 - Dimensional aerodynamic effects acting at the model wingtips.

Model I results were, however, left uncorrected for Reynolds number and aspect ratio. The primary purpose of the model was to provide a qualitative indication of the effect of the leading edge device.

Model II was designed as a larger scale version of model I. The main wing chord length was increased to 350mm and the span increased to 600mm. The slat chord: wing chord ratio, c_s:c_w, remained at 1:5, Thus the large span, although reducing the Aspect Ratio from model I, produced a large bending moment on the leading edge slat. Thus, the slat was pivoted at the mid-span point, which is the point of maximum bending.

The wing and slat sections remained as NACA 0018 & 0010 respectively. Endplates were added to the model in order to reduce the 3 dimensional aerodynamic effects caused by wingtip vortices. Endplates also increased the effective aspect ratio of the model. Finally, 20 pressure tappings were placed on both the upper and lower surfaces of the wing, staggered at 45˚ to prevent any interference from an upstream tapping. Model II is shown in **Figure 4:10**.

Following flow visualisation experiments, both force and pressure results for model II were considered unreliable. Flow visualisation showed very large flow disturbance over the wing caused by both the central slat support and the main wind tunnel support attachments. It was proven that the flow disturbance from the tunnel supports was interfering with the pressure tappings on the model surface. Cowling the tunnel attachments did nothing to reduce this effect. The flow disturbance created by the central slat support was considered too great, to guarantee accurate force results. Therefore, results from model II do not appear in this work.

4.15 Model Mounting

A previous research project in windtunnel no.1 [33] at Salford University showed that mounting a wingsail in vertical manner, using the main spar or 'mast' as the balance support, produced inaccuracies. A balance interference between the sideforce (lift for the wingsail) and drag force was noticed. This interaction became greater with increasing wingsail test incidence.

This balance interaction is not due to a fault in the balance itself, but to the way that the balance is designed to support models. The balance is designed to support models mounted in a horizontal plane, at the centre of the working section. As a result of the balance configuration, vertical loads and horizontal loads in the plane of the airflow (lift and drag forces for a horizontally mounted wing) may be large, whereas the maximum balance loads in the horizontal plane across the airflow (sideforce for a horizontally mounted wing) and the three moments are all small. The vertically mounted model creates forces and moments which are greater than balance tolerances; hence the balance arms rest upon limiters and render any results erroneous.

If a model is supported in such a manner that lift is created in a vertical direction, the horizontal forces of drag and sideforce will not interfere. All three models tested in this thesis have been two dimensional and supported in the horizontal plane. As stated in the introduction, **Section 1.2.2**, wingsail sections using auxiliary power units (APU's) rarely taper. In this APU role, emphasis is placed on the simplicity of the device. Aircraft wing technology is suitably advanced to allow untapered sections to be constructed to the required structural integrity. The additional heeling moment created by an untapered wing is negligible on the size of vessel likely to use a wingsail as an APU. However, pure sailing vessels may require a tapered section to reduce heeling moment.

CHAPTER 5 - APPARATUS & CALIBRATION

A = Cross Sectional Area

k_1,k_2,k_3 = Loss Coefficients

K = Tunnel Calibration Factor

P = Pressure

q = Dynamic Pressure

u = Instantaneous Voltage

u′ = Voltage Deviation

U = Average Velocity

$_D$ = Upstream Station 2

$_J$ = Test Section Station

$_U$ = Upstream Station 1

Chapter 5

APPARATUS & CALIBRATION

5.1 Windtunnel

All experimental work for the research was conducted in the No.1 low speed windtunnel, located in the Department of Aeronautical Engineering at the University of Salford. This low speed, closed return tunnel is shown schematically in **Figure 5:1**. The wind tunnel has a 0.91 x 1.22 x 1.83 metre, (3′ x 4′ x 6′) working section. Power is provided by a 150 kW variable speed electric motor driving an eight bladed fan via a belt drive. This combination provides an air speed in an empty tunnel section of between 0 and 50ms^{-1}

5.1.1 Model Mounting

All three models were mounted in a horizontal plane (the manner normal for an aircraft or wing), with two main supports and a single trailing arm. The main supports record lift, drag and side forces along with rolling and yawing moments. The pitching moment is recorded by the trailing arm.

The model III trailing arm support attached to the balance single moment arm, then forked, attaching the model as two supports. This twin trailing support design reduced the spanwise bending moment on the trailing edge of the model.

5.2 Tunnel Calibration

As both the tunnel motor and fan had recently been replaced, it was necessary to establish the flow quality in the working section. Therefore, a 'survey' of the flow quality and nature throughout the windtunnel working section was performed. This was done in three stages:

i) Pitot Static scan

ii) Assessment of crossflow components.

iii) Turbulence investigation.

5.2.1 Pitot Static Scan

A Pitot static rake, shown in **Figure 5:2a**, was used to record the tunnel dynamic pressure. The rake consists of eight Pitot static tubes arranged at various points in the y-direction, enabling the whole height of the tunnel to be scanned at each station. The rake was positioned at 7 stations across the width of the tunnel (in the x-direction), giving a grid of 8 x 7 for every traverse. The rake was traversed at 5 stations, in the streamwise direction (or the z-direction), and the grid created is also shown in **Figure 5:2b**. Station 3 is the mid-point of the working section and is where the main balance struts are located.

The results from the Pitot static rake were plotted to show the pressure or velocity variations in isobaric form, constant pressure contours, at each of the five stations in the streamwise direction. The results for static pressure were also analysed in the streamwise direction, to verify that no pressure gradient existed along the working section. The results are shown as constant pressure contours in **Figures 5:3 a-e**, as a percentage deviation from the average flow velocity U_∞ (U_∞ = 42.3 ms^{-1}, for the results shown) at streamwise stations 1-5.

5.2.2 Velocity Distributions

The variations of the tunnel velocity do not show any large fluctuations in the flow at any point. This is borne out by the percentage deviation graphs of

flow velocity which vary by less than 1% in the centre 50% (0.45 x 0.6 m) of the tunnel and less than 5% by the working section door.

As expected, the largest deviations of flow velocity, from average, are found at the tunnel walls. The actual section of the tunnel which the model will occupy (station 3), is shown in **Figure 5:3c**. This figure shows a maximum deviation from average flow velocity, in the centre region, of less than 1%, the equivalent of +/- 0.3ms^{-1} at 40 ms^{-1}. To put this deviation into perspective, the manometer reading, due to human experimental error, can only be justified to +/- 1mm. This deviation would create a velocity variation of +/- 0.2ms^{-1}. The tunnel velocity variations are therefore assumed to be acceptable.

5.2.3 Tunnel crossflow components

This test is performed using two Pitot tubes, arranged as shown in **Figure 5:4a**, known as a 'yawmeter'. A tapping is connected to either side of a U-tube manometer. When the tunnel is run, the yawmeter is rotated until the fluid in the U- tube Manometer is level (i.e. there is equal pressure on the two tubes). The angles of the tubes to the flow are then recorded. At various coordinates, the cross flow meter was traversed across the tunnel to create a grid also shown in **Figure 5:4b**. These readings were performed with a vertical and horizontal axis of rotation. The results were then resolved as shown in **Figure 5:4c**. Vertical and horizontal crossflow components are calculated, by trigonometry, from the tunnel velocity and crossflow angles recorded at each position shown in **Figure 5:4b**. The horizontal and vertical components are then resolved into one single resultant vector which describes the magnitude and angle of the crossflow components. An example of the calculation method described, is shown in **Figure 5:4c**.

5.2.4 Crossflow Results

The cross flow results are shown in **Figure 5:5**. These results show relatively small cross flow components in the working section.

The tunnel crossflow distribution does not show any major flow circulation;

again, as expected, the cross flow values are largest around the bevelled tunnel corners. If the centre 50% of the tunnel section is considered, **Figure 5:5** shows that the average flow deviation is less than 2°. The accuracy of the crossflow measurement equipment is +/- 1°. Even with a compound error of flow deviation and measurement accuracy of 3°, a C_L of 1.0 would only be altered by a maximum of 3%, this is considered to be reasonable.

5.2.5 Turbulence Measurements

The tunnel turbulence measurements were recorded by a thermo-resistive hot-wire anemometer. The hot wire is held at a constant temperature in the flow. The variation in resistance needed to maintain a constant temperature of the wire is then manipulated, to calculate the turbulence intensity. The turbulence intensity is calculated using **Equation 5:1** from the flow velocity fluctuation, shown in **Figure 5:6**. U = average voltage, u = instantaneous voltage, u' = voltage deviation and $\bar{u}'$ = time averaged voltage deviation.

$$LONGITUDINAL\ TURBULENCE\ \ INTENSITY\ \ = \frac{\sqrt{\bar{u}'^2}}{U} \qquad 5:1$$

This test was performed at station 3, the mid-point of the working section, using the same x & y coordinates as **Figure 5:2**. The results for this test were recorded by the DANTEC hot-wire anemometry software on a personal computer. DANTEC software is widely used across the fluid dynamics field and allows easy and accurate calibration of the hotwire prior to use, along with instantaneous results and an instantaneous graphical output of turbulence levels.

5.2.6 Turbulence Conclusions

The results from the turbulence intensity test are shown as a percentage turbulence value in **Figure 5:7** (average freestream velocity U_∞ = 42.3 ms^{-1}, for the results shown). The results for this test were extremely encouraging, turbulence intensity levels were less than 0.5 percent throughout the section. The highest turbulence intensity occurred close to the tunnel walls and the lowest occurred in the tunnel centre. These results agree with the velocity

profile plots discussed earlier.

It is usually stated that the percentage turbulence intensity for a tunnel of this kind is less than 2-3%. In the case of this tunnel section, the highest turbulence intensity measured was 0.4%, the average intensity in the centre of the working section being 0.3%. These values show the high quality of flow in the tunnel. Credit for this accuracy is due to tunnel design and the servicing of all tunnel vanes and mesh upstream of the working section prior to testing.

5.3 Aerodynamic Balance

The aerodynamic balance is a model 158 manufactured by TEM Engineering Ltd. and installed in 1974. The balance is serviced regularly, most recently in 1994. It is a six component virtual axis type balance, capable of measuring drag, lift, side force, pitching moment, rolling moment and yawing moment. Pitch and yaw angles are controlled by electric motors and gearboxes, angular ranges being +/- 40 degrees of incidence and -115 to +225 of yaw. For the purposes of this testing, only the pitch variation is of interest.

Load and moment capacities of the balance are as follows:-

Drag	+/- 70 N
Lift	+/- 220 N
Sideforce	+/- 140 N
Pitching moment	+/- 12 Nm
Rolling moment	+/- 4 Nm
Yawing moment	+/- 4 Nm

For the purpose of this experimentation a greater lift, drag and pitch maximum were required in the one direction. As a result, mechanical counterbalances were employed to alter the balance range. The new ranges are as follows:-

Drag	+120 to -20 N
Lift	+400 to -40 N
Pitching moment	-18 to +6 Nm

Force transducers connected to the balance provide an electrical output proportional to the load or moment. Voltages produced are displayed on a digital voltmeter (DVM), but are also recorded by a digital data acquisition system (DAS) described below. Prior to the DAS calibration, the linearity of the balance (with counterbalances in place) was investigated. This linearity was found to be within 2% and considered acceptable. All forces and moments are also accurate to within 2%. An inclinometer was used to investigate the accuracy of the DVM calibration for incidence angle. The DVM readings were found to be within 3% of the actual incidence angle across the entire incidence range, +/- 30˚.

5.4 Data Acquisition Software

The aim and objective of the data acquisition software was to increase the speed and accuracy of the data recorded at the testing stage.

The original data acquisition method consisted of the six force/moment coefficients being fed down from the balance to a Wheatstone bridge, and then recorded manually from a digital volt meter. Any analysis of pressure tappings required was also performed manually on an inclined manometer bank.

The data acquisition software was designed to eliminate some of the possible sources of error in the original data acquisition system. Listings of the PASCAL programs used to record the force and pressure measurements are shown in **Appendix B**. The software requires two additional boards to be fitted to a personal computer:

i) PC27 - An analogue to digital signal convertor.
ii) PC14AT - A counter/timer board.

The 'balance' section of the program obtains the forces or moments required from the balance, samples each force 100 times (each sample taking just over a millisecond)

and writes the average force recorded to file. This function can be repeated over a range of incidence angles.

The 'scani' section of the program uses a scanivalve to perform the role of a manometer. A scanivalve is an electronic device, powered by a stepper motor, which rotates, aligning its single pressure transducer with the corresponding pressure tapping required. The scanivalve is first set to 'home', which would correspond to the pressure tapping zero, and is then stepped one tapping at a time up to a maximum of 48. The program sets the scanivalve to a home position, and then steps it through the requested pressure tappings. Each tapping is sampled/averaged a specified number of times, and the data are then written to file. This function can also be repeated if a range of readings is required. The scanivalve and transducer were both manufactured by the Scanivalve Corp, San Diego, the pressure transducer having a range of +/- 1 Psi.

Both programs can be run in harmony on a single microprocessor, therefore allowing balance readings and then pressure tappings to be recorded at each incidence. The program was written in the PASCAL programming language although it can be operated as a stand alone executable program.

The data acquisition software fulfils its aim to eliminate possible sources of error at the data acquisition stage in the following ways:

i) The time taken to record the readings is vastly reduced (especially those taken from the manometer), therefore reducing the windtunnel temperature (and therefore Reynolds number) change during readings.

ii) Manometer readings cannot be erroneous due to 'human errors'. The largest human error is due to parallax whilst reading the fluid heights.

iii) All readings are sampled and averaged around 100 times, giving a consistent statistical accuracy of results.

iv) Finally, the data acquisition software itself is checked regularly, to ensure that the calibration settings remain correct.

5.5 Dynamic Pressure Measurement

An AVAG Betz manometer is used in order to calculate the test section dynamic pressure. The manometer is connected to static wall pressure tappings at two positions in the wind tunnel contraction. Calibration of this arrangement is required because the pressure tappings are not actually situated within the test section. With reference to **Figure 5:8**, J is the position of the Pitot static tube in the centre of the working section. The total pressure at the two points U and D should the same. However, due to loss, the downstream pressure is slightly smaller. Hence;

$$P_U + q_U = P_D - q_D k_1 + q_D \qquad 5:2$$

where k_1 is the loss coefficient of the section between the static readings. P and q are static and dynamic pressures respectively.

$$P_U - P_D = q_D - k_1.q_D - q_U \qquad 5:3$$

If the cross sectional area = A

$$A_U.U_U = A_D.U_D. \qquad 5:4$$

Squaring and multiplying by $\rho/2$:

$$\rho/2\ A^2_U.U^2_U = \rho/2\ A^2_D.U^2_D \qquad 5:5$$

Let $q = \frac{\rho U^2}{2}$, $k_2 = \frac{A^2_D}{A^2_U}$

then;

$$q_U = k_2.q_D \qquad 5:6$$

Therefore:

$$P_U - P_D = q_D - k_1.q_D - k_2.q_D \qquad 5:7$$

$$= q_D (1-k_1-k_2)$$

Also, since,

$$q_U = q_J \frac{A^2_J}{A^2_U} \qquad 5:8$$

$$= k_3 q_J,$$

where

$$k_3 = \frac{A^2_J}{A^2_U}. \qquad 5:9$$

Hence;

$$P_U - P_D = (1-k_1-k_2).k_3 q_J \qquad 5:10$$

$1/(1-k_1-k_2).k_3$ is known as the tunnel calibration factor *'K'* and was derived experimentally as described below.

With the tunnel section empty, values of $P_U - P_D$ were read from the Betz manometer for several tunnel speeds. Corresponding test section dynamic pressures (q_J) were obtained from the average Pitot static readings taken at the working section mid-point. **Table 5:1** gives the resultant experimental values. From these figures a tunnel calibration factor *'K'* of 1.18 was determined for the tunnel at all velocities.

BETZ READING (mmH_2O)	K	VELOCITY (ms^{-1})
8.93	1.175	40
7.47	1.176	37.5
6.51	1.175	35
4.61	1.175	30
3.20	1.177	25

TABLE 5:1

5.6 Model III Description

A full set of drawings for model III are shown in **Appendix C**. The aerofoil sections which comprise the complete triple element aerofoil were all constructed to a high level of surface finish. The main wing and flap are constructed from 2mm thickness steel plate, onto which aluminium main and rear spars are attached. Aluminium is employed here to reduce the model weight. The main spar is two 25.6 x 12.8 x 800 mm bars which are drilled and tapped, and attached by countersunk screws. The rear spar consists of two 12.8 x 12.8 x 800 mm bars attached to the steel plate using the same method employed for the main spar. The tunnel supports are attached to the main spar, which is situated on the 1/4 chord point of the main wing section. Two blocks of expanded polyurethane foam sandwich this frame. Accurately shaped templates are then attached to either end and used to give the final profile of the wing. Grooves are milled spanwise along the wing and 3/32″ brass tubing is laid in, to be used for pressure tappings. A skimming plaster is then used to fill any air bubbles in the foam. Several coats are applied to provide a smooth surface, on to which several coats of paint are also applied. Finally the wing is polished with 800 grade 'wet and dry' sandpaper.

The slat was constructed in the University Departmental workshops from hardened steel bar. This bar was then milled to the appropriate NACA section coordinates, accurate to 5/1000th inch (1/8th millimetre). The result after polishing was a high quality, geometrically accurate finish. Model III plan and profile are shown in **Figure 5:9**.

5.6.1 Pressure Tappings

The main wing is pressure tapped at 24 chordwise stations. The tappings are staggered at 45°, to prevent any flow disturbance from an upstream tapping. The layout of both wing and flap tappings is shown in **Figure 5:10**. The first 10 tappings are closely spaced. This gives the best possible results in the rapidly changing pressure distribution which occurs in the first 25% chord. The pressure tappings on the flap are similarly arranged; 16 tappings, 7 in the first 25% flap chord. The wing and flap tapping positions are shown in **Table 5:2**.

MAIN WING		FLAP	
TAPPING NO.	x/c_w	TAPPING NO.	x/c_f
1	0.00	1	0.04
2	0.01	2	0.07
3	0.02	3	0.11
4	0.04	4	0.14
5	0.07	5	0.18
6	0.09	6	0.22
7	0.11	7	0.25
8	0.14	8	0.29
9	0.17	9	0.36
10	0.21	10	0.43
11	0.26	11	0.50
12	0.31	12	0.58
13	0.36	13	0.65
14	0.41	14	0.72
15	0.46	15	0.79
16	0.51	16	0.86
17	0.55		
18	0.60		
19	0.65		
20	0.69		
21	0.74		
22	0.79		
23	0.83		
24	0.90		

TABLE 5:2

Although it would have been interesting and informative to have pressure tappings on the leading edge slat, this was not possible. Milling a channel for pressure tappings was prohibited by the thinness of the section and the reduction in structural integrity this would cause.

5.6.2 Variable Geometry System

The flap adjustment system is identical to that used on models I and II and is designed to allow flap deflections up to +/- 30˚, in 5˚ increments and is shown in **Figure 4:8**.

It was necessary to provide a number of pivot points for the slat itself and a number of 'overlap' settings. Overlap distance is defined as the distance by which the slat is overlapping the main wing, measured when the slat is at 0˚ incidence. The arrangement allows any slat angle between 0 and 60˚, and 25 combinations of overlap and pivot point, with the slat positioned (or overlapping) either side of the main wing section, thus maintaining symmetry.

5.6.3 Endplates

Endplates were fitted to the model in an attempt to reduce the three dimensional aerodynamic effects caused by wing tip vortices. Endplates are attached directly to the model, allowing force measurements to be recorded by the balance via model supports.

The endplates are constructed from 7mm thick transparent perspex sheet, with all four edges chamfered to an angle of 45 degrees to reduce any turbulence caused by the endplate leading edges. Endplate size is 0.6 x 0.24m.

CHAPTER 6 - CFD DESCRIPTION & THEORY

C_1, C_2 = Turbulent Flow Constants

C_μ = Turbulent Model Parameter

G = Mean Strain Rate

k = Turbulent Kinetic Energy

P = Fluid Pressure

u = x-velocity Component

u_δ = Velocity Parallel to the Wall

v = y-velocity Component

y^+ = Turbulence Inner Variable

B = Dimensionless Turbulence Constant

Γ = Turbulent Dissipation Transport Coefficients

δ = Distance from Wall

ϵ = Turbulent Dissipation Rate

κ = Dimensionless Turbulence Constant

μ = Fluid Laminar Viscosity

μ_e = Effective Velocity

ν = Kinematic Velocity

ρ = Fluid Density

τ_w = Wall Shear Stress

Chapter 6

CFD Description & Theory

6.1 Introduction to CFD

In the past, analytical methods and/or experimental measurements have been used to study flow fields around objects. Computational Fluid Dynamics (CFD) did not emerge as a new entity, but rather as a refinement of an existing discipline. This discipline is the numerical analysis of Partial Differential Equations (PDE's). The vast improvements in computers in the past 20-25 years have made CFD possible as a supplement to analytical and experimental methods.

Experimental testing is still the major tool used to understand flows around or inside objects. CFD is unlikely to replace windtunnel testing and experimental measurements for the foreseeable future. The advantages and drawbacks of CFD and experimental work are shown below:

EXPERIMENTAL ANALYSIS	CFD
Limited measurements at limited points	Most parameters defined throughout the flowfield
Some conditions impossible	Most conditions can be calculated
Running costs high	Development cost high
Reliability established (With good experimental procedures)	Reliability not established

It is not the aim of CFD in engineering to solve PDE's, the result of which may have no correlation with the physics of the flow. The aim of CFD in most cases in engineering is to try to simulate flow fields.

For CFD work, the physical space is divided into a mesh or grid. At each point a set of PDE's are solved with the appropriate boundary conditions and initial conditions. This process is repeated until the solution has settled down, or in the CFD terminology converged. Time independent equations are solved by an iterative process, altering flow parameters and re-calcualting the solution until these solutions do not change from one iteration to another. This process is common to incompressible viscous and inviscid flow calculations.

Alterations in CFD can be made very easily to flow conditions. For example, to simulate sea level flight and cruise at high altitude are just a matter of altering a few initial & boundary conditions. Alterations in geometry are also relatively simple; altering aerofoil thickness or profile is as simple as typing in the new geometry. A similar alteration for an experimental model could involve building a new model or requiring a different windtunnel to simulate the correct Reynolds number & Mach number. CFD is also useful if experimental testing is impossible at operational Reynolds numbers. A qualitative relation can be made between experiment and CFD at an experimental Reynolds number. This relation can then be used to give an approximate result at the operational Reynolds number.

CFD, however, is not an exact science, since the whole concept is based on a series of assumptions and simplifications. Applying CFD to actual flow fields requires good knowledge of aero or fluid dynamics, together with an understanding of the capability of CFD and the computational methods used to simulate the flow. The most important aspects of CFD modelling are described in **Chapter 7**.

6.2 Numerical Methods

The basic flow equations are, as stated, PDE's and have to be solved numerically. There are various methods which solve these equations, the following being the most common methods in use today:

i) Finite Difference/Volume Methods (FDM/FVM)

The most commonly used model for CFD. A FDM/FVM is a numerical approximation scheme. There are a large number of different FDM/FVM methods for incompressible, compressible, steady and unsteady flow problems.

ii) Finite Element Method (FEM)

This is a relatively new method for fluid problems, although it has been used extensively on structural problems for many years. Since this method allows the free division of elements, the mesh can be either structured or unstructured. This flexibility allows complex geometry such as multi element wings to be handled easily. This method is, however, more complex and requires more computing power than the FDM/FVM methods.

iii) Boundary Integral Methods (BIM)

There are various methods in this category: Panel method, Singularity method, Vortex-Lattice method and the Discrete vortex method. Most BIM concern only the boundaries of flow, such as wing and body surfaces. The discrete vortex method only concerns flow vorticity and/or boundaries.

Table 6:1, shows the relative advantages/disadvantages of each method:

	FDM/FVM	FEM	BIM
MESH	Structured	Structured and unstructured	Only boundaries
FLOWS	Almost any	Almost any	Potential,Stokes
MATRIX	Large, inversion may be needed	Large and inversion needed	Relatively small
FEATURES	Widely used	Complex Geometry	Body surface & boundaries in unidirectional flows

TABLE 6:1

6.3 Choice of Numerical Method

It has already been stated that FEM is one of the most applicable CFD methods for multi element wing sections. The disadvantages of FEM are outweighed by the increased accuracy which can be obtained by creating an effective mesh around the elements. Therefore, FEM will be used.

6.4 Commercial Package vs. Purpose Written Code

Due to the combined experimental/computational nature of this research, time constraints made it impossible to develop a purpose-written CFD code. Therefore, a commercially written CFD package is employed. This package has the advantage of being robust and comprehensive in terms of functions available and adaptability. The penalty paid for this versatility is that packages are relatively slow and inefficient, as many unwanted parameters and functions are computed. This inefficiency manifests itself in increased Central Processor Unit (CPU) time and storage requirements.

6.4.1 Finite Element Package Employed: FLOTRAN™ & ANSYS™*

A Pre/Post-processor ANSYS™ *v5.0* was used in conjunction with FLOTRAN™ *v2.0*, a FEM fluid dynamic solver.

* *ANSYS™ is primarily a FEM structures package in which only the mesh generation and post-processor are used.*

The operational stages involved with the package are shown in **Figure 6:1**. A full description of these stages is given in **Sections 7.3-7.6**.

6.5 Pre-Processing

Grid generation is the main task involved in pre-processing. In some packages, such as ANSYS, initial conditions must be applied in pre-processing, although initial conditions may also be applied prior to solving in FLOTRAN.

6.5.1 Grid Generation

The initial stage of a CFD calculation is to create a grid or mesh in the physical space (domain) around the model to be tested. This is one of the, if not the most important, preparations for CFD testing. A well constructed grid, e.g. without a significantly skewed mesh, will require no sudden changes in mesh interval. At each grid point, calculations are carried out for each equation, e.g. continuity, momentum and energy equations. The quality of the mesh affects the results in the following ways:

a) CPU memory size
b) CPU time
c) Accuracy
d) The stability and convergence speed of the solution

A mesh should also be smooth, as orthogonal as possible, and dense where flow properties change rapidly and gradients are steep, thus maintaining accuracy. Mesh generation is described in detail in **Section 7.4**.

6.6 Solver

FLOTRAN contains no graphical interface, just a basic DOS text style input/output. The purpose of this is to minimise time wasted with unnecessary display functions and maximise processing speed. FLOTRAN can also be run embedded in the ANSYS pre/post processor; this is, however, extremely slow and inefficient.

6.7 Post-Processing

Data presentation is very important since it allows the user to display the model, mesh and results in almost any format which the user desires. Velocity and pressure distributions can be displayed as contours of equal value, vectors or text format at any node, line or area in the entire flow domain and streamlines can be traced both upstream and downstream. Any available parameter can also be output directly to file, enabling a graphical output to be quickly and simply obtained.

6.8 FLOTRAN Technical Formulation

The FLOTRAN formulation [20] is fully three-dimensional, but the current application considers steady two-dimensional turbulent flow in Cartesian coordinates. For the purposes of clarity, the following discussion will be limited to the formulation as it applies to the solution type, i.e. only the two-dimensional governing equations are discussed.

6.8.1 Governing Equations

The governing equations are the two momentum equations and the continuity equation. Dependent variables are the x & y velocity components and pressure. The following equations are the time averaged forms where turbulence effects are modelled by the inclusion of an effective viscosity.

$$\rho u\frac{\partial u}{\partial x}+\rho v\frac{\partial u}{\partial y}=-\frac{\partial P}{\partial x}+\frac{\partial}{\partial x}(\mu_e\frac{\partial u}{\partial x})+\frac{\partial}{\partial y}(\mu_e\frac{\partial u}{\partial y})$$

$$\rho u\frac{\partial v}{\partial x}+\rho v\frac{\partial v}{\partial y}=-\frac{\partial P}{\partial y}+\frac{\partial}{\partial x}(\mu_e\frac{\partial v}{\partial x})+\frac{\partial}{\partial y}(\mu_e\frac{\partial v}{\partial y})$$

$$\frac{\partial(\rho u)}{\partial x}+\frac{\partial(\rho v)}{\partial y}=0 \qquad 6:1$$

In the above equations, ρ is the fluid density, P is the fluid pressure, u is the x-velocity component and v is the y-velocity component. The effective viscosity, μ_e, is the sum of the turbulent or eddy viscosity and the laminar fluid viscosity.

The formulation embodied in FLOTRAN allows for variable density and viscosity. The current thesis is involved with steady incompressible problems. The basic formulation is not necessarily restrained to the above constraints, however.

Turbulence is modelled using a two equation k-ϵ turbulence model. The two equation turbulence model requires the solution of two additional governing equations to determine the turbulent kinetic energy and the turbulence dissipation rate. The governing equations for the turbulent kinetic energy (k) and the turbulence dissipation rate (ϵ) are as follows:

$$\rho u\frac{\partial k}{\partial x}+\rho v\frac{\partial k}{\partial y}=\frac{\partial}{\partial x}(\Gamma_k\frac{\partial k}{\partial x})+\frac{\partial}{\partial y}(\Gamma_k\frac{\partial k}{\partial y})+\mu_t G-\rho\epsilon$$

$$\rho u\frac{\partial \epsilon}{\partial x}+\rho v\frac{\partial \epsilon}{\partial y}=\frac{\partial}{\partial x}(\Gamma_\epsilon\frac{\partial \epsilon}{\partial x})+\frac{\partial}{\partial y}(\Gamma_\epsilon\frac{\partial \epsilon}{\partial y})+C_1\mu_t\frac{\epsilon}{k}-C_2\rho\frac{\epsilon}{k} \qquad 6:2$$

The governing equations for the turbulent kinetic energy and turbulent dissipation rate are quite similar. In both equations, the terms to the left of the equality sign represent advection transport, whilst the first two terms to the right of the equals sign represent diffusive transport. The turbulent diffusion transport coefficients (Γ_k and Γ_ϵ) are taken as proportional to the turbulent viscosity. The remaining terms represent production and dissipation. The production of turbulent kinetic energy is proportional to the mean strain rate (G) of the fluid. The two constants (C_1 and C_2) appearing in **Equation 6:2** are derived from a comparison with experimental data from several different types of turbulent flow including plane jets, mixing layers and shear layers. FLOTRAN uses the standard values $C_1 = 1.44$, $C_2 = 1.92$.

The turbulent effective viscosity is calculated as a local function of the turbulent kinetic energy and dissipation rate using the following relation:

$$\mu_e = C_\mu \frac{k^2}{\epsilon} + \mu, \qquad 6:3$$

where μ is the fluid laminar viscosity, and C_μ is the turbulence model parameter. FLOTRAN uses the standard value $C_\mu = 0.09$.

6.9 Near-Wall Turbulence Model

The k-ϵ model implemented in FLOTRAN is a high Reynolds number model and is therefore not valid near a no-slip wall. Consequently, the law-of-the-wall and log-law-of-the-wall models are used to approximate the turbulent boundary layer velocity profile. These approximations are often used in numerical modelling of turbulent flows to avoid having to refine substantially the mesh in the area of the wall. The law-of-the-wall is used very close to the wall in the laminar sublayer and the log-law-of-the-wall model applies to the overlap layer, as illustrated in **Figure 6:2**.

The law-of-the-wall velocity profile is defined as:

$$u_\delta = \delta \frac{\tau_w}{\mu} \qquad 6:4$$

where δ is the distance from the wall, u_δ is the velocity parallel to the wall, τ_w is the wall shear stress and μ is the laminar viscosity. The log-law-of-the-wall profile is:

$$\frac{u_\delta}{\sqrt{\frac{\tau_w}{\rho}}} = \frac{1}{\kappa} \ln \left(\frac{\delta}{\nu} \sqrt{\frac{\tau_w}{\rho}} \right) + B \qquad 6:5$$

where B and κ are dimensionless constants, ν is the kinematic viscosity. FLOTRAN uses the standard values (B = 5.5 and κ = 0.4). **Equation 6:5** can be rewritten using the inner variable y^+.

$$y^+ = \frac{\delta}{\nu} \sqrt{\frac{\tau_w}{\rho}} \qquad 6:6$$

Using y^+, equation 6:5 becomes:

$$\frac{u_\delta}{\sqrt{\frac{\tau_w}{\rho}}} = \frac{1}{\kappa} \ln y^+ + B \qquad 6:7$$

6.10 Finite Element Mesh

For this application, the solution domain is descretized using 4-node quadrilateral elements. A typical element is illustrated in **Figure 6:3**. Both components of velocity are defined at the four node points (i,j,k,l) indicated in the figure. Most previous FEM's have used a mixed order approximation for velocity and pressure, where the pressure approximation is one order lower than the approximation used for velocity. The FLOTRAN formulation, however, is based on an equal order approximation. All variables, including both velocity components and pressure, are approximated over an element using the same bi-linear shape functions. The shape functions (N) have the following form:

$$N(x, y) = ax + by + cxy + d$$

where the four constants (a,b,c,d) are determined from the element geometry.

CHAPTER 7 - CFD TESTING PROCEDURE

C_f = Friction Coefficient

$u_{(x,y)}$ = Local Flow Velocity

U_∞ = Free Steam Velocity

δ_1 = Displacement Thickness

δ_2 = Momentum Thickness

Chapter 7

CFD Testing Procedure

7.1 Model Construction Process

As described, prior to testing the computational model must be created. This is done in three stages. Firstly, the model geometry is defined, followed by mesh construction and finally, the boundary conditions are applied. The parameters which define model geometry, mesh structure and boundary conditions are all contained in a file, known as a '.log' file. A .log file may be viewed in a 'text editor' program, or executed in the ANSYS pre-processor.

*The **.log** files which define the computational models are included with this thesis on 3.5" disk. Some of the more important **.log** files (that of the flat plate model, the plain NACA 0018 wing and the full, final triple element model) are all shown in **Appendix B**.*

7.2 Finite Element Mesh Construction

External flow analyses typically employ what is referred to as either an O, C or H type mesh. These three basic mesh types are illustrated in **Figure 7:1**; some of the advantages/disadvantages of these meshes are shown in **Table 7:1**.

	C - MESH	H - MESH	O - MESH
ADVANTAGES	Refined mesh at aerofoil surface	Few skewed elements	Refined mesh at aerofoil surface
DIS-ADVANTAGES	Unrequired mesh density downstream of the model	Unrequired mesh density both up & downstream of the model	Insufficient mesh density at the aerofoil trailing edge and wake

TABLE 7:1

After testing all three types of mesh, for convergence speed, accuracy and memory required the O-mesh was chosen for the aerofoil section and the C-mesh for the flat plate model. The O-mesh was designed by modifying the ANSYS benchmark NACA 0012 mesh (shown in **Appendix B**) to suit the required aerofoil and mesh density. This O-mesh overcomes the lack of mesh density found at the trailing edge of an aerofoil by adding in two patches which provide a bridge between the required density and the rapidly diverging element size. The paper written by J.G. Rice et al. (FLOTRAN developers) [21] describes the procedure for creating an O-mesh for a multi element model. In the multi element case each aerofoil element is placed in a dense O-mesh. Then a larger O-mesh of radius equal to the total chord length is placed around the model. Finally, a large O-mesh, with a 10 chord length radius, is created to describe the entire flow domain.

7.3 Model Geometry

The construction of the finite element model is a two-step process. The first step is to construct the geometry of the model, the second to apply a finite element mesh to that geometry. ANSYS allows the user to construct interactively the geometry and FE mesh; at each step in this process, the model is displayed graphically.

The process involved in constructing a geometry model for a aerofoil system is described as follows: the lines defining the surfaces of aerofoil elements are defined using various curve fit options, most commonly splines. The overall solution domain is constructed from a series of two-dimensional 'patches' or areas, shown in **Figure**

7:2b. Initially, the patch structure in the region near the surface of the model creates an 'O' mesh with a radius of approximately 1 chord length, as shown in **Figure 7:2a**. Around this dense mesh, another 'O' mesh is created extending to approximately 10 chord lengths from the aerofoil shown in **Figure 7:3**.

7.4 Mesh Generation

Once the geometry has been defined, the finite element mesh is then generated for that geometry. Again this is an interactive process and the resulting mesh is viewed graphically as it is created. The mesh generation process is performed on a patch by patch basis, thus allowing the construction of very complex geometries. This process enables mesh density to be controlled precisely.

Using the properties listed above, the mesh shown in **Figure 7:3** was created. An O-type mesh is placed around the aerofoil element, and then a larger O-type mesh around the entire flow domain. This approach allows for a very effective mesh design. The density of nodes in the region near the aerofoil surface is high and, at the same time, the nodal density smoothly decreases away from the surface region. The resulting elements do not have excessive aspect ratios or skew angles.

7.5 Boundary Conditions

The final step in the generation of the finite element model is the specification of the required boundary conditions for the problem. The three types of boundary conditions were common to all models tested: a free-stream, a constant pressure boundary and no-slip surface boundaries.

7.5.1 Free Stream Boundaries

Since the solution coordinate system is fixed relative to the aerofoil, at a free-stream boundary it is assumed that the velocity is undisturbed. Therefore the free-stream boundary is simply the velocity of the undisturbed air in which the aerofoil is moving. This boundary must then be sufficiently far from the surface of the aerofoil for this approximation to be reasonable. As mentioned earlier, the overall solution domain, and hence the free-stream boundary, are placed approximately ten chord lengths away from the aerofoil surface.

7.5.2 Constant Pressure Boundary

At a downstream boundary, it is assumed that the static pressure is undisturbed by the presence of the aerofoil and the pressure value is uniform at an arbitrary level. As with the free-stream boundary, this boundary must also be sufficiently far away from the aerofoil for this approximation to be reasonable. This boundary is again placed ten chord lengths away from the aerofoil surface. For an O-mesh, the pressure boundary is applied over 120° degrees of the circular outer boundary. If the analogy of clock face is used, this boundary would occupy 60° either side of 3 o'clock. The free-steam velocity condition is applied over the remaining 240° of the solution domain.

7.5.3 No-slip Boundaries

The surfaces of the aerofoil elements are no-slip boundaries, i.e. the fluid velocity (x & y) is zero at this point.

7.6 Solving

The geometrical model, including the mesh and boundary conditions, are then written to a Database (.DB) file. As described earlier, the free-stream values may either be entered in ANSYS, then saved to a RUN (.RUN) file, or entered prior to solving in FLOTRAN. The values to be entered are: properties of free stream air, free-stream velocity, x and y flow components (which creates angle of incidence).

The ISA properties of freestream air at 1 atmosphere were used in all CFD calculations: T_a = 288 K, P_a = 1.01 x 10^5 Pa, ρ_a = 1.225 kg/m^3 and μ_a = 1.79 x 10^{-5} kg/ms

7.7 CFD Testing

As previously discussed, results derived from computational analyses cannot be assumed correct or accurate without comprehensive validation tests of the code or package used. Benchmarking is a term used to describe the comparison of computational results against results for a model of known behaviour. Four benchmark tests were carried out to describe the behaviour of the FLOTRAN

package, with relation to the experimental models tested:

i) Mesh Dependency test.

ii) Flat Plate boundary layer test.

iii) Plain NACA 0018 section at NACA test Reynolds number (3.2×10^6).

iv) Plain NACA 0018 section at proposed windtunnel test Reynolds number (1.0×10^6).

v) NACA 0018 aerofoil with NACA 0010 slat at proposed windtunnel test Reynolds number (1.0×10^6).

7.8 Mesh Dependency

Before benchmarking can be performed accurately, any 'mesh dependency' of the package must be explored. Mesh dependency is the amount by which the solution will alter, when the number of elements used around the model, is altered. Obviously, the solution for an aerofoil with 5 nodes along its surface will be much less accurate than one with 100 nodes along its surface. A large number of nodes are needed to describe the large pressure gradients encountered at an aerofoil leading edge. The number of nodes required to give an accurate result is however an extremely important factor. Fewer nodes require reduced CPU memory size, reduced CPU time and thus, converge faster.

To investigate mesh dependency, a plain NACA 0009 aerofoil, with similar O-type and H-type meshes, was tested with 8000, 12000, 15000 and 20000 nodes (25000 is the maximum number of nodes the package can handle). Plotting 'Lift force' created against 'Number of Nodes' will create a curve similar to **Figure 7:4**. For this test, lift was chosen as the solution stability factor, as lift is derived from the integration of the pressure distribution over the aerofoil surface, thus indicating when the pressure solution is stable.

Solution convergence is displayed in four ways by the FLOTRAN solver. The first three are: magnitude of pressure, P, turbulent kinetic energy, k, and turbulent dissipation rate ϵ. The magnitude by which these parameters have changed is displayed at every step of the solution. These three parameters clearly show if the

solution is indeed converging or diverging. The fourth convergence parameter is known as the lumped convergence coefficient *LCC*. The *LCC* is an averaging of the three separate convergence criteria for *P*, *k* and ϵ. The individual convergence criteria is determined by the magnitude of the iterative change. In general, *P*, *k* and ϵ are considered to have converged when the magnitude of each iteration becomes less than 1.0×10^{-4}. The FLOTRAN operation manual suggests that a satisfactory value of lumped convergence criteria should be less than 0.2; for the purposes of all computational work values of *LCC* > 0.1 were not accepted. Many flow cases reached an *LCC* of 0 (all iteration magnitudes < 1.0×10^{-4}).

Of the two mesh types tested (O & H), the O-mesh was selected since it had a very low ratio of distorted elements, 25% faster convergence and a more efficient mesh distribution. A difference of less than 2% on lift and drag was found between the 12000 and 20000 node solutions. The dense mesh (20000 nodes) increases the computation time by 12 hours, from 14 to 26 hours (486 DX33 P.C.), and requires an additional 6 Megabytes of memory. It was therefore decided to use medium density meshes between 12-15000 nodes.

7.9 Flat Plate Testing

It was necessary to test the accuracy of a FLOTRAN's basic boundary layer prediction capability. In order to test the accuracy of the turbulence model, a flat plate model was used. A description of the theory and equations used by the software's boundary layer modelling function can be found in **Chapter 6**.

FLOTRAN does not have the capability to model a developing laminar-turbulent boundary layer. Either the laminar or turbulent modeller is specified along with the solution initial conditions. As a result, in order to test the accuracy of the FLOTRAN turbulence modeller, a simplified flat plate case must be used.

The simplest case of a turbulent boundary layer occurs on a flat plate at zero incidence. In the following case it is assumed that the boundary is already turbulent at the leading edge. The flat plate model is shown in **Figure 7:5**.

The flat plate model was tested at a chord based Reynolds numbers of 1 x 10^6 , 2 x 10^6 and 5 x 10^6. Results from this testing were compared with the flat plate theory and shown in **Table 7:2**. Less than 3% error was found in friction coefficient C_f and momentum thickness δ_2 at 1 metre from the plate leading edge. This error rose to 6% at 5m from the plate leading edge.

7.9.1 Theoretical Formulae

Approximate formulae were derived by Prandtl (see Schlichting [16]) from the empirical velocity distribution for a turbulent boundary layer in zero pressure gradient:

$$C_f = 0.0592 \quad Re_x^{-1/5} \qquad \delta_2 = 0.036\, x \; Re_x^{-1/5}$$

THEORETICAL RESULTS	1m	2m	5m
REYNOLDS NUMBER (Re)	1.0 x 10^6	2.0 x 10^6	5.0 x 10^6
FRICTION COEFFICIENT (C_f)	4.539 x 10^{-3}	3.952 x 10^{-3}	3.29 x 10^{-3}
MOMENTUM THICKNESS (δ_2) m	2.27 x 10^{-3}	3.952 x 10^{-3}	8.23 x 10^{-3}
COMPUTATIONAL RESULTS	1m	2m	5m
REYNOLDS NUMBER (Re)	1.0 x 10^6	2.0 x 10^6	5.0 x 10^6
FRICTION COEFFICIENT (C_f)	4.419 x 10^{-3}	3.88 x 10^{-3}	3.48 x 10^{-3}
MOMENTUM THICKNESS (δ_2) m	2.21 x 10^{-3}	3.867 x 10^{-3}	8.712 x 10^{-3}
% DISCREPANCY (C_f)	3.08	1.77	5.78
% DISCREPANCY (δ_2)	2.64	2.15	5.86

TABLE 7:2

7.10 Plain Wing Testing

The results from the following plain wing tests are shown and discussed in **Chapter 9**:

i) NACA 0018 single aerofoil model tested at a Reynolds number of 3.2 x 10^6 and compared with NACA published data [17].

ii) NACA 0018 single aerofoil model tested at the current windtunnel experimental Reynolds number of 1.0 x 10^6 and compared with experimental data.

iii) Comparison of NACA 0018 'plain wing' model results from the two Reynolds numbers: 3.2 x 10^6 and 1.0 x 10^6.

7.11 Aerofoil with Leading Edge Device

Following the benchmarking of CFD versus the initial windtunnel & NACA published results, it was then necessary to investigate CFD results with regard to the experimental slat behaviour. It was known from the experimental testing of model I that the symmetrical leading edge high lift device did indeed increase C_{Lmax} and maximum stall incidence. As a result, the NACA 0010 section was added to the computational 'plain wing' model and tested at the experimental Reynolds number (1.0 x 10^6).

7.12 CFD Design Procedure

Following the benchmarking of the CFD software, a clear representation of how CFD results reflected those found theoretically and experimentally existed. It was now possible to begin the design process using the CFD package. As described earlier, geometrical alterations to windtunnel models are both expensive and time consuming, whereas they are relatively simple when testing computationally. The configurations to be tested computationally are as follows:

All design testing was conducted at the expected experimental 'chord based' Reynolds number of 1 x 10^6.

The results and a description of wingsail behaviour from the following tests are shown and discussed in **Chapter 9**:

7.12.1 Flap Comparison

Three flap types were investigated, shown in **Figure 7:6**. A plain flap, slotted flap and a multi-element flap were all compared. The slotted flap was based on a NACA 0018 wing section, the flap section being pivoted from the centre of curvature of the flap leading edge. The Multi-element section is a NACA 0018 main wing section, with a NACA 0015 flap section, pivoted $0.2c_w$ upwind of the wing trailing edge. The ratio of wing to flap in all cases was 60:40.

7.12.2 Wing:Flap Chord Ratio

From the three flap types, the multi-element flap gave the best results and was selected for the remainder of the wingsail design. The wing and flap chord ratio was the first parameter to be tested. An initial ratio of 60:40 was set, and then ratios either side, 50:50 and 70:30, were also tested.

7.12.3 Wing:Flap Thickness Ratio

Having optimised the wing and flap chord ratio, the thickness ratio was the next parameter to be tested. Initially an 18% thickness chord t/c ratio wing section was tested with a 15% t/c flap section. The main wing section was altered to both a 21% t/c and 15% t/c section, to investigate any increase in performance which may occur. The flap section was also tested at a higher

and lower t/c ratio, 18 and 12%. The flap section investigations were carried out over a range of flap displacements to gain yet more information on how various flap/wing sections interact and behave.

7.12.4 Slat Section and Chord Length

A model with the wing and slat only was then used to investigate the optimum slat section and chord. The wing section was left fixed at the NACA 0018 section, shown to be the optimum from previous testing, the slat section then altered. The slat section was altered from a 10% t/c to a 9, 12 and 15% section. Each slat section was tested in both the initial 20% wing chord ratio and a long (25%) and short (15%) configuration.

7.13 Final Model Design

The results from the above test configurations provided the optimum configuration of slat:wing:flap chord ratio and slat:wing:flap thickness ratio for the wingsail. These results were used when designing and constructing the final windtunnel model, Model III.

Chapter 8

EXPERIMENTAL PROCEDURE

8.1 Experimental Procedure

i) The model is mounted in windtunnel No.1 with the balance supports at a span of 600mm.

ii) An inclinometer is placed on a special model mounting which records model incidence relative to geometrical zero incidence. The inclinometer is used to ensure that the geometrical incidence of the model is zero, and that the balance digital voltmeter (DVM) for recording pitch is also adjusted to 0.00 volts. Adjustments to the DVM reading are made by lengthening or shortening the trailing (pitching moment) support.

iii) The laboratory pressure is recorded from the Fortin barometer situated in the Aerodynamics laboratory.

iv) The tunnel is run at the test velocity (approx. 30ms^{-1}) for 3-4 mins to allow the tunnel temperature to stabilise. This ensures that testing is conducted at a consistent air density and viscosity. However, temperature is recorded at every reading.

v) The mechanical adjustors on either end of the model are altered in order to set the slat and flap configurations. These adjustments alter the slat overlap, slat angle and flap setting angle.

vi) Zero readings of lift, pitching moment and drag are recorded, prior to and following testing. Attention is paid to the slight hysteresis which occurs infrequently in the balance zero drag reading. This hysteresis in the zero drag reading can be cured simply by tapping the main balance supports.

vii) The tunnel is then run at test velocity and readings of lift, pitching moment and drag are taken at 2° increments, up to 4° past the stall incidence.

Attention was paid to:

i) All wind tunnel mountings, to ensure that no fouling can occur either with the tunnel roof or the strut cowling.

ii) The forces being recorded are within the windtunnel balance limits.

iii) The tunnel speed, to ensure that the slat will not distort to an extreme where it distorts the readings or could approach a failure situation.

iv) The windtunnel temperature should be stabilised prior to testing, thus reducing the density, viscosity and therefore Reynolds number variation during a tunnel run.

8.2 Pressure Measurements

Piping for the pressure tappings was connected after the force measurements had been completed, thus preventing the piping from either causing aerodynamic drag or fouling tunnel mountings. All tappings were cleared prior to testing with an air line. Prior to connection to the scanivalve, tappings were connected to a standard 'bank' manometer. By varying the aerofoil incidence, any totally or partially blocked tappings could be observed by their lack of, or slow, response to alterations in pressure.

8.3 Order of Testing

To allow the characteristics of the two high lift devices to be quantified, each device was tested separately:

8.3.1 Force Measurements

i) The wing only was tested initially, with and without endplates. This allowed the magnitude of 3-dimensional effects to be investigated.

ii) The wing and flap were tested, at flap angles from 0-30 degrees.

iii) The wing and slat were tested, with overlaps between 0-25mm. The slat was tested at angles between 0-30°.

iv) Finally, the triple element aerofoil was tested, at the flap and slat angles/overlaps which created the highest lift.

8.3.2 Pressure Measurements

There are no tappings on the leading edge slat, as the aerofoil is not thick enough and does not have the structural integrity required to fit them. The following tests were performed:

i) The wing only, with and without endplates.

ii) The wing and flap.

iii) The triple element aerofoil.

CHAPTER 9 - RESULTS AND DISCUSSION

l = Flat Plate Length

p = Pressure

u_e = Local Flow Velocity

γ = Resultant Angle

δ = Boundary Layer Thickness

$_s$ = Static

$_\infty$ = Reference

Chapter 9

Results & Discussion

9.0 Results and Discussion

The results presented at the start of this chapter are grouped into three sections: CFD results, force measurement results and pressure results. Each group of results is discussed individually. The results are then discussed as a whole at the end of the chapter.

Both the computational and experimental models are tested in a similar order throughout this chapter. To quantify the effects of each high lift device, they were tested individually with the plain wing, prior to all three elements being combined. Results are presented in the following order:

i) Plain wing
ii) Plain wing and flap
iii) Plain wing and slat
iv) Triple element aerofoil

With so many wing combinations, the parameters defining the model configuration should be defined.

9.0.1 Flap Configuration

Figure 9:1 shows the definition of flap chord and slat setting angle. Flap chord is the length of the flap section, measured along the centreline from the leading to trailing edges. Flap setting angle is the angle between the main

wing centreline and the flap centreline. Technical diagrams for the model are shown in **Appendix C**.

9.0.2 Slat Configuration

Figure 9:1 shows the definition of slat chord and slat setting angle. Slat chord is the length of the slat section, measured along the centreline from leading to trailing edges. Slat setting angle is the angle between the slat centreline and the main wing centreline. A description of slat overlap and pivot point are given in **Section 4.13.2**, the geometry is shown in **Figure 4:8**. Technical diagrams for the model are shown in **Appendix C**.

9.0.3 Force Coefficients and Reynolds numbers

The force coefficients and Reynolds number for each wingsail configuration are defined as follows:

$$(\ All\quad configurations\quad) \quad C_L = \frac{L}{1/2\,\rho V^2 S} \quad and \quad C_D = \frac{D}{1/2\,\rho V^2 S}$$

where, S = Surface area of the model in m^2.

$$(\ wing\quad only\ ) \quad R_e = \frac{\rho V c_w}{\mu}, \quad C_{\bar{M}} \frac{M}{1/2\,\rho V^2 S c_w} \qquad \textbf{9:1}$$

$$(\ wing + flap\ ) \quad R_e = \frac{\rho V (c_w + c_f)}{\mu}, \quad C_{\bar{M}} \frac{M}{1/2\,\rho V^2 S (c_w + c_f)} \qquad \textbf{9:2}$$

$$(\ wing + slat\ ) \quad R_e = \frac{\rho V (c_w + c_s)}{\mu}, \quad C_{\bar{M}} \frac{M}{1/2\,\rho V^2 S (c_w + c_s)} \qquad \textbf{9:3}$$

$$(\ wing + slat + flap\ ) \quad R_e = \frac{\rho V (c_s + c_w + c_f)}{\mu}, \quad C_{\bar{M}} \frac{M}{1/2\,\rho V^2 S (c_s + c_w + c_f)} \qquad \textbf{9:4}$$

9.1 CFD versus Experimental Results

After extensive testing, and comparison with either published or experimental results, the following section summarises the behaviour of the CFD model.

Table 9:1, contains a summary of the graphs discussed in the following section:

GRAPH DESCRIPTION	FIGURE NUMBER	REYNOLDS NUMBER	COMMENTS
PLAIN WING	9:1:1	3.2×10^6	CFD RESULTS VERSUS NACA PUBLISHED RESULTS
PLAIN WING	9:1:2a	1.0×10^6	CFD RESULTS VERSUS EXPERIMENTAL RESULTS
PLAIN WING	9:1:2b	1.0×10^6	SKIN FRICTION DRAG EFFECT ON CFD RESULTS
PLAIN WING	9:1:3	COMPARISON	CFD RE. NO. COMPARISON (3.2×10^6 VERSUS 1.0×10^6)
WING & SLAT	9:1:4a	1.0×10^6	C_L WITH TWO SLAT SETTINGS
WING & SLAT	9:1:4b	1.0×10^6	C_D WITH TWO SLAT SETTINGS

TABLE 9:1

9.1.1 CFD versus NACA Published Results

Figure 9:1:1 shows lift and drag coefficient versus incidence, at a Reynolds number of 3.2×10^6. The NACA data is taken from NACA Technical Report 460 [17], which defines the characteristics of 78 aerofoil sections, including the '00' range of symmetrical aerofoils. The NACA data and computational results are calculated at a Reynolds number of 3.2×10^6. The CFD C_L curve has a C_{Lmax} value of 1.62, compared with a value of 1.49 for the NACA curve. This C_{Lmax} discrepancy is a 9% overestimation by the computational results, which have a non-linear lift profile in comparison to the NACA curve. Both computational and experimental C_L curves, show a maximum lift

incidence between 20° and 22°. The computational results also overestimate the magnitude of drag for the wing section. The CFD results predict a C_D at 0° incidence of 0.03, compared with the NACA C_D of 0.01, also at 0° incidence. This drag discrepancy is increased further, as the CFD result (shown) does not include the skin friction drag component, which has the effect of increasing total drag. Again, both C_D curves indicate a stall incidence of between 20° and 22°.

The difference noticed between the computational and NACA lift and drag results, shown in **Figure 9:1:1**, have the following explanations. The CFD results are subject to several simplifications, which FLOTRAN requires to solve the problem. The major discrepancy between the computational and experimental results is due to the modelling of the boundary layer. The computational model cannot simulate boundary layer transition. Calculations are performed assuming that the boundary layer flow is either wholly laminar or wholly turbulent. Simulating flow with a permanently turbulent boundary layer has several effects on both lift and drag results. Firstly at the NACA test Reynolds number, the boundary layer flow over the wing leading edge will be laminar. Therefore, the boundary layer model applied by the FLOTRAN solver over this section of the wing is incorrect. Assuming a turbulent boundary layer from the wing leading edge will overestimate the lift created in this region. Secondly, the boundary layer is thicker across the wing, causing a large wake and therefore larger pressure drag. Another difference between the computational and NACA results is due to the aspect ratio of the NACA model. The computational flowfield over the wing section is perfectly two dimensional, a phenomenon which cannot be perfectly simulated in a windtunnel. The NACA results are taken from a model of finite span, which is then corrected to infinite aspect ratio. However, a three dimensional experimental model, corrected to infinite aspect ratio, may still contain three dimensional effects.

9.1.2 CFD versus Experimental Model

Figure 9:1:2a shows lift and drag coefficients, plotted against incidence, at a Reynolds number of 1.0 x 10^6 for the computational model, and 0.5 x 10^6 for the experimental plain wing. The experimental wing is fitted with endplates and results are corrected for tunnel blockage effects. The CFD C_L curve can be seen to reach a C_{Lmax} of 1.5 at an incidence of around 22°. However, the experimental C_L curve only reaches a C_{Lmax} of 1.01 at an incidence of 18°. The CFD model predicts a value of C_D at 0° incidence, 0.029, compared with a C_D of 0.04 for the experimental model. The CFD result does not, however, contain skin friction drag.

The discrepancy between computational and experimental results in **Figure 9:1:2a** is much greater than that noticed between the computational and NACA results. The Reynolds number difference between experimental and computational results is obviously an influential factor. The effect of having a lower experimental Reynolds number will delay boundary layer transition. This lower Reynolds number, and thus delayed transition, will reduce the stall incidence of the wing and increase the C_D at higher incidences.

A trip was not used to promote boundary layer transition at this stage. The main reason for this is the difficulty in determining the precise transition position with the various geometrical configurations, Reynolds numbers, angles of attack and the settings of high lift devices. Preliminary experiments showed that, with the Reynolds numbers tested, the correct positioning of a trip wire or a gritted strip is very important for a smooth and reliable transition. With the many model configurations altering the parameters that influence transition position, it may have been necessary to move and alter the size of the trip. Preliminary experiments also showed that moving a trip can cause serious damage to the model surface.

The experimental model shown has an aspect ratio of 4, compared with the computational model which has an effective aspect ratio of infinity. Aspect ratio corrections are discussed and shown later in this chapter.

The difference between experimental and computational Reynolds number in **Figure 9:1:2a** is due to constraints on windtunnel size and speed. The intended experimental Reynolds number during the CFD design stage was 1.0 x 10^6, therefore this value is used throughout the CFD design stage. As the experimental model dimensions were finalised, towards the end of the computational design stage, it became apparent that testing the experimental model at 1.0 x 10^6 would not be possible. Predicted lift values at the design Reynolds number, were greater than windtunnel balance maximum limits. All computational testing remained at the Reynolds number of 1.0 x 10^6, however, to ensure that the effect of model configuration changes could be quickly and easily compared.

The discussion of this section has focused solely on the experimental results. The computational model also contains assumptions, which have the effect of overestimating the values of C_L and C_D. As discussed in **Section 9.1.1**, FLOTRAN can only simulate either a wholly laminar, or a wholly turbulent boundary layer. The result of applying the boundary layer model this way will overestimate the CFD predictions of both lift and drag.

The computational drag results shown are derived solely from the normal pressure drag, which is the drag arising from the resolved components of the normal pressure in the boundary layer. The results, therefore, do not contain the drag component due to skin friction, which is described in the next section.

9.1.3 The Effect of Skin Friction Drag

Figure 9:1:2b shows drag coefficient plotted against angle of incidence, for the computational and NACA published results [17]. The CFD results are calculated by integrating the pressure coefficient over the wing chord, and resolving this pressure force to produce the lift and drag components. This pressure drag result, the equivalent of form drag over the wing, does not include drag created by skin friction. The computational curve, $C_D + C_f$, shows form drag plus skin friction drag, calculated by integrating wall shear

stress τ_w over the chord length using the following equation:

$$C_f = \int_0^{c_{upper}} \frac{\tau_w}{\frac{1}{2}\rho u_e^2 c} dx + \int_0^{c_{lower}} \frac{\tau_w}{\frac{1}{2}\rho u_e^2 c} dx \qquad 9:5$$

The C_D curve, including skin friction drag can be seen to increase C_D at 0° incidence from 0.03 to 0.05.

Figure 9:1:2b shows skin friction drag increasing the value of C_D by approximately 50% at 0° incidence. This force remains almost constant until stall. As the value of C_D increases toward stall, and the value of skin friction remains constant, the effect of C_f upon total drag decreases, with increasing incidence.

Both CFD drag curves shown in **Figure 9:1:2b** have very high drag coefficients when compared with the NACA results. As discussed in **Sections 9.1.1 and 9.1.2**, the normal pressure drag values of C_D are overestimated due to the boundary layer modelling employed by FLOTRAN. The result of overestimating boundary layer thickness is that values of τ_w, wall shear stress, are also overestimated. This has the effect of increasing skin friction drag.

9.1.4 CFD Reynolds Number Comparison

Figure 9:1:3 shows results for the plain wing CFD model, tested at two Reynolds numbers, 1.0 x 10^6 and 3.2 x 10^6. Lift and drag coefficients are both plotted versus angle of incidence, α. Both curves reach C_{Lmax} at between 20° and 22° incidence, although the 3.2 x10^6 Reynolds number curve stalls more sharply. The higher Reynolds number curve reached a C_{Lmax} of 1.65 compared with 1.5 for the 1.0 x10^6 Reynolds number case. The two C_D curves show very similar results, with the higher Reynolds number creating a slightly higher C_D across the incidence range. Drag coefficient is normally expected to decrease with increasing Reynolds number, a trend most noticeable at the higher lift incidences.

9.1.5 Wing and Slat (CFD versus Experimental Model)

Figures 9:1:4a-b show the comparison between computational and experimental lift and drag coefficient results, for the wing and slat configuration. Both CFD and experimental models were tested at the Reynolds number of 1.0 x10^6. The wing and slat model, comprises a plain NACA 0018 main wing section and a plain NACA 0010 slat section. The ratio of slat chord, c_s, to wing chord, c_w, is 1:5. The two curves shown for each model are for differing slat setting angles, 16˚ and 21˚. Slat setting angle is measured between the wing centreline and to the centreline of the slat section. Definitions of slat angle and slat chord are both shown in **Figure 9:1.**

Figure 9:1:4a shows four curves, split into two obvious pairs. The higher pair consists of the computational results for the 16˚ and 21˚ slat setting, the second, lower, pair consists of the experimental results for these slat settings. Examination of the two experimental curves shows that both the 16˚ and 21˚ slat setting angles produce results with a very similar C_L/α gradients. The experimental curves maintain this trend up to an incidence of 18˚, after which the 16˚ slat angle setting begins to stall. The experimental 21˚ slat angle setting results can be seen to continue, with a constant C_L/α gradient, until a much sharper stall at 24-26˚.

The CFD results follow a similar trend to the experimental model, with a very similar C_L/α gradient until 19˚ incidence, where the 16˚ slat setting begins to stall. The 21˚ slat setting curve, also like the 21˚ experimental curve, continues with a constant C_L/α gradient until stall at 24-26˚. Although the trend of the experimental model is predicted well by the CFD, the magnitudes of C_L and C_D are not. CFD predicts a C_{Lmax} 100% greater than the experimental value.

Figure 9:1:4b shows form drag coefficient results for the CFD model, plotted against the experimental model. The figure shows four curves, split into two obvious pairs, the higher pair consisting of the computational results for the 16˚ and 21˚ slat setting, the second, lower pair, consisting of the experimental

results for the 16° and 21° slat setting. As with the C_L graph, there is a strong agreement in the trend shown between the CFD and the experimental results. Both methods show the 16° slat setting angle creating slightly less drag at incidences below 5°. After 6-8°, both computational and experimental solutions show that the 16° slat setting angle creates increasingly greater drag over the remaining incidence range. The results, at 0° incidence, show a C_D value of 0.04 for the CFD results, compared with the higher C_D value of 0.07 for the experimental results. The experimental model is not corrected for windtunnel blockage.

9.2 Summary of CFD Behaviour

Both the computational model for the plain wing and the wing & slat (at similar Reynolds numbers) predicted similar lift and drag characteristics to those found by experiment. The magnitude of these forces was significantly overestimated. This is thought to be due to several factors, some derived from experimental testing creating less lift than expected, and some from the computational calculations.

The greater magnitude of computational results is mainly due to the turbulence modelling equations used in FLOTRAN. The assumption of a permanently turbulent boundary layer affects the lift, drag and wall shear stress results. However, results from the comprehensive validation exercise provided confidence that the CFD package, if correctly used, could predict the trend but not the magnitude of lift and drag forces for a multi element aerofoil.

The experimental results have a test Reynolds number which is lower than the design case, thus preventing the CFD and the experimental results from being compared at similar Reynolds numbers. Another difficulty is due to three dimensional aerodynamic flow effects, which cannot be completely eliminated. As a result, the lift curve slope of experimental results is shallower than that of the CFD results.

If results from the computational package are used solely as a qualitative indication of design alterations to the model, then these results can be used to predict the most effective multi element design configuration for the wingsail. Although results do not have the accuracy to quantitatively predict experimental behaviour, CFD is a very useful and time-saving design tool.

9.3 CFD Design Process

As stated previously, CFD was introduced to speed the design process for the wingsail and provide rapid qualitative feedback on design changes. Wingsails have differing parameters for optimisation, which depend upon the apparent wind direction the vessel is encountering. The design philosophy used to select wingsail characteristics is discussed in the Wingsail Theory **Section 2.2** and shown in **Figure 2:2** diagrams '**a**' and '**b**', the upwind and downwind force resolutions.

A vessel travelling upwind, **Figure 2.2 a** with an apparent wind angle β, between +/-40° to +/-90°, will create maximum forward thrust when a wingsail is configured for the maximum lift/drag ratio.

A vessel travelling downwind, **Figure 2.2 b** with an apparent wind angle β, between +/-90° to +/-180°, requires the wingsail to be configured for maximum lift to create maximum thrust. However, when two lift configurations create a similar lift at similar incidence, the lower drag case and therefore higher L/D ratio is normally preferable due to the reduction in heeling moment created.

To arrive at the most efficient wingsail, one of these two alternatives must be given priority. As a result, the downwind design optimisation was chosen. There are two reasons for this:

i) Wingsails are at their most efficient at apparent wind angles between 90° and 140°. Therefore, maximum wingsail performance is obtained if lift, and hence thrust, is produced at these apparent wind angles. However, as stated above, the lift/drag ratio of configurations which create a similar lift force, at similar incidence, should be used as the secondary design criteria.

ii) The downwind configuration covers a greater percentage of wind direction. A wingsail, or any sail, is very rarely used for sailing at an apparent wind angle of less than 30°. Even with a high lift/drag ratio, a prohibitive amount of heeling force is created, for a relatively small forward thrust.

9.3.1 Wingsail Design Criteria

Selection for wing sections and configurations are therefore made on the following criteria:

The wingsail should be configured to create maximum lift and therefore maximum thrust. However, when two wingsail configurations create a similar lift at similar incidence, the lower drag, higher L/D case is normally preferable due to the reduction in heeling moment created.

9.4 Flap Testing

Table 9:2, contains a summary of the graphs discussed in the following section:

GRAPH DESCRIPTION	FIGURE NUMBER	REYNOLDS NUMBER	COMMENTS
FLAP TYPE COMPARISON	9:2:5a	1.0 x 10^6	PLAIN, SLOTTED AND MULTI ELEMENT FLAPS (10°,30° & 50°)- C_L
FLAP TYPE COMPARISON	9:2:5b	1.0 x 10^6	PLAIN, SLOTTED AND MULTI ELEMENT FLAPS (10°,30° & 50°)- L/D RATIO
WING:FLAP 't/c' COMPARISON	9:2:6	1.0 x 10^6	SIX CONFIGURATIONS AT 15°INCIDENCE, 30° FLAP.
WING:FLAP CHORD COMPARISON	9:2:7	1.0 x 10^6	THREE c_w:c_f RATIOS AT 15°INCIDENCE, 30° FLAP.

TABLE 9:2

9.4.1 Flap Type

Figure 7:6 Shows the three flap types tested, the plain flap, single slotted flap and the multi element flap. **Figures 9:2:5a-b** show the C_L and L/D results for each flap design, tested at a Reynolds number of 1.0 x 10^6. Testing is at a constant aerodynamic incidence of 15°, with three flap setting angles 10°, 30° and 50°.

The C_L values of the three flap types and angles are shown in **Figure 9:2:5a**. When the model is configured with a 10° flap angle all three results were within 7% of the plain flap C_L value. The plain flap configuration created the highest C_L of 1.86. The 30° flap setting curves show the multi element flap achieving a C_L of 2.56, 15% higher than the slotted flap configuration and nearly 20% higher than the plain flap configuration. When the flap is set at 50°, the highest C_L is achieved by the plain flap configuration. The 50° flap

angle, plain flap setup reaches a C_L of 2.5, slightly lower than the highest C_L achieved by the multi element flap at the 30° flap setting. The 50° flap setting appears too great for both the single slotted and the multi element flap configurations. They both achieve significantly lower C_L results of 1.9 and 1.7 respectively.

The lift/drag ratios for the three flap configurations are shown in **Figure 9:2:5b.** The maximum L/D configuration is achieved by the plain flap, at a flap angle of 10°. The multi element and slotted flap arrangements also achieve their maximum L/D ratios at the 10° flap setting angle, although both configurations show the drag penalty incurred by having a slot in the flap configuration. The plain flap also has the highest L/D value at the 30° and 50° flap setting angles.

The maximum lift configuration, at 15° aerodynamic incidence and a Reynolds number of 1.0×10^6, is achieved by the multi element flap. **Figure 9:2:5a** shows that when the multi element flap is set at an angle of 30°, it achieves the highest C_L of 2.56. The highest L/D ratio at all flap settings was, however, achieved by the plain flap. This configuration is also given serious consideration. The results implied that the multi element flap configuration would create higher C_L values at flap angles between 10° and 30°; therefore, the primary design criteria for choosing the maximum lift configuration was employed.

9.4.2 Thickness/Chord Ratio Comparison

Following selection of the multi element flap, the optimum wing section:flap section thickness ratios were explored. All wing sections used are the NACA '00' symmetrical series. The last two digits of the '00' number refer to the maximum section thickness as a percentage of the section chord or t/c value. **Figure 9:2:6** shows C_L, C_D and lift/drag ratio for the six wing:flap configurations which created the greatest lift at the test Reynolds number, 15° aerodynamic incidence and 30° flap setting. The sections tested for the wing t/c ratio were the NACA 0021, 0018 and 0015. NACA 0018, 0015 and 0012

sections were tested for flap t/c ratios. Inspection of **Figure 9:2:6** reveals the NACA 0021:0015 wing:flap t/c configuration creates the greatest C_L, 2.7. This configuration also creates the highest L/D ratio. The 21:18%, 18:18% and 18:15% thickness/chord configurations all share very similar results for lift coefficient and L/D ratio.

At this stage, if the design process were going no further, the highest lift and lift/drag configuration of 21:15% wing:flap t/c would be selected. However, firmly selecting the wing section is not possible at this stage as the thickness/chord ratio is crucial in the operation of the leading edge device. As a result, all four maximum lift configurations are carried forward into the following design stages.

9.4.3 Wing:Flap Chord Ratio Comparison

Three wing:flap or c_w:c_f chord ratios are shown in **Figure 9:2:7**, all of which were tested at 15˚ aerodynamic incidence and 30˚ flap setting angle. C_L, C_D and L/D ratios are shown for all three configurations. From the graph, the 60:40 c_w:c_f chord ratio configuration clearly creates the greatest C_L, 2.56. This lift value is almost 8% greater than the 50:50 chord configuration and over 30% greater than the 70:30 c_w:c_f ratio.

From the results of the wing:flap chord ratio testing, the 60:40 c_w:c_f ratio clearly creates the greatest lift force. The 60:40 c_w:c_f ratio is therefore selected for the model at this stage, although the overall model chord ratio changes when the leading edge device is added to the design.

9.5 Slat Testing

Table 9:3, contains a summary of the graphs discussed in the following section:

GRAPH DESCRIPTION	FIGURE NUMBER	REYNOLDS NUMBER	COMMENTS
c_s:$c_{(w+f)}$ CHORD COMPARISON	9:3:8	1.0 x 10^6	15° INCIDENCE; 15,20 & 25% SLAT CHORD c_s.
SLAT SECTION COMPARISON	9:3:9	1.0 x 10^6	15° INCIDENCE; 9,12 & 15% t/c RATIO.
TRIPLE ELEMENT AEROFOIL SECTION COMPARISON	9:3:10	1.0 x 10^6	18 & 21% WING t/c RATIO; 10°,20°& 30°FLAP ANGLE
COMPARISON OF ALL FIVE SLAT CONFIGURATIONS	9:3:11	1.0 x 10^6	9,12 & 15% t/c RATIO VERSUS 15,20 & 25% c_s.

TABLE 9:3

9.5.1 Slat Chord Comparison

For this design stage, the leading edge high lift device is added to the model configuration. The flap is preserved throughout slat testing, although it is set at an angle of 0°.

Figure 9:3:8 shows a NACA 0012 section used for testing possible slat:wing:flap chord ratios of 3:12:8, 4:12:8 and 5:12:8. For the purposes of this section, slat chords are more easily described as percentages of the total wing chord; 15%, 20% and 25%. During testing, the flap is set at an angle of 0° and the model aerodynamic incidence is 15°. The 15% chord ratio can be seen to achieve the highest C_L of 1.43, 7% higher than the 20% chord ratio C_L value and 17% higher than the 25% chord ratio C_L. Looking at the lift/drag ratios for these three configurations, the 15% chord ratio has a 12% lower L/D ratio than the 20% chord ratio and nearly 20% lower L/D ratio than the 25% chord ratio.

The primary design criterion for selecting the maximum lift configuration is used to select the 15% chord ratio. The 15% chord ratio is also known as the 3:20 c_s:c_w configuration for the wing and slat model, and the 3:12:8 c_s:c_w:c_f chord ratio for the triple element model.

9.5.2 Slat Thickness/Chord Comparison

The NACA 0012 slat section used in the **Section 9.5.1**, was chosen to test alterations to the slat chord length. Possible slat t/c ratios were then tested at the new design chord length ratios of 3:12:8, slat:wing:chord. **Figure 9:3:9** shows C_L, C_D and L/D ratio for three slat t/c sections; NACA 0009, 0012 and 0015. These three sections are tested on an 18% t/c wing section with a flap, although the flap angle was set to zero. All three slat sections create very similar C_L values, within just 1% of each other. The 9% and 12% slat t/c ratios however, create more drag than the 15% t/c ratio. In consequence, the 15% t/c slat section, creates an 8% greater L/D ratio than the other two configurations.

As the C_L values of the three designs are all within 1%, the secondary design parameter is employed. The lift/drag ratio of the 15% t/c ratio is 8% higher than the other three designs and will therefore create slightly less heeling moment.

9.6 Triple Element Model

The slat:wing:flap t/c ratios must now be chosen before the model design is finalised. **Figure 9:2:6** showed wing:flap t/c ratios, which were discussed in **Section 9.4.2**.The four optimum configurations of wing:flap t/c ratio are therefore carried forward into the slat:wing:flap t/c design stage.

After initial tests on the four highest wing:flap t/c ratios, the best two configurations were investigated further; these are shown in **Figure 9:3:10**. The figure shows C_L, C_D and L/D ratios for the two optimum configurations of flap:wing t/c section tested. They were 18:15% and 21:15%. The optimum slat section of 15% t/c ratio is used along with the design c_s:c_w:c_f chord ratio of 3:12:8, the aerodynamic incidence is set

at 15° and the two configurations are tested at flap angles of 10°, 20° and 30°. Inspection of **Figure 9:3:10** shows that the combination of NACA 0015:0018:0015 sections for the slat:wing:flap creates the highest lift for all three flap angles. This configuration also creates less drag at all three flap settings than the alternative NACA 0015:0021:0015 configuration.

After the slat is included in the design process, the results from the two wing:flap t/c ratios vary greatly. The most likely cause for this is the differing leading edge radius of the two wing sections. The NACA 0018 is preferable to the NACA 0021 main wing section for both maximum lift and L/D ratios, when the slat is added to the model.

The final multi element configuration is therefore defined as 15%,18% and 15% t/c ratios for the slat, wing and flap respectively, and a 3:12:8 c_s:c_w:c_f chord ratio.

This final model configuration, which was constructed and known as Model III has the NACA section, chord, flap and slat arrangements described above. A diagram of this configuration is shown in **Figure 9:9** and technical drawings of the model are shown in **Appendix C**.

9.7 Experimental Results: Force Measurements

To quantify the effects of each high lift device, they were tested individually with the plain wing, prior to all three elements being combined. **Table 9:4,** contains a summary of the graphs discussed in this section. *[All results shown are corrected for blockage effects]*

WING	FLAP	SLAT	REYNOLDS NUMBER	FIG. No.	COMMENTS
YES			$0.5x10^6$	9:4:1	EXPERIMENTAL vs. NACA
YES			$0.5x10^6$	9:4:2	C_L, C_D and C_M vs. α
YES	YES		$0.62x10^6$	9:4:3a	C_L vs. α; 0-25° FLAP
YES	YES		$0.62x10^6$	9:4:3b	C_D vs. α; 0-25° FLAP
YES	YES		$0.62x10^6$	9:4:3c	C_M vs. α; 0-25° FLAP
YES		YES	$0.5x10^6$	9:4:4a	C_L @ OPTIMUM SLAT ANGLES
YES		YES	$0.5x10^6$	9:4:4b	C_D @ OPTIMUM SLAT ANGLES
YES		YES	$0.5x10^6$	9:4:4c	C_M @ OPTIMUM SLAT ANGLES
YES		YES	$0.5x10^6$	9:4:4d	L/D @ OPTIMUM SLAT ANGLES

TABLE 9:4

9.7.1 Wing Only

Figure 9:4:1 shows the experimental results for the plain NACA 0018 wing section, with and without endplates. The experimental model, with an aspect ratio, *AR,* of 4, is tested at a chord based Reynolds number of $0.5x10^6$ and compared with NACA published results [17]. NACA results show the same aerofoil section tested at a Reynolds number of $3.2x10^6$. The figure shows lift and drag coefficient plotted against angle of attack, α, in degrees.

It is apparent from **Figure 9:4:1** that the presence of endplates has little effect on the stall angle of the wing section. The wing does, however, achieve a higher C_{Lmax} when fitted with endplates. The plain wing with endplates has a lower drag than the wing without, even with the drag created by the presence of the endplates included in the results. The increased C_L/α gradient and reduced drag of the wing appear to demonstrate that adding endplates to the model has achieved the intended effect of reducing three dimensional aerodynamic effects.

The NACA results, also shown in **Figure 9:4:1**, show a slightly shallower C_L/α gradient than the plain wing with endplates, which are linear until stall at an incidence of 22°. The NACA C_D values are significantly lower those of the experimental model with endplates, over the entire incidence range. For example, the NACA result for C_D is 66% lower, at 0° incidence, than the plain wing result. The difference between experimental and published data is largely due to the difference in test Reynolds number. The effects of increasing the test Reynolds number should be to increase stall incidence and to reduce drag, therefore reducing the difference between NACA and experimental results.

Figure 9:4:2 shows C_L, C_D and C_M values for the plain wing NACA 0018 section, at the test Reynolds number of 0.5×10^6. Inspection of the C_L curve shows stall occurring between 14 and 16° at a C_{Lmax} of 0.93. C_D at 0° incidence is 0.04 and the pitching moment of the wing is constant until stall, at which point C_M gradient becomes negative. The pitching moment characteristics for the section are consistent with the NACA published pitching moment trend; a zero value of pitching moment until stall, after which, $dC_M/d\alpha$ has a negative value.

9.7.2 Wing and Flap

A NACA 0015 flap section is now added to the plain wing. The following three graphs, **Figures 9:4:3 a-c**, show C_L, C_D and C_M versus incidence for a range of flap setting angles, 0-25° in 5° increments.

Figure 9:4:3a shows C_L versus aerodynamic incidence for a range of flap setting angles. The 0-20° flap setting angles have similar $dC_L/d\alpha$ values. However, the whole curve shifts in a positive direction as flap incidence is increased. The 20° flap angle achieves the highest C_{Lmax}, 1.7 at an incidence of between 14 and 16°. Stall incidence remains constant at 14-16° for all slat settings, unchanged from the plain wing case.

Figure 9:4:3b shows C_D versus aerodynamic incidence for the same range of flap setting angles, 0-25°. The effect of increasing flap angle between 5° and 20° appears to increase drag constantly across the whole incidence range. A large increase in drag for the 25° flap setting occurs at a similar incidence to the relative loss of lift noticed in **Figure 9:4:3a**.

Figure 9:4:3c shows C_M versus aerodynamic incidence for flap setting angles between 0-25°. Increasing the flap setting angle affects all pitching moment results in a similar manner. As flap settings are increased, the pitching moment curve shifts negatively. This shift is large between 0° and 5° flap, reducing as flap angles increase. The negative pitching moments became so large at 15° and above, that the balance limit for pitching moment was reached. The balance was no longer operating without external interference and so results above 15° are invalid.

Figure 9:4:3a demonstrates that lift coefficient is increased, with increasing flap angle, up to 20°. At the 25° flap angle flow cannot remain attached and separates at a low aerodynamic incidence. This separation creates the large drag force noted in **Figure 9:4:3b**. The maximum lift coefficient for the wing and flap combination occurs at a flap setting angle of 20°.

9.7.3 Wing and Slat

The next stage of the design process is to test the plain wing section with the leading edge high lift device. The slat section has a NACA 0015 profile and a chord length of 0.052m. The ratio of slat chord:wing chord is 3:12, 25%; which is different from the design configuration of 3:20, or 15%. The

difference in slat:wing chord ratio is due to the multi element design of the model. The slat is the correct ratio when the flap is attached. A description of slat geometry, including slat overlap and slat angle definitions, is shown in **Section 9.0**.

Wing and slat configurations were tested at five overlap settings, 0-20mm overlap, at 5mm intervals. The optimum slat setting angle was then investigated for each setting. **Figures 9:4:4 a-d** show C_L, C_D, C_M and L/D ratio respectively for the maximum slat angles at each overlap. The 15mm and 20mm overlap settings are not shown, as they did not produce high lift coefficients.

Figure 9:4:4a shows C_L for the four best slat overlap and angle settings plotted against aerodynamic incidence, α. The 0mm overlap, 20˚ slat angle setting has the highest C_{Lmax},1.37, at an incidence of 20˚; although all four settings achieve maximum lift coefficients within 3% of this value. The two 20˚ slat angle settings share very similar lift values, stall angles and stall characteristics. The 10mm overlap setting has the highest slat setting angle, 22.5˚, which causes a more negative C_L at 0˚ incidence than the other curves. This 10mm overlap setting also has the highest stall angle, 22˚, occurring at a very similar C_{Lmax} to the other configurations. The negative C_L values at 0˚, shown by all four curves, are due to the slat, which is remains at a fixed incidence. The effect of this is to cause flow interference over the wing upper surface at low incidences, thus causing the negative lift at 0˚ incidence.

Figure 9:4:4b shows C_D for the four best slat overlap and angle settings plotted against aerodynamic incidence, α. All four slat settings have very similar C_D values up to 12˚ incidence; above this incidence, all four curves show a sharp increase in C_D/α gradient. The 0mm, 17.5˚ setting is the first to demonstrate this trend at an incidence of 12˚, followed by the two 20˚ slat setting angles at 14˚ incidence. The 22.5˚ slat setting angle is the last to show the sharp increase in C_D/α gradient, at 18˚ incidence.

Figure 9:4:4c shows C_M for the four best slat overlap and angle settings plotted against aerodynamic incidence, α. The pitching moment curves demonstrate the differing aerodynamic incidence at which various slat settings begin to affect the flow over the wing leading edge. The 17.5° slat angle shows an increase in C_M/α gradient at just 4° incidence. The two 20° slat angles show a similar trend at 6-8° but create almost 15% less pitching moment at stall. The 22.5° slat angle shows a very gradual increase in $dC_M/d\alpha$, never becoming linear. All four curves show C_M/α gradient decreasing briefly prior to C_{Lmax}. After stall, all four slat settings have a negative pitching moment gradient.

The final graph of the group, **Figure 9:4:4d** shows lift/drag ratios for the four best slat overlap and angle settings plotted against aerodynamic incidence, α. The 17.5° slat setting angle and two 20° slat setting angle curves share a similar L/D profile until 10° incidence. The 0mm overlap, 20° slat angle setting achieves a L/D_{max} value of 13, at 10° aerodynamic incidence. Compared with the other three curves, the 22.5° slat angle achieves relatively poor L/D ratios until 16°, above which incidence maximum L/D ratios are achieved.

9.8 Full Wing: Slat, Wing and Flap

Table 9:5a contains a summary of the graphs discussed in this section. The test Reynolds number is 0.73×10^6 for all graphs. *[All results shown are corrected for blockage effects]*

SLAT OVERLAP (mm)	SLAT ANGLE (deg)	FLAP ANGLE (deg)	FIGURE NUMBER
0	17.5	10, 15 & 20	9:5:5a
0	20	10, 15 & 20	9:5:5b
0	22.5	10, 15 & 20	9:5:5c
5	17.5	10, 15 & 20	9:5:5d
5	20	10, 15 & 20	9:5:5e
5	22.5	10, 15 & 20	9:5:5f
10	20	10, 15 & 20	9:5:5g
10	22.5	10, 15 & 20	9:5:5h
10	25	10, 15 & 20	9:5:5i

TABLE 9:5a

9.8.1 High Lift Device Settings

The 9 graphs, **Figures 9:5:5 a-i**, each display C_L versus aerodynamic incidence at a specific slat overlap and angle. There are three curves on each graph, displaying flap setting angles of 10°, 15° and 20°. Therefore, 27 possible configurations of slat and flap are compared, with the intention of finding the arrangement which creates maximum lift force.

All 9 graphs follow a very similar lift trend; C_L and C_{Lmax} increase as flap angle is increased, up to 20° flap angle. Stall occurs at aerodynamic incidences above 20°. To investigate slat and flap settings further, the four configurations achieving maximum lift are plotted.

9.8.2 Maximum Lift, Slat and Flap Settings

Table 9:5b, contains a summary of the four maximum lift settings of slat overlap, slat angle and flap angle. Inspection of the four curves displayed reveals that a 20° flap setting angle, the preferred wing and flap setting, also achieves the maximum lift for the triple element aerofoil.

SLAT OVERLAP (mm)	SLAT ANGLE (deg)	FLAP ANGLE (deg)
0	20	20
0	22.5	20
5	20	20
5	22.5	20

TABLE 9:5b

Table 9:5c, contains a summary of the four graphs which display the aerodynamic characteristics of the slat and flap settings described in the table above. *[All results shown are corrected for blockage effects]*

COMMENTS	REYNOLDS NUMBER	FIGURE NUMBER
C_L VERSUS α	0.73×10^6	9:5:6a
C_D VERSUS α	0.73×10^6	9:5:6b
C_M VERSUS α	0.73×10^6	9:5:6c
L/D RATIO vs. α	0.73×10^6	9:5:6d

TABLE 9:5c

Figures 9:5:6 a-d show the maximum slat, wing and flap configurations of the full, triple element aerofoil section. The graphs present C_L, C_D, C_M and L/D ratio versus incidence for four combinations of slat overlap, slat and flap angle.

Figure 9:5:6a displays lift coefficient versus aerodynamic incidence, α. All four configurations create C_{Lmax} values within 3%. The 5mm overlap, 22.5° slat setting achieves the highest C_{Lmax} of 1.69 at 18° incidence. The 5mm, 20° slat setting creates the lowest C_{Lmax} of 1.65, and displays sharper stall characteristics than the other three curves. All four curves stall between 18° and 21° although with differing characteristics, the two 22.5° slat angles stall more gently than the 20° slat angle settings.

Figure 9:5:6b, drag coefficient versus aerodynamic incidence, shows all four slat and flap configurations demonstrating similar drag trends. The trend of these C_D results is different from that observed for the two single high lift device arrangements and the wing only results. A plain wing C_D curve normally remains at a value close to that of the 0° incidence value for 5-10°. After 5-10°, the gradient of the curve increases. This increase in drag normally coincides with the onset of stall. **Figure 9:5:6b** shows all four curves following an almost straight line gradient, until well past stall. The normally shallow C_D curve at low incidences is replaced by a much steeper C_D gradient which gradually increases after 0-12° incidence. This gradient remains linear until 24° incidence. Comparison with **Figure 9:5:6a** shows that the triple element aerofoil adopts a linear increase in drag, as C_L/α gradient lessens, having no sharp increase in drag at stall. This trend may indicate a gradual separation of flow, and thus the gradual onset of stall, for the triple element aerofoil. Of the four curves shown in **Figure 9:5:6b**, the 0mm overlap, 20° slat setting creates the greatest C_D across the range. The 5mm overlap, 22.5° slat setting creates the least drag; however, all four curves have drag values within 5%.

Figure 9:5:6c displays pitching moment coefficient versus aerodynamic incidence, α. The four aerofoil configurations, which have similar lift and drag characteristics, show two different pitching moment trends. The two 20° slat setting angles have a slowly increasing C_M/α gradient from 2-12° incidence, followed by a very sharp increase in C_M/α gradient between 12° and 14° incidence. Between 14° and 24° incidence, the two 20° slat angle

settings display an almost constant C_M/α gradient. After 24° they both develop a large negative C_M/α gradient. The two 22.5° slat angle settings also show a slowly increasing C_M/α gradient, between 2° and 14° incidence. After 14°, their C_M/α gradients are constant until 18°, before gradually reducing, finally becoming negative at 24° incidence. The negative $dC_M/d\alpha$ noticed between 0° and 2° incidence is due to the deflection of the slat and flap at 0° incidence.

Figure 9:5:6d shows L/D ratios for the four combinations of slat overlap, slat and flap angle, plotted versus incidence. The maximum L/D ratio is achieved at 0° incidence; L/D ratio decreases with a linear gradient, both up to, and past, stall incidence. Again, the slat configurations fall roughly into two groups, although on this occasion it is the common slat overlap settings which link the two groups. The two 5mm overlap settings achieve the maximum L/D ratio over the entire incidence range. The two 0mm overlap settings share a similar gradient for most incidences, although the 22.5° slat setting achieves the slightly higher L/D of the two curves. After 12°, however, all four triple element configurations share a very similar gradient.

The lift and lift/drag ratio trends of the triple element aerofoil have characteristics which satisfy the required wingsail design criteria. Upwind sailing requires a high lift/drag ratio, whilst the downwind optimisation requires maximum lift force. High C_{Lmax} incidences, and generally high C_L values across the incidence range, allow a wingsail to be set at an appropriate angle to create maximum thrust. A high thrust setting can be achieved without approaching a very high incidence angle, where a gust or windshift could stall the wingsail.

9.9 Experimental Results: Pressure Tappings

In order to quantify the effect that each individual high lift device had on aerofoil pressure distribution, the devices were tested separately, prior to combining all three elements. Pressure coefficients are plotted with negative C_P values above the x-axes; the standard format for displaying aerofoil pressure data. Pressure coefficient is plotted against x/c, where c is the relevant total chord i.e.:

$c_{(w)}$ (wing only) $= c_w$

$c_{(w+s)}$ (wing & slat) $= c_w+c_s$

$c_{(w+f)}$ (wing & flap) $= c_w+c_f$

$c_{(Tot)}$ (full aerofoil) $= c_w+c_s+c_f$

The slat section does not contain pressure tappings. This was due to the slat section, at model scale, being too thin to house pressure tubing. Any milling of the slat section surface would have seriously impaired the structural integrity of the leading edge high lift device. When the slat is included in the aerofoil configuration, x/c values begin at the slat leading edge, for that reason pressure results do not begin at the zero value of x/c when the slat is present.

Table 9:6, contains a summary of the graphs discussed in this section, *[All results shown are corrected for blockage effects]*:

WING	FLAP	SLAT	REYNOLDS NUMBER	FIGURE NUMBER	COMMENTS
YES			$0.5x10^6$	9:6:1	0°α; ENDPLATES ON/OFF
YES			$0.5x10^6$	9:6:2	12°&16°α; ENDPLATES ON
YES	YES		$0.62x10^6$	9:6:3a	12°α; 10,15 & 20° FLAP
YES	YES		$0.62x10^6$	9:6:3b	16°α; 10,15 & 20° FLAP
YES	YES		$0.62x10^6$	9:6:4	12°&16°α; 20° FLAP
YES		YES	$0.5x10^6$	9:6:5a	12°&20°α; 0mm OVERLAP
YES		YES	$0.5x10^6$	9:6:5b	12°&20°α; 5mm OVERLAP
YES		YES	$0.5x10^6$	9:6:5c	12°&20°α; 10mm OVERLAP

TABLE 9:6

9.9.1 Wing Only

Model III has pressure tappings fitted to one side of the aerofoil only, hence upper and lower surface pressure readings are obtained by reversing the incidence of the model. In this case, the upper and lower surface readings should be identical. One disadvantage of this design feature is that aerodynamic zero incidence cannot be found using the pressure distribution. The incidence at which an aerofoil creates zero lift force is used as a datum, known as aerodynamic zero, and all other incidences are set from this angle. Aerodynamic zero incidence is an important test for a symmetrical aerofoil, which should create zero lift force when the model is at 0° geometrical incidence. Force measurements were used to identify the incidence at which the model created zero lift force. A survey of model position confirmed that the centreline of the wing section was horizontal in relation to the tunnel. Therefore, having found zero lift force when the model centreline is horizontal (i.e. when the model is at geometric 0° incidence), suggests that the plain wing is geometrically symmetrical. **Figure 9:6:1** shows the plain NACA 0018 wing section pressure distribution at 0° incidence.

Figure 9:6:2 shows C_P versus x/c_w for the plain wing case, at the experimental Reynolds number of 0.5 x 10^6. The figure shows pressure coefficients for the wing upper and lower surfaces. These pressure coefficients are plotted for two incidences, 12° and 16°. The 16° results show a suction, or low pressure peak C_P of -4.3, compared with a C_P of -3.3 for the 12° case. This indicates that the velocity of flow has increased over the leading edge of the wing upper surface. This increase in velocity is caused by flow travelling around an area of increased curvature at the aerofoil leading edge. The opposing effect is noticed on the lower surface of the aerofoil, where flow is retarded. Inspection of the lift force curve for the plain wing, **Figure 9:4:2**, shows that the plain wing begins to stall at 10-12° and that complete stall occurs after 16°. The upper surface of the 16° incidence case has a flat profile, with a slightly higher pressure coefficient over the rear half of the wing chord, c_w. This flattening pressure coefficient profile and slight pressure increase may be due to the progressive separation of flow from the

wing trailing edge, preceding a full trailing edge stall.

9.9.2 Wing and Flap

Figures 9:6:3 a-b show C_P versus $x/c_{(w+f)}$ for the wing and flap combination. Figures '**a**' and '**b**' show pressure distribution for the upper and lower aerofoil surfaces, at incidences of 12° and 16° respectively. Three curves are shown on either graph, representing flap setting angles of 10°, 15° and 20°.

Inspection of **Figures 9:6:3 a-b** raises two important points for discussion. Firstly, the effect that increasing flap angle has on C_P, whilst the aerofoil remains at constant aerodynamic incidence. Secondly, the effect that increasing aerodynamic incidence has on C_P, whilst at constant flap angle.

It can be seen from **Figures 9:6:3a-b**, that the effects of increasing flap incidence are similar at both aerodynamic incidences. Increasing flap angle has little effect on the pressure distribution at the main wing leading edge. However, increasing flap angle does cause a pressure decrease over the trailing 40% of the main wing chord. The greatest pressure decrease noticed over this region is between 10° and 15° flap angle. Increasing the flap angle a further 5° has a relatively small effect on C_P. The pressure coefficient decreases over the upper surface of the flap leading edge with increasing flap angle. This low pressure region on the flap upper surface moves upstream towards the flap leading edge as flap angle increases. Changes in flap angle have a much lesser effect on the lower surfaces of both wing and flap. Over the first 80% of the main wing chord, there is little effect from changing flap angle, but a slight decrease in pressure coefficient is noticeable towards the trailing edge. The only area of the aerofoil to display an increasing pressure coefficient with an increase in flap setting angle is the flap lower surface. The increase in pressure noticed is small, and almost constant along the whole flap chord.

The effects, as described above, of increasing flap angle are shown more clearly by looking at the aerofoil as a whole. An increase in flap angle causes

a slight decrease in pressure at the lower surface of the wing trailing edge. This indicates that the velocity of flow in this region is increased, an increase which is confirmed by the relatively large decreases in pressure noticed at the leading edge of the flap upper surface. As expected, a higher pressure region is noticed on the flap lower surface, when the incidence of the flap is increased, due to a decrease in flow velocity. As all these effects increase when flap angle is increased, it is possible to conclude that the geometry of the wing and flap combination is optimised with increasing flap angle, up to 20°. However, pressure results were not recorded for the 25° flap setting angle as this configuration created very poor lift force results.

The only pressure characteristic not yet discussed is the differing pressure distribution over the trailing 40% of the main wing upper surface. Pressure decreases over this region, with increasing flap angle. It is likely that this is caused by the pressure gradient created between the leading and trailing edges of the wing chord. The flow velocity over the flap leading edge is greater than the freestream velocity, thus creating a low pressure area. The flow over the main wing is, therefore, placed in a lesser pressure gradient, between the very low pressure at the leading edge and the low pressure at the trailing edge. The velocity of flow over the flap upper surface increases with increasing flap angle. It follows then that this reduces the pressure gradient between the main wing leading and trailing edge still further, and that the decrease in pressure noticed over the wing upper surface is due to the increased velocity flow travelling through the slot between the wing trailing edge and the flap, with increased flap angle.

Figure 9:6:4 shows the pressure distribution of the 20° flap setting angle, the setting which created maximum lift force. Two curves are shown, those of 12° and 16° aerodynamic incidence. The figure shows that increasing the incidence of the aerofoil from 12-16°; has the effect of increasing peak suction at the wing leading edge; downstream of this peak suction region, pressure over the wing upper surface is very similar at both incidences. Increasing aerodynamic incidence causes pressure to rise by a small amount

over the lower surface of the wing. As increasing aerodynamic incidence has very little effect on flow over the flap, it can be assumed that any increase in lift is due to flow over the wing.

9.9.3 Wing and Slat

Figures 9:6:5 a-c show C_P plotted versus $x/c_{(s+w)}$, where $c_{(s+w)}$ is the chord length of the slat and wing. The three graphs represent the slat configurations which achieved the three highest lift values. These slat settings are; 0mm overlap, 20° slat angle; 5mm overlap, 20° slat angle; and 10mm overlap, 22.5° slat angle. Two curves are plotted on each graph showing aerodynamic incidences of 12° and 20°. The x-axes, which show $x/c_{(s+w)}$ begin at a value of 0.2, the maximum value of x/c_s.

Figure 9:6:5a shows the 0mm overlap, 20° slat angle configuration at aerodynamic incidences of 12° and 20°. An increase in aerodynamic incidence can be seen to affect pressure distribution over the entire wing chord. The suction peak, which occupies the leading 10% of the wing upper surface, is increased with increasing incidence, from a C_P of -2.6 to a value of -4.7. However, pressure downstream of this peak suction region is increased. These changes in pressure distribution with incidence indicate that, although flow velocity is increased at the leading edge of the wing, flow over the majority of the chord has a lower velocity. Although this indicates a loss of lift generated from this area of the wing, it should be noted that flow would be completely separated at this incidence of 20°, if the slat were not present. The pressure distribution over wing lower surface is also affected by the increase in aerodynamic incidence from 12-20°. The first tapping on the wing lower surface shows a pressure increase from -0.95 to -0.2, pressure is also increased over the remaining chord length. This increase in pressure is an exaggeration of the pressure distribution change noticed on the lower surface of the plain wing section, with increasing incidence.

The results from **Figure 9:6:5b** are very similar to those for **Figure 9:6:5a**. This indicates that the alteration in slat setting to 5mm overlap, 20° does not

have a great effect on pressure distribution. **Figure 9:6:5c**, however, shows slightly different results. The low pressure area at the wing leading edge is increased at both incidences, most noticeably at 20° incidence. These results imply that the flow velocity through the slot between the slat and the wing is increased for the majority of incidences.

The effects of the slat on the plain wing pressure distribution can be seen by comparing the 12° wing and slat results, **Figure 9:6:5a**, with the plain wing results from **Figure 9:6:2**. The marked difference in results is that the low pressure peak in the leading edge region in **Figure 9:6:5a** is reduced to a C_P of -2.6, from a value of -3.3 for the plain wing. Therefore, the slat appears to have reduced the velocity of flow around the wing leading edge. This alteration in pressure distribution appears to indicate a reduction in lift created over the wing, when the slat is fitted. It is possible to prove that this is not the case by looking at the lift force created by the two configurations. The lift coefficient for the plain wing at 12° is 0.9. The lift coefficient for the wing and slat configuration at 12° is 1.05. The apparent loss of lift shown by the wing and slat pressure distribution, and the increase in lift force recorded, strongly imply that the slat section not only prevents flow from separating at high angles of attack, but also creates a lift force.

9.10 Full Wing: Slat, Wing and Flap

Table 9:7 contains a summary of the graphs discussed in this section. All graphs shown were tested at a Reynolds number of 0.72×10^6. [All results shown are corrected for blockage effects]:

SLAT OVERLAP (mm)	SLAT ANGLE (deg)	FLAP ANGLE (deg)	AERODYNAMIC INCIDENCE (deg)	FIG. No.
0	20	20	12, 20 & 23	9:7:6a
5	20	20	12, 20 & 23	9:7:6b
10	22.5	20	12, 20 & 23	9:7:6c

TABLE 9:7

The configurations shown **Figures 9:7:6 a-c** are defined in **Table 9:7**. These configurations of slat overlap, slat angle and flap angle are those which created the three highest C_{Lmax} values. **Figures 9:7:6 a-c** show the pressure distribution for the triple element aerofoil. These three graphs each contain three curves, representing the aerodynamic incidences of 12°, 20° and 23°.

Figure 9:7:6a shows the triple element aerofoil configured with 0mm overlap, 20° slat angle and 20° flap angle. The figure shows very similar pressure coefficients over wing lower surface for all three aerodynamic incidences. The only obvious effect of increasing aerodynamic incidence is a very small increase of pressure at the first lower surface tapping. Increasing incidence has little effect on the pressure distribution over the flap lower surface, but the incidence angle of the aerofoil has a large effect on the wing and flap upper surfaces. Peak suction at the wing leading edge increases from -2.3, to -3.7, to -3.8, with 12°, 20° and 23° incidences respectively, indicating an increasing flow velocity over the leading edge of the wing upper surface. However, downstream of this low pressure peak, increasing the incidence angle causes an increase in the pressure coefficient, thus decreasing the lift generated over this area of the wing upper surface. Increasing the aerodynamic incidence angle also increases C_p over the upper surface of the flap chord, decreasing lift over this region. Although the flow velocity over the majority of the wing upper

surface is reduced, the aerofoil has not stalled. Consequently, the presence of the slat increases the velocity of flow over the wing leading edge. This increase in velocity allows the flow to remain attached over the entire wing and flap chord.

The results from **Figures 9:7:6 a-c** are very similar. The most noticeable difference between them is the value of the low pressure peak, located at the leading edge of the wing upper surface. The differing low pressure peak is caused by altering the geometrical configuration of the leading edge device, and the slot created between the slat and the wing. The similarity between figures '**a**', '**b**' and '**c**' was not unexpected. The force results for these same configurations, **Figure 9:5b:6a**, showed all three C_{Lmax} values varying by just 3%, at the same incidence.

9.11 Slat, Wing and Flap Configuration Comparison

Table 9:8 contains a summary of the graphs discussed in this section. *[All results shown are corrected for blockage effects]*:

CONFIGURATION	FIGURE NUMBER	COMMENTS
5mm OVERLAP, 20°SLAT, 20°FLAP	9:8:7a	12°α; COMPARISON OF WING ONLY, WING & FLAP, WING & SLAT AND FULL WING. UPPER SURFACE.
5mm OVERLAP, 20°SLAT, 20°FLAP	9:8:7b	12°α; COMPARISON OF WING ONLY, WING & FLAP, WING & SLAT AND FULL WING. LOWER SURFACE.

TABLE 9:8

Figures 9:8:7 a-b compare the effects of each separate high lift device on pressure distribution, at an aerodynamic incidence of 12°. The four curves shown on each graph represent the wing only, wing and slat, wing and flap and full triple element aerofoil configurations. The high lift devices are configured to the same settings, whether used singly, or as part of the triple element aerofoil. The slat, if fitted, has an overlap of 5mm and a setting angle is 20°. The flap, if fitted, has a setting angle of 20°. Figures '**a**' and '**b**', represent the upper and lower surface pressure distributions

respectively.

Figure 9:8:7a shows the upper surface pressure distribution of the four aerofoil arrangements. The effects of the various high lift devices on the main wing leading edge are considered first. The addition of the flap to the plain wing aerofoil creates a small increase to the peak suction value. However, when the flap is fitted, this peak suction occurs in a much smaller region of the wing chord. The plain wing low pressure peak occurs over the leading 10% of the wing chord. The reason for this is not clear. The addition of the flap is not expected to affect the leading edge pressure distribution of the wing. The accuracy of flap pressure results is discussed in **Section 9.12**. This section considers difficulties that were encountered with results when the flap was fitted to the model. The addition of the slat to the plain wing lowers the peak suction value to a C_P of -2.5, while the triple element combination lowers peak suction further still, to a C_P of -2.05. This reduction of flow velocity around the leading edge of the wing was noticed previously in the wing and slat section, **Section 9.9.3**. Although the pressure distribution characteristic appeared to show a decrease the lift created for the wing and slat, the lift force measured at this angle was increased. This increase in lift force is thought to be due to the slat section although it is impossible to confirm this by pressure readings as the slat does not contain pressure tappings. The reduction of the low pressure peak, between the triple element aerofoil and the wing and slat combination, shown in **Figure 9:8:7a**, appears to be due to the geometry of the slot between the main wing and the slat. Although the geometry of the slot is the same for both configurations, the flow through the slot is affected by the differing lower surface pressure distributions that were encountered. This theory is confirmed by the fact that another slat configuration achieved a similar C_P to the plain wing; the results of the 10mm overlap, 22.5˚ slat angle configuration, gave a C_P of -2.5 when in the triple element configuration.

Downstream of the leading edge, the four curves in **Figure 9:8:7a** appear to fall into two groups, those with and without the flap fitted. All four pressure distributions show a gradual increase in pressure over the wing chord. This pressure increase is much more gradual for the wing and flap, and triple element configurations. These configurations have a pressure coefficients at the trailing edge of -0.75 and -0.80

respectively. These differing pressure gradients are most apparent over the trailing 50% of the wing chord. The two configurations without a flap show a larger pressure gradient over the chord, C_P increases to values -0.20 and -0.15 for the wing and slat and the plain wing configurations respectively. Consideration of the C_P results at the flap leading edge may provide an explanation for this effect. The flow velocity over the flap leading edge is greater than the freestream velocity, thus creating a low pressure area. Therefore, the very low pressure flow at the wing leading edge is placed in a lesser pressure gradient between the wing leading and trailing edge, when the flap is present, than the flow over the wing when the flap is not fitted. Conversely, when the flap is not present, flow is subject to a greater pressure gradient, between very low pressure flow at the leading edge and the higher pressure freestream flow at the trailing edge. Over the trailing 50% of the wing chord, the wing and slat configuration has a slightly lower pressure than the wing only configuration. This lower pressure indicates that the flow has a higher velocity over this region. The pressure distribution over the upper surface as a whole, indicates that, although the maximum velocity through the slot between the wing and slat is reduced from the plain wing model, the velocity of flow over the majority of the wing chord is increased. The triple element aerofoil also has a slightly lower pressure than the wing and flap configuration over the trailing 50% of the wing. It is likely then that this pressure difference is due to the pressure gradient to which the flow is subject. The flap leading edge has a slightly lower C_P when in the triple element model configuration than in the wing and flap arrangement.

Figure 9:8:7b shows the lower surface pressure distributions for the four aerofoil configurations. The pressure distribution over the leading edge of the lower surface is considered first. The wing only configuration has the highest pressure reading, at the wing leading edge, a C_P of 1.00. The next highest pressure value is that of the wing and slat configuration with a C_P of 0.75. These high pressure values are found where the flow is moving most slowly around the aerofoil, in this case, close to the stagnation point at the leading edge. The two configurations with the flap fitted have relatively low, high pressure C_P values of 0.6 and 0.5, corresponding to the triple element and wing and flap configurations respectively. The pressure distributions over the aerofoil lower surface, again appear to fall into two categories, those with

and without the flap. This trend was also noticed with the upper surface pressure distributions. The pressure coefficient values over the trailing 80% of the wing chord, for the wing and flap and triple element aerofoils, are higher than for the plain wing and wing and slat results. This again appears to be due to the presence of the flap. The pressure coefficient at the flap leading edge is higher than the freestream flow. Therefore, the high pressure flow at the wing leading edge is placed in a lesser pressure gradient when the flap is present, than the flow over the wing when the flap is not fitted. Similarly, when the flap is not present, the flow is subject to a steeper pressure gradient, between high pressure flow at the wing leading edge and the lower pressure freestream flow at the wing trailing edge. The wing and slat configuration, shows rapid decrease in pressure, C_P falls to the trailing edge value in the leading 40% of the wing chord. The wing only configuration also shows a rapid decrease in pressure, although the C_P remains slightly above the trailing edge value and decreases very slowly to this value over remaining 60% c_w. This difference in leading edge pressure demonstrates that the presence of the slat increases the flow velocity slightly over the wing leading edge lower surface. After the first two tappings on the main wing lower surface, the wing and flap and triple element aerofoils have similar pressure distributions for the leading 50% of c_w. The differing pressure distribution over the trailing 50% of the wing chord corresponds to a difference in pressure at the flap leading edge, the triple element results remain at a higher pressure. This higher pressure noticed at the leading edge of the flap, when in the triple element configuration, decreases rapidly toward the flap trailing edge. The wing and flap pressure distribution has a slightly lower pressure coefficient at the flap leading edge, while the pressure distribution at the flap trailing edge is higher than the triple element result. Therefore, the wing and flap combination has a slower flow velocity over the majority of the flap chord.

9.12 The Accuracy of Pressure Results

The accuracy of pressure coefficient results is dependent upon a number of parameters.

The position and quality of the pressure tappings on the model is of primary importance. The tappings on model III are placed at a 45° angle to the flow direction,

with the tapping on the mid-point of either the wing or flap chord, positioned on the centreline of the model span. Positioning the tappings along the centreline of the model span ensures that the flow over the tappings is as free from three dimensional aerodynamic effects as possible. The tappings are also positioned well away from the wind tunnel support struts and any flow disturbance caused by them. The position of the pressure tappings is shown in **Figure 5:10** and described in **Section 5.6.1**. The surface finish of the pressure tappings, particularly where they met the aerofoil surface were clean, smooth and free from any distortions to the aerofoil surface finish which may have affected results.

The second parameter affecting the accuracy of pressure results is the quality of the pressure transducer which records the pressure at each tapping. The pressure transducer was calibrated against known static pressure values and verified against a bank manometer. The accuracy of the Scanivalve results depends upon the number of readings which are taken and then averaged. The total time taken to sample and average each tapping is used as the reference. Calibration results showed an accuracy of within 2%, for a 10 second total sampling time. It is, however, impractical to sample 40 tappings with a 10 second total sampling time as this would take almost 7 minutes. It was found, however, that a 5% accuracy could be achieved with a total sampling time of just 3 seconds. Although a 2% accuracy of pressure results was considered to be favourable, a test time of 7 minutes is not feasible, as that length of test time would allow inaccuracies due to tunnel heating effect to affect results. Tunnel heating has the effect of changing the air temperature in the tunnel, which in turn will alter the air density and thus affect the Reynolds number at which the test is conducted. Therefore, it was decided to use a sampling time of 3 seconds per tapping, giving a total test time of 2 minutes. This test time was considerably less than could be achieved using a manometer bank.

The third parameter affecting the pressure results is the effect of tunnel blockage. The force and moment results recorded from the balance were all corrected using Maskell's blockage theory [13]. The pressure coefficient results were also corrected using Maskell's blockage theory. The equation used is derived from the tunnel velocity correction equation, **Equation 4:13**.

The final parameter which can affect the accuracy of pressure coefficient results, is the way in which the C_P equation itself is applied. Pressure coefficient, C_P, is defined as follows:

$$C_p = \frac{p - p_\infty}{\frac{1}{2}\rho V^2} \qquad \textbf{9:6}$$

Where p = static pressure at the aerofoil surface, p_∞ = reference static pressure, ρ = the tunnel air density and V = the velocity of the tunnel freestream flow.

For the C_P calculations, the reference pressure, p_∞, was taken to be the laboratory atmospheric pressure, p_{atm}. The use of the laboratory atmospheric pressure as a reference pressure for C_P calculations is valid only when the tunnel static pressure is equal to atmospheric pressure. Immediately downstream of the working section the tunnel has an open gap of approximately 30mm. Therefore, it is assumed that the working section static pressure is equal to the laboratory atmospheric pressure. The reference pressure, p_∞, was recorded before starting the tunnel by recording the pressure at tappings on the upper surface of model. The results from all 40 tappings were monitored prior to each run for any spurious readings which could be caused by a pipe blockage etc.

During analysis of the C_P results for Model III, it was noticeable that the values of C_P for model configurations with the flap attached were very high. These results could not be explained by any aerodynamic characteristic and so the method of recording C_P was investigated further. A simple flow visualisation experiment, using a 0.5 metre long piece of cotton attached to stick, showed that with the flap attached, the flowfield at the tunnel roof had not returned to a direction parallel with the tunnel wall. The same experiment with the plain wing model proved that the flowfield around the model returns to a direction parallel to the tunnel wall. The tunnel wall is perforated to keep the static pressure equal to the atmospheric pressure even when a certain amount of blockage exists. The tunnel roof has a number of 13mm (1/2″) holes cut at an angle of 30° to the horizontal, in the direction of the flow. These holes have centre-points spaced at 51mm (2.0″) intervals across the width of the tunnel. The centre position of the holes on the downstream row are on a centreline

between the two upstream holes. If the flowfield is constrained or blocked above certain limits then the flow in the working section may start escaping through these holes into the laboratory.

The effect of the flowfield dispersing into the laboratory was to alter the reference pressure, p_∞ used to define pressure coefficient. To investigate the error caused by this, the static pressure measured on the wall immediately upstream of the working section, p_{up}, was used as a reference pressure to represent the working section static pressure. The laboratory atmospheric pressure, p_{atm} and upstream static pressure, p_{up}, were measured for all model configurations. Results from this comparison verified that any change in tunnel reference pressure only occurs when the flap is fitted to the model.

To quantify the change in reference pressure, a Betz manometer was used to measure the difference between p_{up} and p_{atm} . When the flap is not attached to the model, the static pressure in the tunnel was found to be equal to atmospheric pressure, however, for both wing & flap and triple element configurations this was not the case. The measurement of p_{up}- p_{atm} was performed at the same tunnel test velocities and model configurations that were used for C_p calculations and the pressure difference, p_{up} - p_{atm}, was plotted against velocity, V. With the model at test aerodynamic incidences of 12, 20 and 23°, for the small range of tunnel velocities, 30-35ms^{-1}, the pressure difference remained approximately constant. It was therefore safe to assume that the difference between p_{up} and p_{atm} could be used to correct the value of p_∞. This correction, equivalent to ΔCp, was calculated to be -0.63. This correction allows C_p comparison between flap on and flap off configurations. Although the change in p_∞ was measured accurately using a 'Betz' manometer, the correction factor was only calculated over a small range of velocities using relatively few points, the error is could to be in the order of 10%. Therefore, C_p results with the flap attached should be observed with caution.

9.13 The Effect of High Lift Devices on Stall

In the following section, the stall type of all four wing combinations, from plain wing through to triple element section, are discussed. Comments are made upon the stall type, with and without high lift devices. The discussion is based on the effects of configuration changes upon pitching moment coefficient and aerofoil pressure distribution. The model is pivoted about the plain wing 1/4 chord point, which is also the 1/4 chord point for the full aerofoil section. A nose-up pitching moment is defined as positive.

9.13.1 Wing Only

A wing section of 18% t/c ratio would normally be expected to display a trailing edge stall. However, the relatively low test Reynolds number 0.5 x 10^6 may alter stall characteristics. A trailing edge stall is normally characterised by a pressure distribution with a rounded suction peak around 10% c_w. This type of stall, as the name states, involves the flow separating from the trailing edge of the wing. Therefore after C_{Lmax} a trailing edge stall will display a gradual loss of lift, with increasing incidence, as separated flow moves steadily upstream from the trailing edge. This progressive separation gives the trailing edge stall a gentle stall characteristic. In contrast, a leading edge stall normally displays a sudden loss of lift at stall, due to the bursting of a transition bubble, see **Section 4.1.2**.

Figure 9:6:2 shows the plain wing C_P distribution plotted versus x/c_w. The figure shows a suction peak between 0 and 0.1 c_w, or 10% wing chord, which grows until stall. This figure also shows a gradual loss of lift from 10-16° incidence. The combination of these two characteristics implies that the plain wing has a trailing edge stall characteristic.

9.13.2 Wing and Flap

The flap and wing combination creates a large negative pitching moment. **Figure 9:4:3c** shows C_M plotted versus incidence for small flap angles 0-15°. However, pitching moment curves for larger flap angles 20°and 25° are not shown, due to the pitching moment rising above balance limits and creating

a balance interference. The pitching moment gradient of the 0° to 15° flap settings does not change significantly after stall, thus little can be deduced from this. However, the lift coefficient graph for the flap and wing combination **Figure 9:4:3a** has some characteristics of note. At all flap settings, the trend is for a gradual loss of lift prior to stall. As discussed in the plain wing section, this gradual loss of lift is normally associated with a trailing edge stall, which may not be the case for a multi element aerofoil, such as the flap and wing configuration, where a combined stall may occur.

Figure 9:6:4 shows C_P versus $x/c_{(w+f)}$ for the wing and flap combination, at increasing aerodynamic incidence. The flap is set at an angle of 20°. Increasing incidence appears to effect C_P over the leading 10% of the plain wing upper surface. The increase in lift between the 12° and 16° incidence curves appears solely due to this increase in peak suction at the wing leading edge. In **Figures 9:6:3a-b**, increasing the flap angle, and hence effective wing camber, appears to effect the flow over the latter 50% of the wing upper surface. However, **Figure 9:6:4** demonstrates that increasing aerodynamic incidence, with constant flap angle, has little effect on flow over the trailing edge of the wing section. The lack of effect that the increase in incidence has on the wing trailing edge suggests that flow may be separating from this region. If this were the case, and flow was separating from the wing trailing edge, the absence of any large changes in pitching moment after stall would imply that, as the wing stalls, disturbed flow moving downstream stalls the flap almost simultaneously.

9.13.3 Wing and Slat

The configuration of the wing and slat is described in **Section 9.0.2**. The pitching moment coefficient versus incidence Figure, **Figure 9:4:4c**, demonstrates the wing and slat stall behaviour. All four wing and slat configurations shown display a reduction in pitching moment gradient prior to stall. All four curves also adopt a negative pitching moment gradient after stall. This gradual loss of pitching moment coincides with a gradual loss of lift at the same incidence; shown in **Figure 9:4:4a**. A negative pitching

moment gradient after stall would be consistent with a leading edge stall. This does not appear likely, however, due to the gentle loss of lift prior to stall. It is more likely that the decrease in pitching moment, prior to stall, is due to a decrease in lift created by the aerofoil as the slat incidence increases past its most efficient. The pressure distribution for the wing when the slat is attached is shown in **Figures 9:6:5 a-c**. All three graphs clearly show that increasing aerodynamic incidence increases the peak suction at the wing leading edge and that the loss of lift occurs at the wing trailing edge. The combination of the force and pressure results implies that the wing and slat combination also has a trailing edge stall, although at a greater aerodynamic incidence than the plain wing. It appears logical that a plain wing displaying a trailing edge stall should maintain that characteristic after a leading edge high lift device is fitted.

9.13.4 Full Aerofoil: Slat, Wing and Flap

Figures 9:5b:6 a-d show the four optimum lift settings for the triple element section. The four settings are shown here either created maximum lift, or created a lift force very close to maximum, whilst maintaining a high L/D ratio. The four figures a) to d) show C_L, C_D, C_M and L/D ratio respectively, plotted versus aerodynamic incidence, α.

Figure 9:5b:6c, shows C_M versus incidence, α. From this figure, it can be seen that the triple element combination operates with large negative pitching moments. This would appear to be caused by the presence of the trailing edge high lift device. The wing and flap figure, **Figure 9:4:3c**, showed increasingly negative values of C_M, with increasing flap angle, eventually beyond the balance C_M limits. **Figure 9:5b:6c**, the triple element figure, shows slightly less negative values of C_M, presumably due to the positive moment caused by the slat. As the flap and wing alone have a very linear negative gradient, and this is altered to a positive gradient by the addition of the slat, it appears likely that the changing C_M gradient is due largely to the effect of the slat on the aerofoil. The pitching moment behaviour shortly before and after stall is similar to that noticed in the wing and slat only graph, **Figure 9:4:4c**. Both

graphs display a gradual decrease in pitching moment gradient, coinciding with a gradual decrease in lift. However, the two 20˚ slat settings in **Figure 9:5b:6c** demonstrate a much sharper change in C_M gradient at stall, when the flap is attached.

Figures 6:7:6 a-c show C_P curves for the three configurations discussed above, which are plotted versus x/c_{tot}, where c_{tot} is the sum of the wing, slat and flap chord lengths. Figures '**a**' to '**c**', show differing slat overlap values, although all share a similar C_P profile. Increasing aerofoil incidence from 12˚ to 20˚ shows peak suction increasing at the wing leading edge, although there is little change between 20˚ and 23˚ incidence. Downstream of the area of peak suction, pressure increases over the upper surface of wing and flap sections. Increasing aerodynamic incidence appears to have little effect on the wing and flap lower surfaces. Unfortunately, it is not possible to describe the pressure distribution over the slat.

From the C_L, C_M and C_P behaviour, it does not appear likely that the triple element aerofoil stalls from the wing trailing edge, which is thought to be the case for the wing only and wing and slat combination. It does, however, appear much more likely that the gradual loss of lift is due to a loss of effectiveness of the slat at increasing incidences. A decrease in effectiveness of the leading edge device would have the effect of causing the pitching moment trend noticed in **Figure 9:5b:9c**. It is difficult to suggest the stall type for the triple element aerofoil. It is possible that, as aerodynamic incidence becomes too great for the slat to operate, the wake from the slat interferes with the flow over the upper surface of the main wing section, thus stall is induced. The logic behind this theory is that the C_M characteristics noticed prior to stall are similar to those noticed when the slat is added to the plain wing. This indicates the influence that the slat has on the aerofoil characteristics prior to stall. This theory would agree with the decrease in flow velocity over the main wing upper surface, and hence reduction in lift, towards stall.

9.14 The Effects of Scale

Wingsails, unlike aircraft wings which operate in a fairly limited range of Reynolds numbers, can operate in a vast range of Reynolds numbers, depending on wind speed.

Table 9:9, shows the Beaufort Windforce scale, used by sailors worldwide, for classifying wind and sea conditions. In the table, windspeed, traditionally shown in Knots (Kts), the equivalent of 1 nautical mile per hour, is converted into metres per second (ms^{-1}).

BEAUFORT FORCE	WINDSPEED (Kts)	WINDSPEED (ms^{-1})	REYNOLDS NUMBER *
0 - CALM	<1	< 0.514	0.067×10^6
1 - LIGHT AIR	1-3	< 1.54	0.202×10^6
2 - LIGHT BREEZE	4-6	< 3.09	0.405×10^6
3 - GENTLE BREEZE	7-10	< 5.14	0.674×10^6
4 - MODERATE BREEZE	11-16	< 8.23	1.08×10^6
5 - FRESH BREEZE	17-21	< 10.8	1.42×10^6
6 - STRONG BREEZE	22-27	< 13.9	1.82×10^6
7 - NEAR GALE	28-33	< 17.0	2.23×10^6
8 - GALE	34-40	< 20.6	2.70×10^6

TABLE 9:9

** The last column in **Table 9:9** shows the Reynolds number. To calculate Reynolds number for a wingsail four parameters are required; air density, the viscosity of air, a reference length (usually the wing chord) and the flow velocity. The parameters for air are taken from International Standard Atmosphere ISA tables, at sea level. The chord length of the model is 2 metres, a typical chord length for a full scale wingsail. Reynolds number is also based upon flow velocity, or windspeed. The windspeed used to calculate Beaufort windforce, and thus Reynolds number, is the true windspeed without any vessel velocity components.*

It can be seen in from **Table 9:9**, that a wingsail of 2 metres chord may be required to operate in a Reynolds number range between 0 - 2,700,000. As lift force is proportional to windspeed squared, significantly greater thrust will be produced at the higher windspeeds. For the 2 metre chord wingsail considered, the majority of the wingsail boundary layer will be wholly turbulent after force 4, a moderate breeze.

Experimental Reynolds numbers were limited to a range between 0.5-0.75 x 10^6. This was due to tunnel blockage and balance limits. The windtunnel model has a blockage ratio of 15%, when at 30° incidence with a 20° flap angle, which is the highest blockage ratio considered acceptable for experimental testing. The model size, already limited by this blockage ratio, was still great enough to require the balance range of +/- 220 Newtons to be altered. This was achieved by means of counterweights. The new balance limits were -40 to +400 Newtons. Unfortunately, due to the high lift force created, the model required a great deal of reinforcement in order to withstand the bending moments encountered. This reinforcement, which took the form of front and rear steel spars, increased the weight of the model significantly, thus reducing the measurement range of the balance.

9.14.1 Effects of Scale on Drag

Drag force on the model consisted of three parts, form drag, skin friction drag and induced drag. Form drag for streamlined bodies, such as aerofoils, is largely independent of Reynolds number. Skin friction drag varies with boundary layer state and is therefore affected by Reynolds number, surface finish and transition point. Induced drag, however, is a function of both three dimensional aerodynamic effects and form drag. The main effects of scale on drag force are due to skin friction.

9.14.2 Skin Friction Drag

Skin friction, as defined in **Section 9.1.3**, is proportional to τ_w, wall shear stress, over the wing chord. In the plain wing case **Figure 9:1:2b** skin friction drag is approximately 50% of the total C_D at 0° incidence. During the CFD design stage, similar aerofoil sections were tested at a constant Reynolds number and incidence. Therefore, the factors which affect skin friction drag;

Reynolds number, incidence, transition point, surface finish and boundary layer state were all constant. It was not necessary, therefore, to include drag due to skin friction in the computational design stage as it had no affect on the percentage improvement of a design change.

9.14.3 Effects of Scale on Lift

Scale effects on lift are difficult to predict, as lift force is also dependent on Reynolds number, incidence, transition point, surface finish and boundary layer state. The effect of scale poses difficulties when testing any aerofoil section other than the most common, as these characteristics are well documented. When the aerofoil to be considered is a multi element section, such as the one in discussion here, the effects are hard to predict accurately.

9.15 The Effects of Aspect Ratio

If it were possible to create a perfect two dimensional model, subject to no three dimensional flow components and with a uniform lift distribution along the entire span, then that model would have an effective aspect ratio of infinity. Model III, tested here uses endplates to minimise three dimensional aerodynamic effects. These endplates are intended to simulate the model spanning the entire tunnel section, thus creating uniform loading distribution across the wing span. Unfortunately, it is unlikely that a uniform spanwise loading will be established, partly due to the complex variable geometry required at the model wing tips. Therefore, three dimensional effects, and those of aspect ratio, may not be ignored.

If it is assumed that the endplates perform no function and the geometric aspect ratio is equal to the effective aspect ratio of the model, AR=4, the aspect ratio can be corrected using Prandtl's correction, taken from Rae and Pope [15], as described in **Section 4:5**. Aspect ratio is corrected to values of 5 and infinity. An aspect ratio of 5 is the likely aspect ratio for a full scale wingsail 10m high (span), with a 2m chord.

The aspect ratio is corrected and plotted: for the wing only case, **Figure 9:10a**; the wing & slat configuration, **Figure 9:10b**; the wing & flap configuration, **Figure 9:10c**; and finally for the triple element aerofoil, **Figure 9:10d**. All four aspect ratio graphs show the effect that increasing aspect ratio has, of increasing $dC_L/d\alpha$ whilst maintaining stall angle.

To assist the comparison of the aspect ratio corrections, the C_{Lmax} results from the four configuration cases are displayed on the barchart **Figure 9:11**. The figure clearly shows that the lower the experimental aspect ratio, and the larger the correction, the greater the effect. Therefore, increasing aspect ratio has the greatest effect on the triple element configuration, which had an experimental aspect ratio of 2. The effect of the infinite aspect ratio result, for the triple element model, is greater than the sum of the individual high lift device effects. This phenomenon is suggested by Abbot and Doenhoff [34], and shown by the computational results in the **Figure 9:12**. The results from **Figure 9:12** cannot be compared directly, however, as they are calculated at an incidence of 15°, and not the C_{Lmax} incidence, for each configuration. The low geometrical aspect ratio of the model is due to limitations imposed by the windtunnel on the maximum allowable blockage ratio of the model and the maximum allowable lift, drag and pitching moment forces. These limitations are discussed in the following section.

9.16 Windtunnel Blockage

As stated in **Section 9.14**, concerning the effects of scale, in order to increase Reynolds number in windtunnel no.1, (a standard windtunnel, i.e. not variable density), either the model chord length, or the tunnel test velocity must be increased. As velocity squared is proportional to force created, whereas chord length is directly proportional to force created, increasing chord length creates a much smaller increase in force. Computational predictions were that the model would create lift values very close to the balance maximum limit, therefore it was preferable to reach maximum Reynolds number by increasing model chord length. Increasing the chord length of a model increases the percentage of the working section cross sectional area that the model occupies. This percentage is known as the tunnel blockage ratio. Maximum blockage ratio is derived from the blockage ratio at which blockage corrections are

still considered to be accurate, in this case 15%. Model III has a blockage ratio of 3%, when the model is at 0° incidence. This increases to a maximum blockage ratio of 15% when the full wing is inclined at 30°incidence, and configured with a 20° flap angle.

The blockage correction employed, Maskell's Theory, [13] gives the following corrections to C_{Lmax}, shown in **Table 9:10**. The corrections shown in this table are taken from the maximum lift setting for each configuration. These settings are:

i) Wing only
ii) Wing & slat - 0mm overlap, 20° slat angle.
iii) Wing & flap - 20° flap angle.
iv) Triple element section - 10mm overlap, 22.5° slat angle, 20° flap angle.

	WING ONLY	WING & SLAT	WING & FLAP	FULL AEROFOIL
UNCORRECTED C_L	1.05	1.44	2.03	2.02
CORRECTED C_L	1.01	1.32	1.73	1.63
UNCORRECTED C_D	0.098	0.23	0.32	0.52
CORRECTED C_D	0.097	0.22	0.28	0.33
TOTAL BLOCKAGE FACTOR ϵ_{TOT}	0.016	0.037	0.068	0.093
% CHANGE TO C_L DUE TO BLOCKAGE CORRECTION	-3.8	-8.3	-14.7	-19.1
% CHANGE TO C_D DUE TO BLOCKAGE CORRECTION	-1.0	-3.9	-11.3	-36.2
WAKE BLOCKAGE, AS A % OF TOTAL CORRECTION	73	90	90	94
SOLID BLOCKAGE, AS A % OF TOTAL CORRECTION	27	10	10	6

TABLE 9:10

It is clear from this blockage comparison table, **Table 9:10**, that the greatest blockage correction was necessary for the triple element configuration. Inspection of the blockage equations, **Equations 4:4 to 4:13**, shows that both solid and wake blockage are based upon the model chord, but that wake blockage is also directly proportional to the uncorrected model drag. It follows then that the largest contributor to the total blockage factor ϵ_{TOT} is wake blockage. Up to 94% of the total blockage correction for the triple element model is due to wake blockage. As the name suggests, wake blockage is caused by the wake behind a body reducing the mean velocity of the freestream. This wake acts as a solid body and effectively reduces the area of the cross section. According to the laws of continuity, a constant volume of fluid must pass through the test section. Therefore, the main streamflow is required to accelerate, which creates a pressure gradient. The wake blockage coefficient is therefore directly proportional to the uncorrected drag coefficient, which is itself 300% greater for the triple aerofoil configuration than for the plain wing. This explains the increasing influence of wake blockage on total blockage. The uncorrected drag coefficient is not, however, directly related to the total blockage correction, which is a function of the total blockage factor and the volume occupied by the model in the tunnel. The triple element model has the largest chord length and creates the greatest drag force of all four configurations shown.

9.17 Analysis of the 'Triple Element Aerofoil' Configuration

Having designed a multi element wingsail, using computational results to predict qualitatively the effects on the experimental model, it is interesting to compare the experimental windtunnel results, for the maximum lift setting of the triple element wingsail design, with those found by CFD.

Figure 9:13, shows the CFD model, configured in the same way as the experimental model which created maximum lift. The t/c ratios for the slat, wing and flap are 15%,18% and 15% respectively. The ratio of chord lengths, c_s:c_w:c_f, are 3:12:8, and the high lift device configuration is 5mm slat overlap, 22.5° slat angle and 20° flap angle.

Figure 9:13 shows C_L and C_D plotted against angle of incidence, α, the experimental Reynolds number is 0.72 x 10^6 and the computational Reynolds number is 1.0 x 10^6. The aspect ratio of the experimental model is 2. The computational model is two dimensional and therefore has an infinite aspect ratio. Correcting the experimental aspect ratio to infinity would increase the C_L/α gradient, whilst maintaining stall incidence and reducing drag, at high incidences. The C_L and C_D curves display the same lift and drag force trends noticed throughout the CFD versus experimental comparisons. The experimental plain wing versus CFD graph **Figure 9:1:2a**, and the experimental slat and wing versus CFD results **Figures 9:1:4 a-b**, all show the CFD results overestimating lift by 50-80%, whilst correctly predicting the stall angle. If the drag results for these figures are compared, the CFD results overestimate C_D at 0° show agreement between 4 to 12° and then overestimate C_D across the remaining incidence range by 15-25%.

Although the discrepancies between experimental and computational lift and drag results are large, the causes for this are well understood and discussed throughout **Sections 9.1 and 9.2**. The conclusion is that it was valid to use the CFD results to predict experimental behaviour, reiterating that a qualitative link between the results could be established. **Figure 9:13** confirms that this decision is justified, by reversing the design procedure. Running the computational model in the same configuration as the experimental model maintains the qualitative agreement formed in the design stage, proving that the design procedure is valid and reversible.

Having confirmed that the agreement, between computational and experimental results is similar to that noticed in the comparison stage, it is now interesting to look at the results with regard to the initial flap, slat and aerofoil predictions:

CFD PREDICTIONS				
CONFIGURATION	C_{Lmax}	α_{max}	ΔC_{Lmax}	$\Delta \alpha_{max}$
PLAIN WING	1.42	18-20°	----	----
WING + SLAT @ 21°, NO OVERLAP	1.66	22-24°	+17%	+2-4°
WING + FLAP @ 20°	2.27	18-20°	+60%	+0°
FULL AEROFOIL 21° SLAT, NO OVERLAP, 20° FLAP.	2.70	20-22°	+90%	+0-2°

TABLE 9:11a

EXPERIMENTAL RESULTS				
CONFIGURATION	C_{Lmax}	α_{max}	ΔC_{Lmax}	$\Delta \alpha_{max}$
PLAIN WING	1.01	14-16°	----	----
WING + SLAT @ 20°, NO OVERLAP	1.29	20-22°	+27%	+4-6°
WING + FLAP @ 20°	1.70	14-16°	+68%	+0°
FULL AEROFOIL 22.5° SLAT, 5mm OVERLAP, 20° FLAP.	1.70	20-22°	+68%	+4-6°

TABLE 9:11b

NOTE: ΔC_{Lmax} and $\Delta \alpha_{max}$ represent the percentage increase in C_{Lmax} and stall incidence, α, respectively over the plain wing C_L and α.

Table 9:11a shows the CFD predictions for the plain wing, the wing with each high lift device individually and the triple element configuration. The configurations shown are those which gave the maximum lift results. **Table 9:11b** again shows predictions for the plain wing, the wing with each high lift device individually and the triple element configuration, but for the experimental model. The experimental configurations shown are those which gave the maximum lift results from the windtunnel. All results are corrected for tunnel blockage effects.

There is a difference in stall angle between the computational and experimental plain wing results. It is likely that this difference is due to the discrepancy between computational and experimental Reynolds number. Increasing the experimental

Reynolds number would increase C_{Lmax} and stall incidence. It also has the effect of making the discrepancy between the experimental and computational results larger than they might otherwise have been.

The model configurations for maximum lift, seen in **Tables 9:11 a-b**, are very similar. The computational result for the highest lift, slat setting was 21°, with no overlap, the experimental result for the same case was different by just 1° of slat angle. The predicted C_{Lmax} increase of the wing and slat combination, over the plain wing was 17%, with a 2-4° increase in stall incidence. The model III results for the wing and slat combination, showed a 27% increase in C_{Lmax} between the plain wing and the wing and slat combination, with a 4-6° increase in stall incidence.

Tables 9:11 a-b also show that the flap setting angle, 20°, creates the maximum lift for both experimental and computational results. In both the computational and experimental results, the effect of the flap increased C_{Lmax} by 60-68%. As expected, the presence of the flap had no effect on the stall incidence of the aerofoil.

Tables 9:11 a-b show the computational and experimental configurations, for maximum lift, for the triple aerofoil results. The CFD configuration for maximum lift is a slat setting of 20° with no overlap, and a flap angle of 20°. The comparable experimental configuration for maximum lift is an aerofoil configuration of 22.5° slat angle, with 5mm overlap and a flap angle of 20°. However, computationally predicted configurations of slat and wing angle created only 3% less lift than the experimentally derived optimum lift combination. The computational triple element configuration shows an increase in C_{Lmax} over the wing and flap combination which is 20% higher than the experimental results. As the aspect ratio of the experimental triple element model is low, AR=2, it is interesting to look at **Figure 9:11**, which shows the triple element result corrected to infinite aspect ratio. The C_L increase over the plain wing result, for this infinite aspect ratio is 120%, which would have given a C_{Lmax} after blockage correction of 2.22. The aspect ratio corrected triple element configuration would have a C_{Lmax} 50% greater than the wing and flap combination.

These C_{Lmax} and α_{max} results are very important, as are the corresponding C_D and L/D results. The significance of these results, on wingsail performance, is clear when they are translated into thrust and heeling forces, described in the following section.

9.18 Thrust Polar

The intention of creating a symmetrical, leading edge high lift device, in conjunction with a trailing edge flap, was to increase the available thrust from a wingsail. Results from **Table 9:11b** demonstrate that the two high lift devices have served their purpose. The flap increased the lift at a given incidence, and the slat delayed stall and thus increased stall incidence. The two devices combined to consolidate the lift increase created by the flap and the incidence increase created by the slat. To judge the effect this will have had on the thrust created by the wingsail, the lift and drag results were resolved using the following equations:

where $\beta - \alpha = \gamma$,

$$C_T = C_L \sin \gamma - C_D \cos \gamma, \qquad 9:3$$

$$C_H = C_L \cos \gamma + C_D \sin \gamma, \qquad 9:4$$

where 'β' = the apparent wind angle and 'α' = the sail setting angle. Force resolution diagrams are shown in **Figs 2:2 a-b**.

Taking the maximum lift arrangement of each configuration separately: wing only, wing & flap, wing & slat and triple element aerofoil, the following Thrust 'Polar' chart is created.

NOTE: *The incidence settings used for this chart were 4-6° below the maximum lift incidence. This was to prevent small wind shifts from stalling the wingsail.*

9.18.1 Thrust 'Polar' Chart

Figure 9:14 is read the following way. The concentric semi-circular construction lines indicate the value of the thrust coefficient, C_T, the scale of which is shown on the corresponding vertical axis. The radial lines emanating from the 0,0 point on the axis show the apparent wind angle. The chart is read as if the vessel is placed with its centre line along the vertical axis, facing the top of the page. The magnitude of C_T, in the direction of the vessel, is then shown for the corresponding apparent wind angle.

The wing only thrust polar can be seen to behave just as predicted, with maximum C_T occurring between 90˚ and 130˚, where C_T is always greater than 0.9.

The wing & slat configuration can also be seen to create a maximum C_T between 90˚ and 130˚, with C_T greater than 1.2 across this incidence range.

The wing and flap configuration shows a C_T greater than 1.4 between 75˚ and 140˚, and a maximum C_T of 1.62 between 100 and 120˚.

Finally, the full aerofoil configuration has a C_T over 1.4 between 80˚ and 155˚, a greater range than the wing and flap configuration. The full aerofoil configuration also reaches a C_T of greater than 1.6 between 95˚ and 140˚, and a C_{Tmax} of 1.75 between 110˚ and 130˚. However, this configuration actually has a lower C_T than the wing and flap configuration between 30˚ and 95˚.

As discussed in **Section 2.2** - 'Wingsail Design Criteria', a wingsail is at its most efficient between 90˚ and 140˚. The triple element wingsail is designed to exploit this region. The figure shows that C_T is increased between 90˚ and 140˚ with the addition of each high lift device. C_T is increased further with the combination of the two high lift devices.

The configuration shown is developed from the experimental testing conducted to investigate maximum lift. Therefore lift and drag values used here, were also those used for the wingsail in the respective maximum lift configurations. It is possible to configure the same combination of aerofoil sections purely for maximum L/D ratio. Thus it may be possible to increase C_T values further by configuring the same wingsail for maximum L/D between 0° and 90°, although this configuration has not been explored.

Chapter 10

CONCLUSIONS

10.1 Objective

The project objective was to maximise the thrust created by a wingsail, without increasing the size of the device. In designing a wingsail to meet this objective, several other project aims were derived:

i) To increase the performance of a wingsail by using high lift devices.

ii) To investigate whether a symmetrical leading edge high lift device could increase either the stall incidence, or the lift force of a wingsail.

iii) To attempt to use computational fluid dynamics (CFD) as a time saving design tool.

It should be re-iterated at this point that, by definition, a wingsail must be symmetrical. A wingsail must be capable of creating equal lift force with flow approaching the leading edge from either side of the wing centreline. This means that equal lift must be created with either of the wingsail surfaces acting as the upper, or lower pressure surface.

10.2 Design Process

Wingsail forward thrust force is the resultant of the aerodynamic components of lift and drag, resolved into the direction of motion of the vessel. A wingsail may use one of two optimum design criteria, either the upwind, or the downwind. The 'downwind'

optimisation was selected. This optimisation was chosen for three main reasons. Firstly, because it covers the majority of apparent wind angles encountered. Secondly, it covers the apparent wind angle region of 90-130°, known to be the optimum angle for creating wingsail thrust. Finally, the downwind optimisation is preferable for the likely use of this wingsail as an auxiliary power unit (APU) on a large vessel. The alternative use of a wingsail, as a sole power unit, or SPU, requires the wingsail to create a thrust for the full range of wind angles and the upwind optimisation must then be applied.

The downwind design optimisation states that maximum thrust can be achieved over wind angles between 90° and 180° by designing a wingsail to create maximum lift force. However, if two aerofoil configurations create a similar lift force, the design creating the least drag will normally be preferable, as this will create the least heeling moment.

The project aim, therefore, was to increase the thrust generated by a wingsail, by optimising the aerofoil design to create maximum lift force. There are two ways to increase the thrust created by a wingsail section. Firstly, by delaying the onset of stall and hence increasing the stall incidence. Secondly, the camber of the section may be increased, increasing lift force created at a given incidence.

To increase available lift, a leading edge high lift device was developed. High lift devices for aircraft are designed to create lift in just one direction and as a result are almost always asymmetrical. Developing a leading edge high lift device, which adheres to the wingsail design requirements of symmetry is a not a new concept, as drop nose wingsails have been tested previously. These devices worked purely by increasing the camber of the wingsail section. However, to increase lift further still, a device that would not only increase the camber of the wingsail, but turn the flow around the leading edge of the aerofoil was required. As a result, a leading edge slat was developed. This leading edge slat must, however, also adhere to the requirement for symmetry and thus a symmetrical slat section was designed. The design aim of the leading edge symmetrical slat was the same as that for a normal slat, i.e. to turn the flow around the leading edge of the aerofoil, thus delaying the onset of

separation. Lift force may also be increased by increasing the camber of an aerofoil section. As stated in the design brief, a wingsail must be symmetrical.

A plain wingsail section must be symmetrical, therefore it will have no camber by definition. Trailing edge high lift devices have been fitted to wingsails to overcome this difficulty since wingsails were first designed in the 1920's. Anton Flettner, the man credited as the designer of the first wingsail, fitted his early devices with plain trailing edge flaps. As stated previously, a flap was also part of this design. A slotted flap was selected, of a similar layout to the Walker Wingsail. This wingsail, designed by Walker [18] is widely regarded as the most efficient wingsail design on the market today. The advantage of selecting a slotted flap over a plain flap was that this flap type not only increases the effective camber of the aerofoil section but also creates a geometrical slot between the trailing edge of the wing and the leading edge of the flap. The slot created ducts high energy air from the lower surface of the wing to the upper surface of the flap. This high energy air then delays the separation of flow over the flap, thus allowing greater flap angles, greater wing camber and consequently greater lift force.

The concept of a symmetrical high lift device was first tested experimentally on model I. This model was designed to allow the slat to be tested at a wide range of setting angles, pivot positions and overlap distance past the wing leading edge. It was found from this model that the symmetrical slat design did indeed increase the stall incidence of the plain wing section and increase the C_{Lmax} of the device.

The next design stage was to investigate whether the leading edge slat would operate in conjunction with a trailing edge high lift device. At this stage in the design process it became apparent that a very large number of design parameters were available to define the slat, wing and flap combination. It was possible to alter the thickness/chord ratio of the slat, wing and flap sections and it was also possible to alter the individual chord length ratios each aerofoil component. At this point it was decided to introduce computational fluid dynamics, CFD, in to the design process. The concept of introducing CFD was to create a qualitative agreement between the experimental results and those found from computational testing. The advantage of

CFD over windtunnel testing is the ability to simply and quickly test alterations in model geometry. Therefore a large number of design changes can be made.

The CFD package employed in this work was FLOTRAN, a commercially available fluid dynamic solver which works in harmony with ANSYS pre-processor package. Commercial CFD packages have the advantage of being robust and comprehensive, but they have the disadvantage of being designed to cope with a large number of applications. As a result, commercial CFD packages are often slow and inefficient compared with a purpose written code designed to solve a specific problem. However, the time required to write and test a CFD code to aid with the design process was not available, but comprehensive testing of the CFD package and comparison with experimental results showed that it was possible to create a qualitative agreement between the computational results and the results of experimental testing.

Over one hundred possible model configurations were investigated, in order to find the computational model solution which created maximum lift. The conclusion from this testing was the model design, shown in **Figure 9.15**. This model was then constructed and tested experimentally.

The slat is a plain 15% t/c symmetrical aerofoil section, NACA 0015, with a chord length which is 15% of the total wing chord. The main wing is plain 18% t/c symmetrical aerofoil section, NACA 0018. Finally, the flap is also NACA 0015 section also, a 15% t/c symmetrical aerofoil. The flap has a wing:flap chord length ratio of 60:40. The overall model has a chord length ratio of 3:12:8, c_s:c_w:c_f, where c_s, c_w and c_f are the chord lengths of the slat, wing and flap respectively.

10.3 Concluding Remarks

From experimental testing of this model design, it was found that the wing and slat combination created a C_{Lmax} which was 27% higher than the plain wing value, and the stall incidence of the plain wing section was increased by between 4° and 6°. The wing and flap combination increased the C_L created by the plain wing by 68%, with no increase in stall incidence. Finally, the triple element configuration, of the slat,

wing and flap also created a C_{Lmax} increase of 68% over the plain wing result, and increased the stall incidence by between 4° and 6°.

The highest lift configurations of the slat overlap and setting angle and the corresponding flap setting angle, were entered back into the computational model. The qualitative agreement shown between the computational and experimental results was shown to still be valid.

Although the triple element aerofoil combination did not increase the C_{Lmax} of the plain wing section by a greater amount than the wing and flap combination, the stall incidence of the aerofoil was increased. It should not be forgotten at this point, that the aim of this work was to create the maximum thrust force from a wingsail.

Wingsail lift and drag forces were resolved into the forward thrust direction, using the **Equations 9:3** and **9:4** shown in **Section 9.18**. The results of this testing showed that:

i) The plain wing achieves a C_{Tmax} of 0.94, at an apparent wind angle of 110°.

ii) The wing and slat combination create a C_{Tmax} of 1.24, an apparent wind angle of 115°.

iii) The wing and flap combination create a C_{Tmax} of 1.65, at an apparent wind angle of 105°.

iv) The triple element aerofoil creates a C_{Tmax} of 1.72, at an apparent wind angle of 115°.

Therefore, the wing and slat combination increases the C_{Tmax} of the plain wing by 32%, the wing and flap combination increases the C_{Tmax} of the plain wing by 75% and finally the triple element combination increases the C_{Tmax} created by the plan wing by 83%. The triple element configuration also creates the maximum thrust

coefficient for apparent wind angles between 95-180 degrees, which was the initial design criteria.

From the initial design objectives, the main one, to maximise the thrust created by a wingsail, was achieved for the chosen design. The maximum thrust of a plain wingsail was increased by 83%, for the 'downwind' design optimisation. An increase in thrust was achieved by the wingsail design over the entire 'downwind' range of apparent wind angles, 95-180°.

An important part of the design procedure when increasing the thrust of a wingsail, was to aid the performance of the wingsail by using high lift devices. This aim was achieved as both the slat and the flap increased lift force created by the wingsail. By increasing the lift force of the wingsail, both wing and slat individually increased the thrust force created by the plain wingsail section.

10.4 Further Work

As stated in **Section 9:18**, the configuration of the triple element model is developed from the experimental testing conducted to investigate maximum lift. Therefore, the lift and drag values used here were those used for the wingsail in the respective maximum lift configurations. It is possible to configure the same combination of aerofoil sections purely for maximum L/D ratio. Thus it may be possible to increase C_T values further by configuring the same wingsail for maximum L/D between 0° and 90°, although this configuration has not been explored. It is possible, therefore, that the maximum lift/drag ratio configuration of the present aerofoil design could be examined further.

Two further approaches exist for the continued investigation of the present wingsail design. Firstly, to design a model to test the wingsail over a wider range of operational wind velocities. It was discussed, earlier in the report, that a wingsail may be required to create a thrust at a vast range of Reynolds numbers. For a 2 metre chord wingsail, this Reynolds number range would be between 0-2,700,000. It would be an interesting project to investigate wingsail performance and optimum thrust configuration over this range of Reynolds numbers. The second approach is

similar to the first, but involves testing the wingsail in a simulated ship mounted environment. This would allow the optimum deck mounting arrangement to be investigated, along with any design changes which may be required from the effects of wind gradient over the wingsail span.

There are many areas of further research which could be conducted by altering the wingsail configuration. However, here are three relatively minor design changes which could be explored.

Firstly, although many design configurations were examined during the CFD design stage, research was not carried out into the effects of altering the flap position with respect to the wing section. The flap pivot point was fixed at a point 0.2 c_w forward of the main wing trailing edge. The possibility of moving this flap, either to another position on the chord, or to a position where the flap overlapped the main wing, could also be investigated.

The second area for further research would be into the effects of moving the slat pivot point. In this work, a possible 25 slat pivot positions were investigated, all using the centreline of the main wing as the pivot axis. The axis of the slat pivot point could be moved off the centreline of the main wing. It would be interesting to investigate whether allowing the slat pivot axis, shown in **Figure 10:1** '**a**' to move above the wingsail upper surface, would create any increase in lift.

The third possible design change also involves research into the effects of moving the slat pivot point. Moving the slat pivot point could create a self-adjusting slat mechanism. If the slat is pivoted upstream of its aerodynamic centre, then the pitching moment created by the slat section should allow the slat to reach its own setting angle, shown in **Figure 10:1** '**b**'.

A combination of these two research areas may create a self-balancing, self adjusting slat mechanism, shown in **Figure 10:1** '**c**'. This proposed configuration would employ the aerodynamic forces of lift, drag and pitching moment to set both the position and the setting angle of the slat, with relation to the wing leading edge. This line of

research would preserve the 'passive' wingsail adjustment philosophy, discussed in **Section 1.2.2**, which is favoured in wingsail design.

[1] Sail-assist alternatives for auxiliary propulsion.
Lloyd Bergeson
5th International marine propulsion conf. (no.03072) 1983 [Q-86018470].

[2] A scheme for ship propulsion by wind power
K.J. England and P. Beardwood (EMAT Engineering consultants)
13th Conf. of the British Wind Eng. Assoc. (1991)

[3] Aerodynamics of high performance wingsails.
J.Otto Scherer
Marine Technology V11. Part 3. July 1974.

[4] A reversible asymmetry rigid aerofoil for sailing vessels.
Kenneth Abel
Oxford Univ. (England) (PB81-240111)

[5] Dynamic response of wingsail mast to unsteady aerodynamic loads including ship motion effects.
G. Firestein
Journal of Wind Engineering and Industrial Aerodynamics. Vol.19 (1985)

[6] Analysis and preliminary design of a sailboat with a self trimming wingsail.
Newman, Fekete
Marine Technology Vol.20 Oct.1983

[7] Windship routeing.
J.A. Spaans
Journal of Wind Engineering and Industrial Aerodynamics. (Elsevier)
Vol.19 (1985)

[8] BWEA initiative on wind assisted ship propulsion.
B.R. Clayton
Journal of Wind Engineering and Industrial Aerodynamics. (Elsevier)
Vol.19 (1985)

[9] The variation of airfoil section characteristics with Reynolds number.
E.N. Jacobs
TR 586, 1937.

[10] Aircraft aerodynamics and performance
J. Roskam
University of Kansas, Press

[11] Windtunnel interference on wings, bodies and airscrews
H. Glauert
Aeronautical Research Council - Reports and Memoranda (HMSO - R & M 1566), 1933.

[12] Blockage effects in a closed or open tunnel
E.W.E. Rogers
Argardograph 109, 1966.

[13] A Theory of the Blockage effects of Bluff Bodies and Stalled Wings in a Closed Wind Tunnel
E.C.Maskell
Aeronautical Research Council - Reports and Memoranda (HMSO - R & M No. 3400)

[14] Blockage characteristics in a closed high speed windtunnel
A. Thom
Aeronautical Research Council - Reports and Memoranda (HMSO - R & M 2033).

[15] Low speed windtunnel testing
W.H. Rae and A. Pope
Wiley & Sons 0-471-87402-7.

[16] Boundary Layer Theory
H. Schlichting
McGraw-Hill (ISBN 0-07-05534-3)

[17] The characteristics of 78 related airfoil sections, form tests in the variable density windtunnel.
E. Jacobs, K.E. Ward, R.M. Pinkerton
Report 460, NACA 19th Annual Report, 1933.

[18] A high performance automatic wingsail auxiliary propulsion system for commercial ships.
J.G. Walker
Journal of Wind Engineering and Industrial Aerodynamics. (Elsevier) Vol.19 (1985)

[19] Separated Flow Past Wind Turbine Aerofoil Sections
H. Khoo
M.Phil Thesis (1991) Dept. of Aeronautics, Imperial College

[20] FLOTRAN Theoretical & Benchmark Manuals (F502:21)
Compuflo, Inc.,2250 Old Ivory Road, Charlottesville, Virginia 22901, USA

[21] Navier-Stokes Computation of a Typical High-Lift Airfoil System
J.G. Rice, R.J. Schnipke et al.
Compuflo, Inc.,2250 Old Ivory Road, Charlottesville, Virginia 22901, USA

[22] Standardised speed prediction for wind propelled merchant ships.
P. Schenzle
RINA Symposium on wind propulsion of commercial ships. (001981)

[23] Wind propulsion for commercial vessels. (Final rept. 1962-63)
P.A Lawrence
Ocean carriers corp. Sausalito, CA April 1983

[24] Sail assist retrofit of the training ship Golden Bear.
L. Bergeson et al.
Windship co. Vol. 1&2 (Final rept. May-Jul 1984) July 1984

[25] Feasibility study of the environmental and economic potential for wind driven cargo vessels.
D.C. Anderson
Sail-Freight International, Westerly, RI 30 Apr. 1980

[26] Sail assisted commercial marine vehicles bibliography and abstracts.
John W. Shortall III
Univ. of South Florida, Tampa Coll. of Eng. Mar. 1983

[27] Evaluation of wingsail interactions for windship propulsion.
A. Daif, B. Kamoun, M. Mundry
European Journal of fluid mechanics Vol.10 Pt.2 1991

[28] Japanese advances in transport technology.
Dr. N. Hamada
Sea Technology Feb 1988

[29] Wind freshens for auxiliary sail-power as Europeans chase Japans lead.
Fairplay Int. Shipping Weekly Vol.290 Oct25 1984

[30] Flow past a wind-assisted ship propulsion device.
H.T Low, S.C Luo, S.H Winoto
Ocean Engineering Vol.18 Pt.6 1991

[31] Aerodynamic characteristics of a 1600dwt tanker
M. Murata, M. Tsuji, T. Watanabe
North East Coast Inst. Engineers.

[32] Modern American developmental sail powered and sail-assisted cargo vessels.
Wayne C. Thiessen (Star shipping assoc. Ltd.)
AIAA, Orange County section Vol.30 1984
Ancient interface 14, symp. on Aero/Hydronautics of sailing.

[33] The determination of the lift characteristics of a rigid aerofoil used as a sail
D.W. Atkins
Undergraduate project report, University of Salford, Dept. of Aeronautical Engineering. 1992

[34] Theory of Wing Sections
I.H. Abbott & A.E. Von Doenhoff
Dover Edition, Dover Publications, Inc. New York. (ISBN 0-486-60586-8)

The following Bibliography References can all be found in:

Journal of Wind Engineering and Industrial Aerodynamics. (Elsevier) Vol.19 (1985)

[35] Outlook for wind assistance
C.T. Nance

[36] Sail assist developments 1979-84
L. Bergeson and C.K. Greenwald

[37] Proposal of a sail system for the propulsion of a 25000tdw bulk carrier.
A. Fiorentino ,L. Lecce et al.

[38] Exposition of calculation methods to analyse wind propulsion on cargo ships.
F. Smoulders

[39] Weather routeing for wind-assisted ships.
A. Blackham

[40] New developments of the Ljungstrom rig for commercial vessels.
O. Ljungstrom

[41] Measurements of the comparative performance of sailing rigs.
C. Palmer

[42] Aerodynamic design of marine aerofoils.
C.J. Satchwell

[43] The foundation Cousteau and windship propulsion 1980-85.
B Charrier, J. Constans, J.-Y Cousteau et al.

[44] Estimation of wind assistance potential.
P.Shenzle

[45] Some comments on the relative merits of wind propulsion devices.
J.F. Wellicome

[46] A review of the methods of calculation of added resistance to ships in a seaway.
P.A. Wilson

[47] An experimental investigation of flow past hulls at leeway.
W.M.S Bradbury

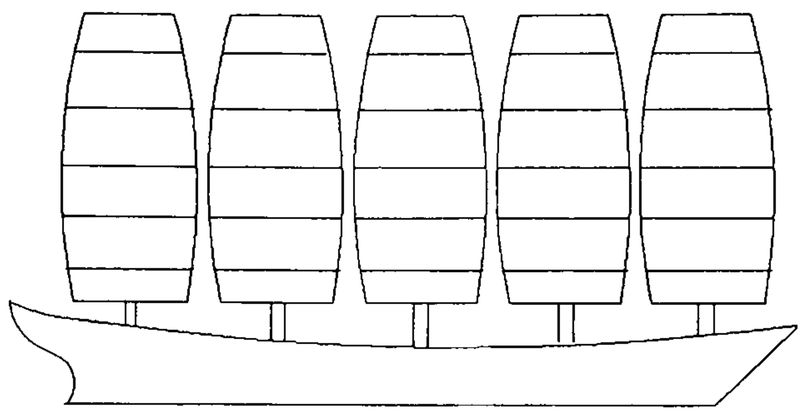

SQUARE RIG
a)

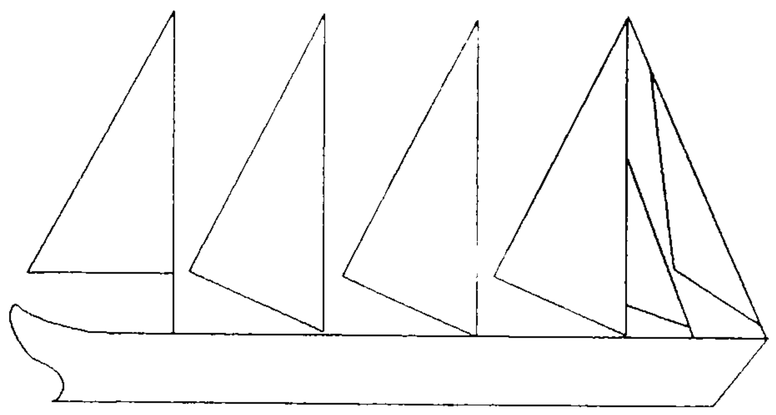

BERMUDAN RIG
b)

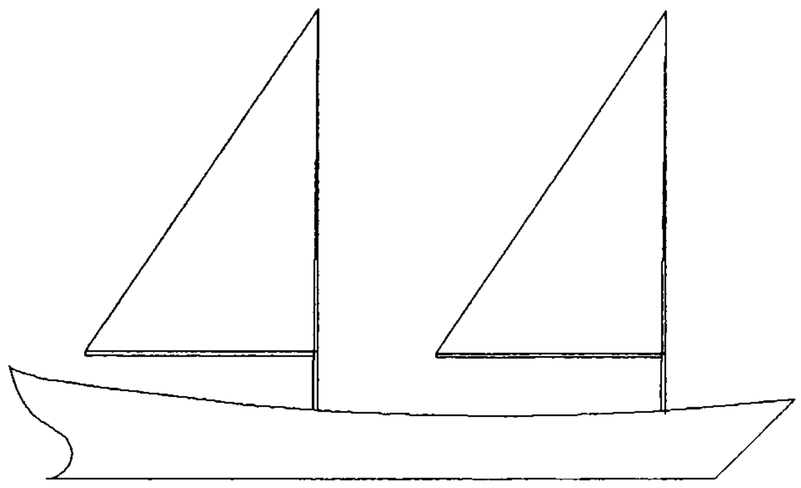

CAT RIG
c)

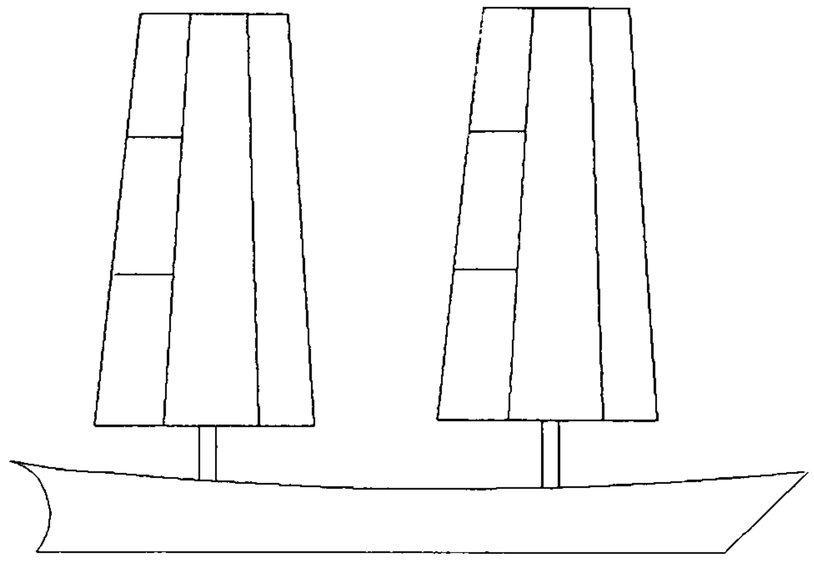

WINGSAIL
d)

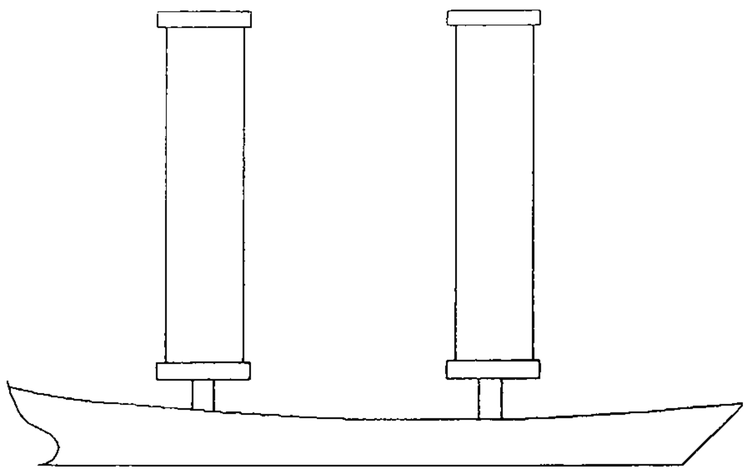

FLETTNER ROTOR
e)

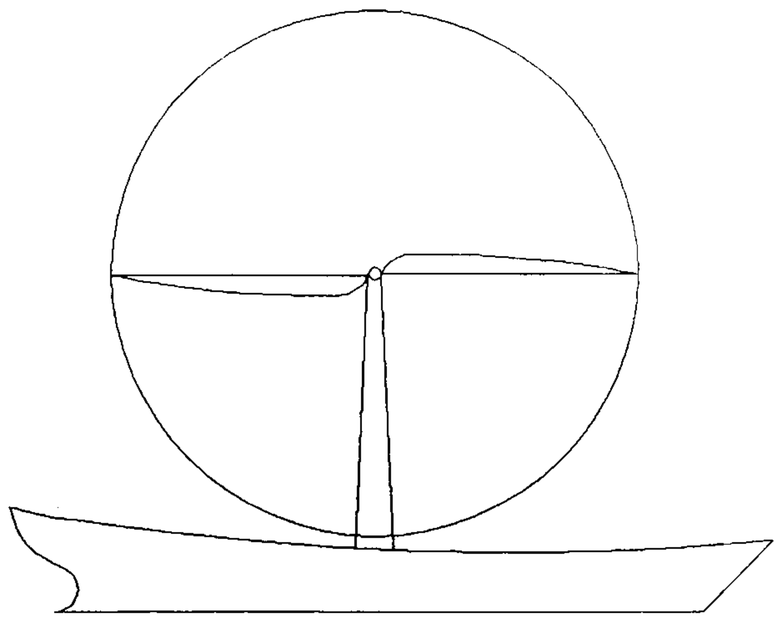

HORIZONTAL AXIS TURBINE
f)

Figure 1:1 Wind Assist Devices

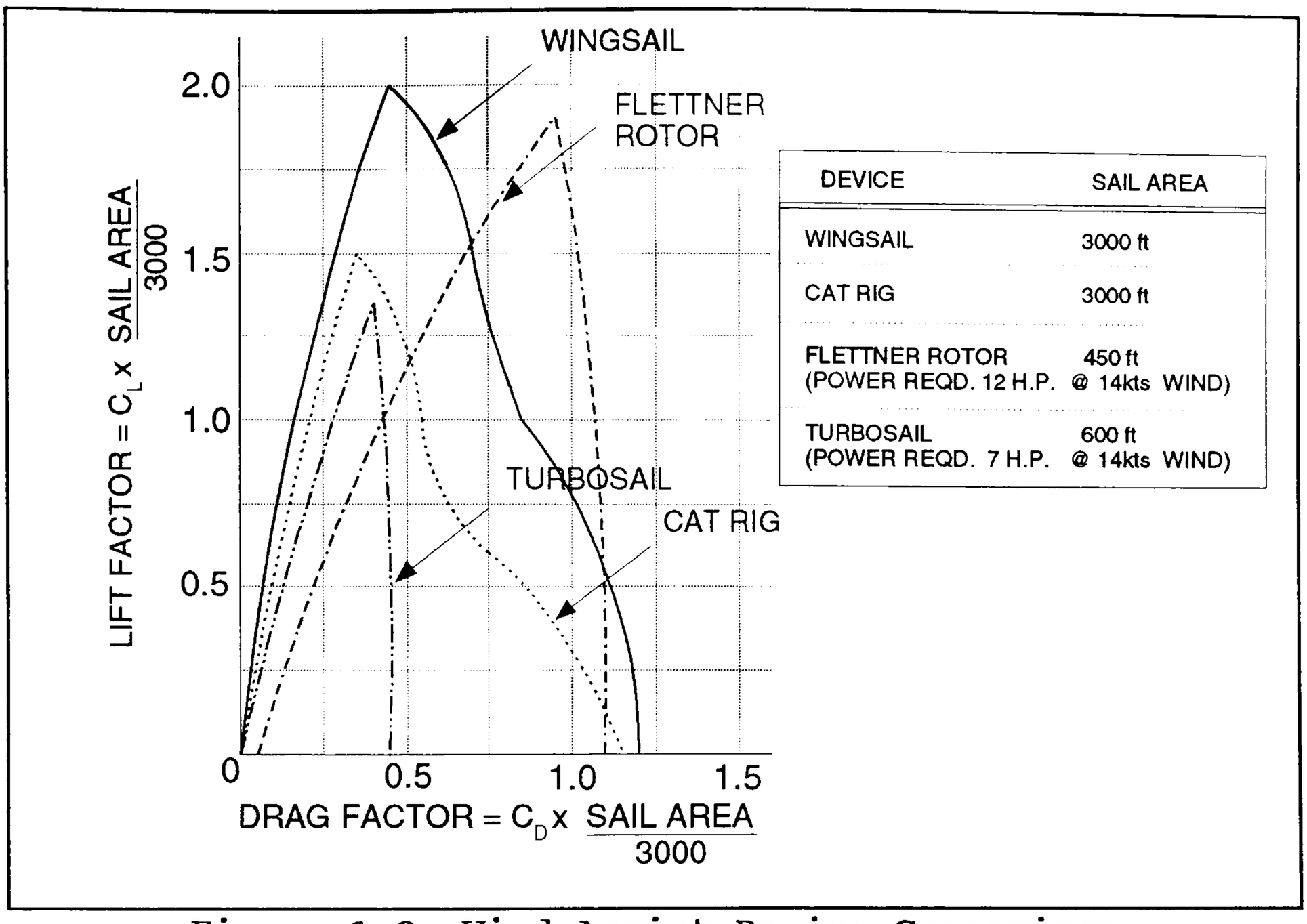

Figure 1:2 Wind Assist Device Comparison

	V_S/V_T	V_A/V_T	β
a	1	1.4	45°
b	2	2.2	26.5°
c	3	3.2	18.5°

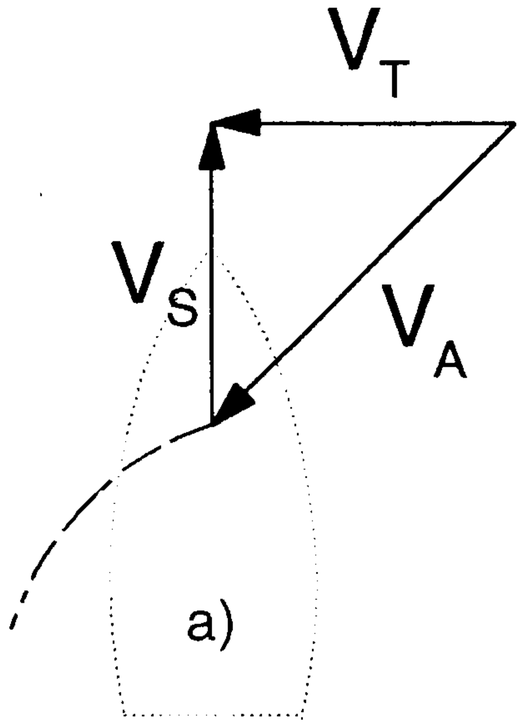

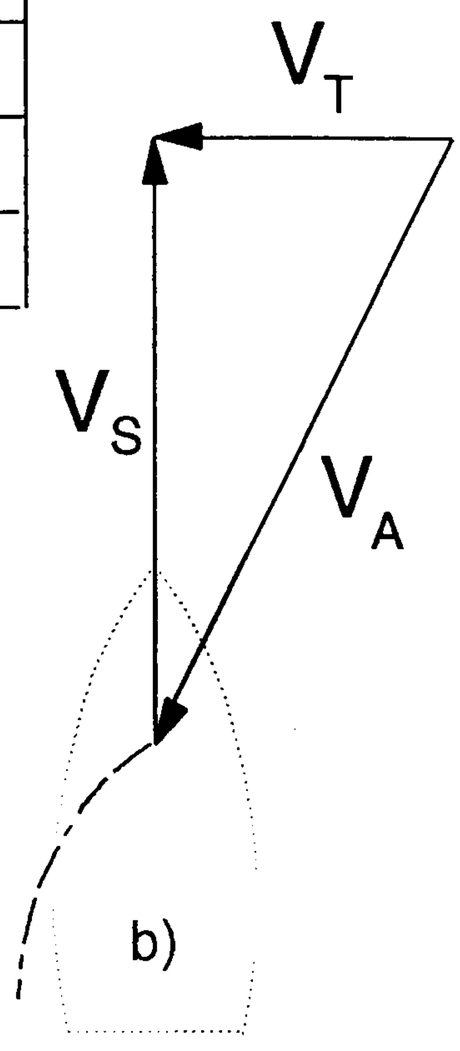

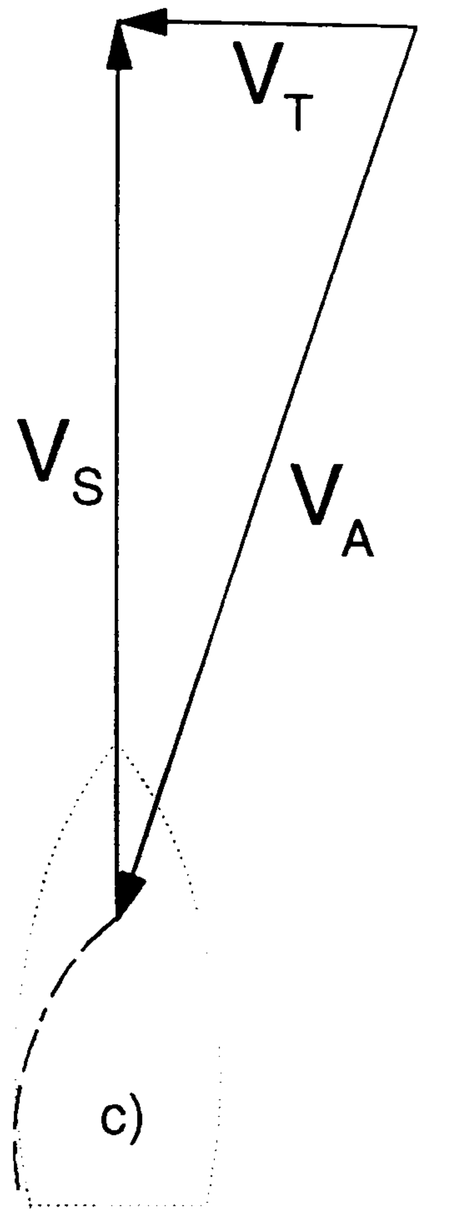

Figure 2:1 Apparent Wind - Velocity Vectors

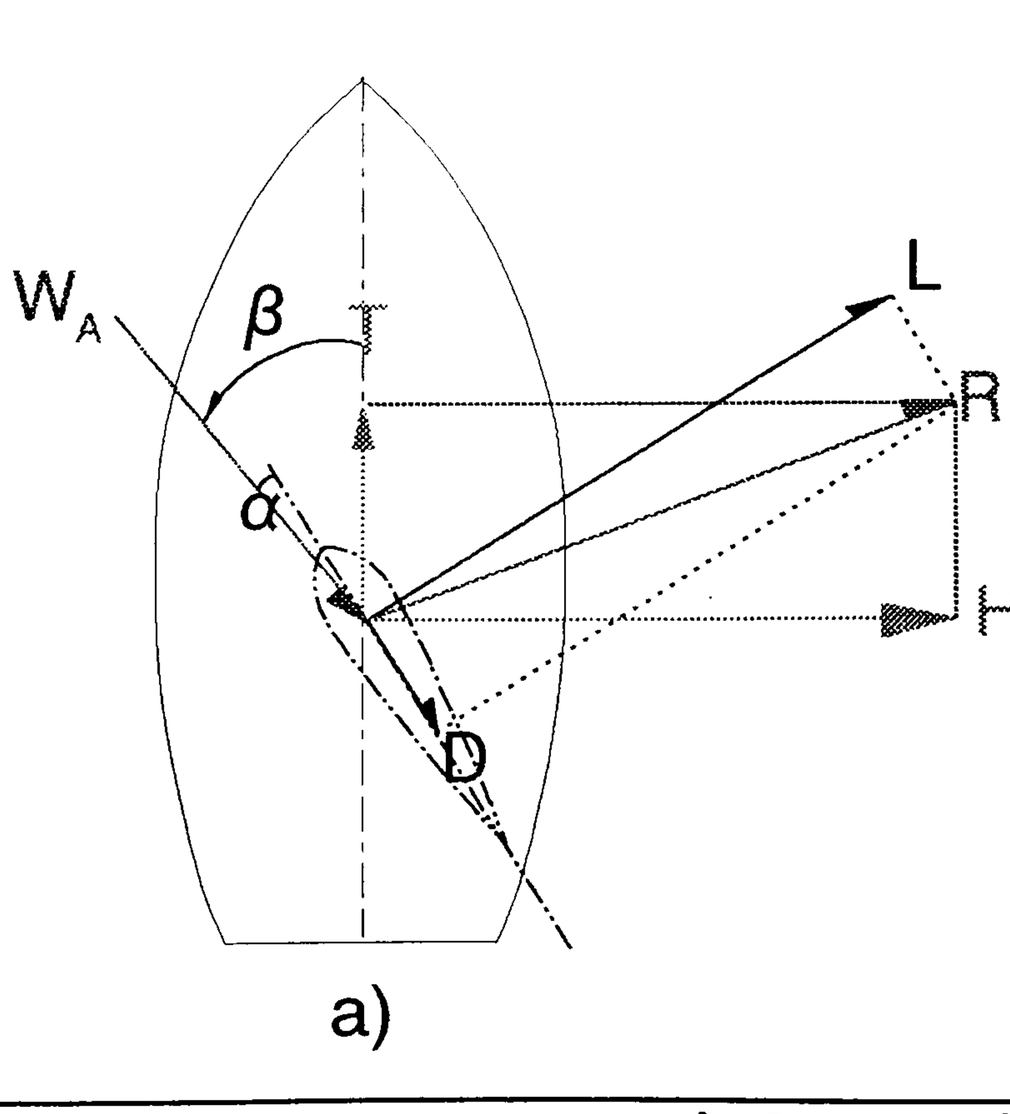

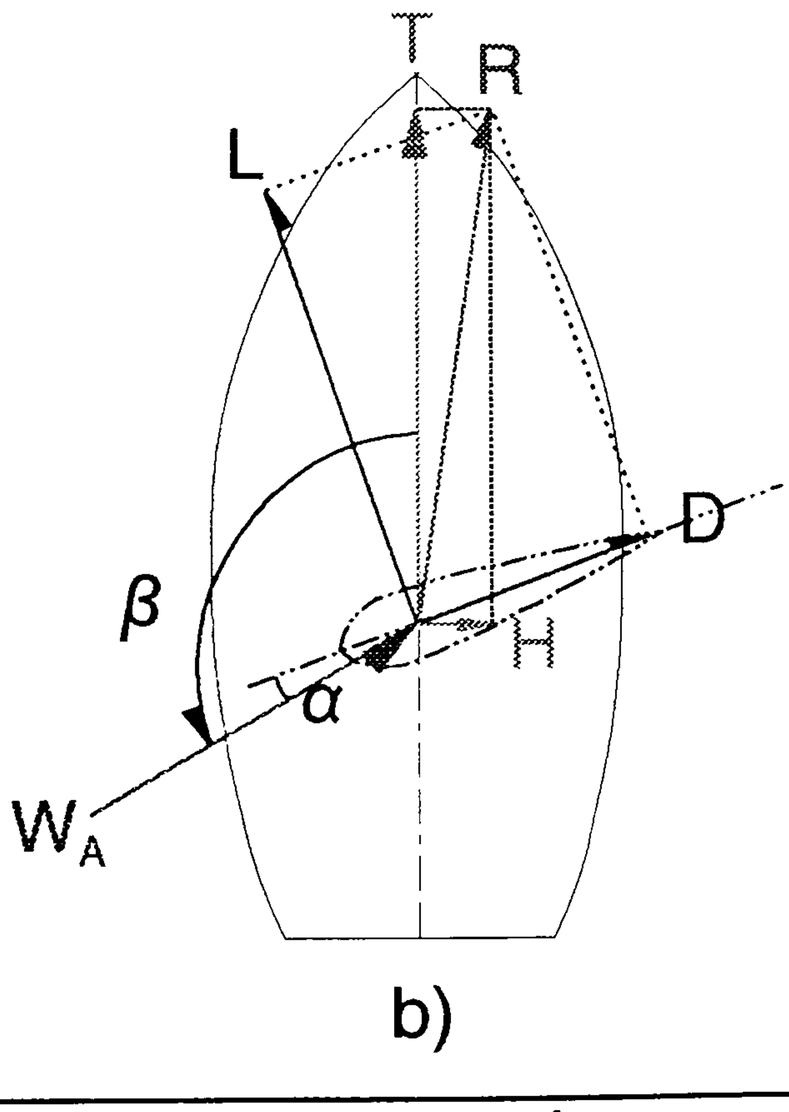

Figure 2:2 Upwind/Downwind Force Resolution

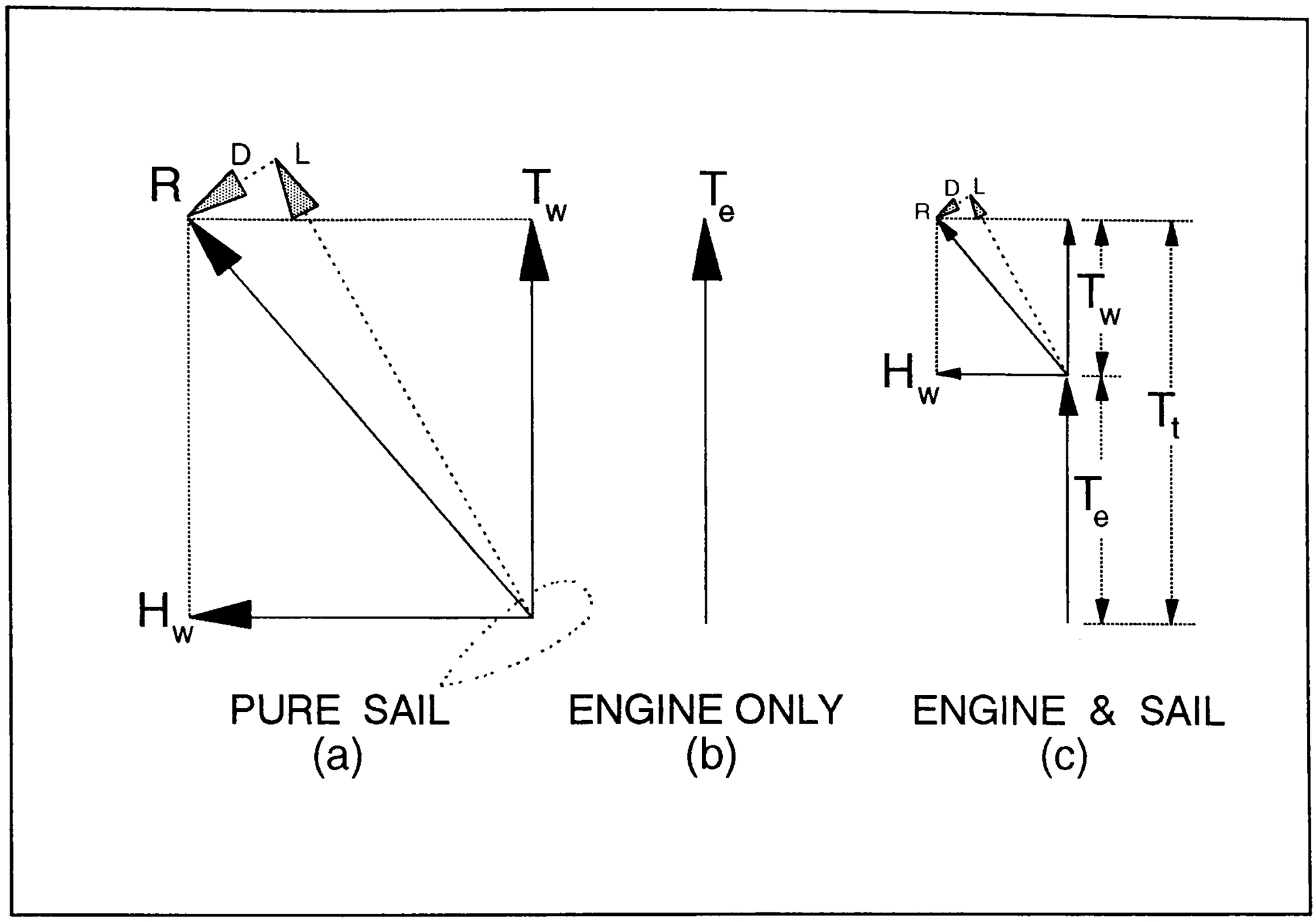

Figure 2:3 Power Versus Sail - Force Resolution

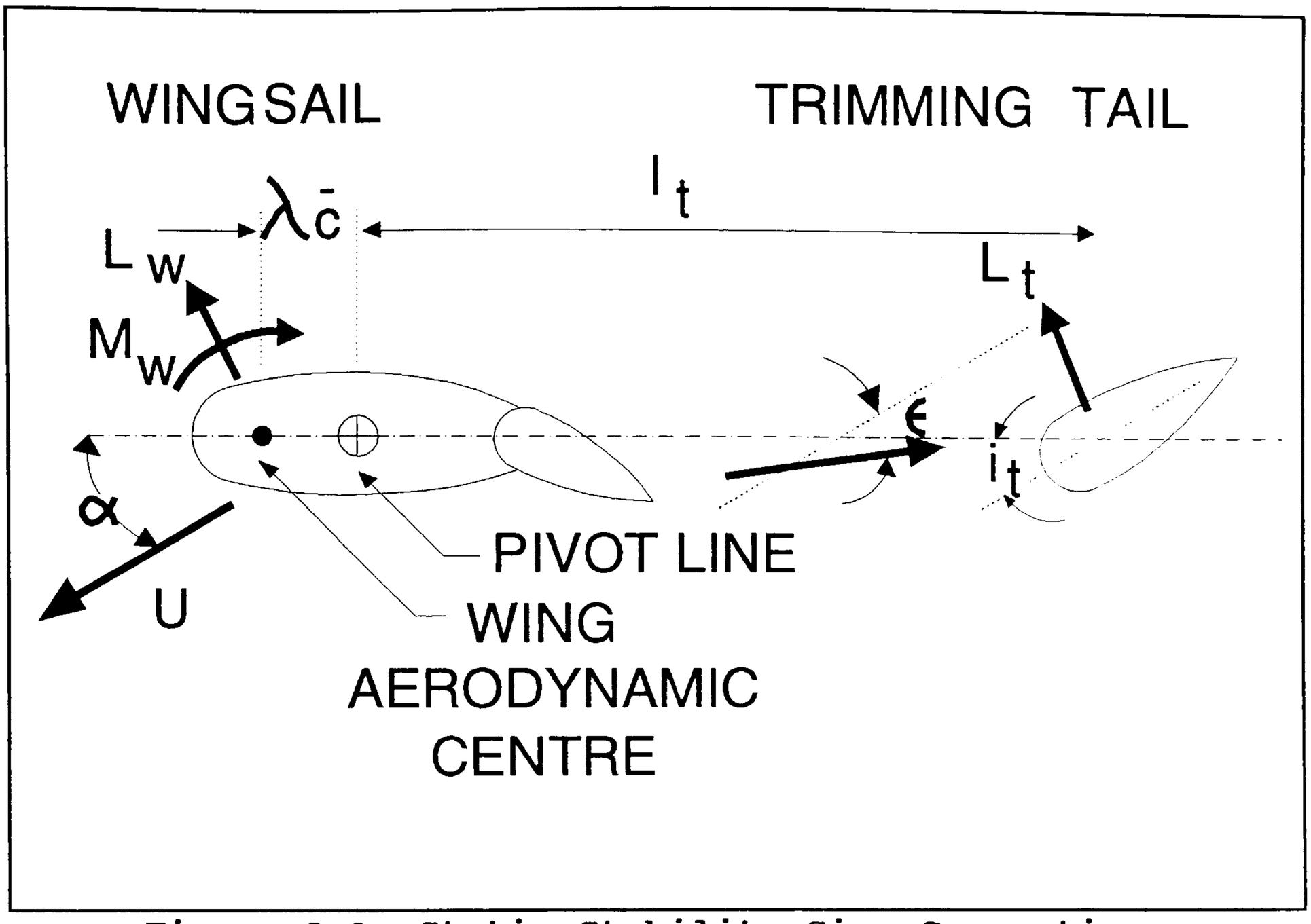

Figure 3:1 Static Stability Sign Conventions

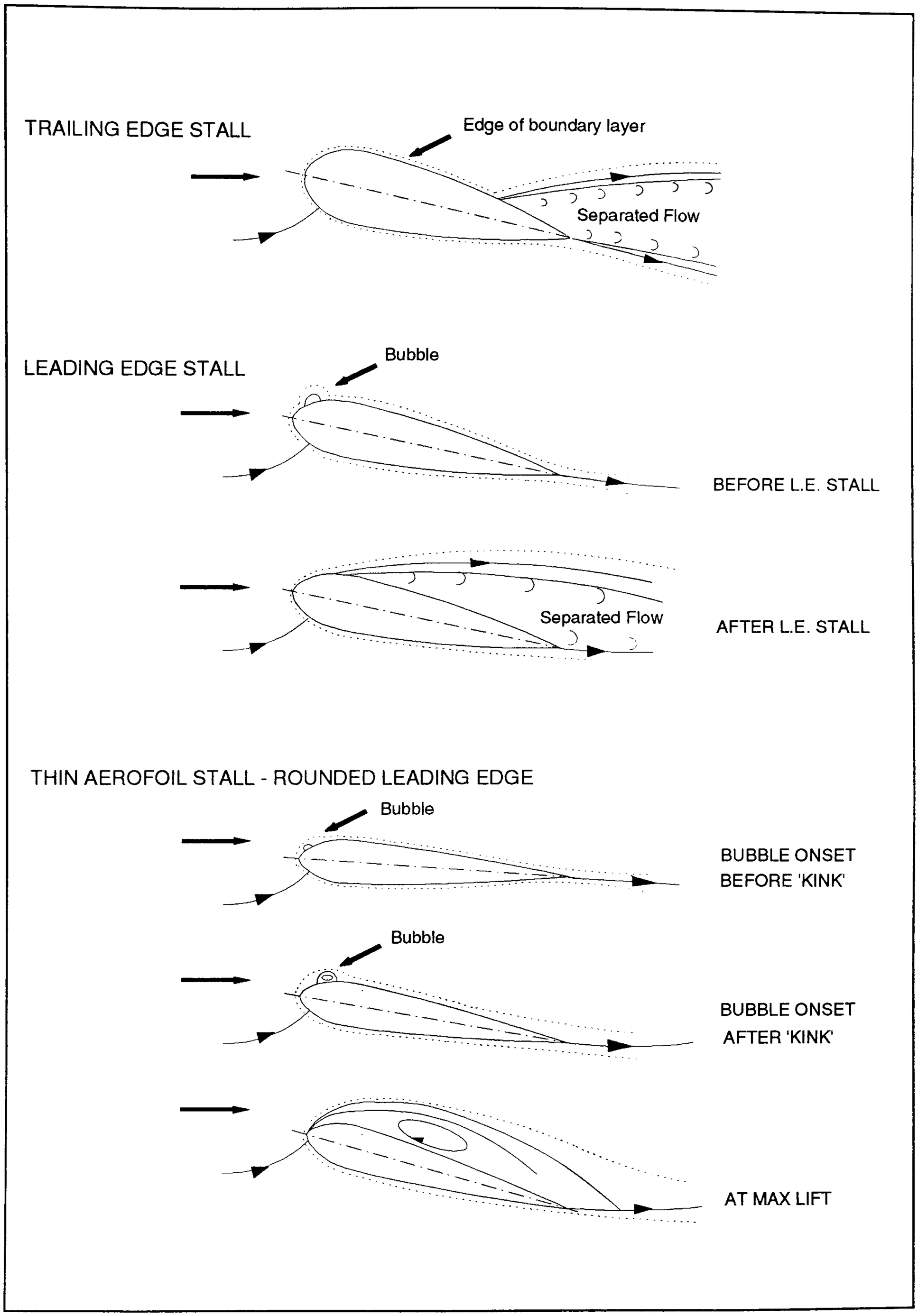

Figure 4:1 Types of Stall

Airfoil NACA	Scale Effects on $C_{L\,max}$	Airfoil NACA	Scale Effects on $C_{L\,max}$
0006	A	23006	A
0009	B_0	23009	C_2
0012	C_0	23012	D_2
0015	D_0	23015	D_2
0018	E_0	23018	E_2
0021	E_1	23021	E_2
0025	E_2		
0030	—	43012	D_4
		43015	D^4
2212	C_3	43018	E_4
2409	B_2	63012	D_6
2412	C_2	63018	E_7
2415	D_2		
2418	E_2		
4406	A_3		
4409	B_4		
4412	C_4		
4415	D_4		
4418	E_4		
4421	E_5		

Figure 4:2a Stall Classification Chart

The Use of Wind Tunnel Data

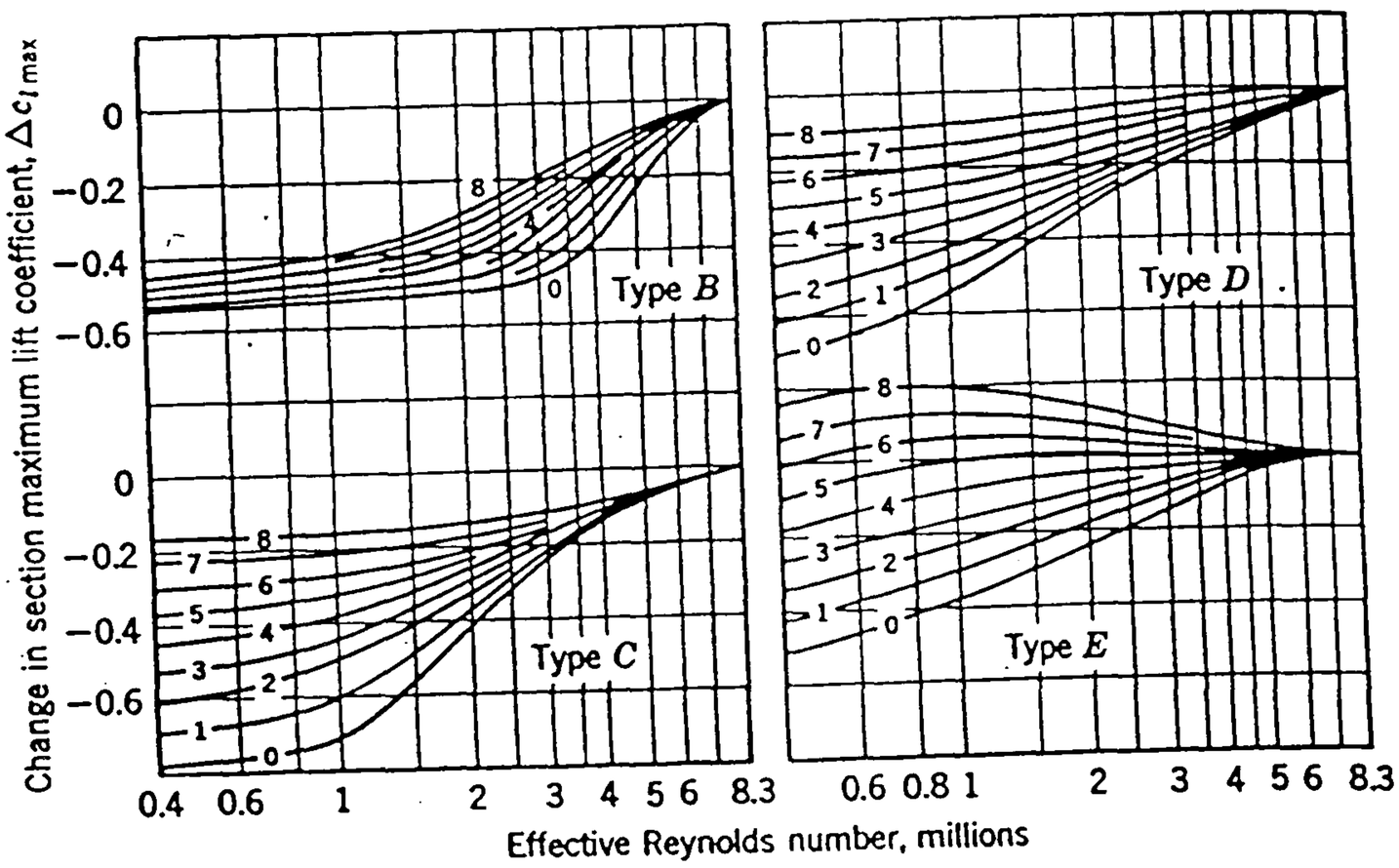

FIGURE 7.11. Effect of Reynolds number on $C_{L\,max}$.

Figure 4:2b $\Delta C_{L_{max}}$ Correction Chart

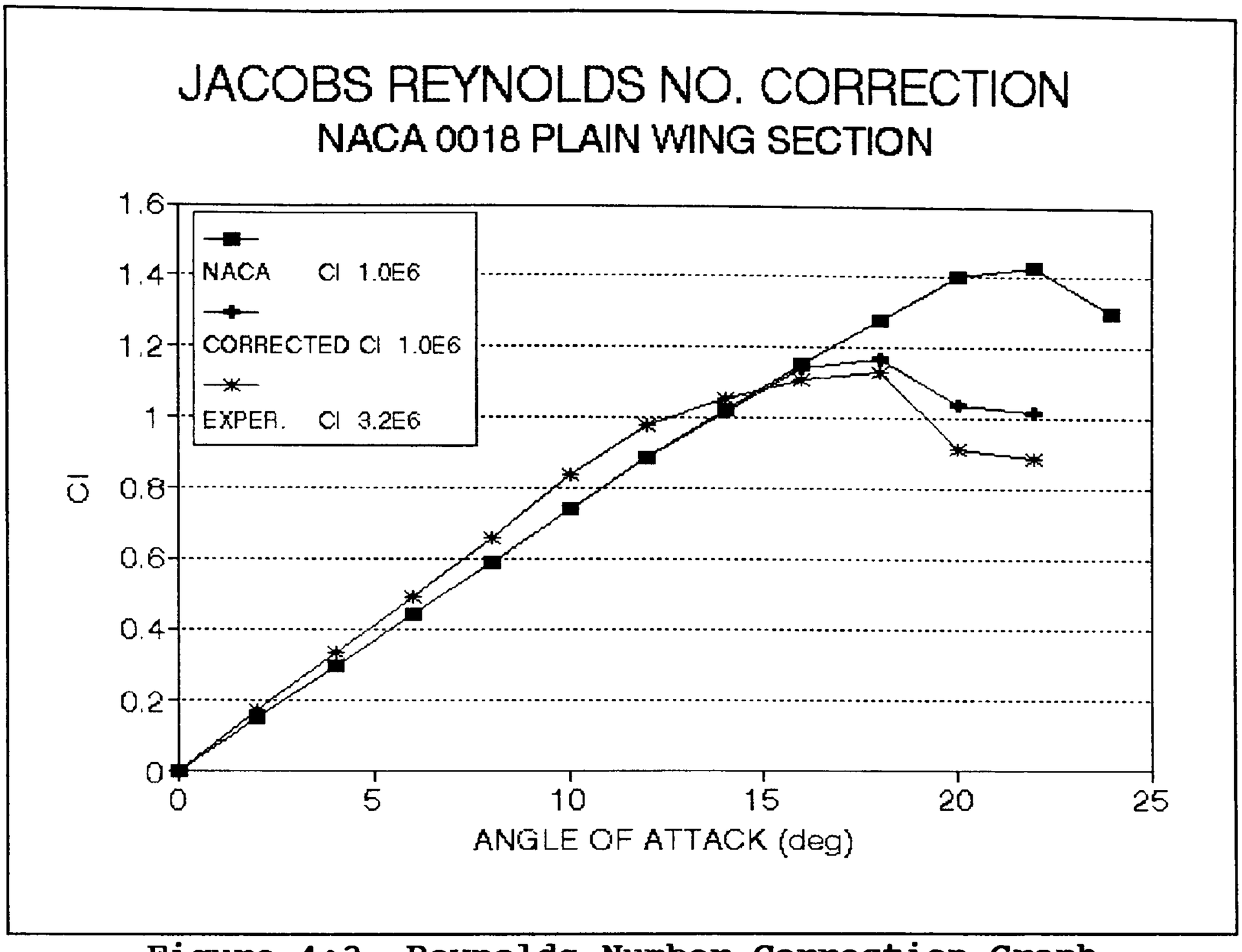

Figure 4:3 Reynolds Number Correction Graph

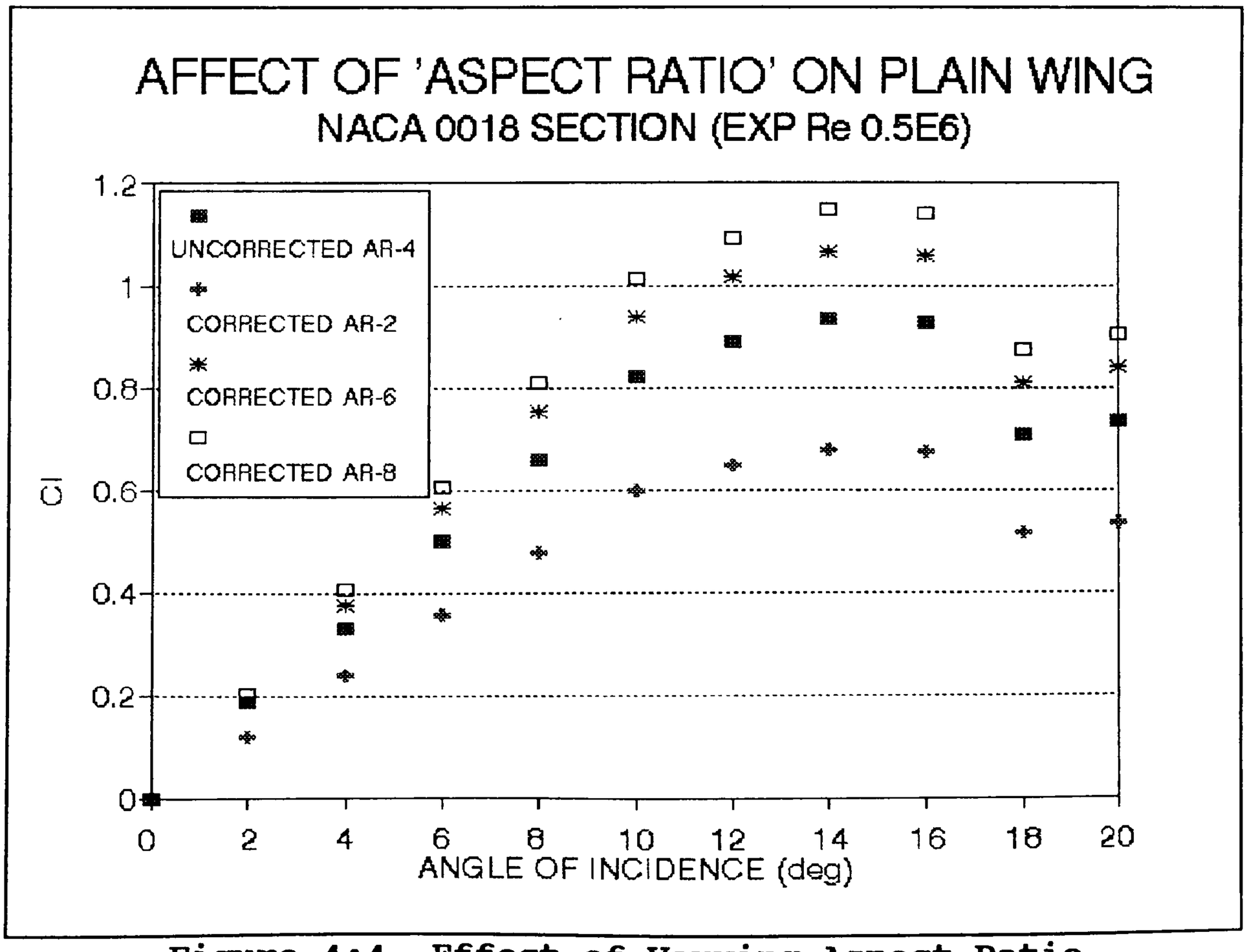

Figure 4:4 Effect of Varying Aspect Ratio

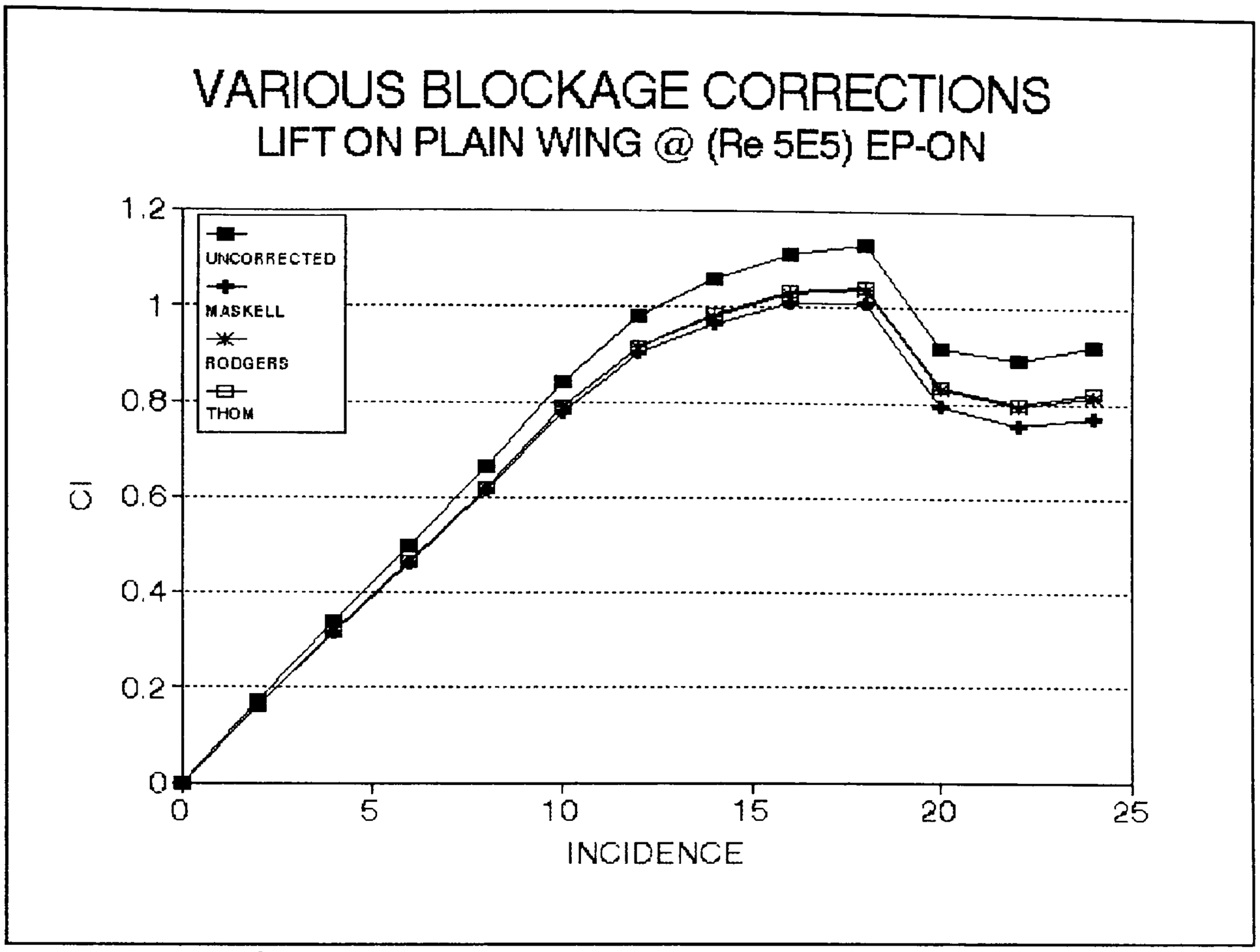

Figure 4:5a Blockage Comparison - C_L

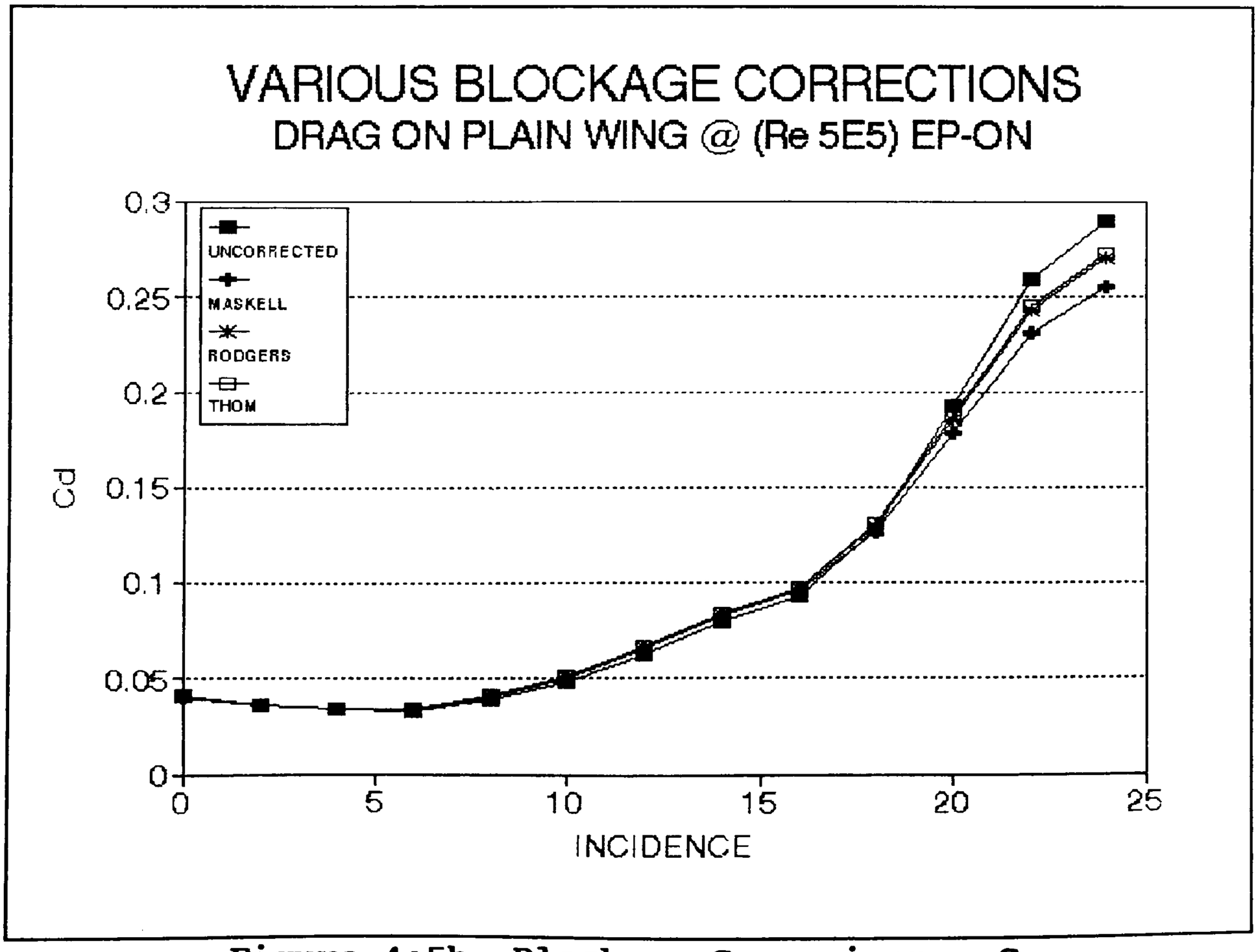

Figure 4:5b Blockage Comparison - C_D

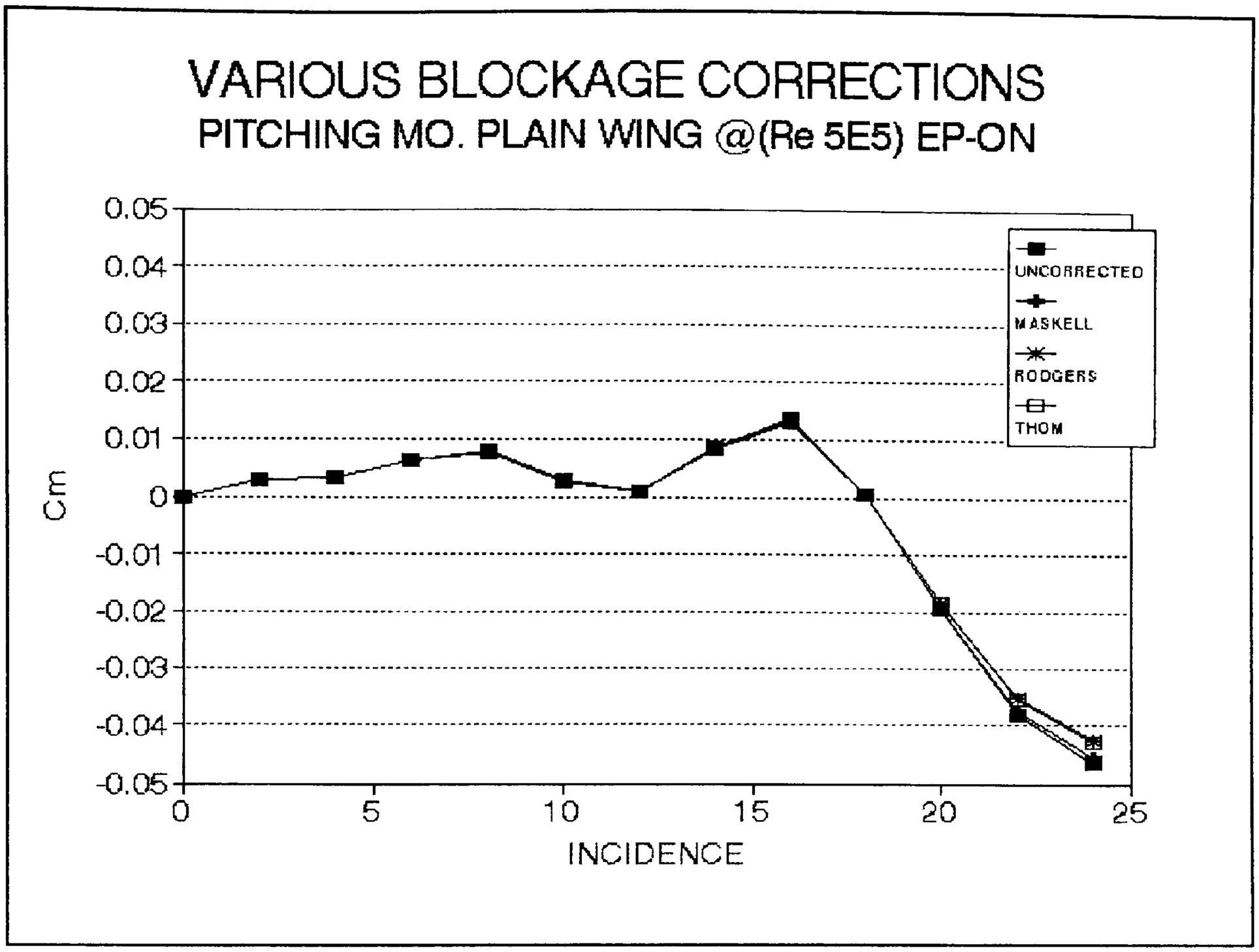

Figure 4:5c Blockage Comparison - C_M

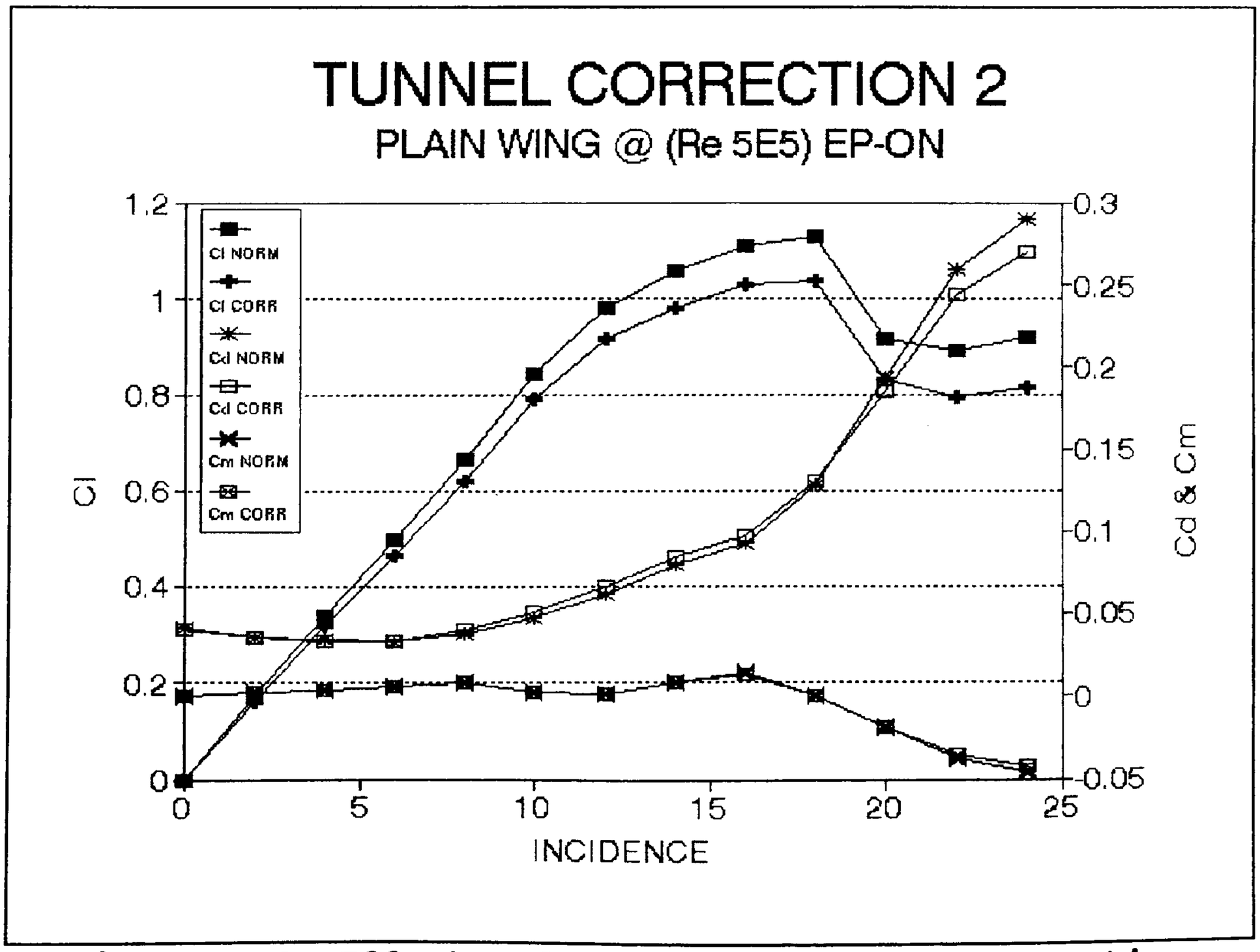

Figure 4:6 Effects of Selected Blockage Correction

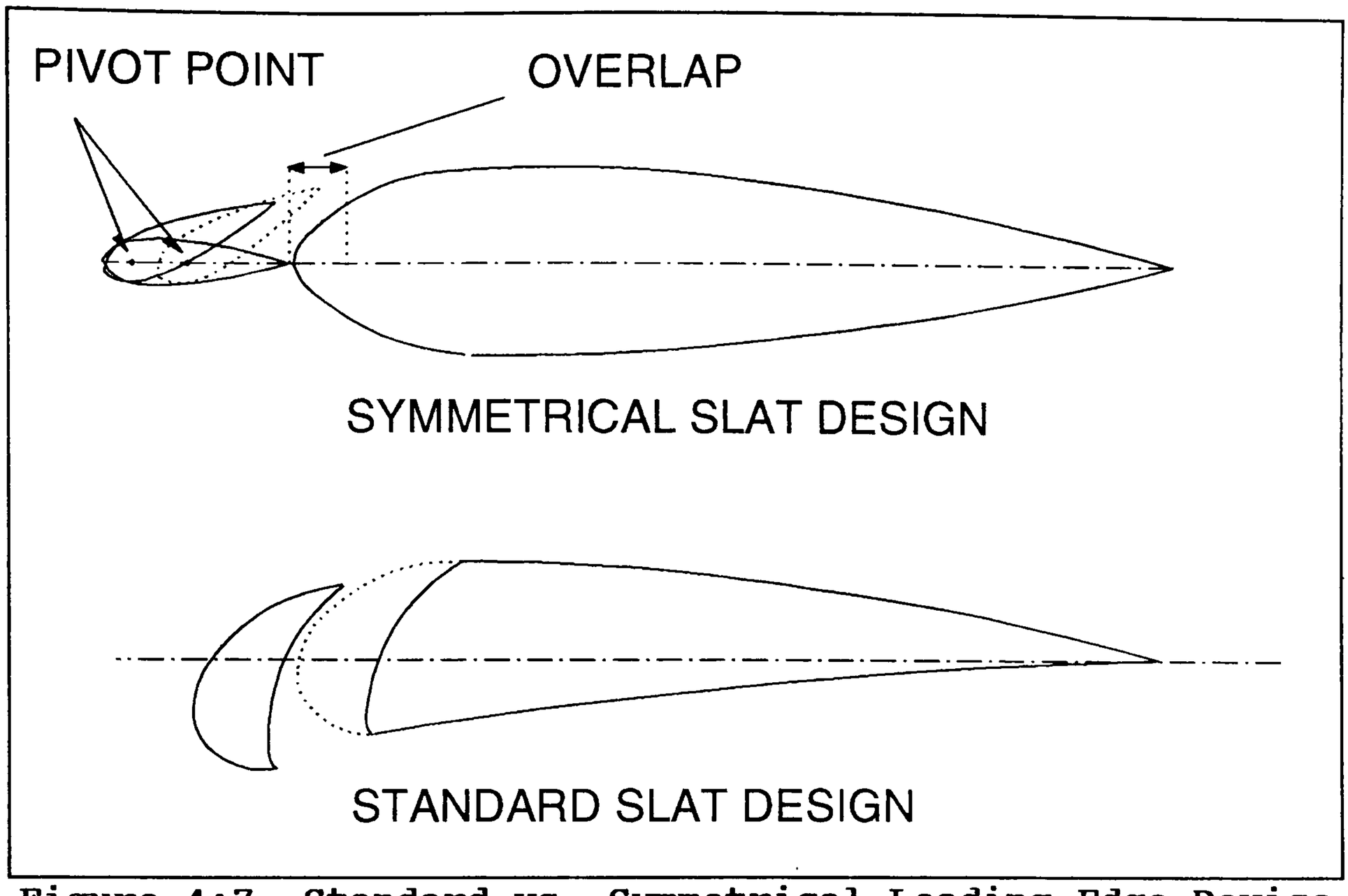

Figure 4:7 Standard vs. Symmetrical Leading Edge Device

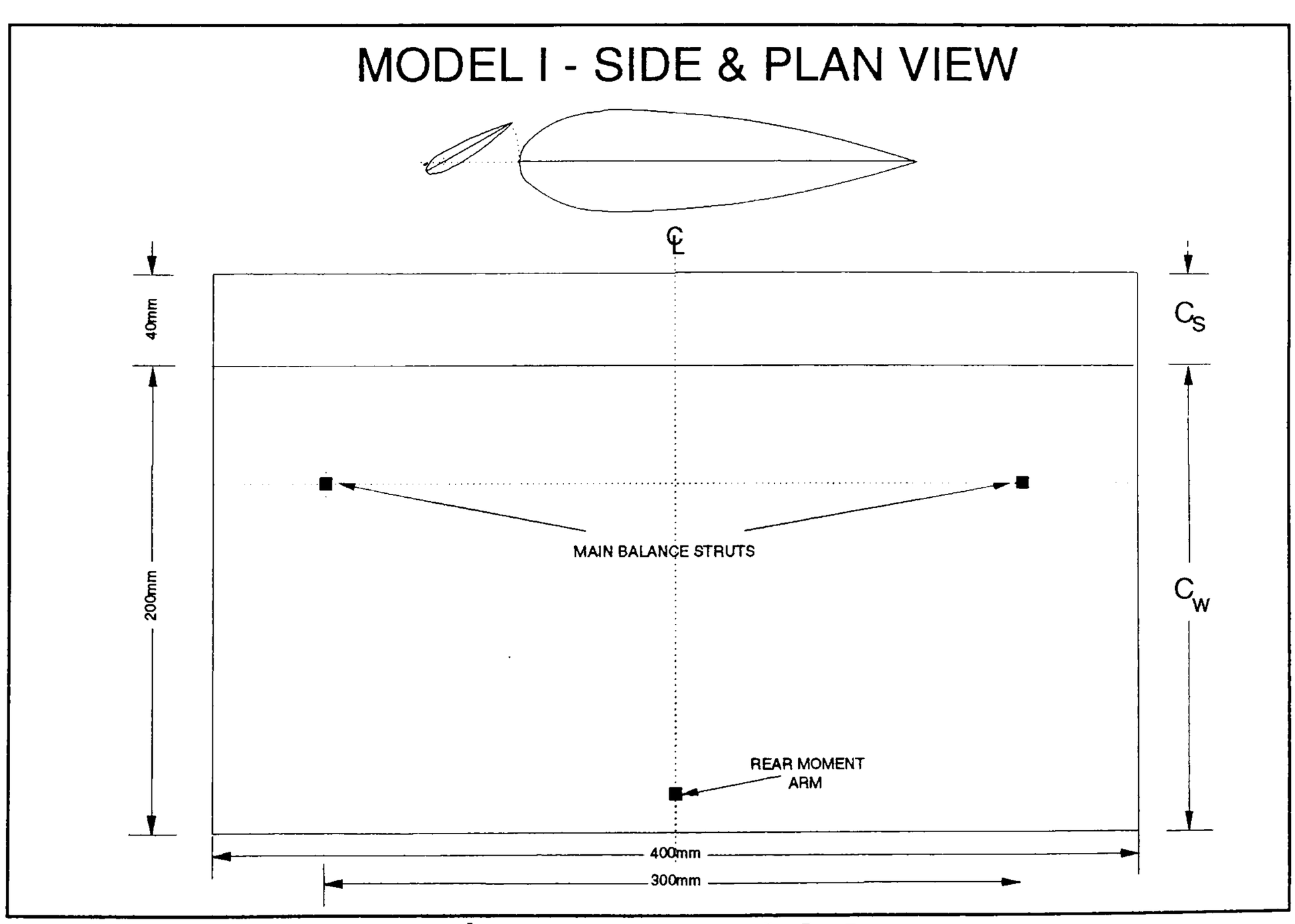

Figure 4:8 Model I

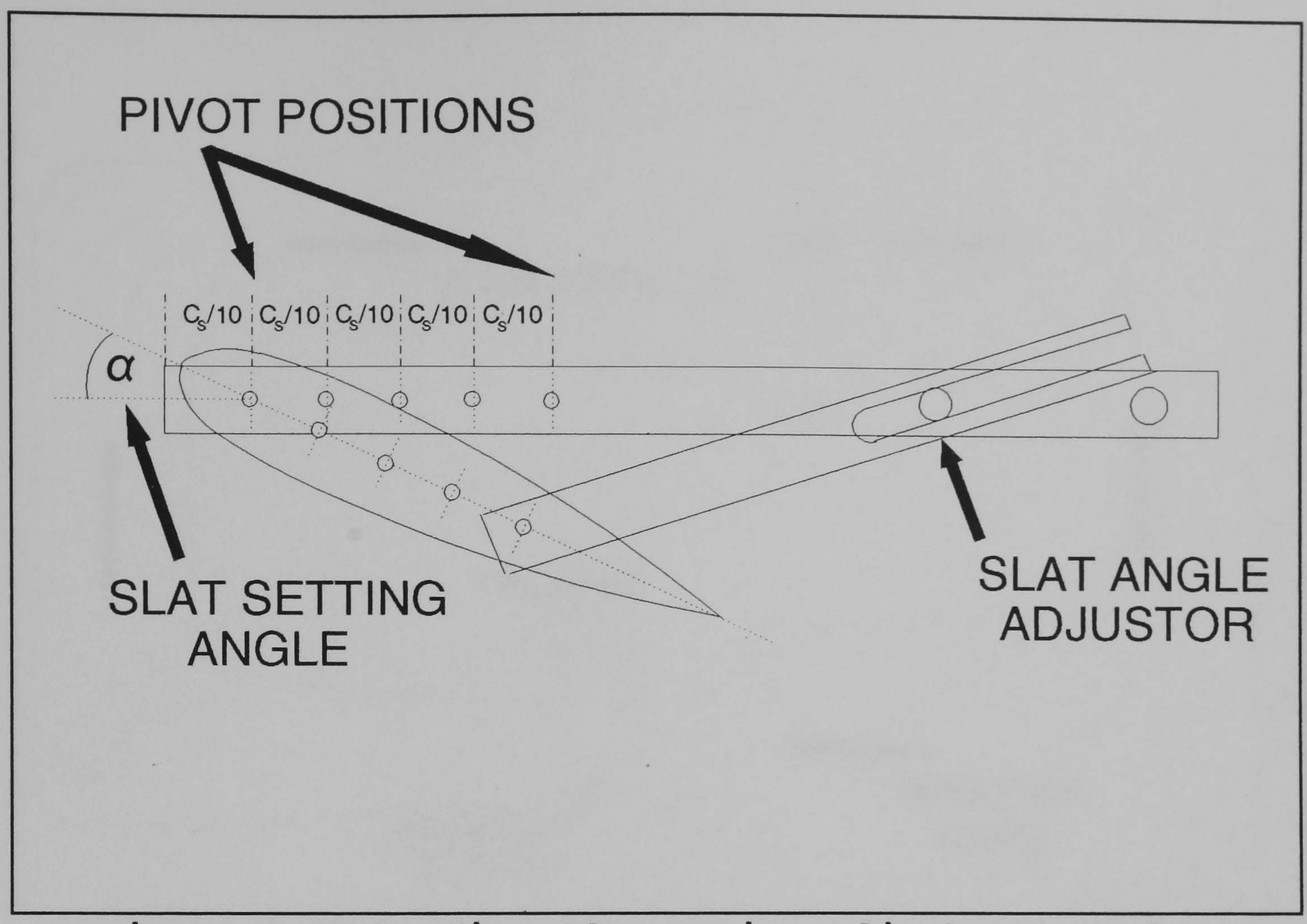

Figure 4:9 Leading Edge Device Adjustment System

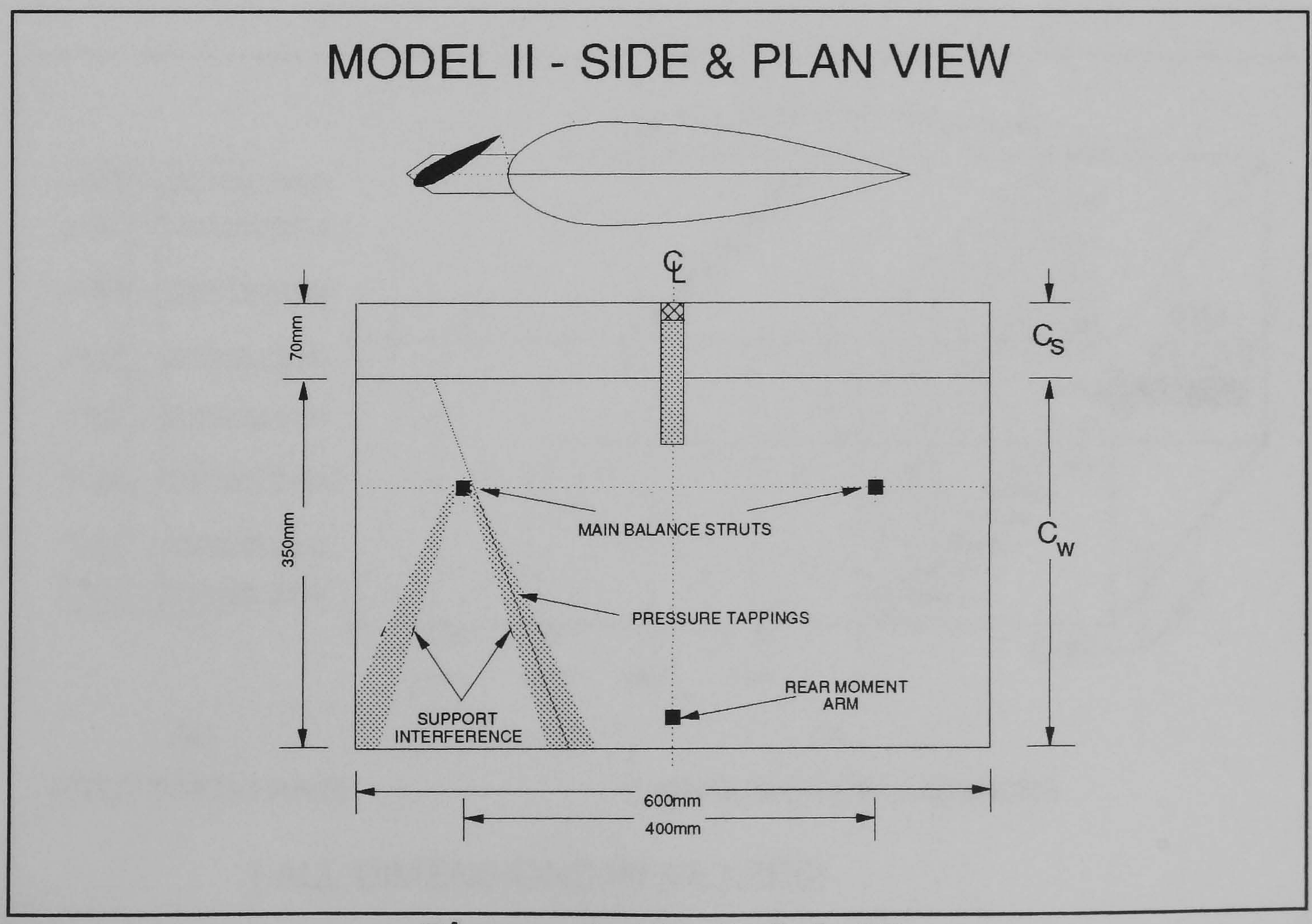

Figure 4:10 Model II

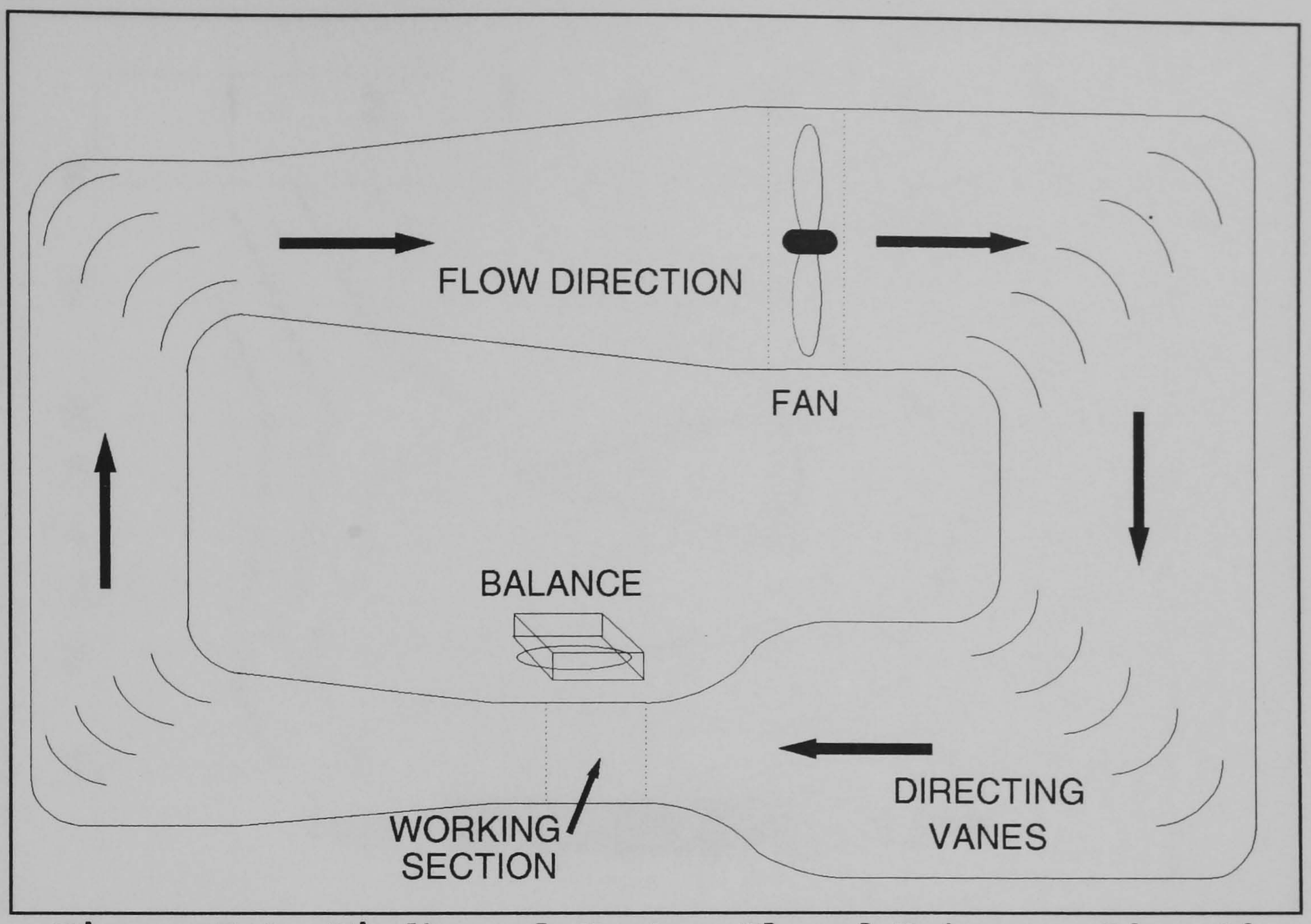

Figure 5:1 Windtunnel No.1 - Closed Return - 3' x 4' Working Section

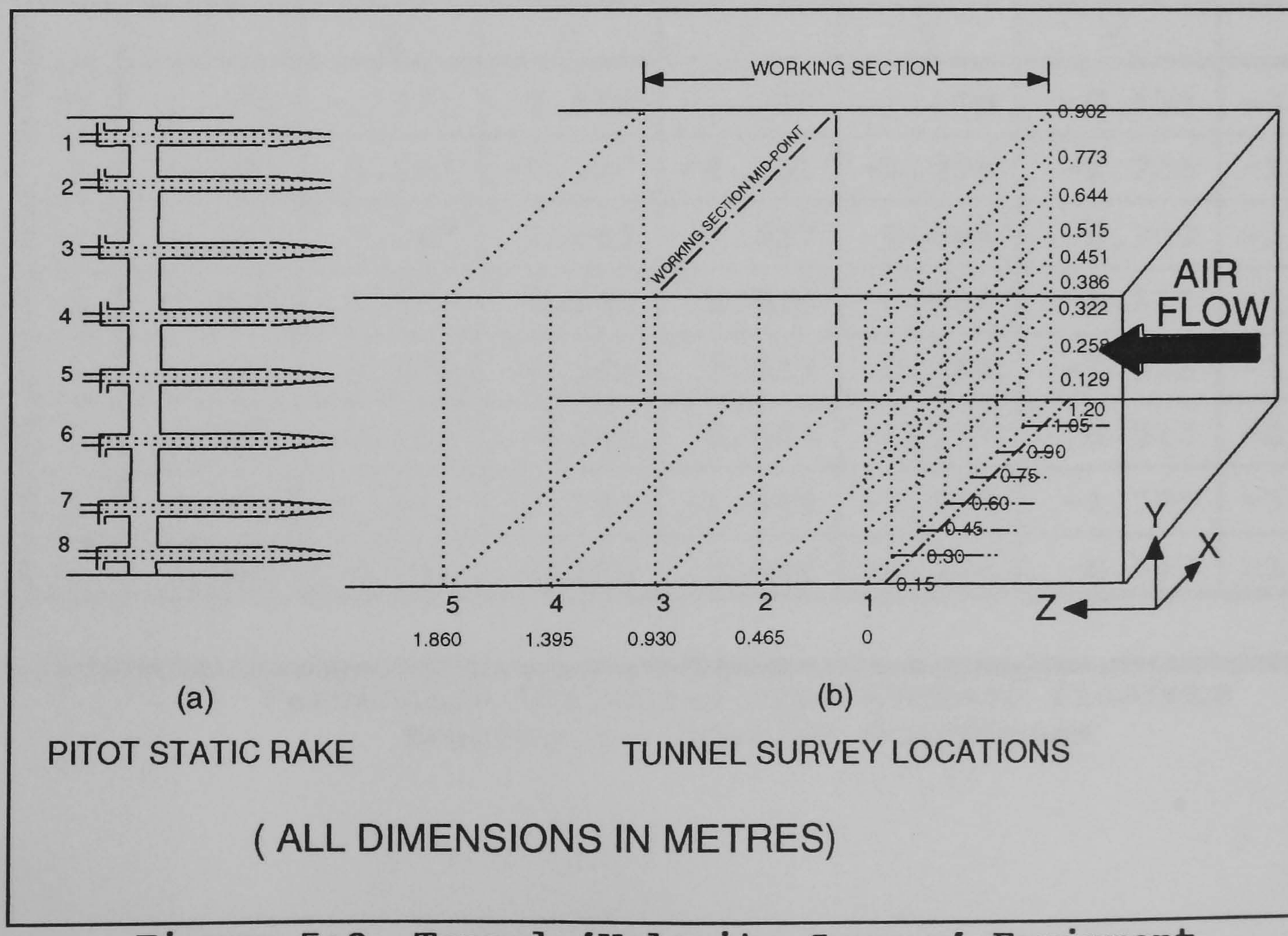

Figure 5:2 Tunnel 'Velocity Survey' Equipment

Figure 5:3a Percentage Deviation from Average Flowrate

	1	2	3	4	5	6	7
8	2.056	-1.461	-0.584	-1.544	-2.105	-0.533	-3.473
7	3.227	0.141	-0.187	-0.351	-0.909	-1.705	-1.864
6	4.768	1.327	0.602	0.437	0.664	-0.909	-1.070
5	4.768	0.538	0.602	0.829	0.664	-0.513	1.070
4	4.385	0.538	0.208	0.437	0.664	-0.513	-1.864
3	4.000	0.141	0.208	0.044	-0.119	-0.513	-2.665
2	2.448	-1.461	-1.383	-1.544	-2.507	-1.705	-3.068
1	3.614	0.141	0.602	0.044	-0.119	-0.513	-1.864

Percentage Deviation from Average Flowrate
Station 1 - Looking Downstream

Figure 5:3b Percentage Deviation from Average Flowrate

	1	2	3	4	5	6	7
8	1.262	0.532	-0.193	-0.356	-0.519	-0.914	-1.472
7	1.262	0.927	-0.193	-0.356	-0.914	-1.710	-1.472
6	2.832	2.103	0.596	0.823	0.659	-0.519	-1.075
5	2.442	1.713	0.596	0.431	0.659	-0.125	-1.075
4	2.442	1.321	0.202	0.823	0.659	-0.519	-1.472
3	2.050	0.927	0.202	0.038	-0.125	-0.519	-2.270
2	0.068	-0.662	-1.388	-1.550	-2.110	-1.710	-2.671
1	1.262	0.927	0.202	0.038	-0.125	-0.519	-1.472

Percentage Deviation from Average Flowrate
Station 2 - Looking Downstream

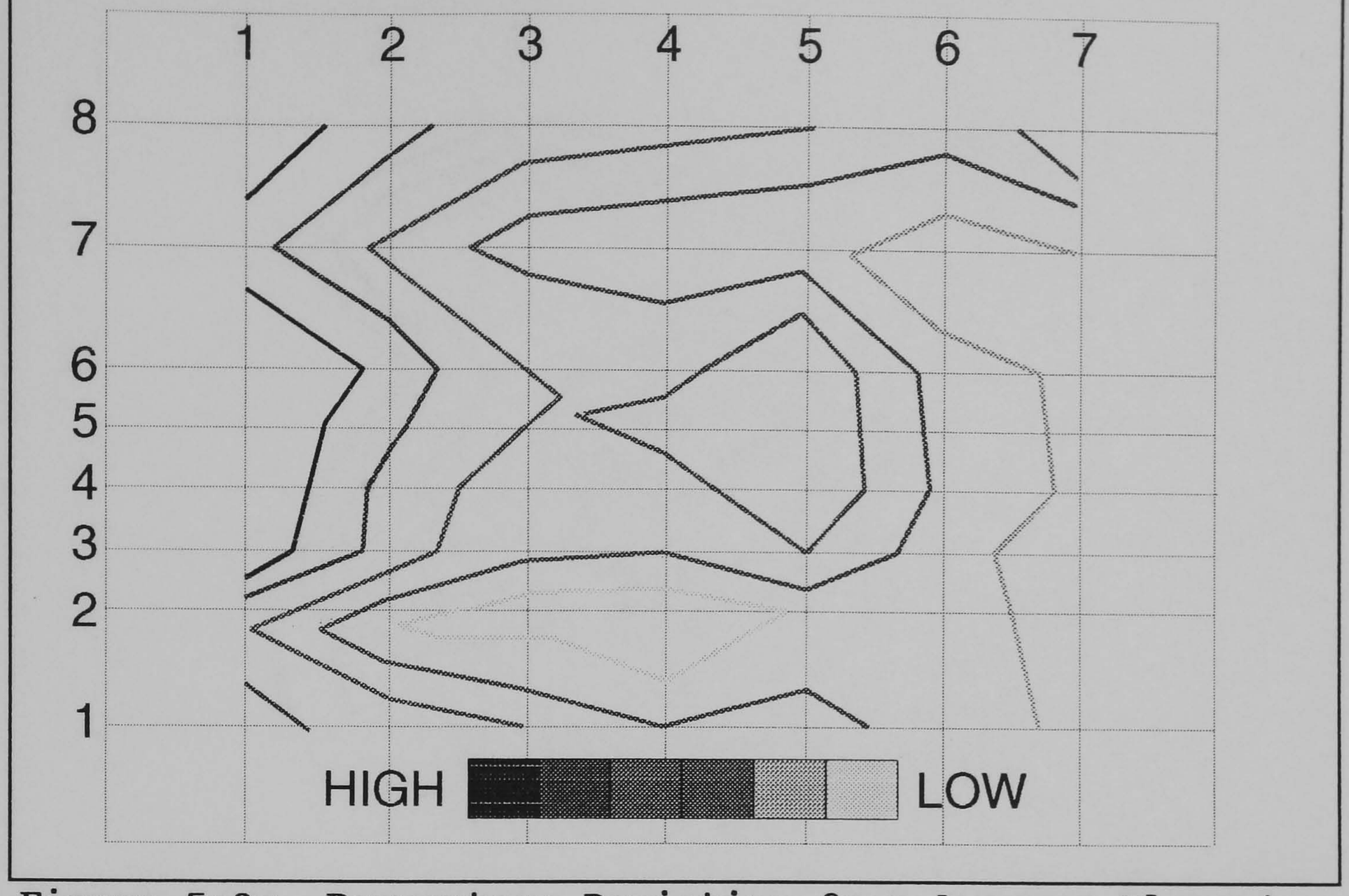

Figure 5:3c Percentage Deviation from Average Flowrate

	1	2	3	4	5	6	7
8	2.064	0.941	0.610	0.445	0.281	-0.111	0.509
7	0.879	0.149	-0.576	-0.739	-0.901	-1.697	-1.062
6	2.456	1.335	0.216	0.052	0.672	-0.505	-1.062
5	2.064	0.941	0.216	0.445	0.672	-0.505	-1.062
4	2.064	0.546	-0.180	0.052	0.672	-0.505	-1.062
3	1.671	0.546	-0.180	-0.343	0.281	-0.505	-1.857
2	0.082	-1.453	-1.375	-1.937	-0.901	-0.901	-1.062
1	1.276	0.546	0.216	-0.343	-0.111	-0.505	-1.458

Percentage Deviation from Average Flowrate
Station 3 - Looking Downstream

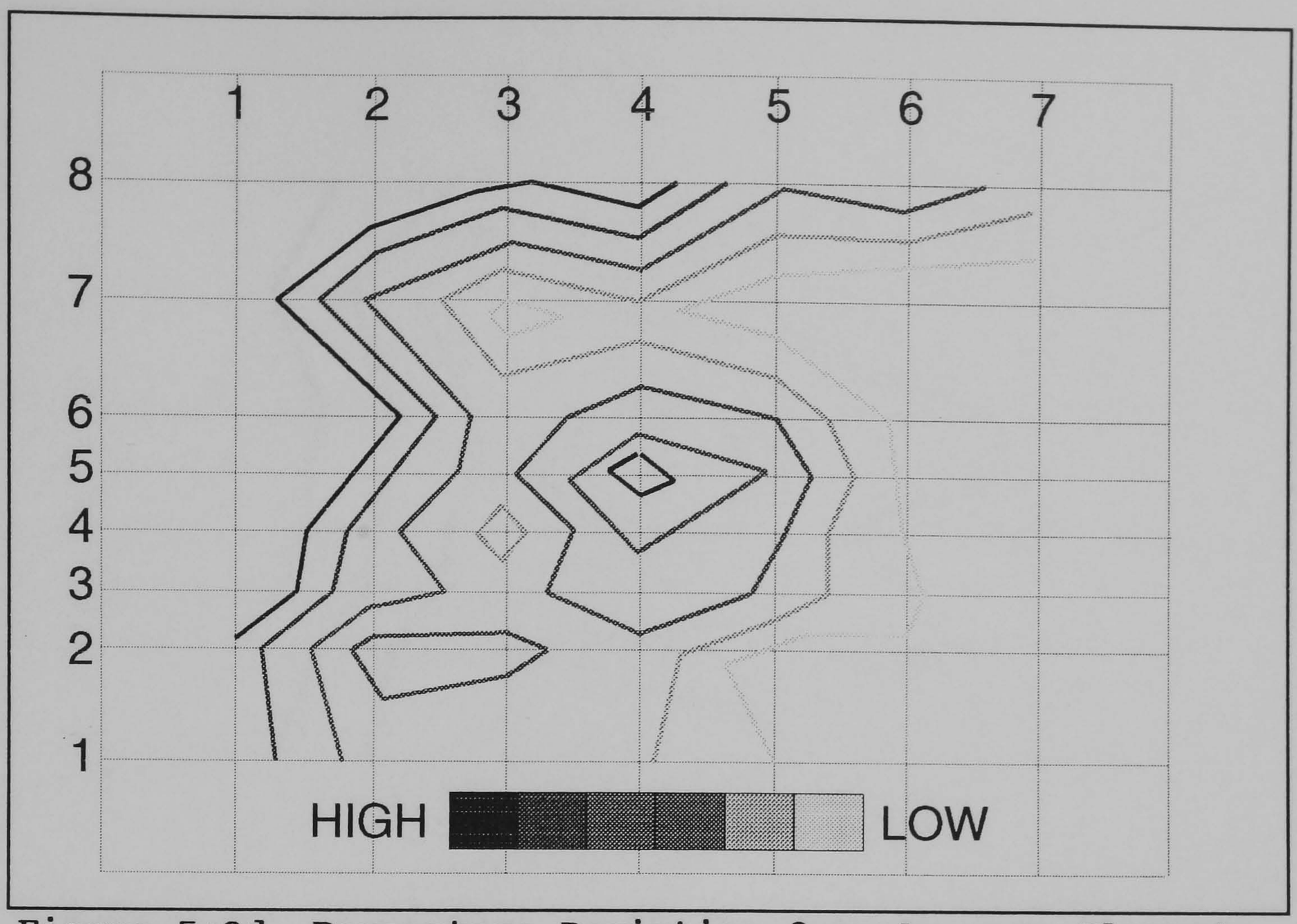

Figure 5:3d Percentage Deviation from Average Flowrate

	1	2	3	4	5	6	7
8	1.862	1.134	0.802	1.026	0.083	0.473	-0.080
7	1.075	-0.049	-0.773	-0.540	-1.097	-1.493	-1.258
6	1.862	1.134	0.017	0.246	0.083	-0.702	-1.258
5	1.862	0.741	0.017	1.026	0.473	-0.702	-1.258
4	1.470	0.347	-0.377	0.637	0.083	-0.702	-1.258
3	1.470	0.347	0.017	0.246	0.083	-0.309	-1.653
2	0.680	-0.446	-0.377	-0.146	-1.097	-0.702	-0.863
1	0.680	-0.049	0.017	-0.146	-0.702	-0.702	-1.258

Percentage Deviation from Average Flowrate
Station 4 - Looking Downstream

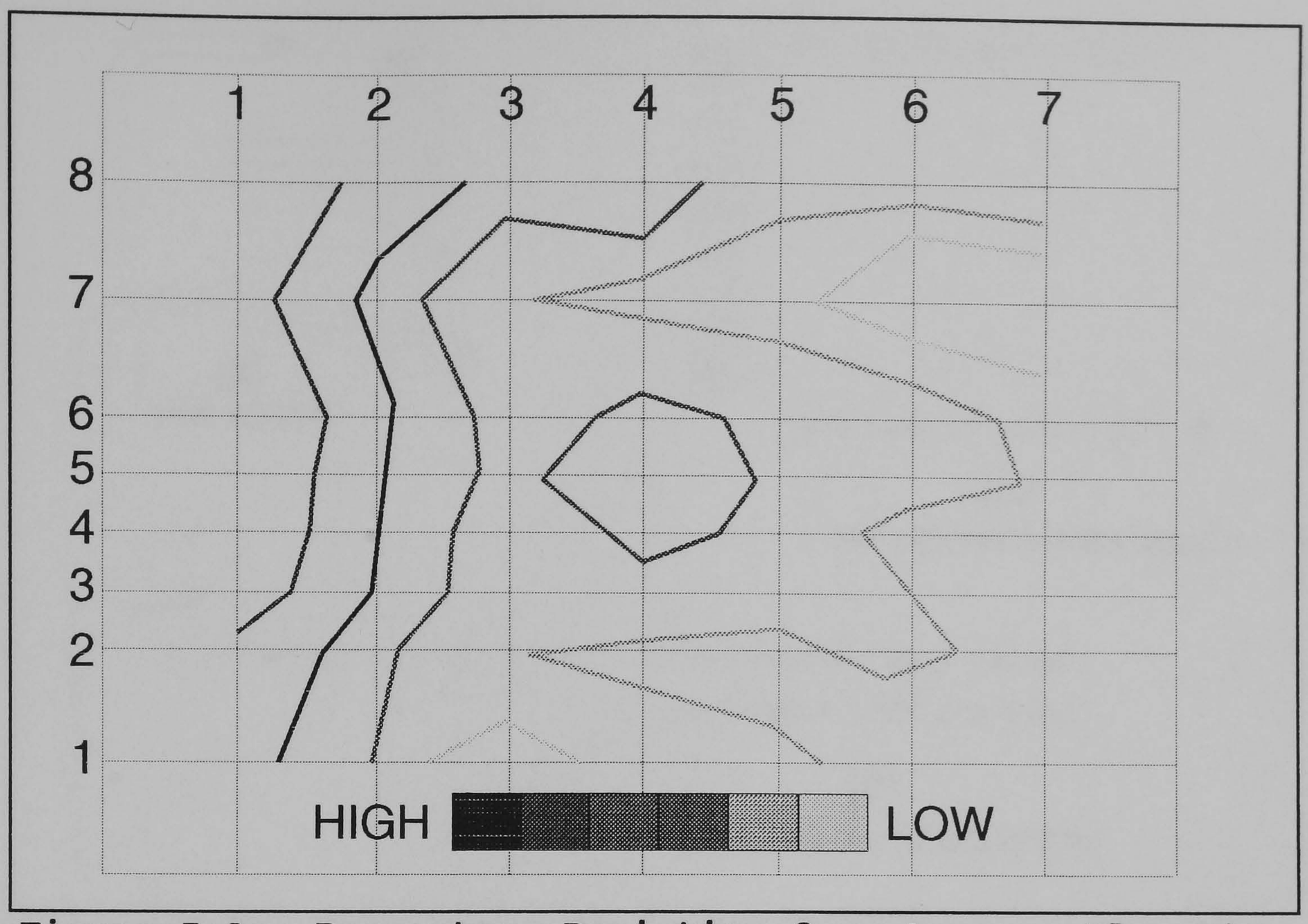

Figure 5:3e Percentage Deviation from Average Flowrate

	1	2	3	4	5	6	7
8	1.788	1.048	0.313	0.552	-0.419	-0.419	-0.177
7	1.383	0.237	-0.500	-0.662	-0.824	-2.051	-1.800
6	2.191	0.643	-0.093	0.149	-0.015	-0.015	-0.580
5	1.788	0.643	-0.093	0.552	-0.015	-0.015	-0.580
4	1.788	0.643	-0.500	0.149	-0.015	-0.824	-0.985
3	1.383	0.643	-0.093	-0.256	-0.015	-0.419	-0.985
2	0.977	-0.172	-0.500	-0.662	-0.824	-0.419	-0.580
1	0.977	-0.172	0.313	-0.256	-0.419	-0.824	-0.985

Percentage Deviation from Average Flowrate
Station 5 - Looking Downstream

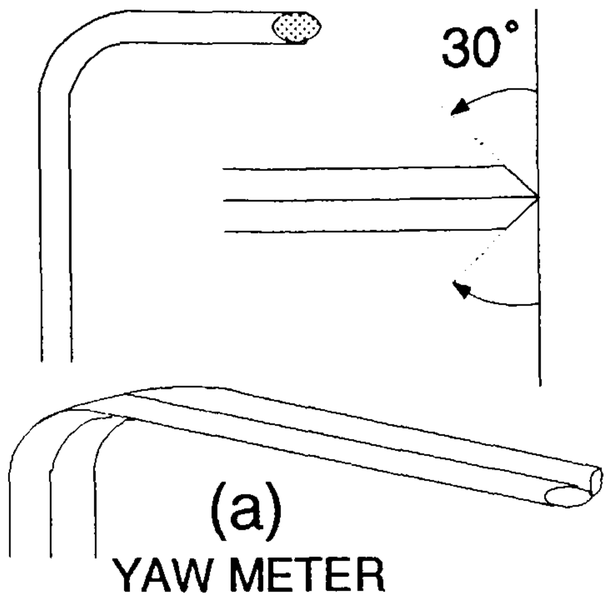

(a)

YAW METER

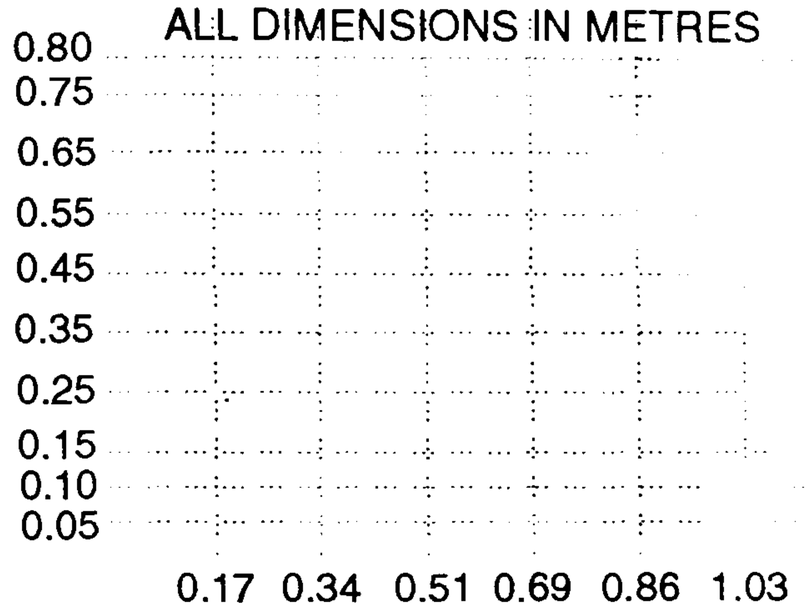

(b)

CROSSFLOW SURVEY POINTS

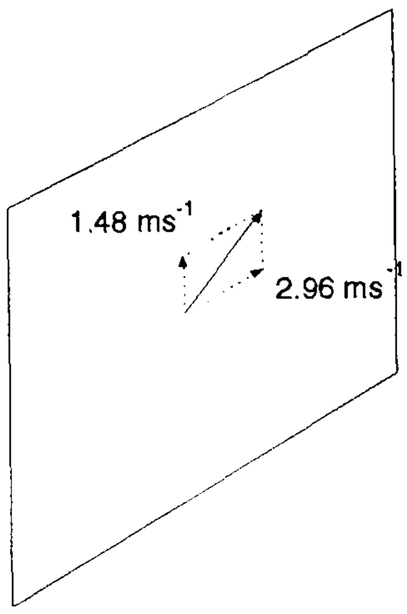

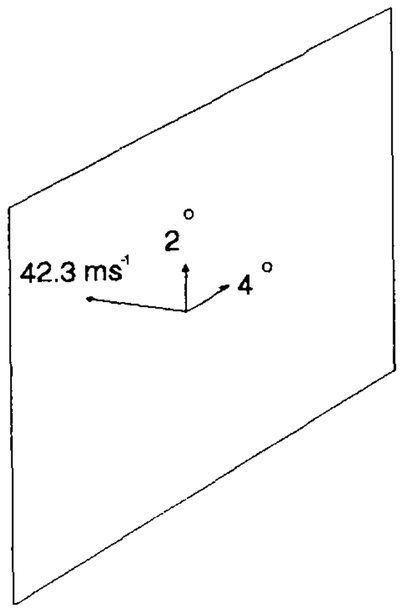

$42.3 \times \tan 2^{\circ} = Vv = 1.48\ ms^{-1}$

$42.3 \times \tan 4^{\circ} = Vh = 2.96\ ms^{-1}$

(c)

CROSSFLOW RESOLUTION

Figure 5:4 Windtunnel 'Crossflow Survey' Equipment

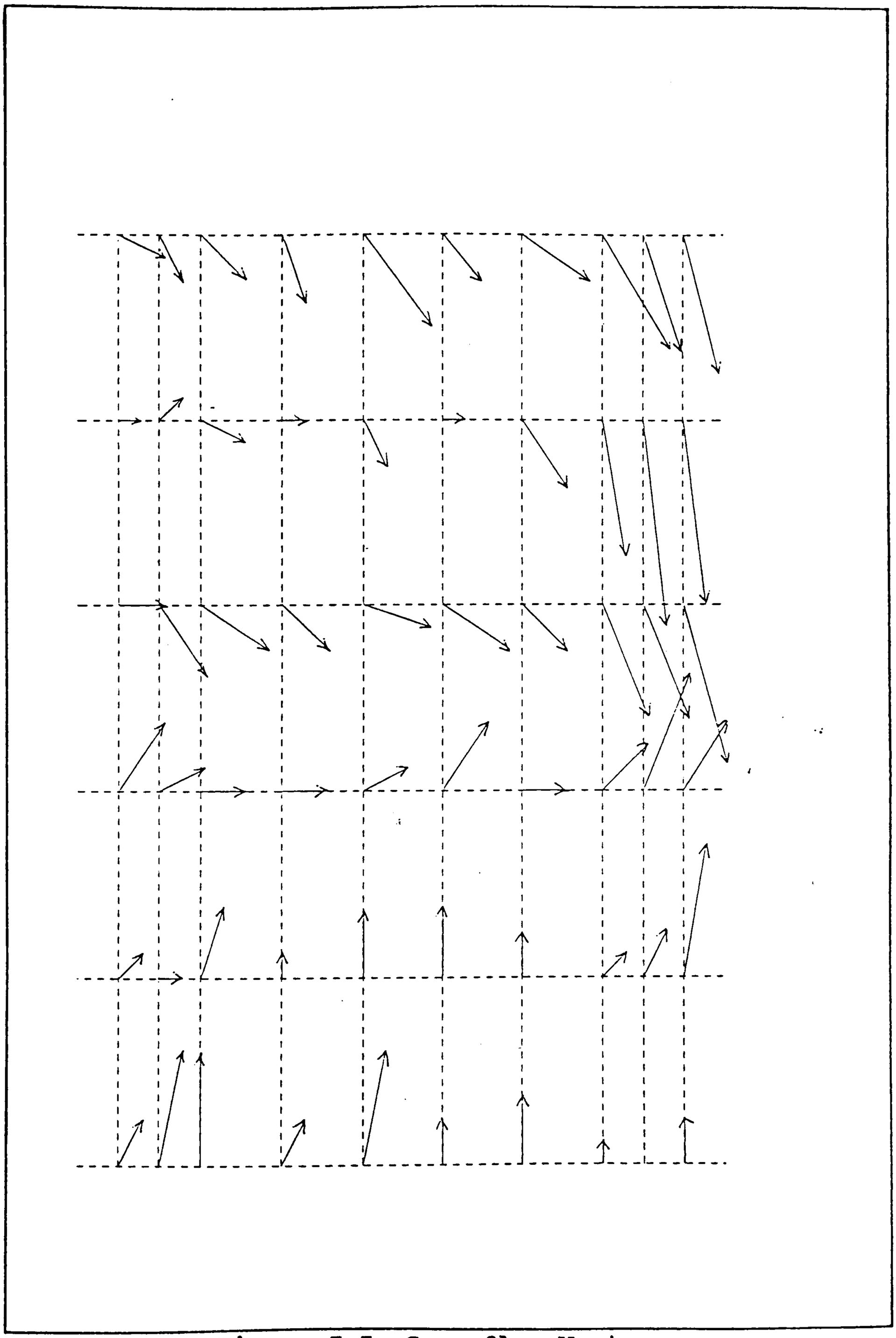

Figure 5:5 Crossflow Vectors

CROSSFLOW COMPONENT TABLES (MAGNITUDE AND ANGLE)
TAKEN AT STATION 3 (MIDPOINT OF WORKING SECTION)
LOOKING DOWNSTREAM

75	4.47	5.69	5.12	2.52	4.25	1.40
70	3.77	6.33	3.74	3.73	1.53	0
65	4.13	4.27	3.77	1.99	0.98	0.69
55	2.54	2.52	1.98	1.40	1.39	2.07
45	1.98	0.70	2.52	2.53	2.08	1.38
35	3.52	1.56	2.22	1.57	2.08	3.53
25	2.22	0.70	1.97	1.40	0.69	1.54
15	1.98	1.56	2.51	1.40	2.20	3.43
10	1.54	0.97	2.47	1.55	0.69	3.53
5	1.57	0.70	1.39	1.97	0.98	1.54
	1	2	3	4	5	6

FIGURE 5:5b CROSSFLOW COMPONENTS (MAGNITUDE ms^{-1})

75	18.38	7.08	15.88	146.32	170.57	180.00
70	21.76	6.29	21.76	158.24	153.44	0.00
65	30.92	9.43	21.76	135.00	135.00	180.00
55	56.32	33.68	45.00	90.00	180.00	180.00
45	45.00	90.00	56.32	146.32	180.00	180.00
35	36.85	26.56	71.58	116.56	180.00	168.72
25	18.42	90.00	45.00	90.00	180.00	153.44
15	45.00	63.44	56.32	90.00	161.58	180.00
10	26.56	135.00	33.68	116.56	90.00	168.72
5	63.44	90.00	90.00	135.00	135.00	153.44
	1	2	3	4	5	6

FIGURE 5:5c CROSSFLOW COMPONENTS: DEGREES FROM HORIZONTAL

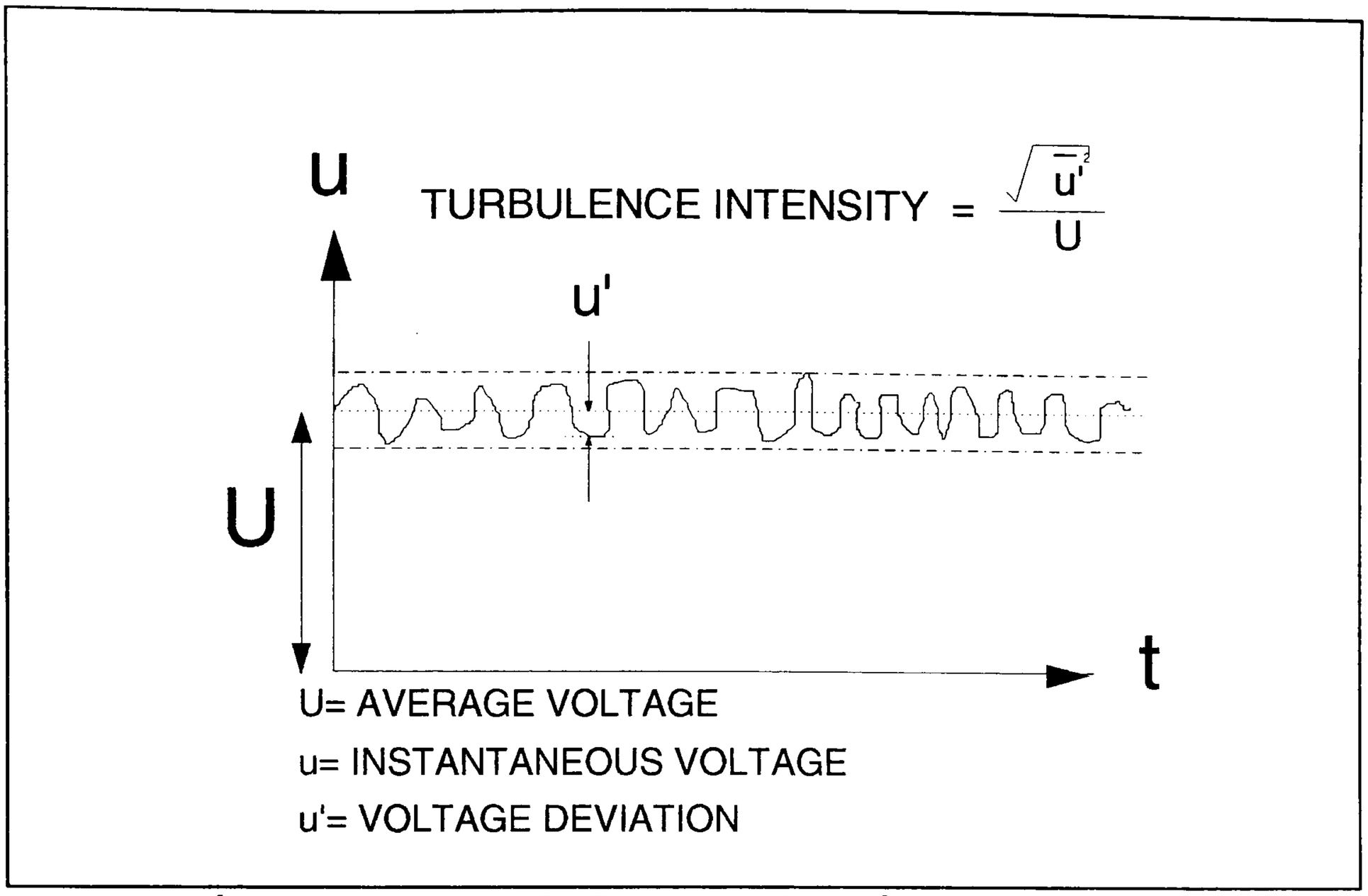

Figure 5:6 Turbulence Intensity Formulae

Figure 5:7 Percentage Turbulence Intesity

	1	2	3	4	5	6
85	0.297	0.261	0.404	0.339	0.344	0.270
80	0.270	0.278	0.285	0.266	0.240	0.272
75	0.245	0.281	0.288	0.267	0.270	0.273
65	0.331	0.313	0.316	0.296	0.297	0.249
55	0.331	0.315	0.267	0.273	0.302	0.361
45	0.222	0.289	0.241	0.329	0.331	0.303
35	0.250	0.289	0.325	0.329	0.276	0.250
25	0.313	0.268	0.274	0.290	0.252	0.279
15	0.239	0.313	0.248	0.251	0.226	0.313
10	0.321	0.301	0.278	0.367	0.256	0.286
5	0.407	0.414	0.311	0.285	0.314	0.462

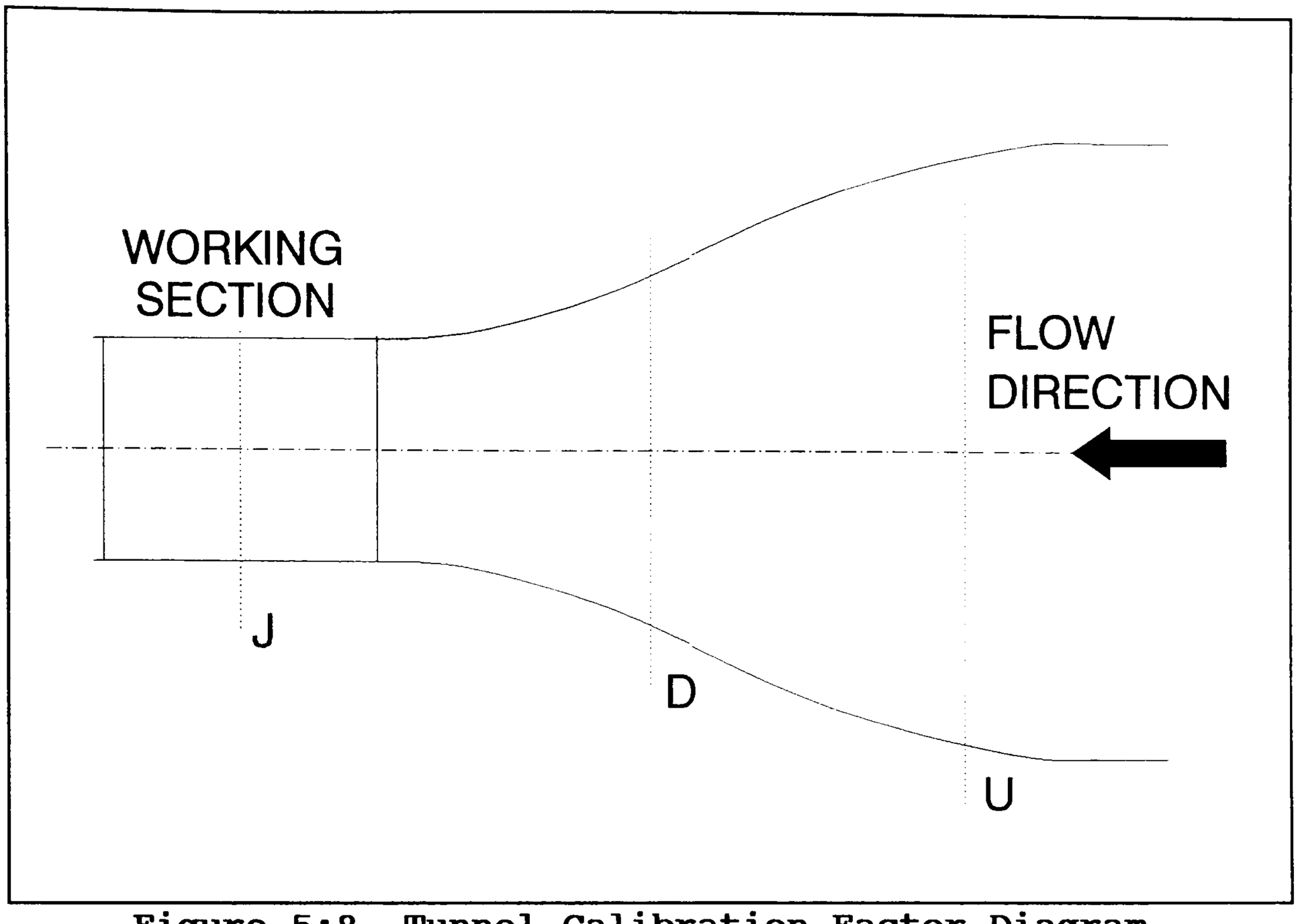

Figure 5:8 Tunnel Calibration Factor Diagram

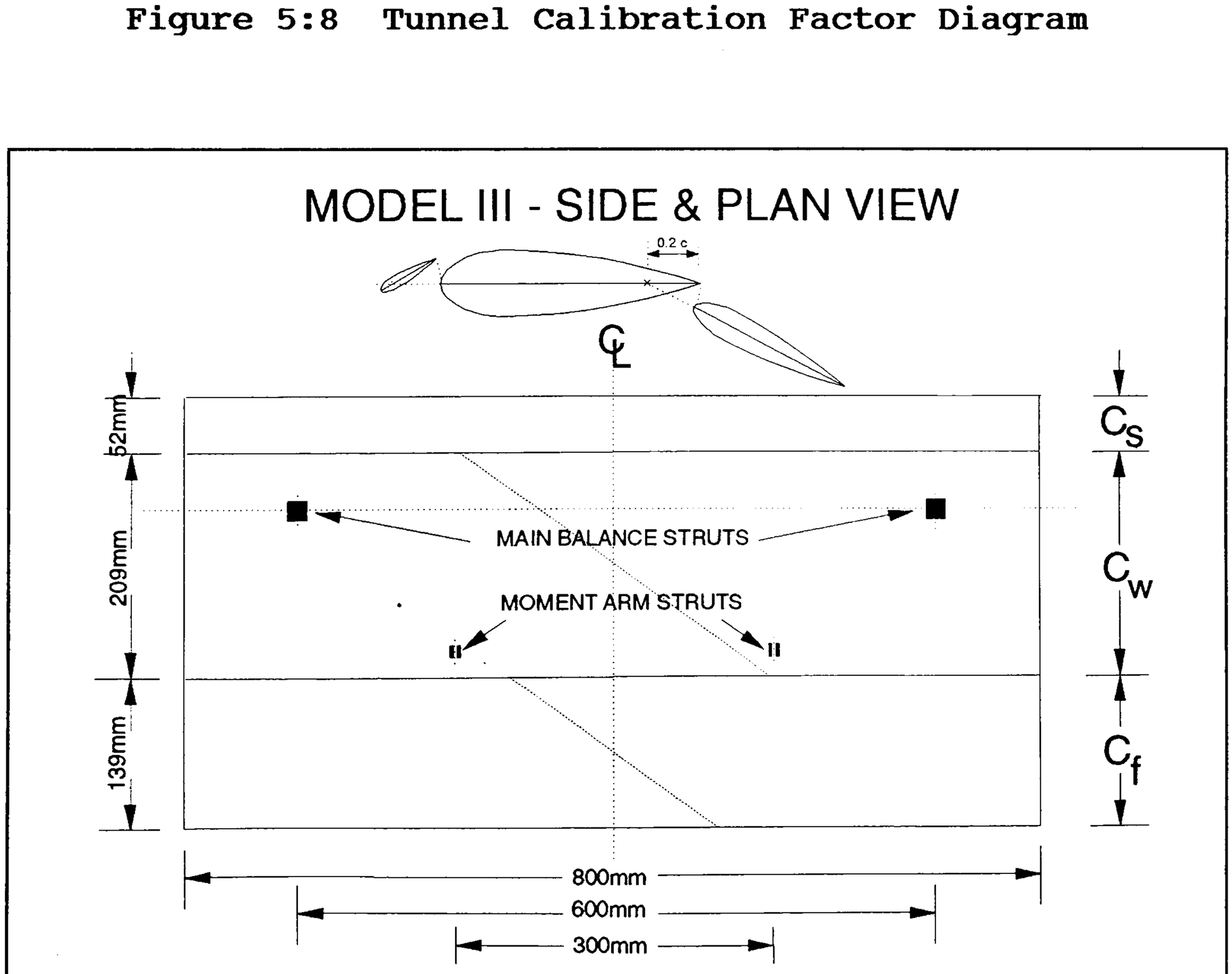

Figure 5:9 Model III

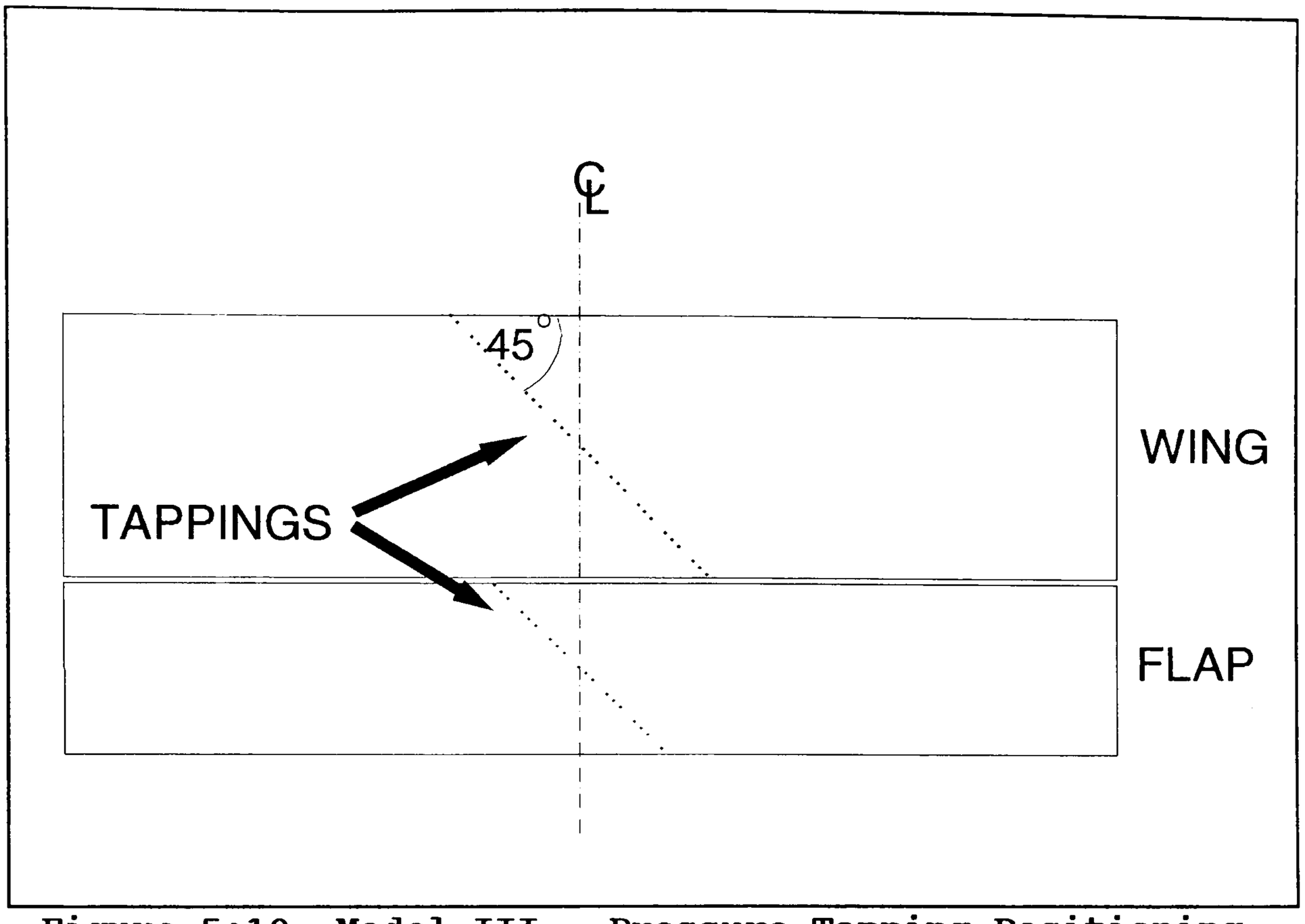

Figure 5:10 Model III - Pressure Tapping Positioning


ANSYS - SOLUTION FLOWCHART
PRE - PROCESSOR
ENTER AEROFOIL COORDINATES
DEFINE AEROFOIL SHAPE USING SPLINES
CREATE 'O' MESH AROUND ELEMENT
CREATE 'O' MESH UPTO FLOW DOMAIN
CHECK MESH FOR EXCESSIVE SKEWNESS OR ASPECT RATIOS
SOLVER
APPLY SOLVER - FLOTRAN
POST-PROCESSOR
PLOT PRESSURE ISOBARICALLY
PLOT VELOCITY ISOBARICALLY
INTEGRATE PRESSURE FOR LIFT, DRAG AND PITCHING MOMENT
PLOT STREAMLINES

Figure 6:1

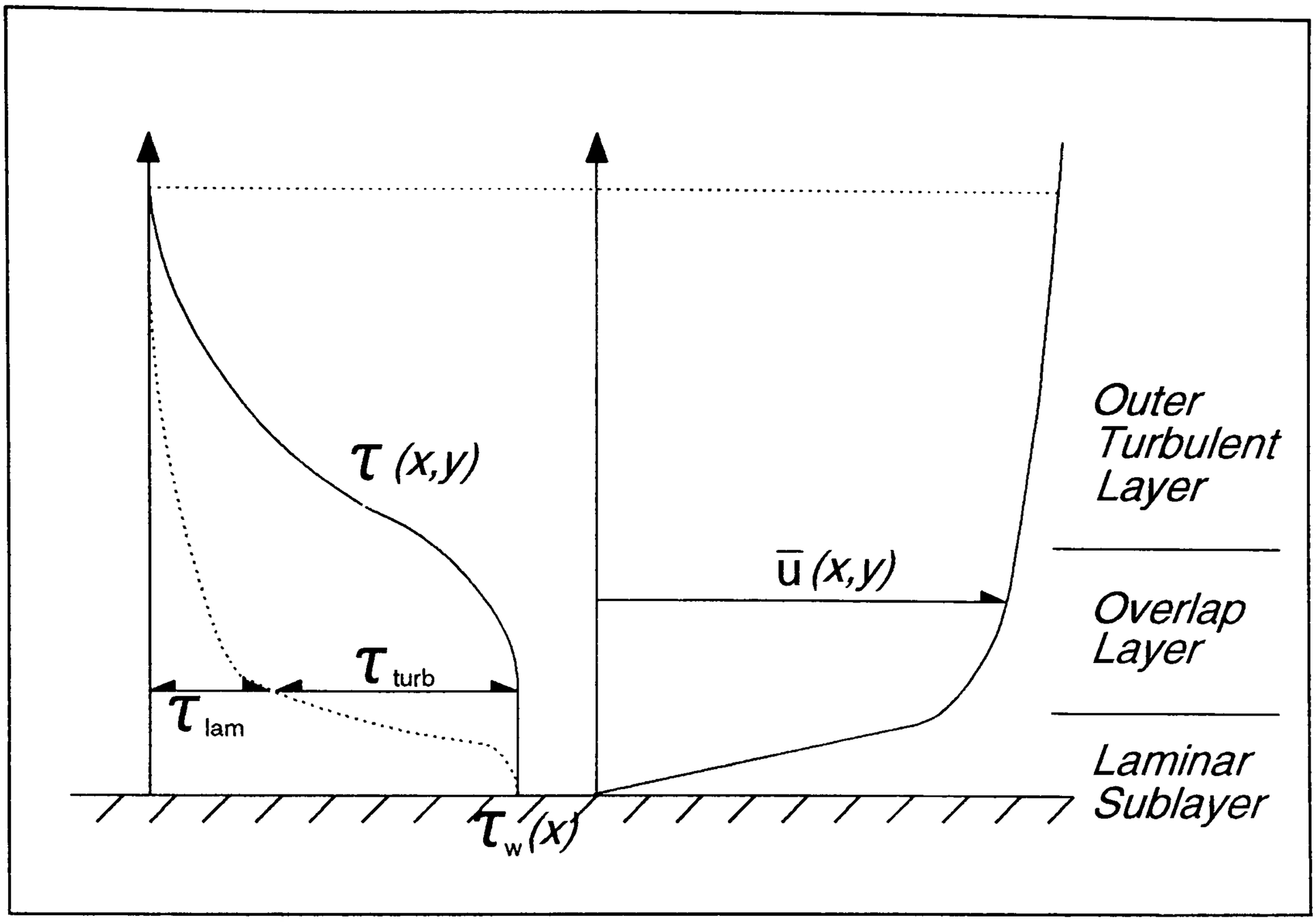

Figure 6:2 FLOTRAN Turbulence Model

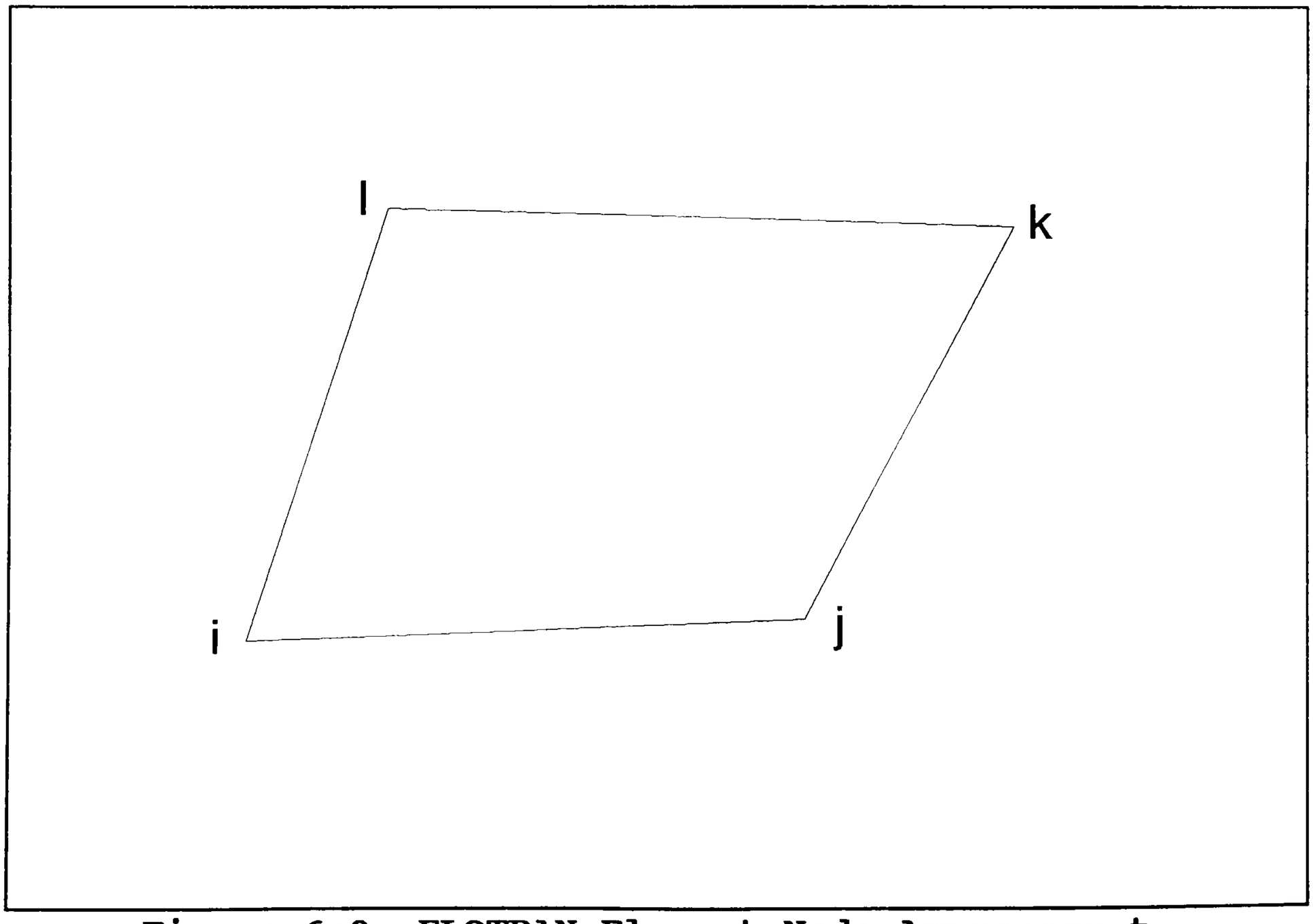

Figure 6:3 FLOTRAN Element Node Arrangement

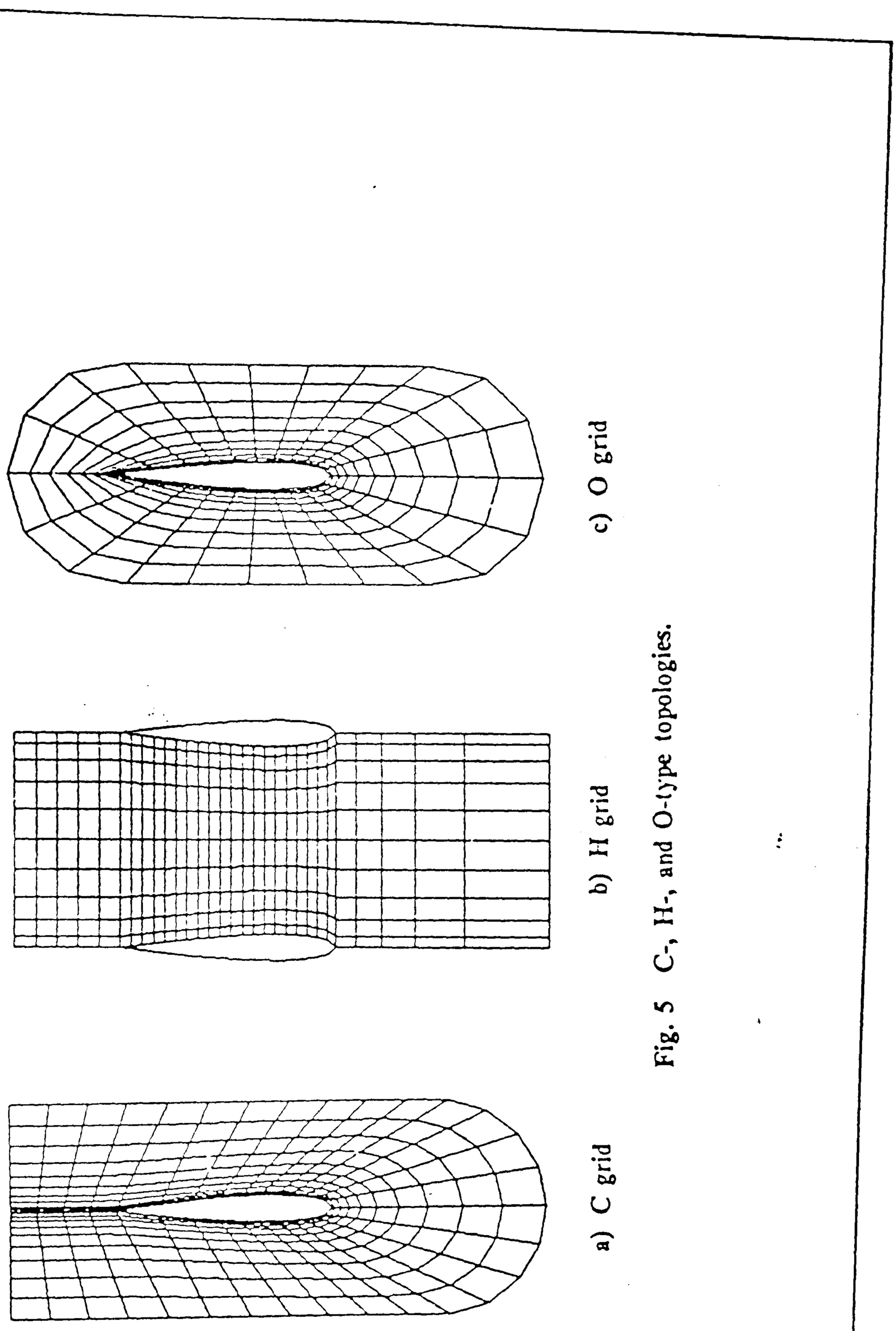

Fig. 5 C-, H-, and O-type topologies.

Figure 7:1 'O','H' & 'C' Mesh Types

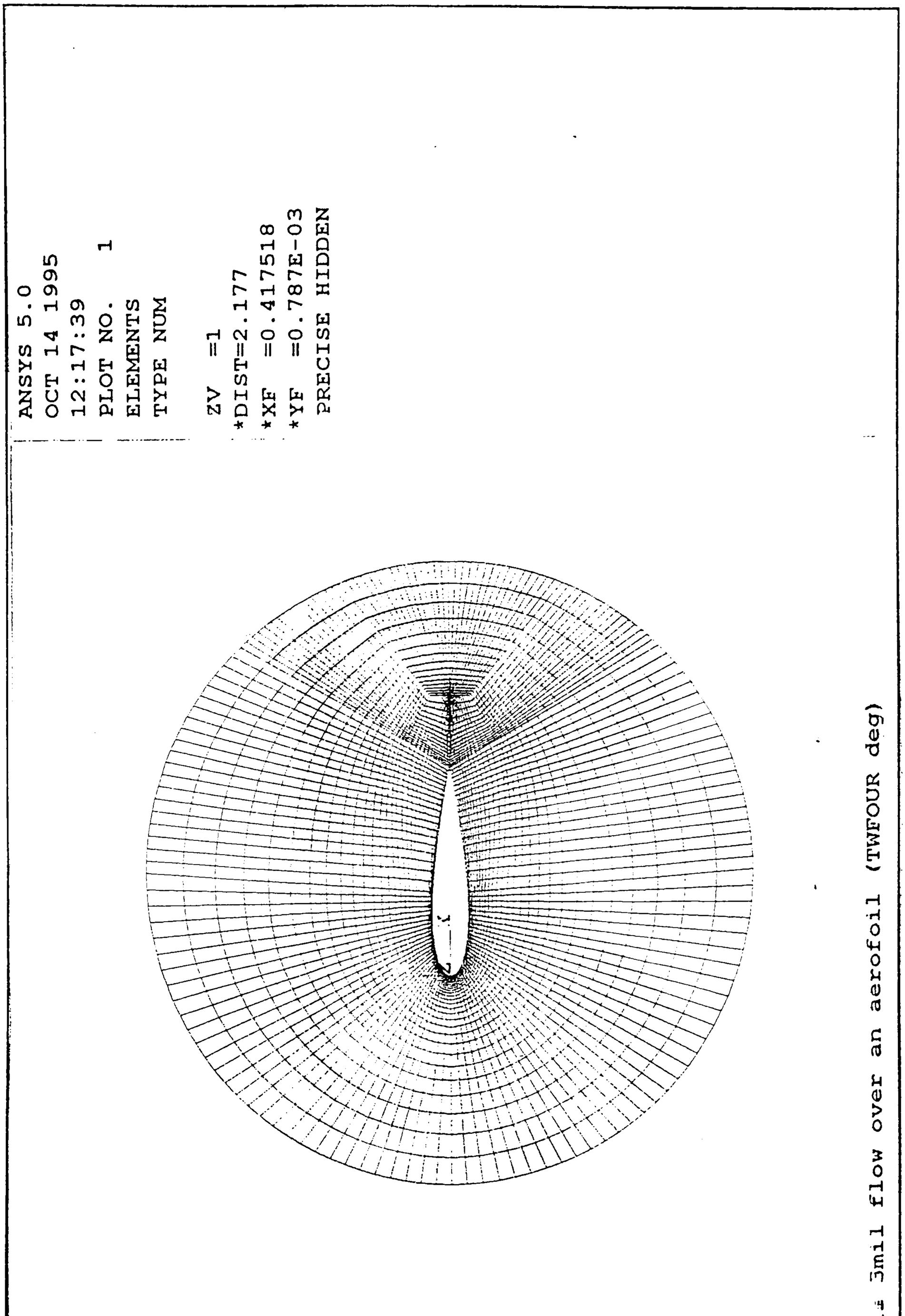

Figure 7:2 1 'Chord Length' Diameter Dense Mesh

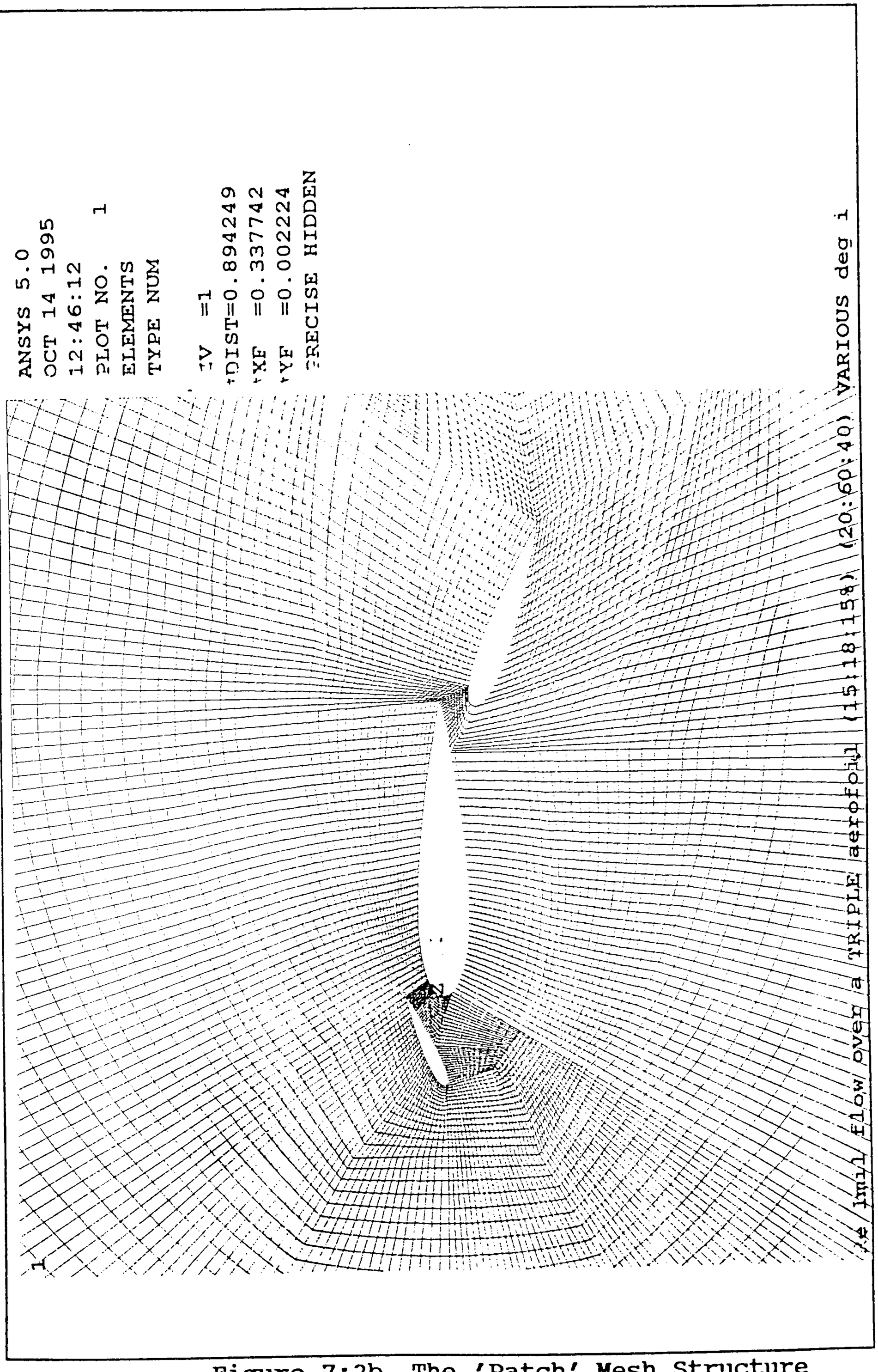

Figure 7:2b The 'Patch' Mesh Structure

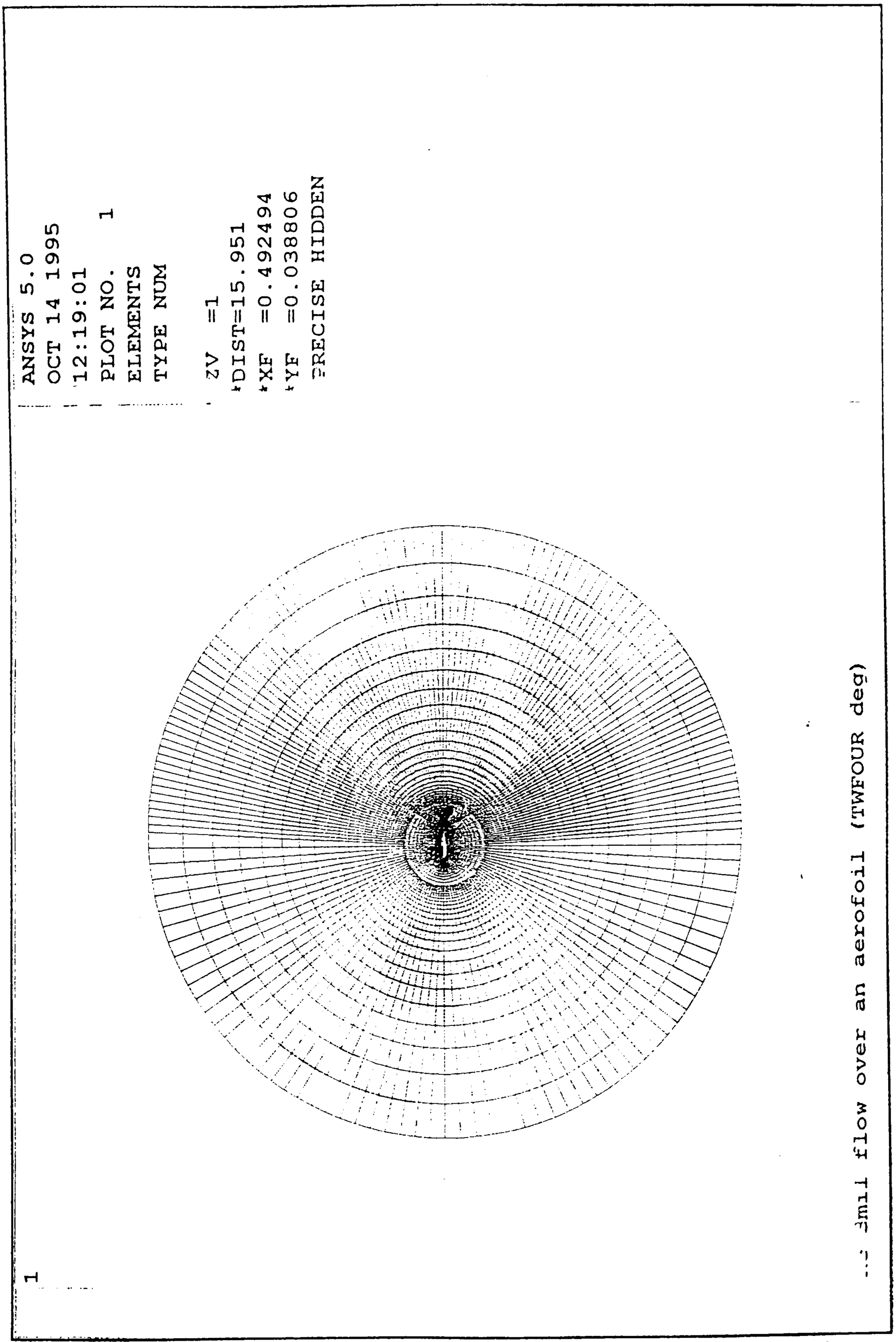

Figure 7:3 10m 'Chord Length' Diameter Outer Mesh

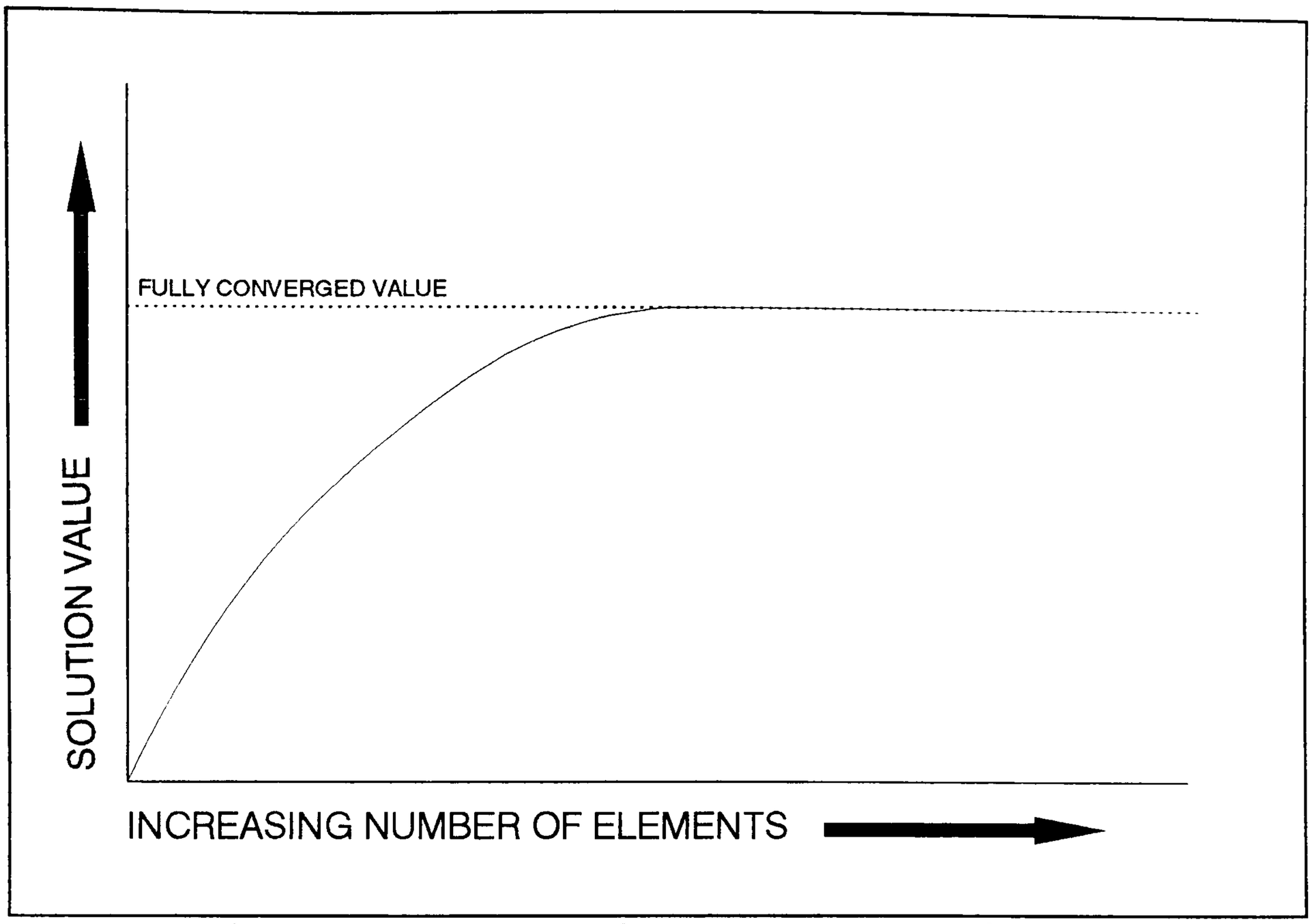

Figure 7:4 Iterative Dependency Diagram

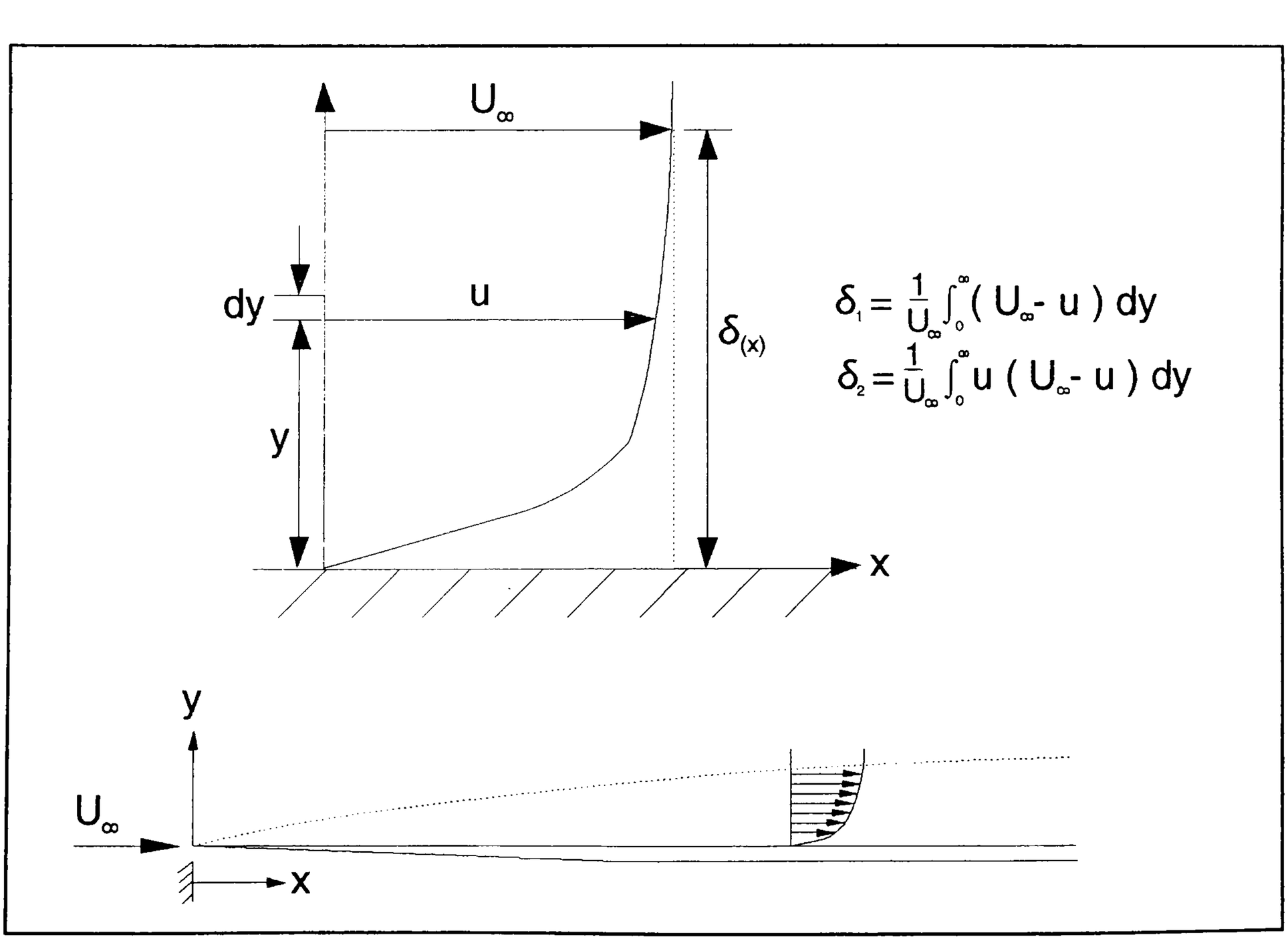

Figure 7:5 CFD 'Flat Plate Test' Model

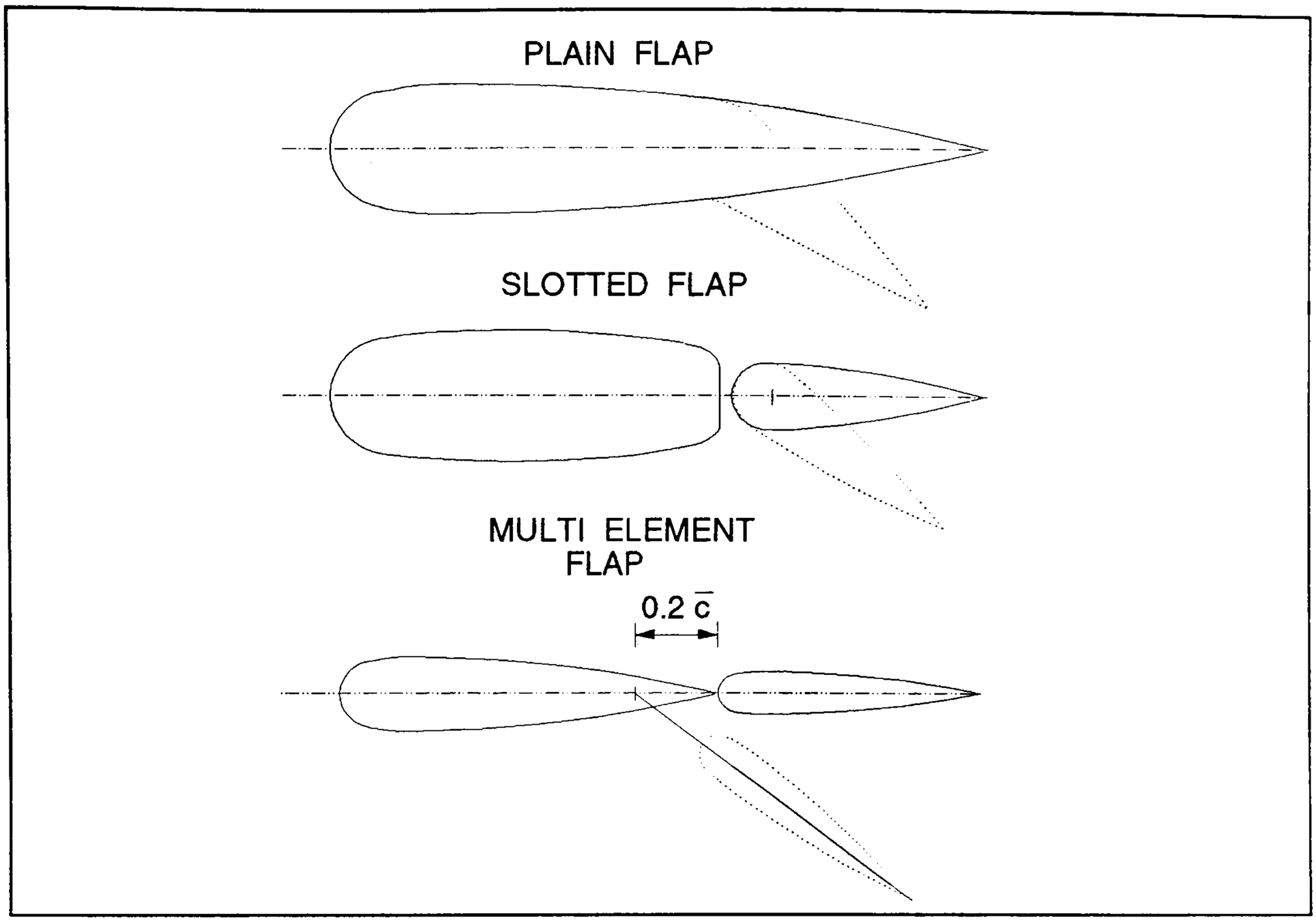

Figure 7:6 Tested Flap Configurations

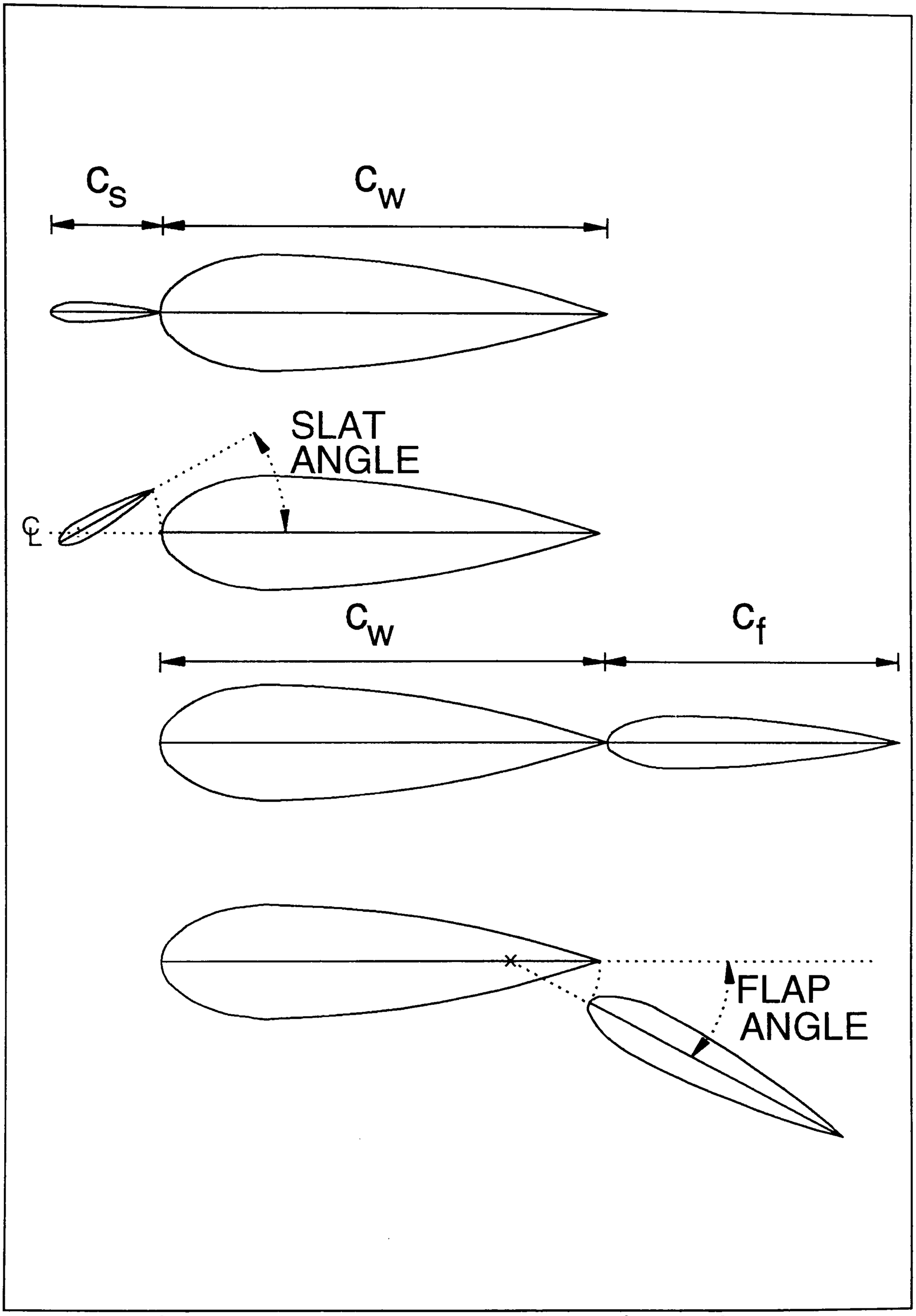

Figure 9:1 Slat and Flap Configurations

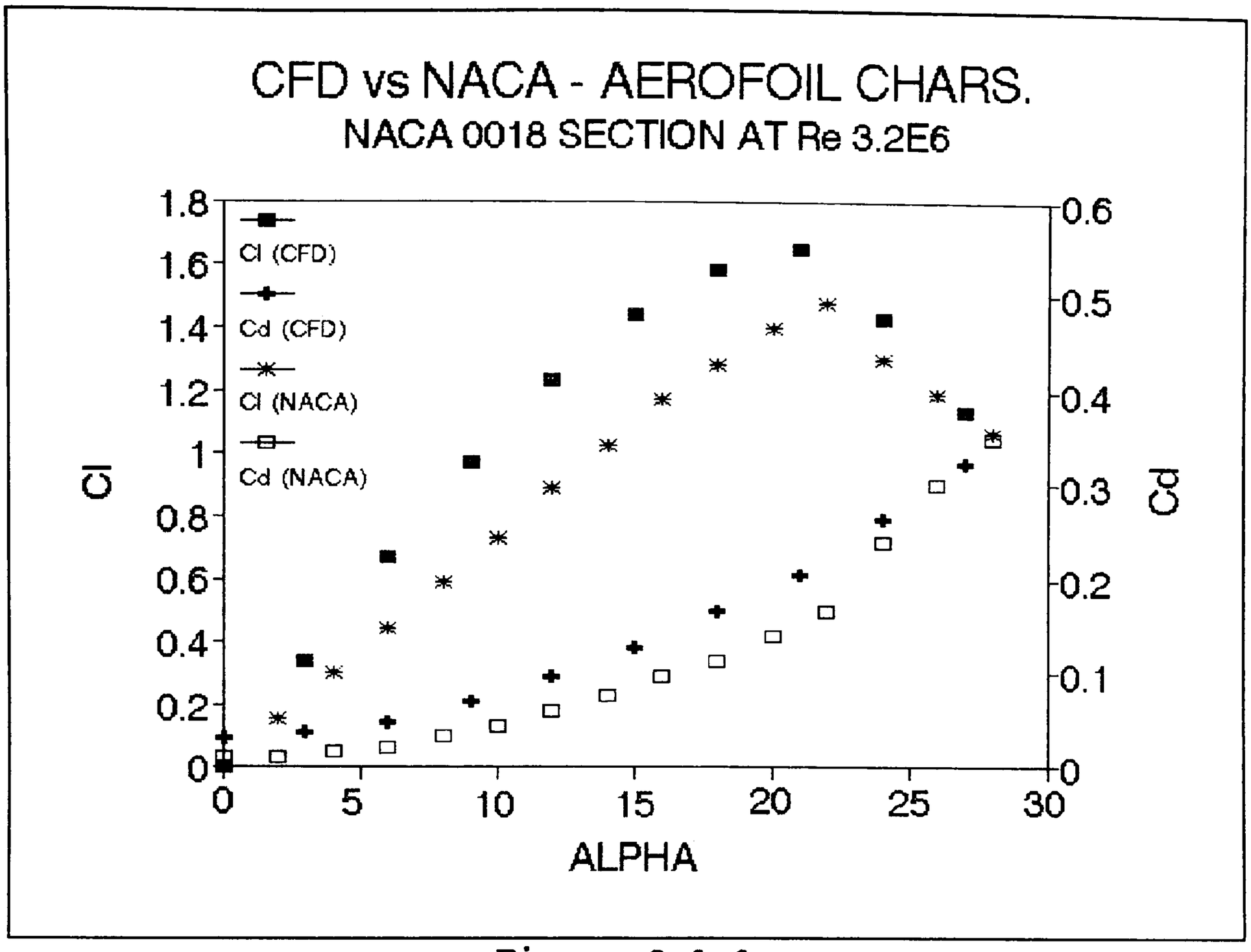

Figure 9:1:1

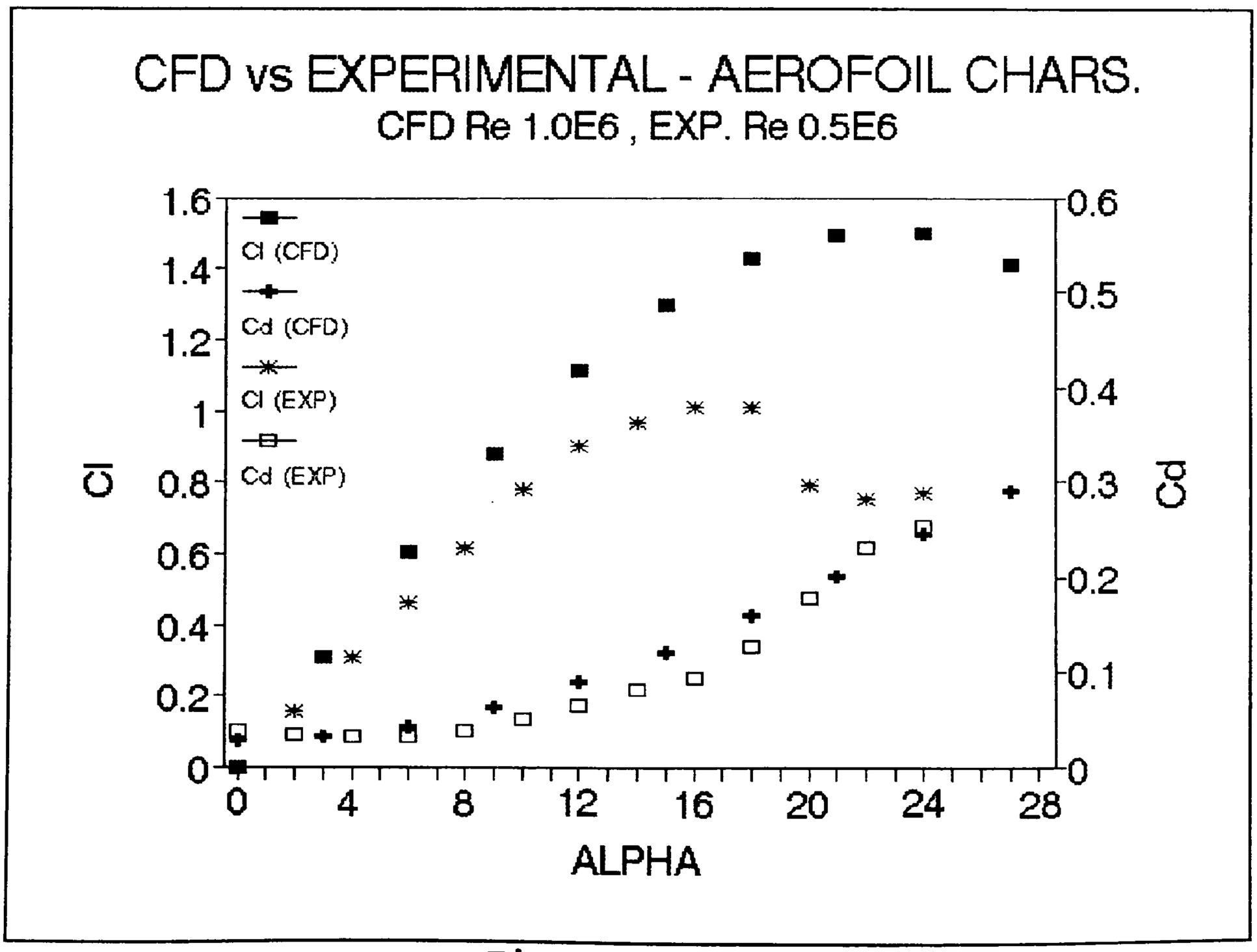

Figure 9:1:2a

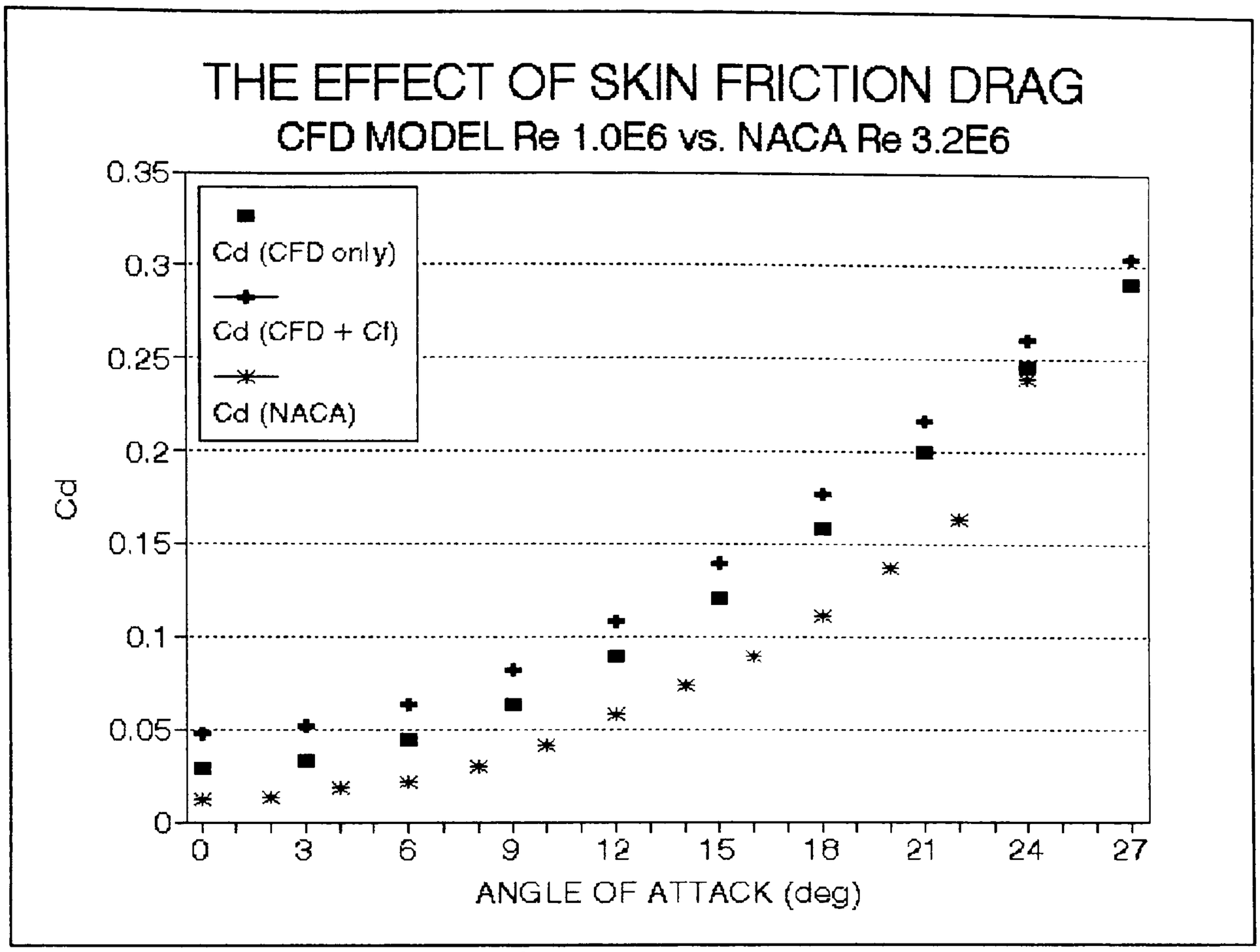

Figure 9:1:2b

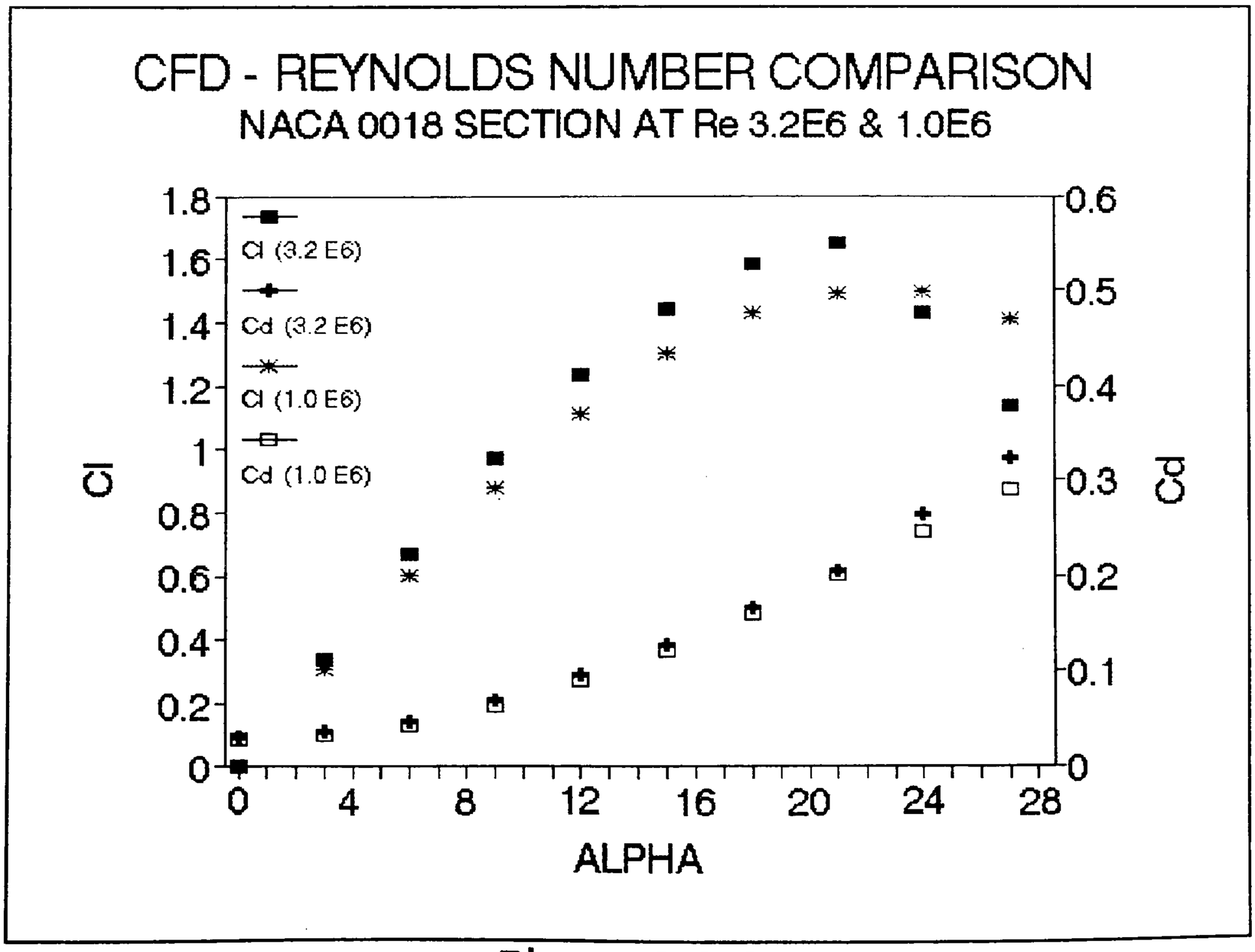

Figure 9:1:3

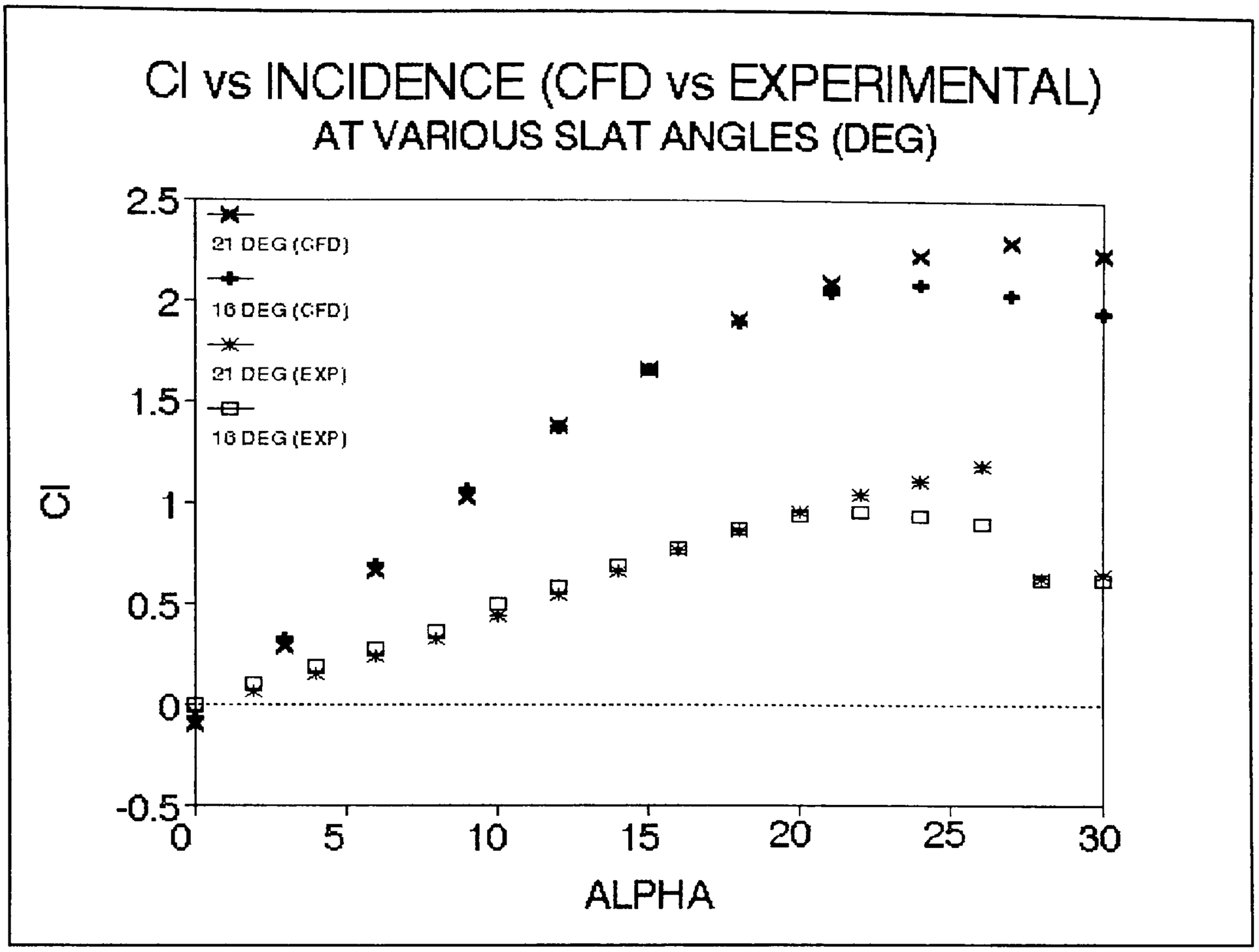

Figure 9:1:4a

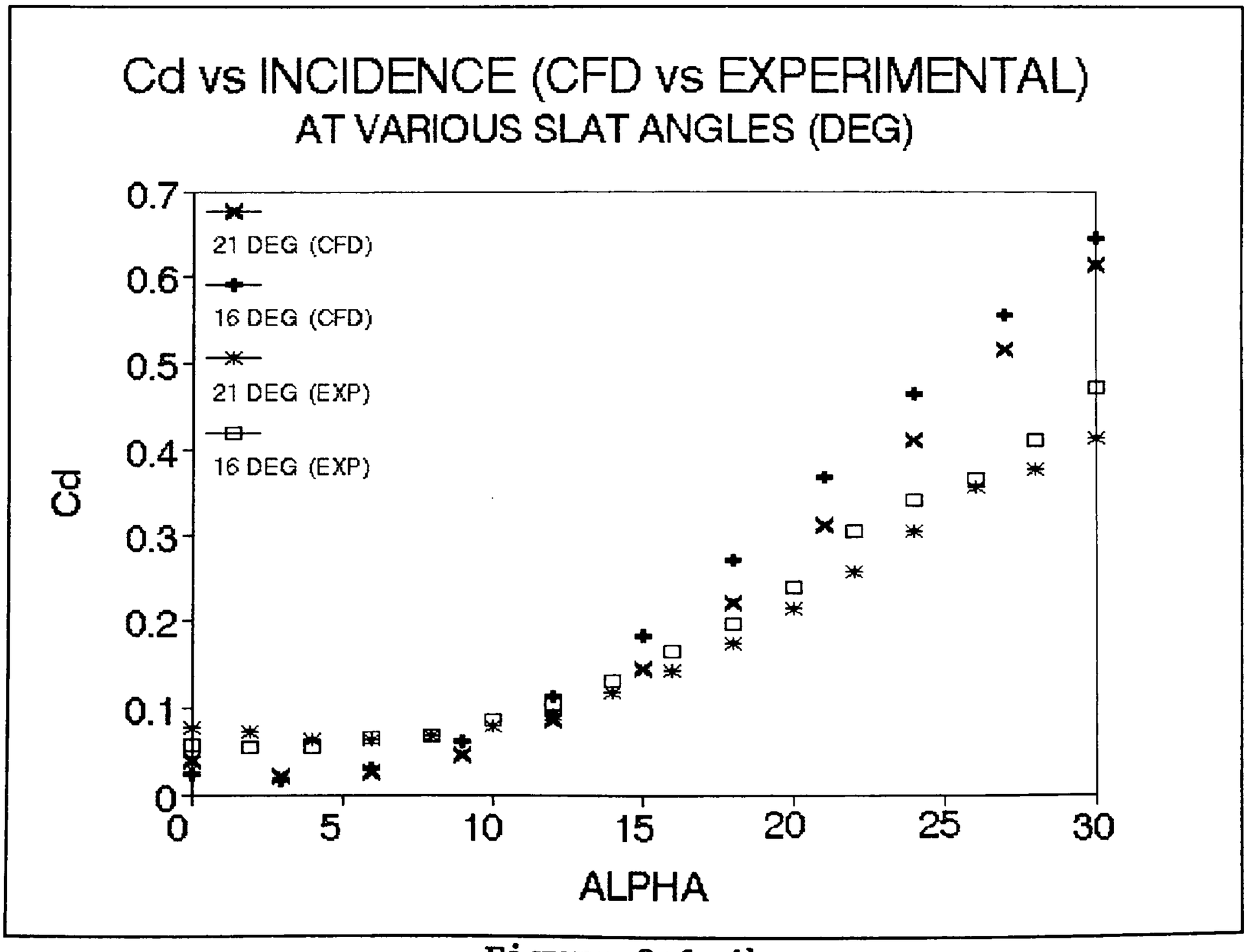

Figure 9:1:4b

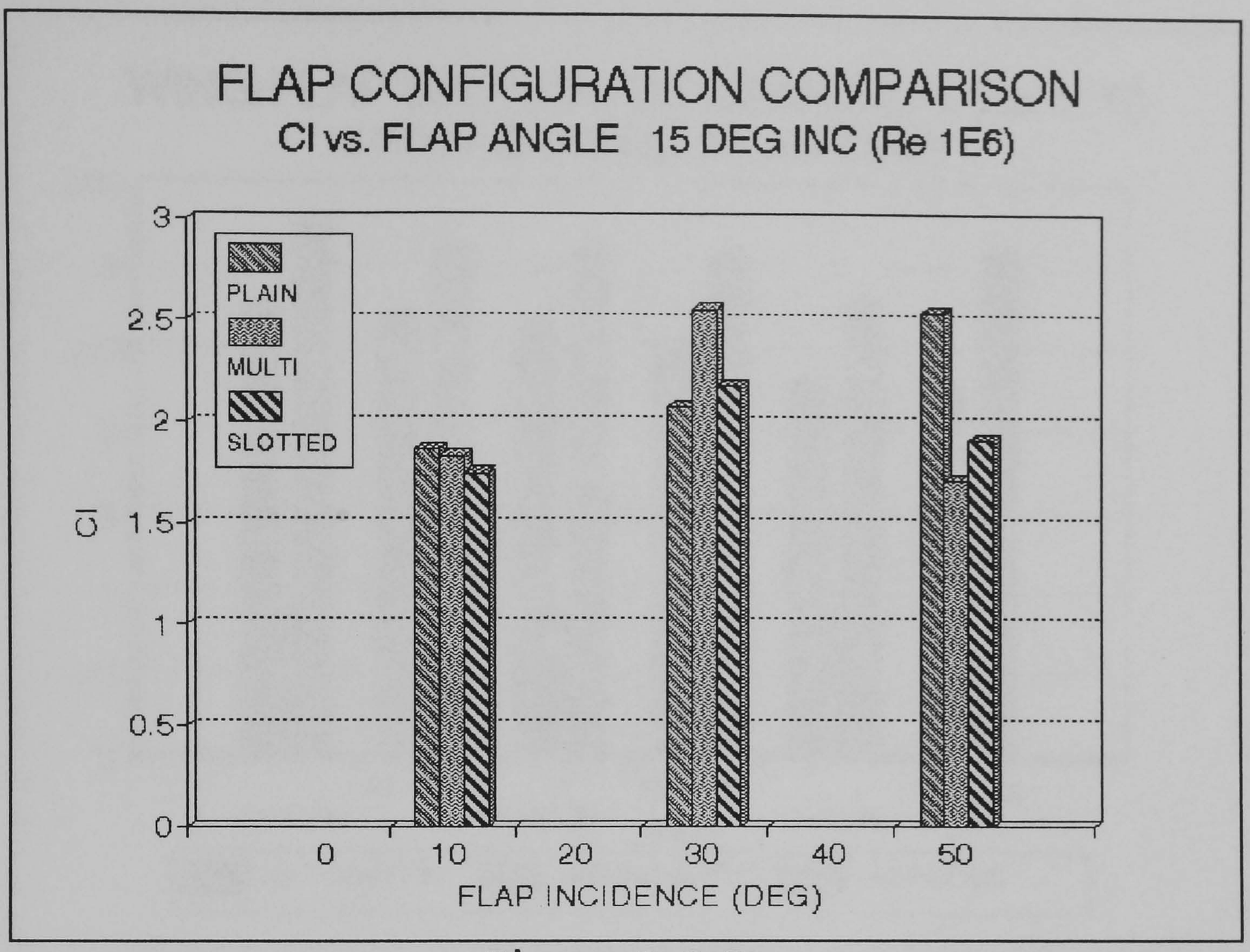

Figure 9:2:5a

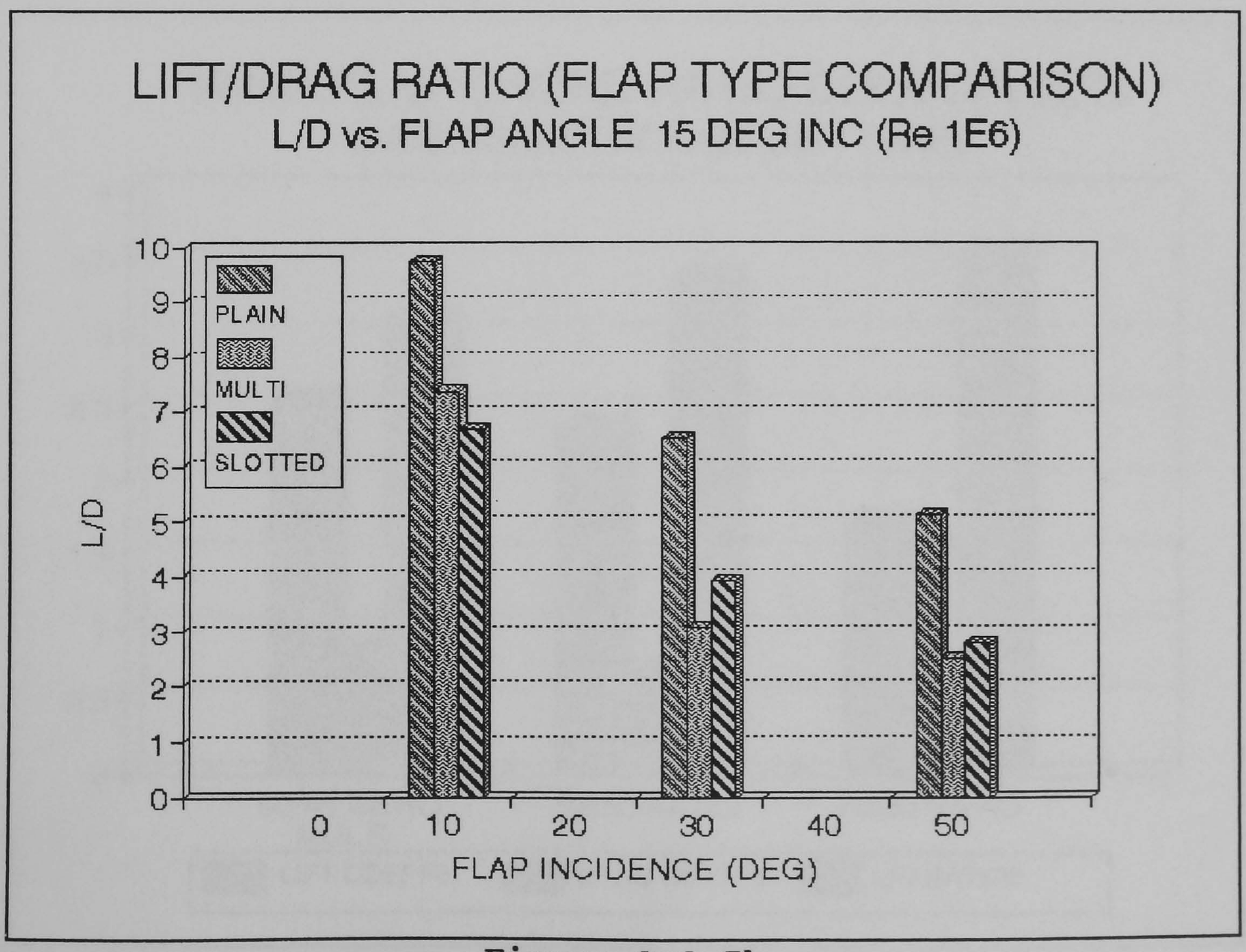

Figure 9:2:5b

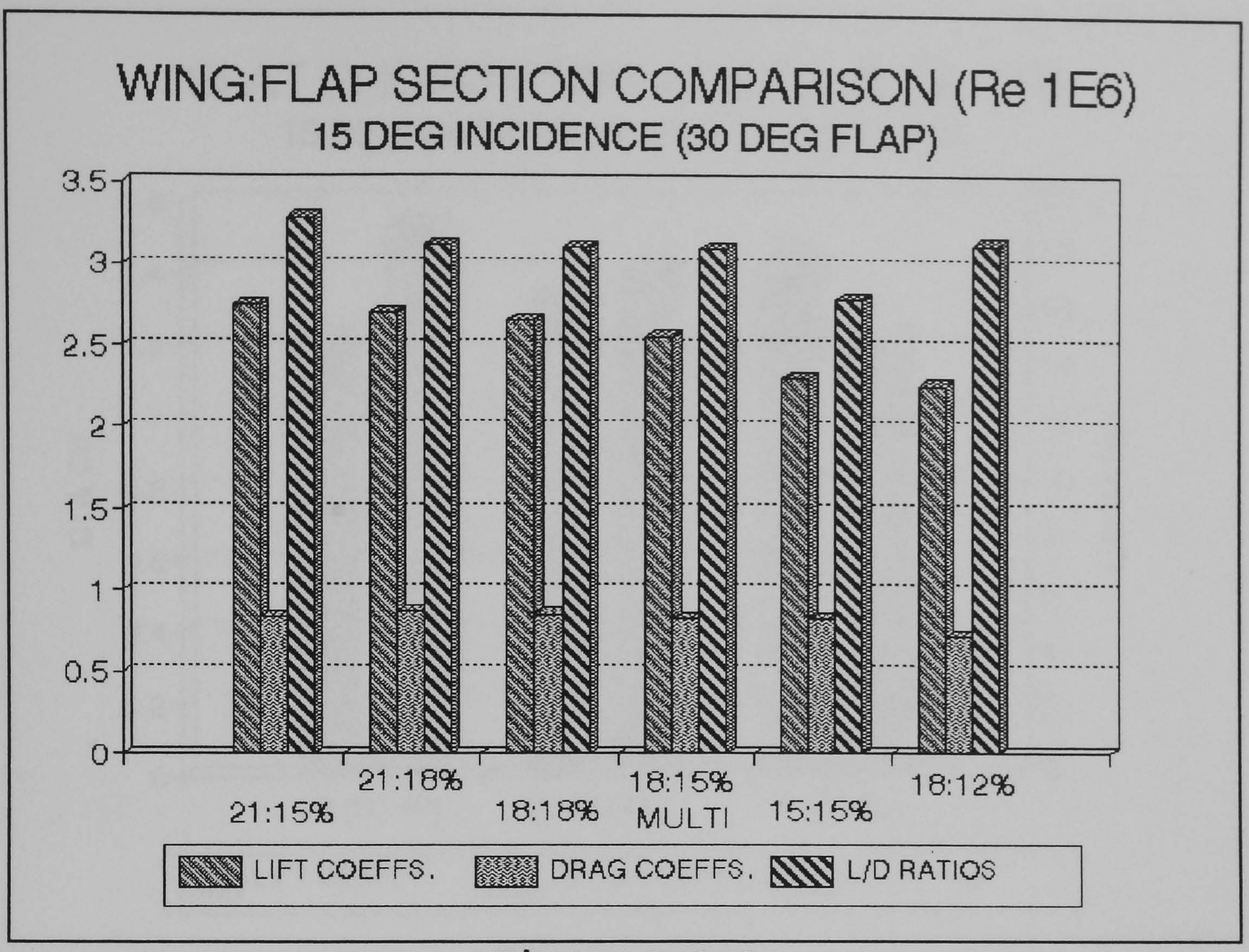

Figure 9:2:6

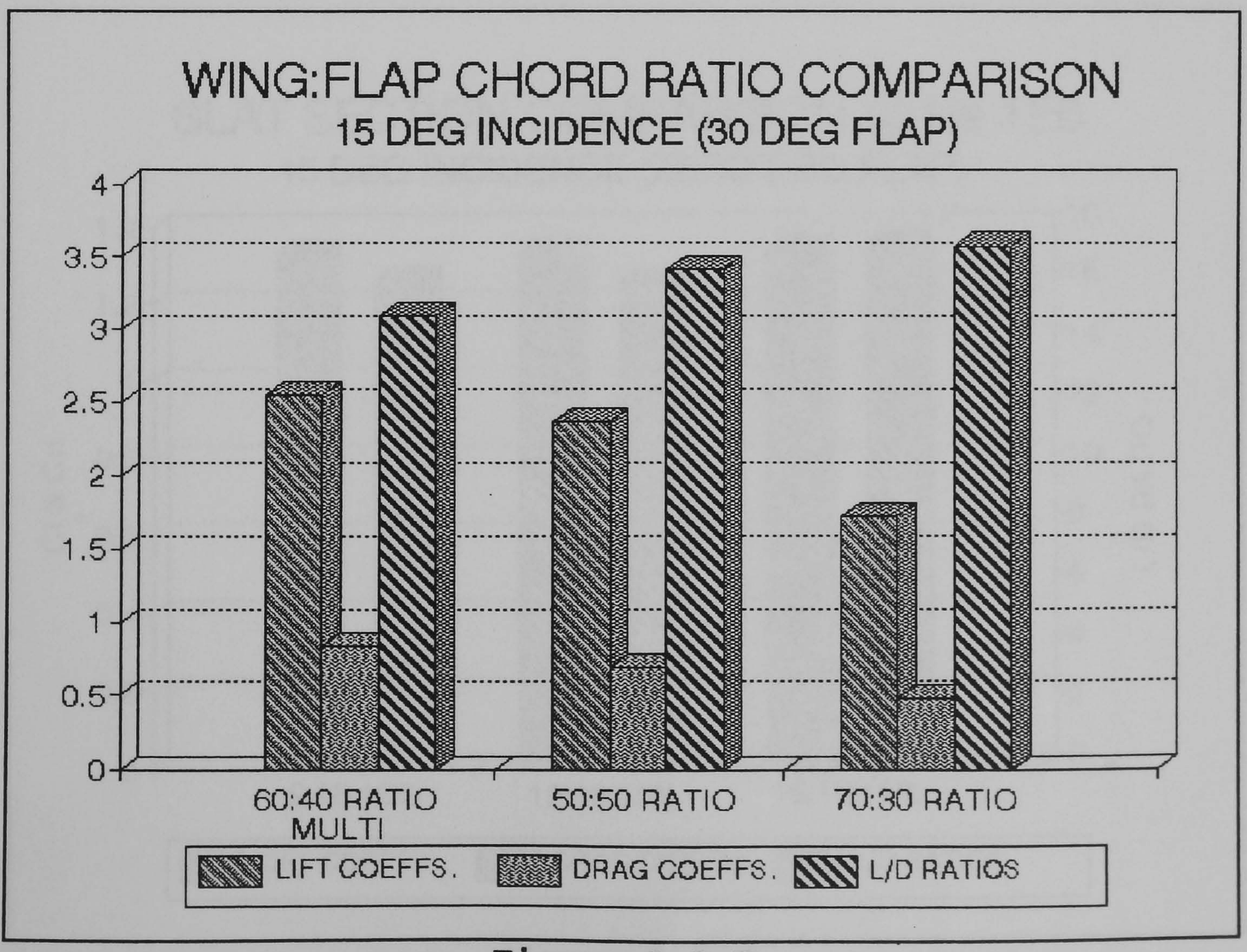

Figure 9:2:7

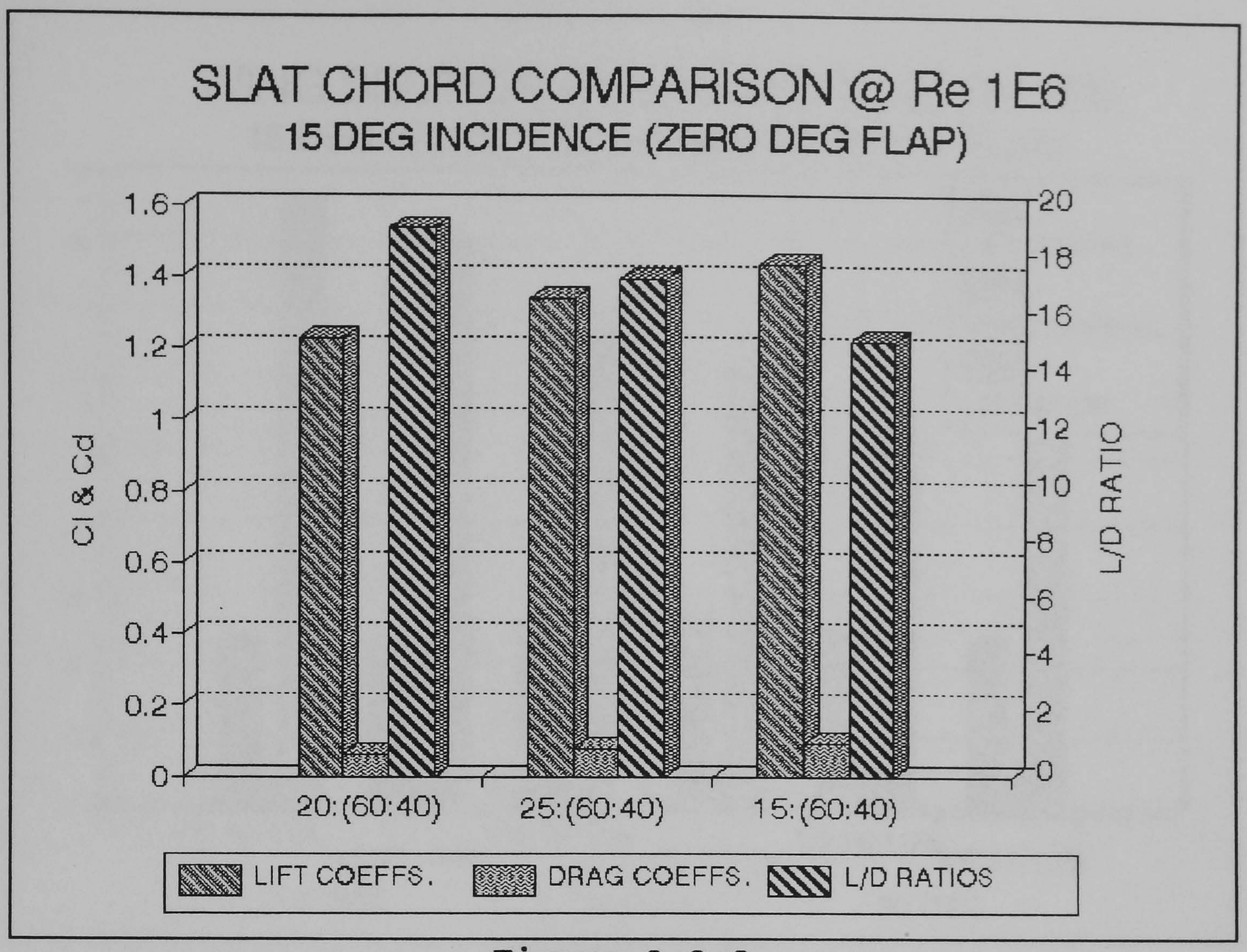

Figure 9:3:8

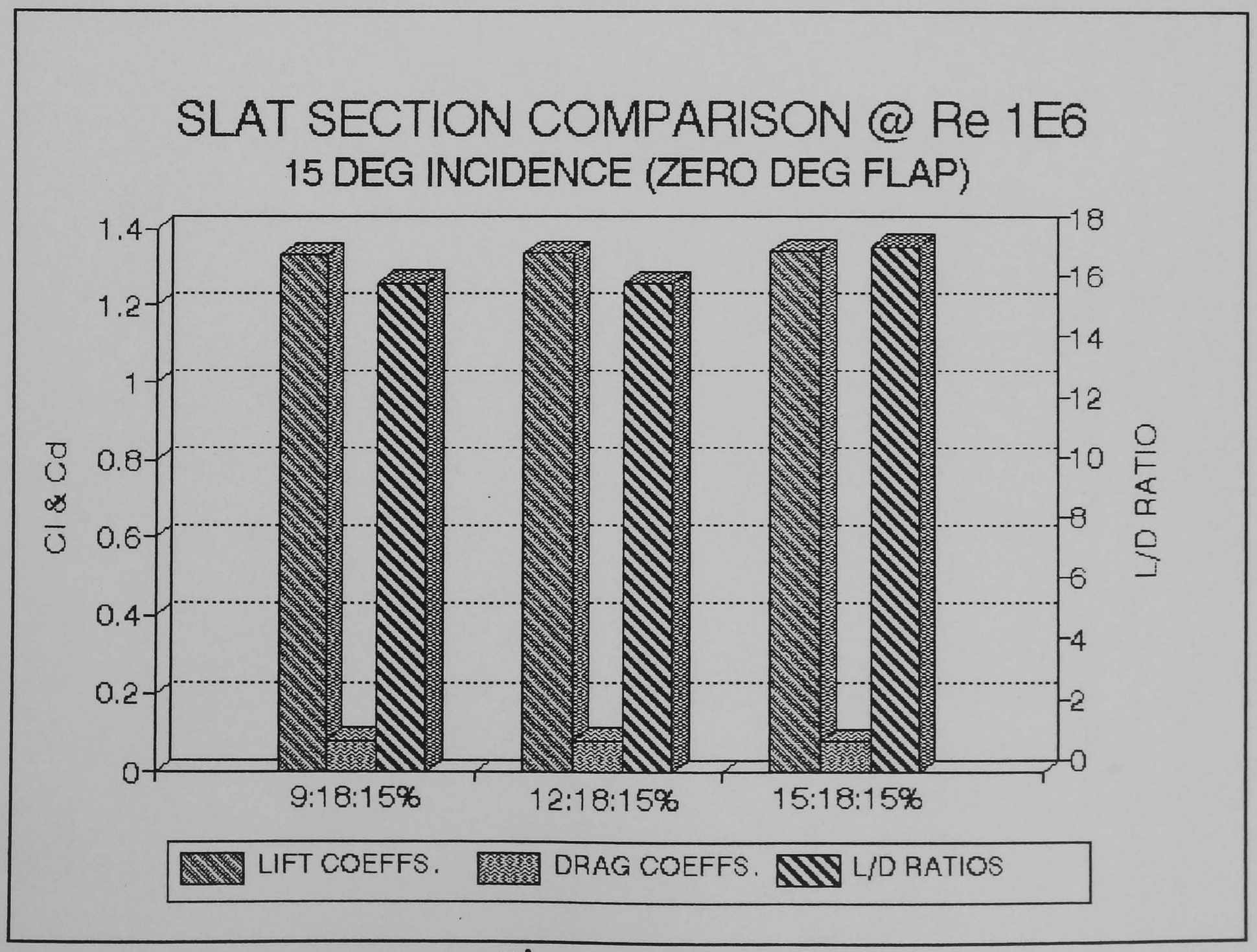

Figure 9:3:9

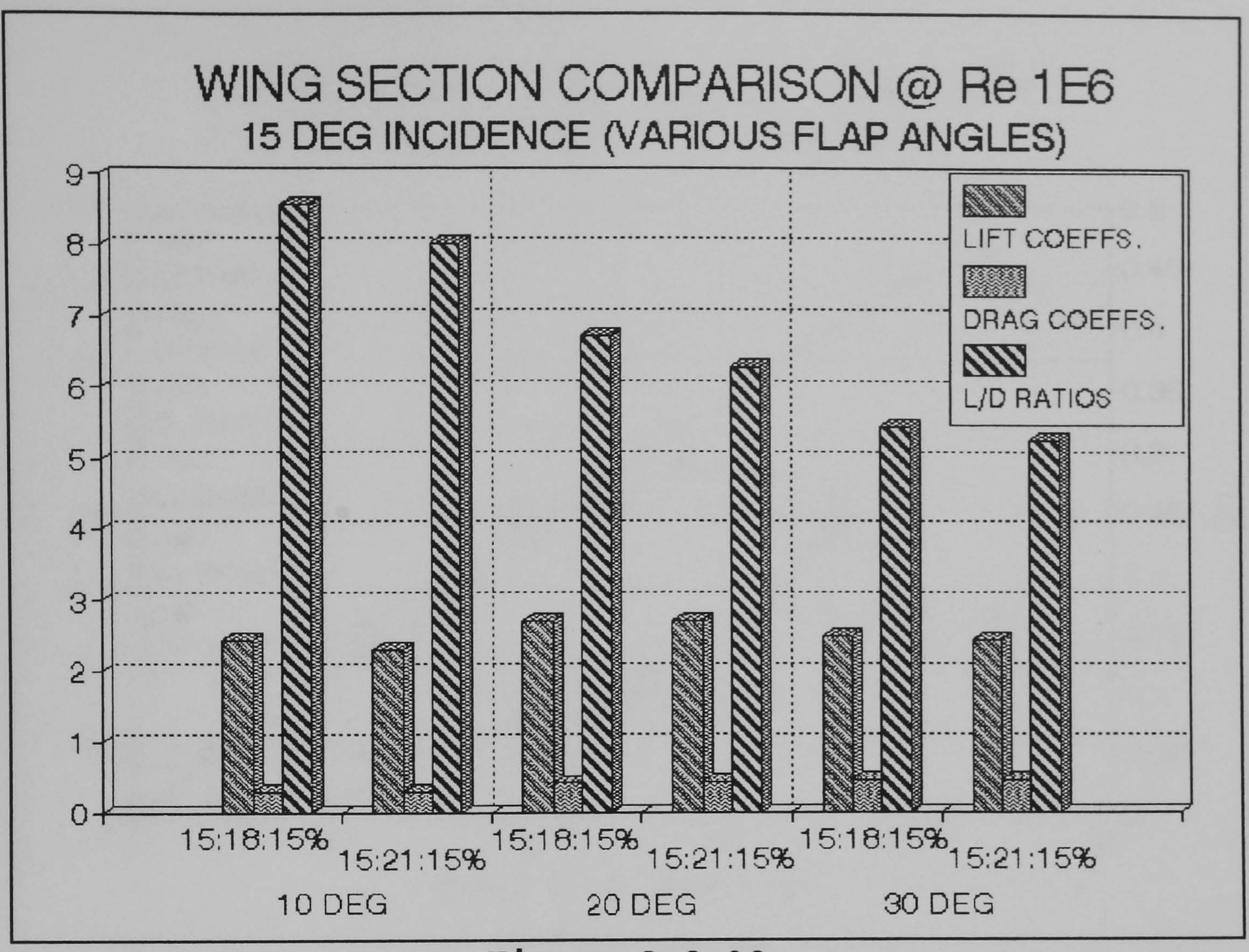
WING SECTION COMPARISON @ Re 1E6
15 DEG INCIDENCE (VARIOUS FLAP ANGLES)
9
8
7
6
5
4
3
2
1
0
LIFT COEFFS.
DRAG COEFFS.
L/D RATIOS
15:18:15%
15:21:15%
15:18:15%
15:21:15%
15:18:15%
15:21:15%
10 DEG
20 DEG
30 DEG

Figure 9:3:10

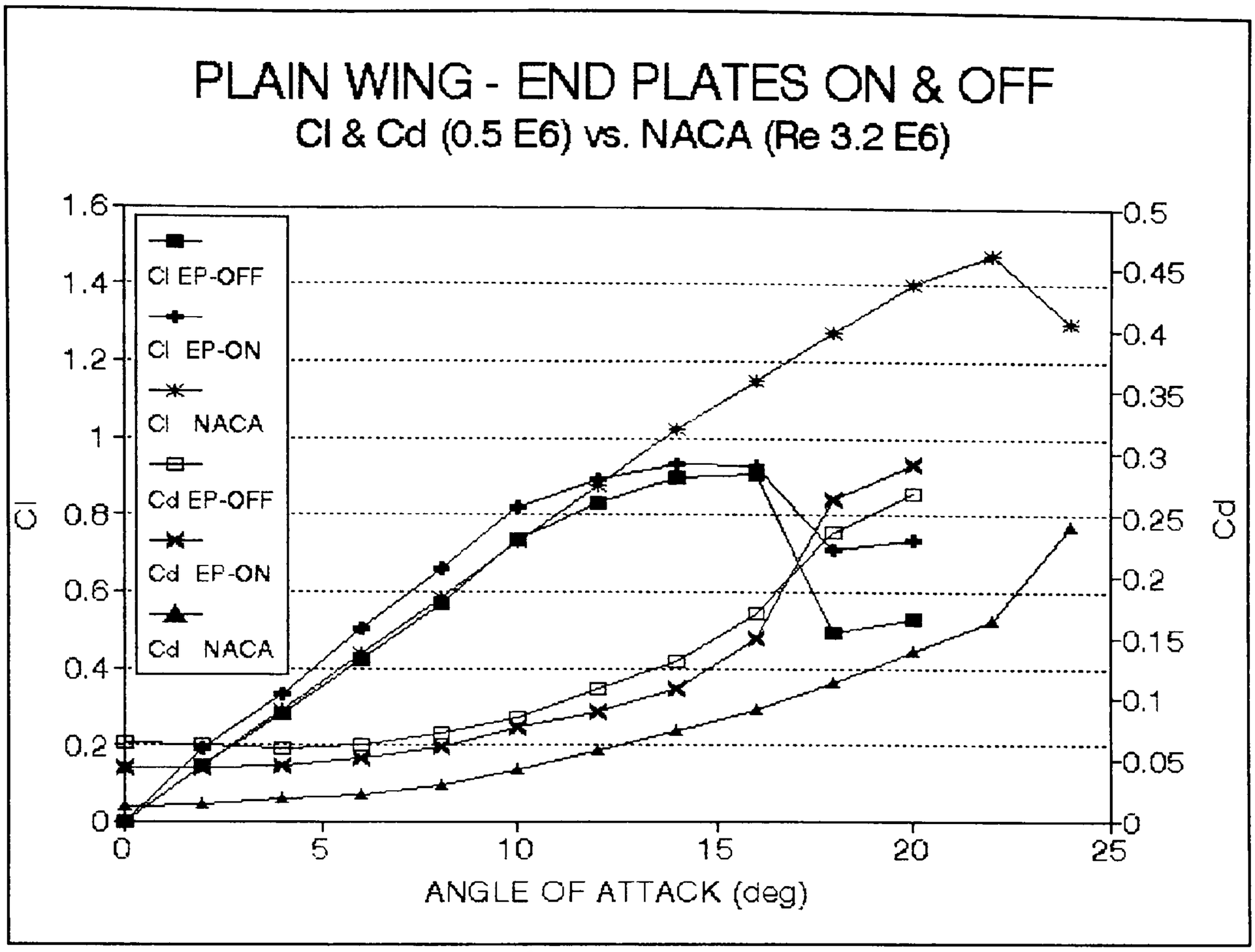

Figure 9:4:1

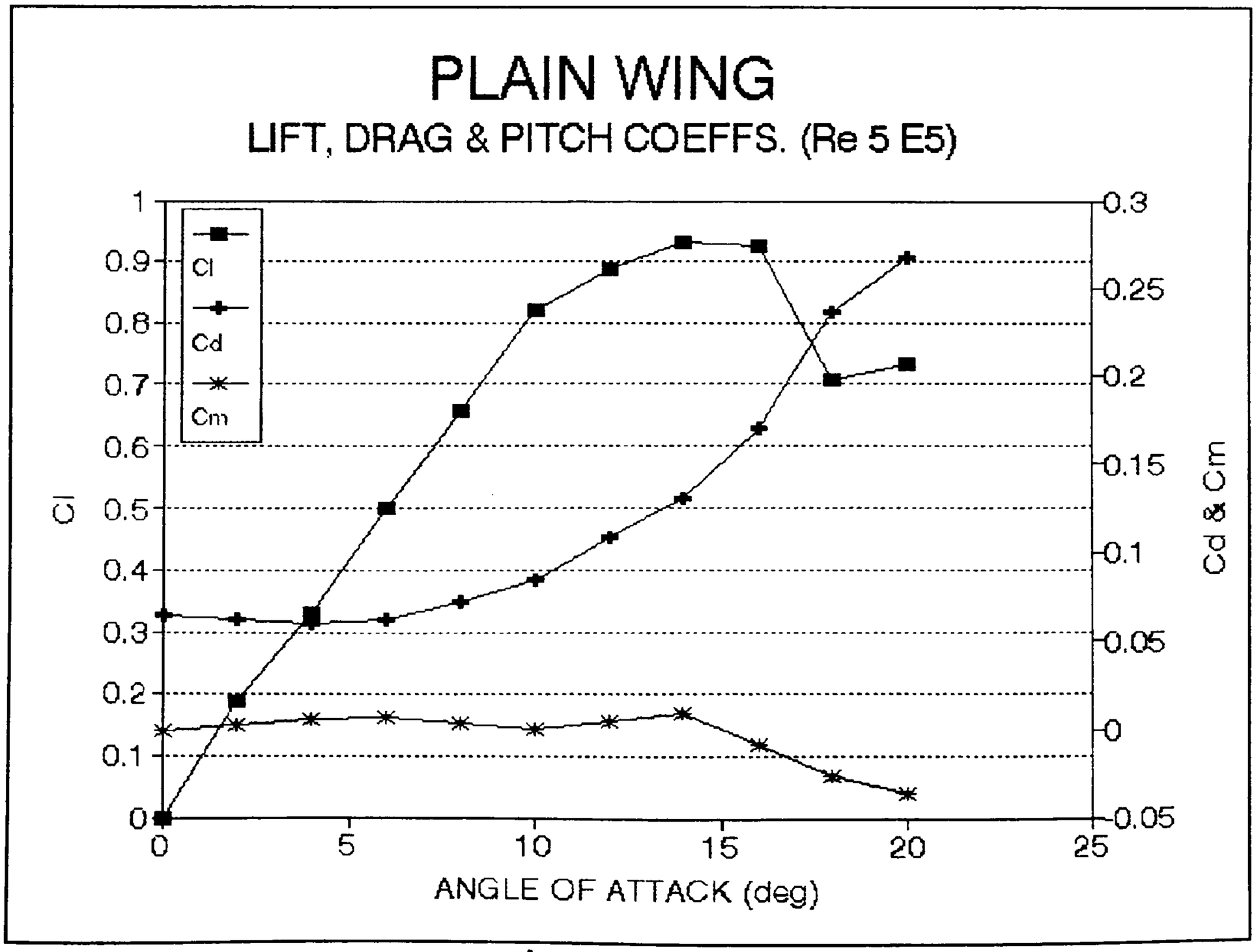

Figure 9:4:2

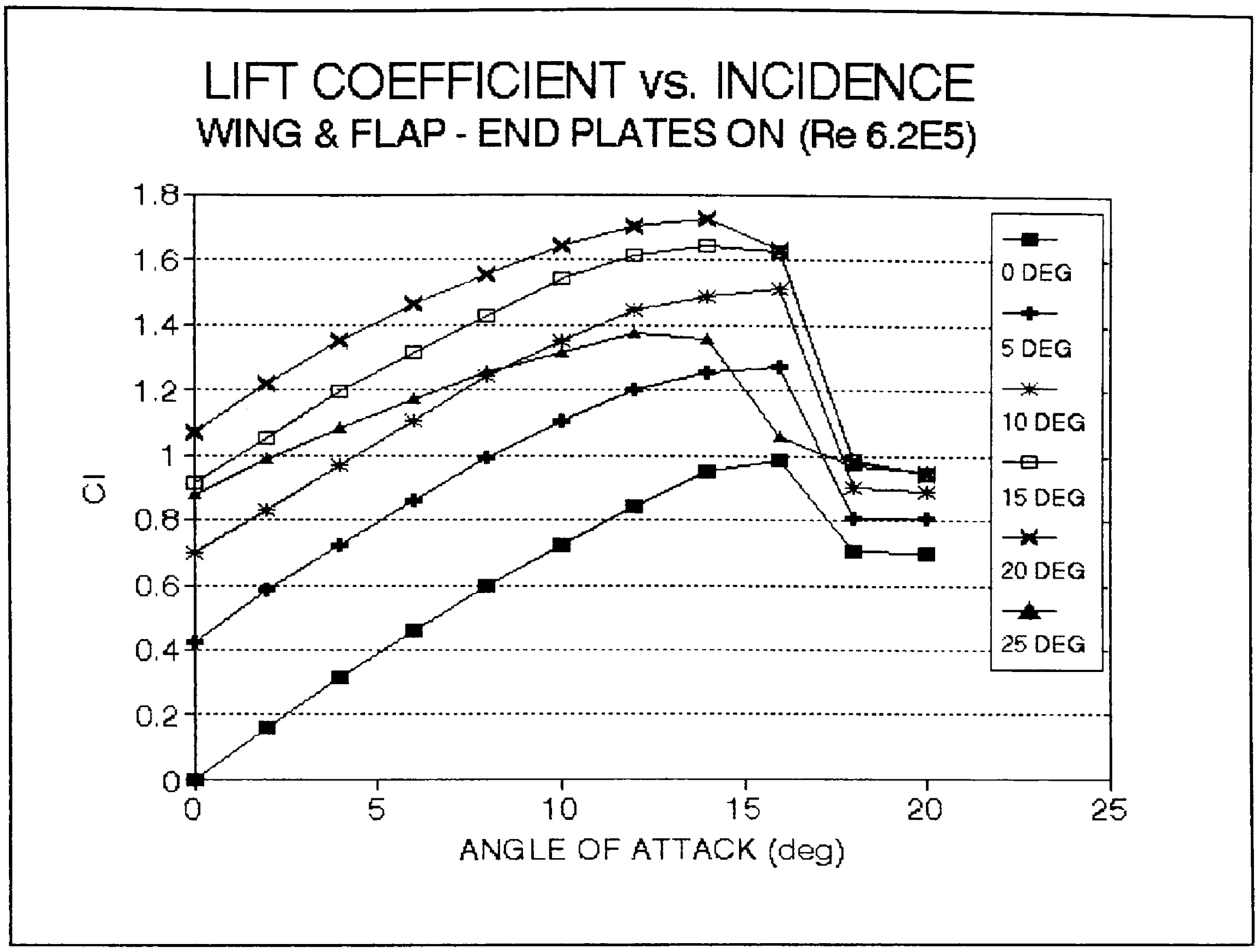

Figure 9:4:3a

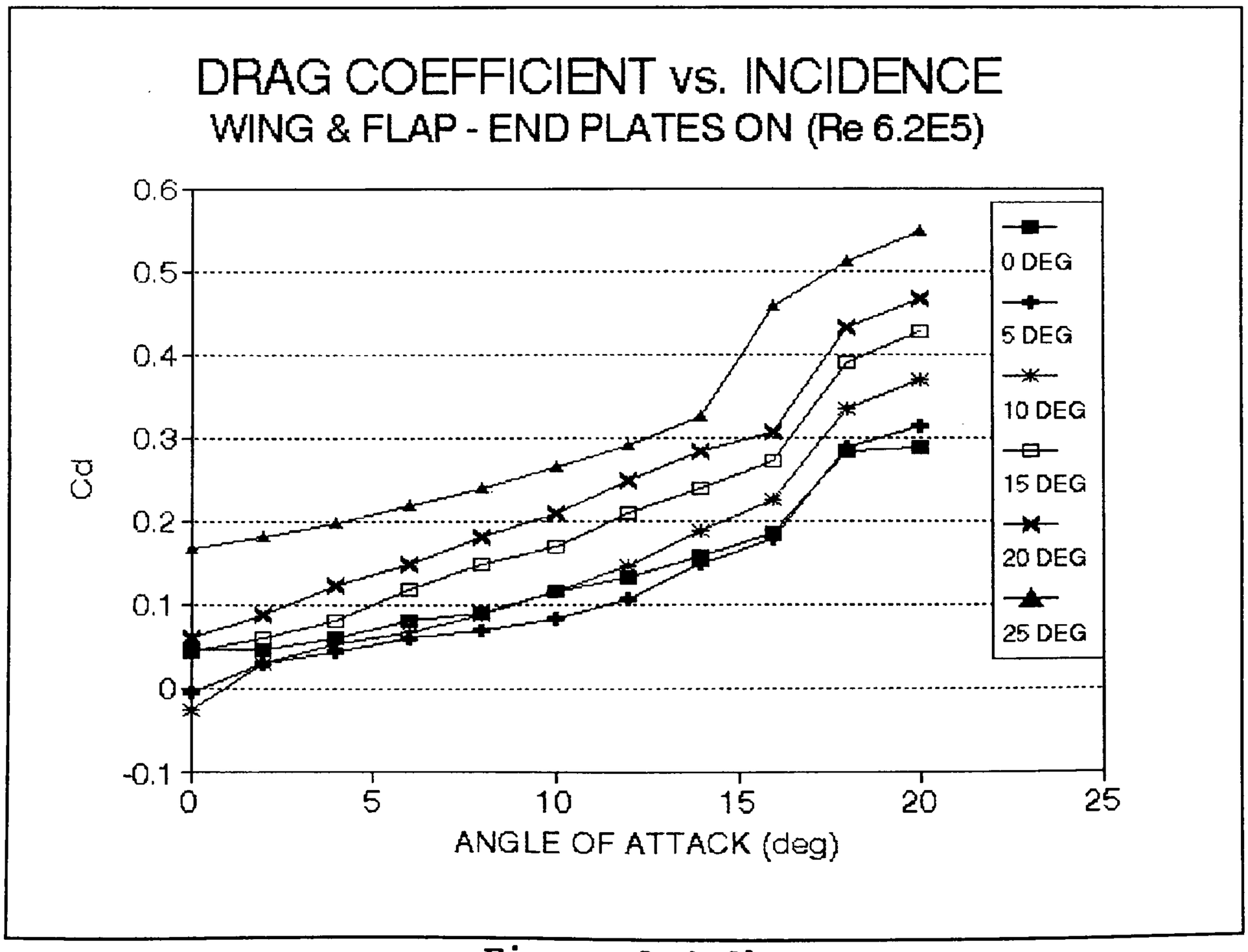

Figure 9:4:3b

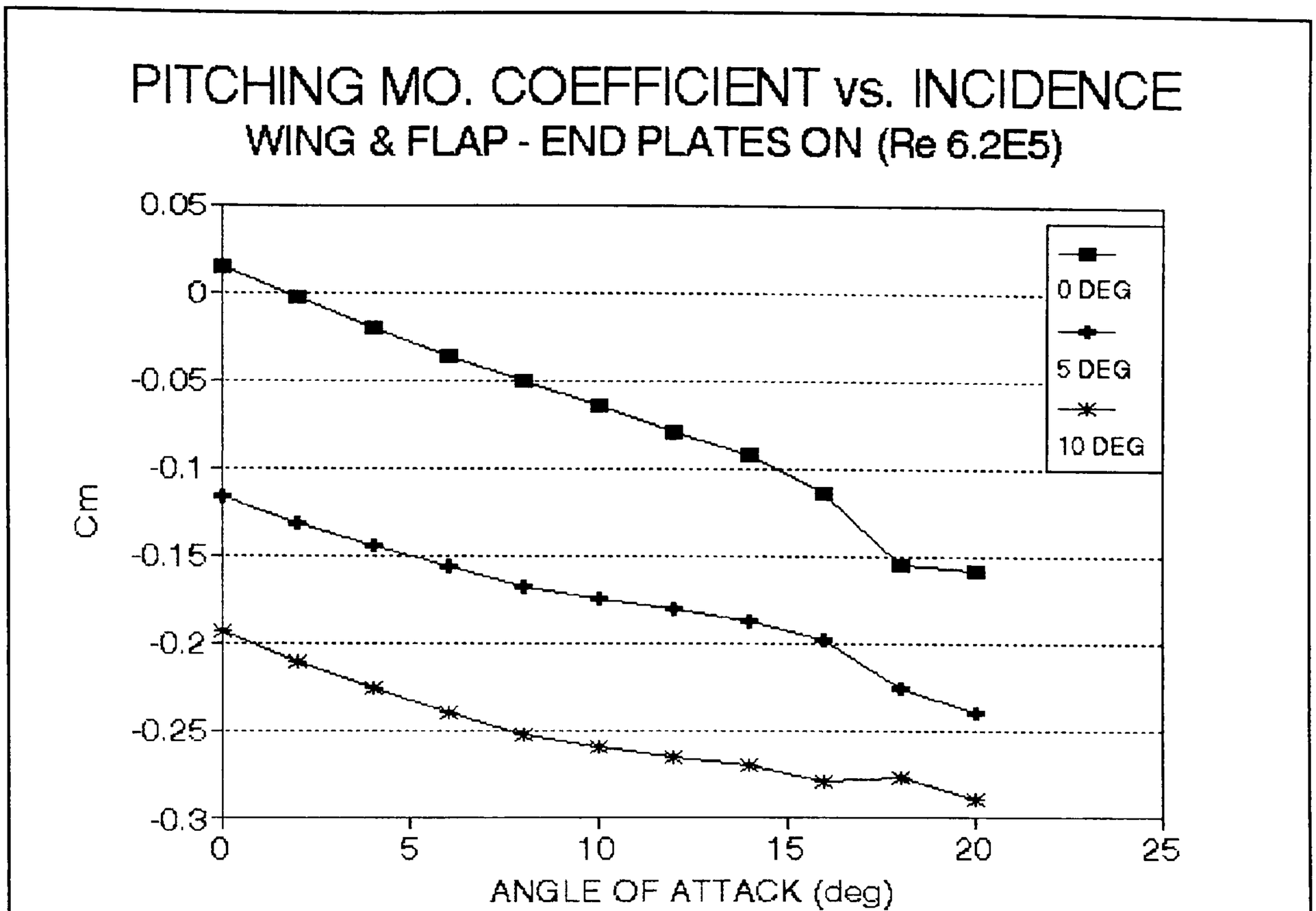

Figure 9:4:3c

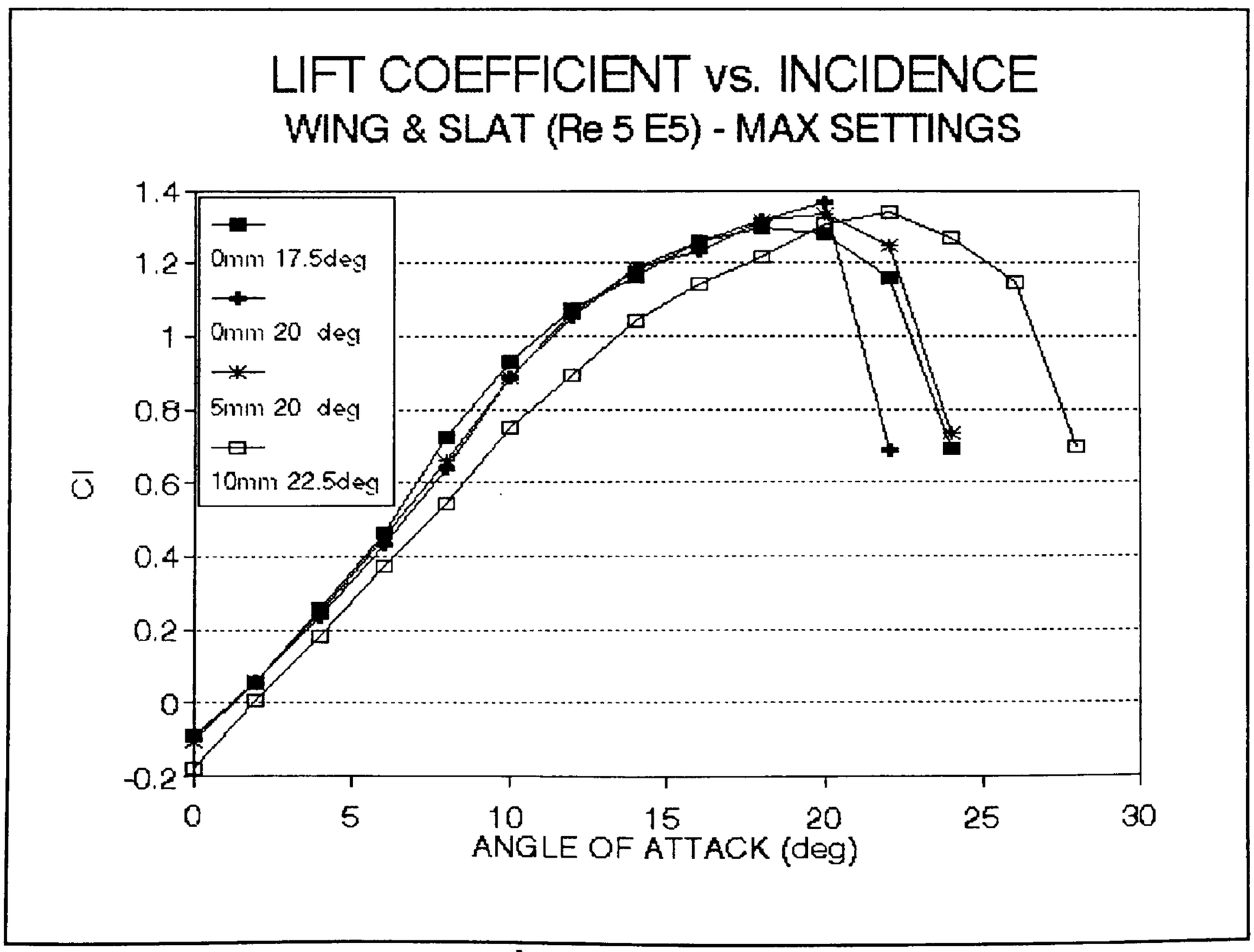

Figure 9:4:4a

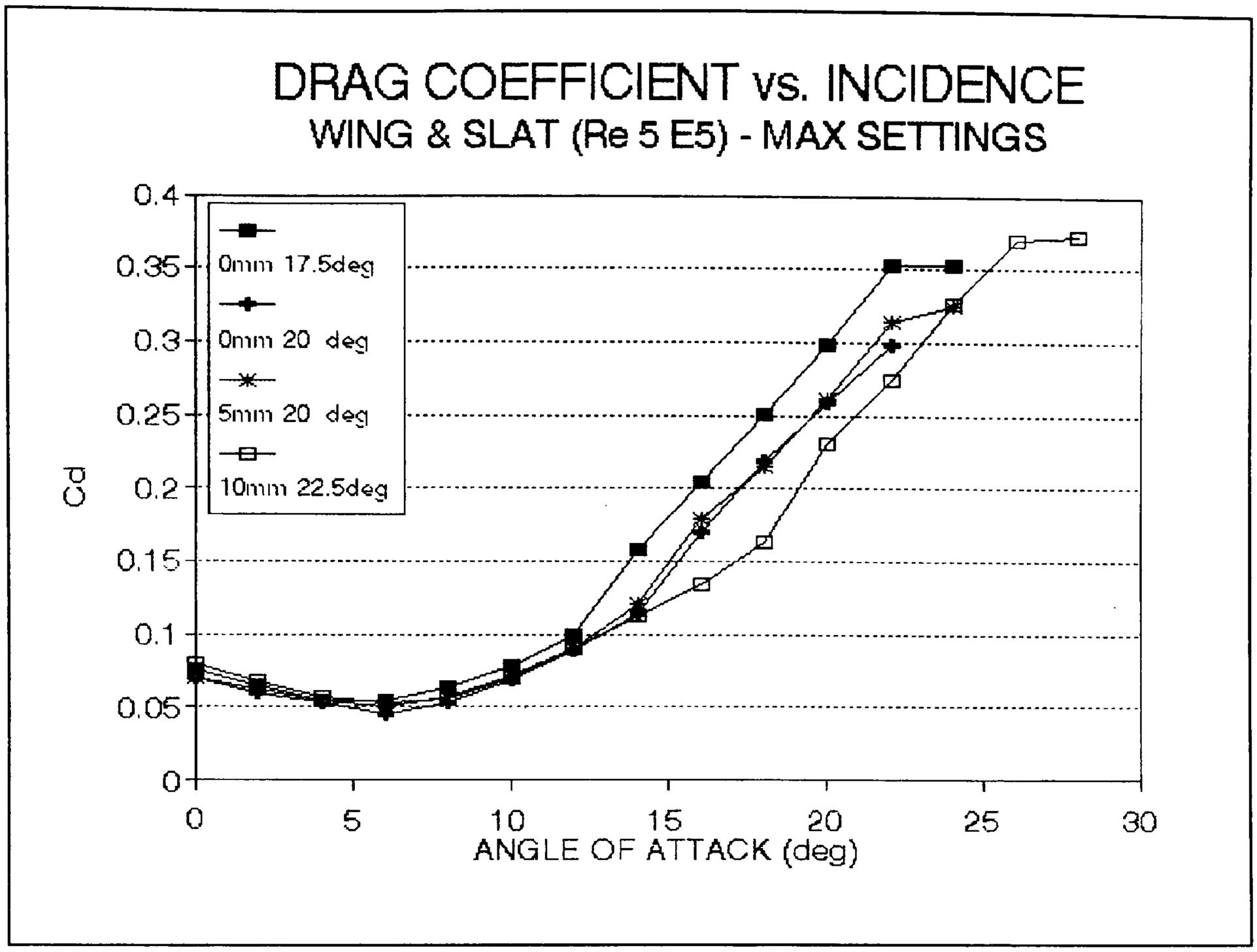

Figure 9:4:4b

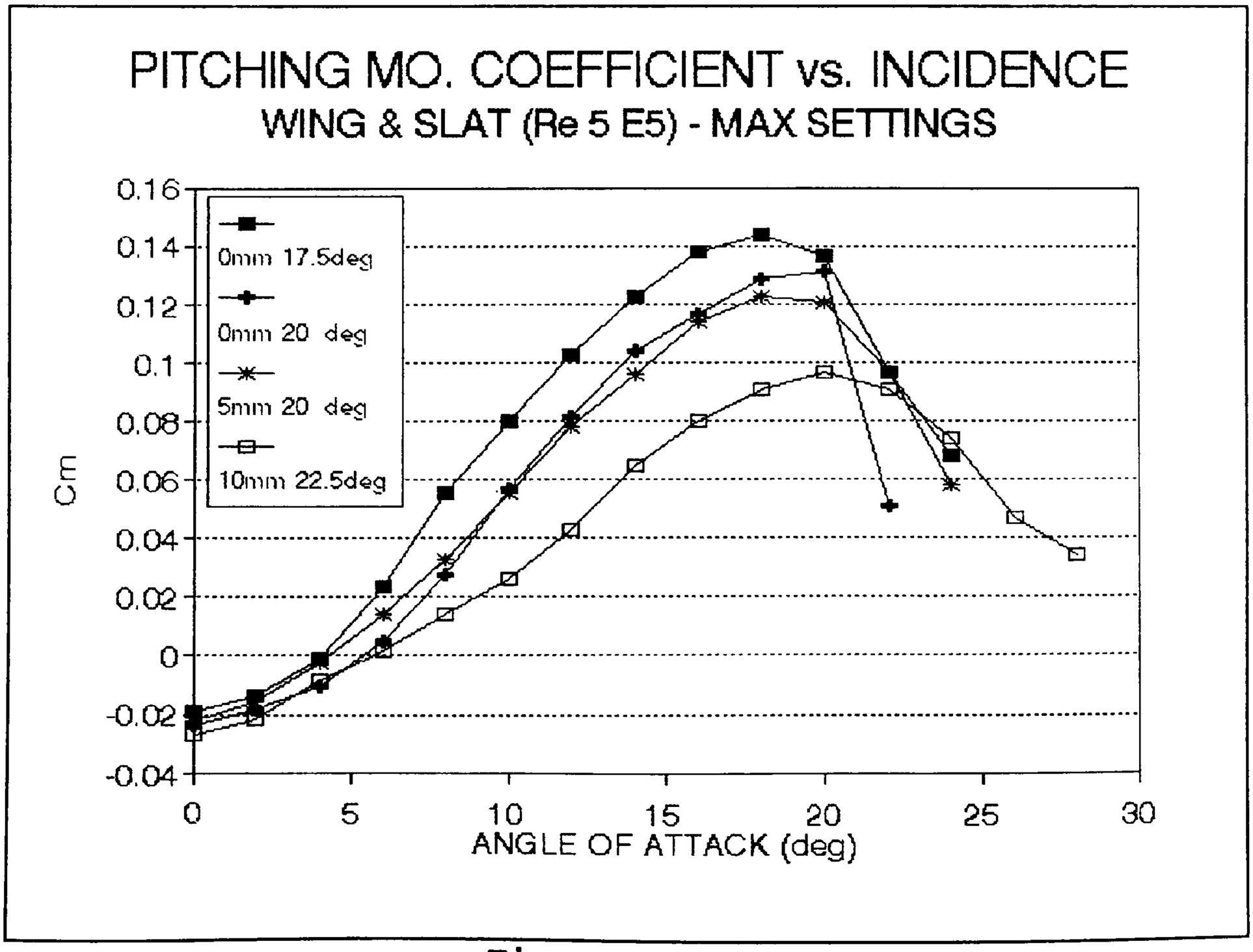

Figure 9:4:4c

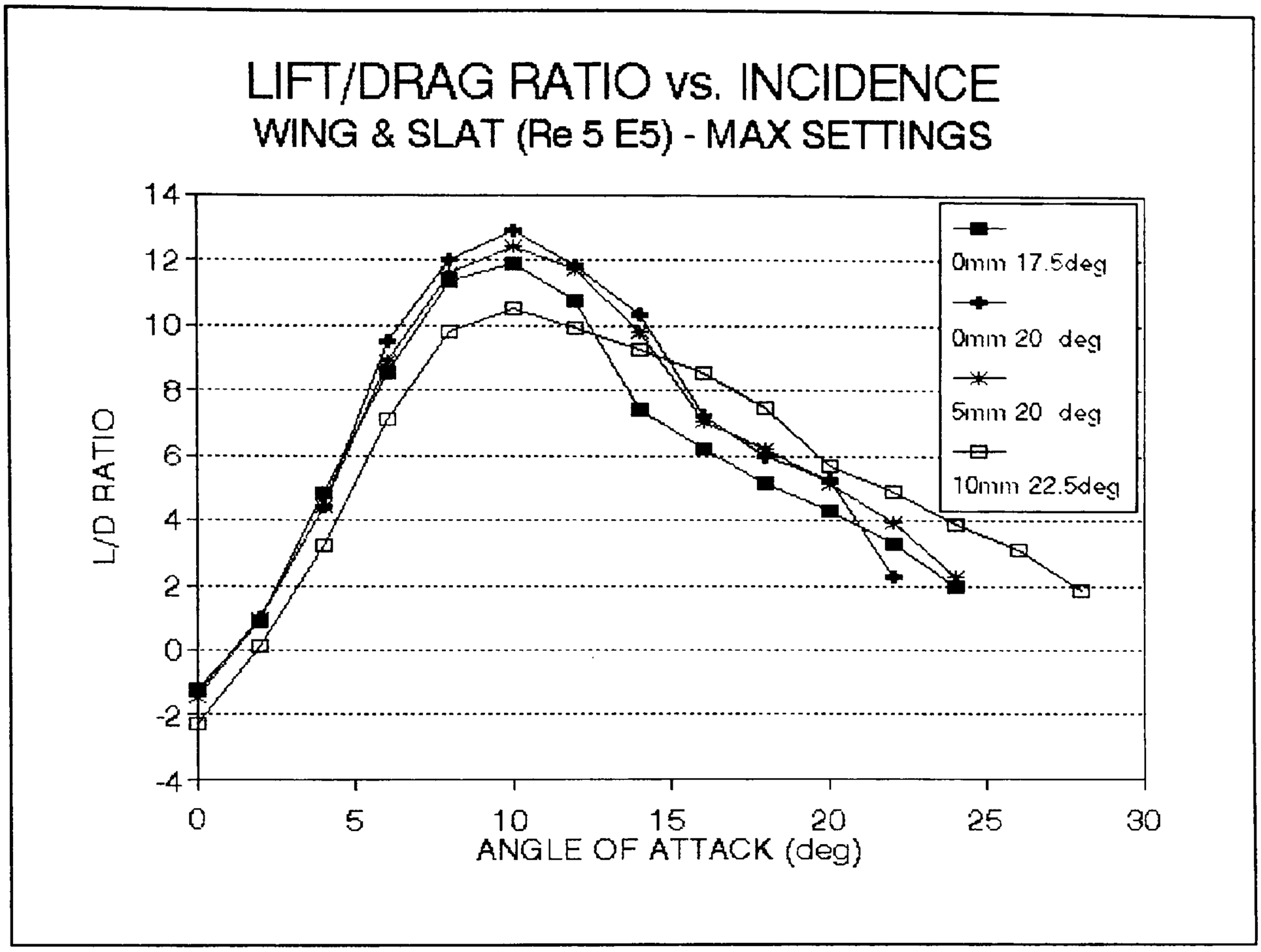
LIFT/DRAG RATIO vs. INCIDENCE
WING & SLAT (Re 5 E5) - MAX SETTINGS
L/D RATIO
ANGLE OF ATTACK (deg)
14
12
10
8
6
4
2
0
-2
-4
0
5
10
15
20
25
30
0mm 17.5deg
0mm 20 deg
5mm 20 deg
10mm 22.5deg

Figure 9:4:4d

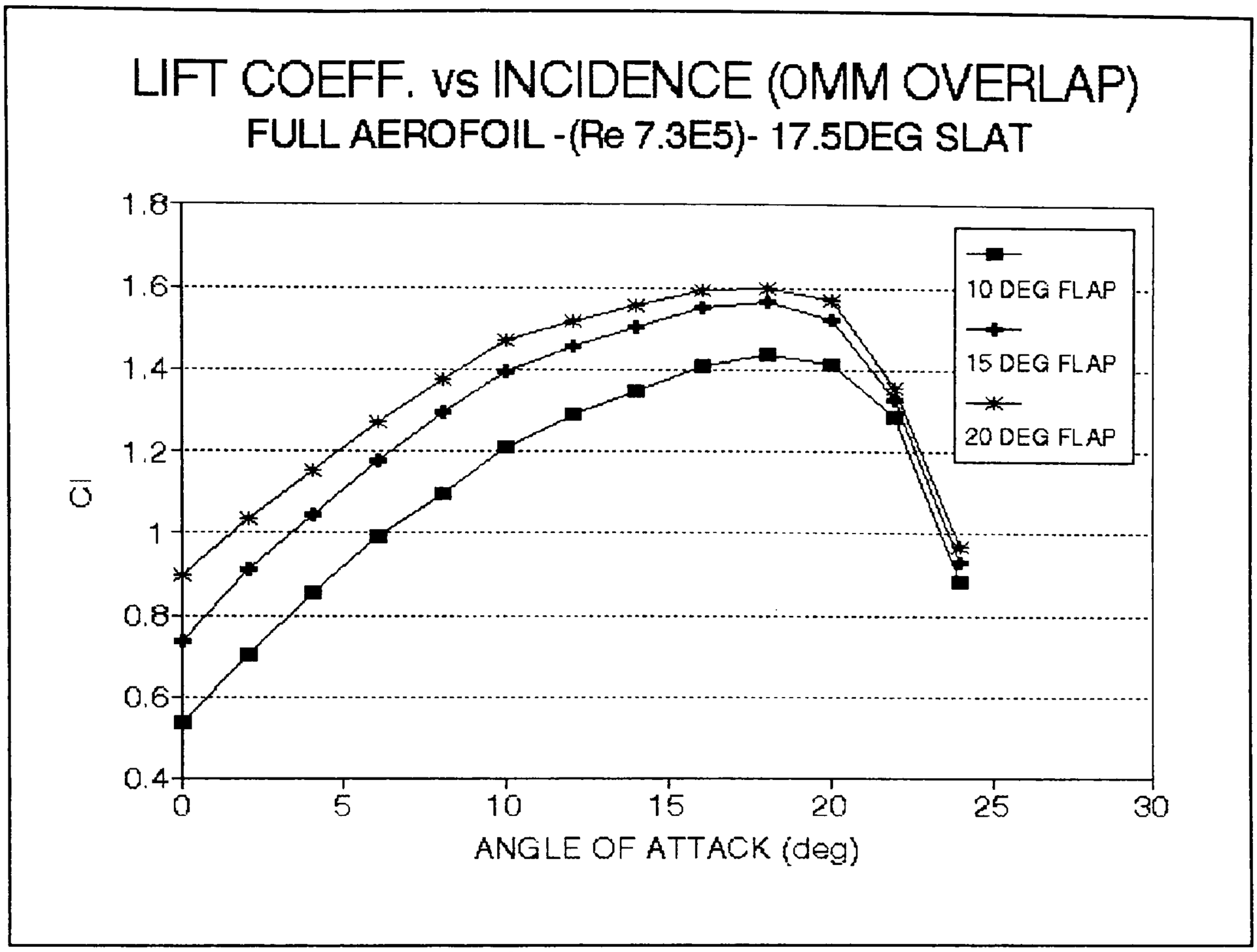

Figure 9:5a:5a

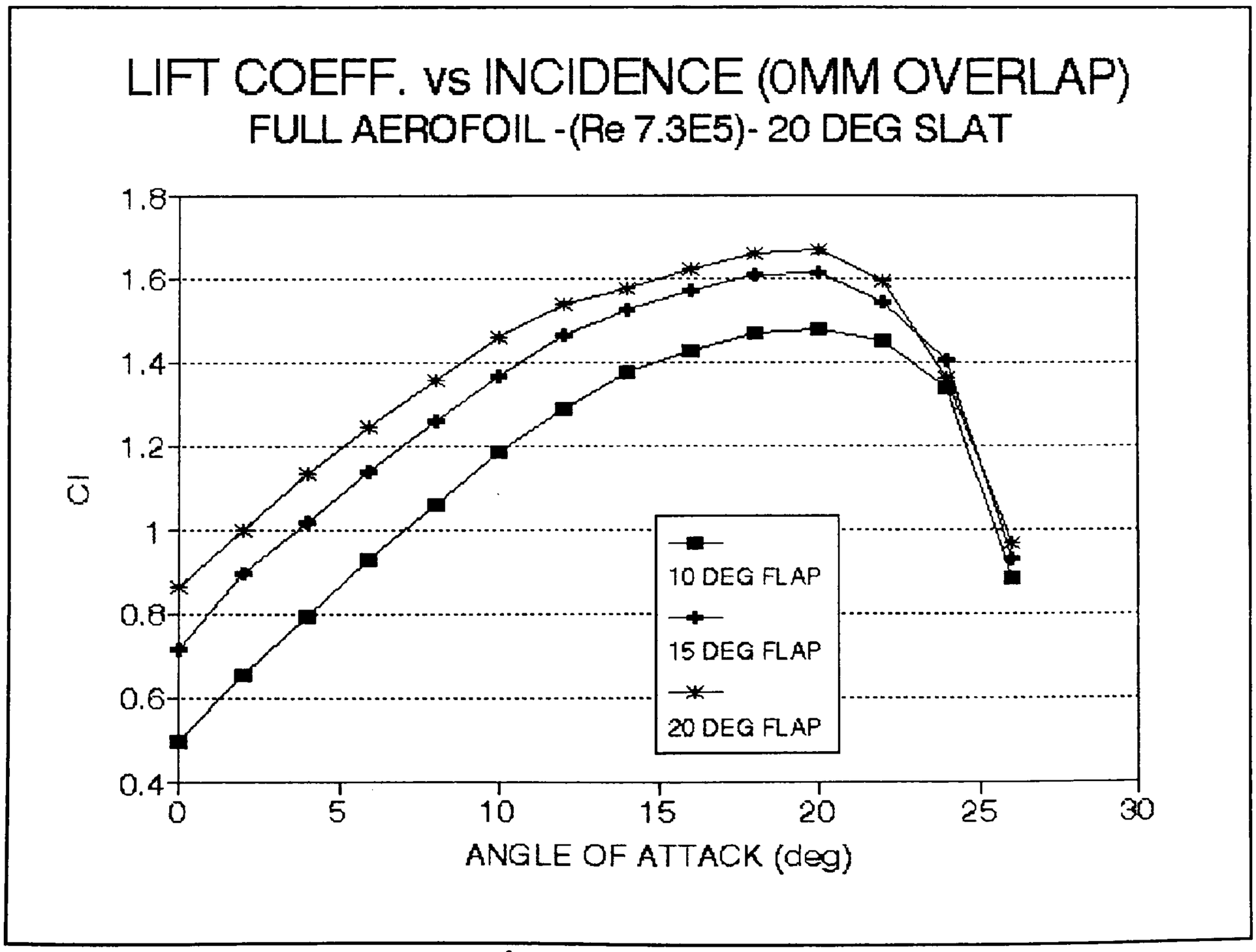

Figure 9:5a:5b

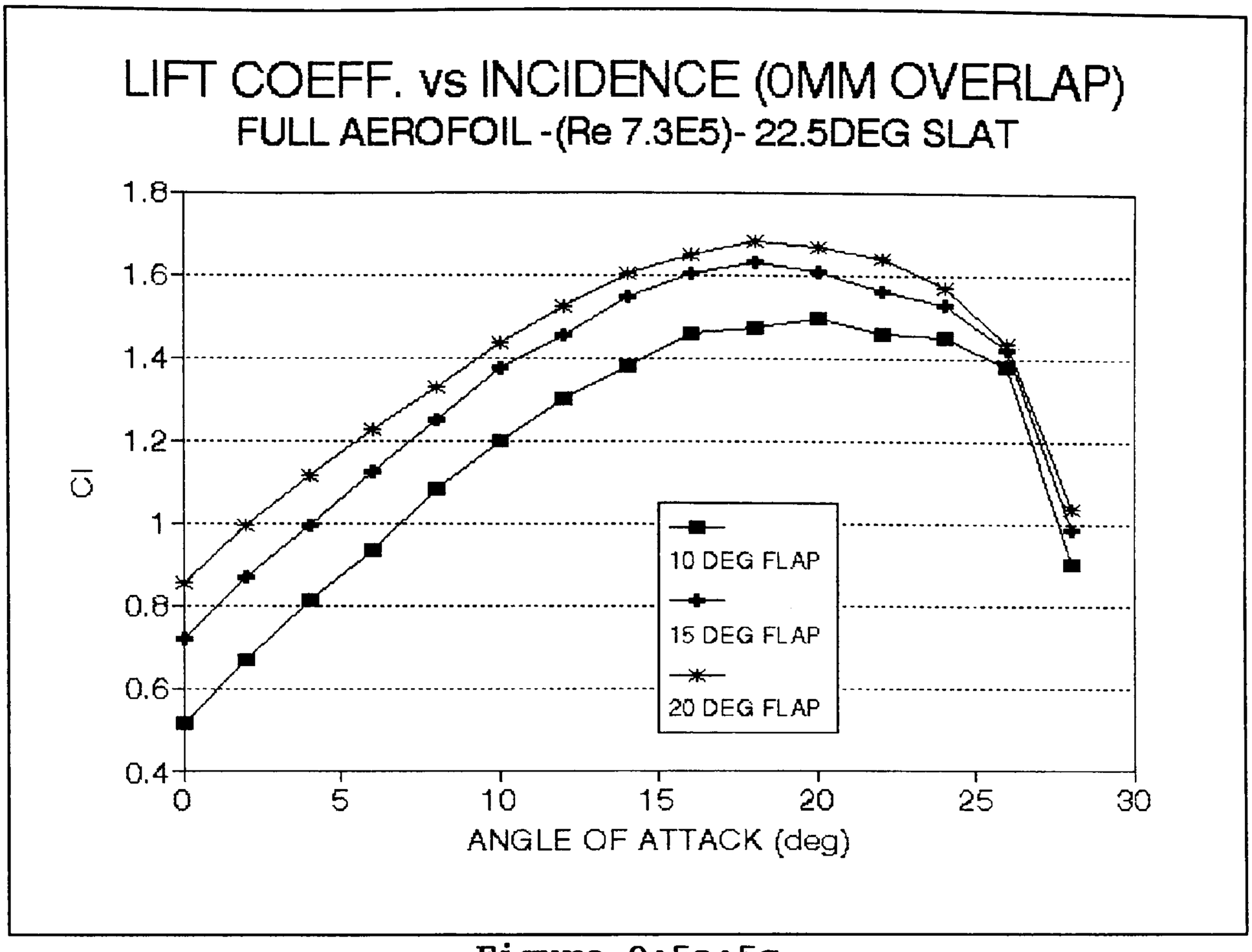

Figure 9:5a:5c

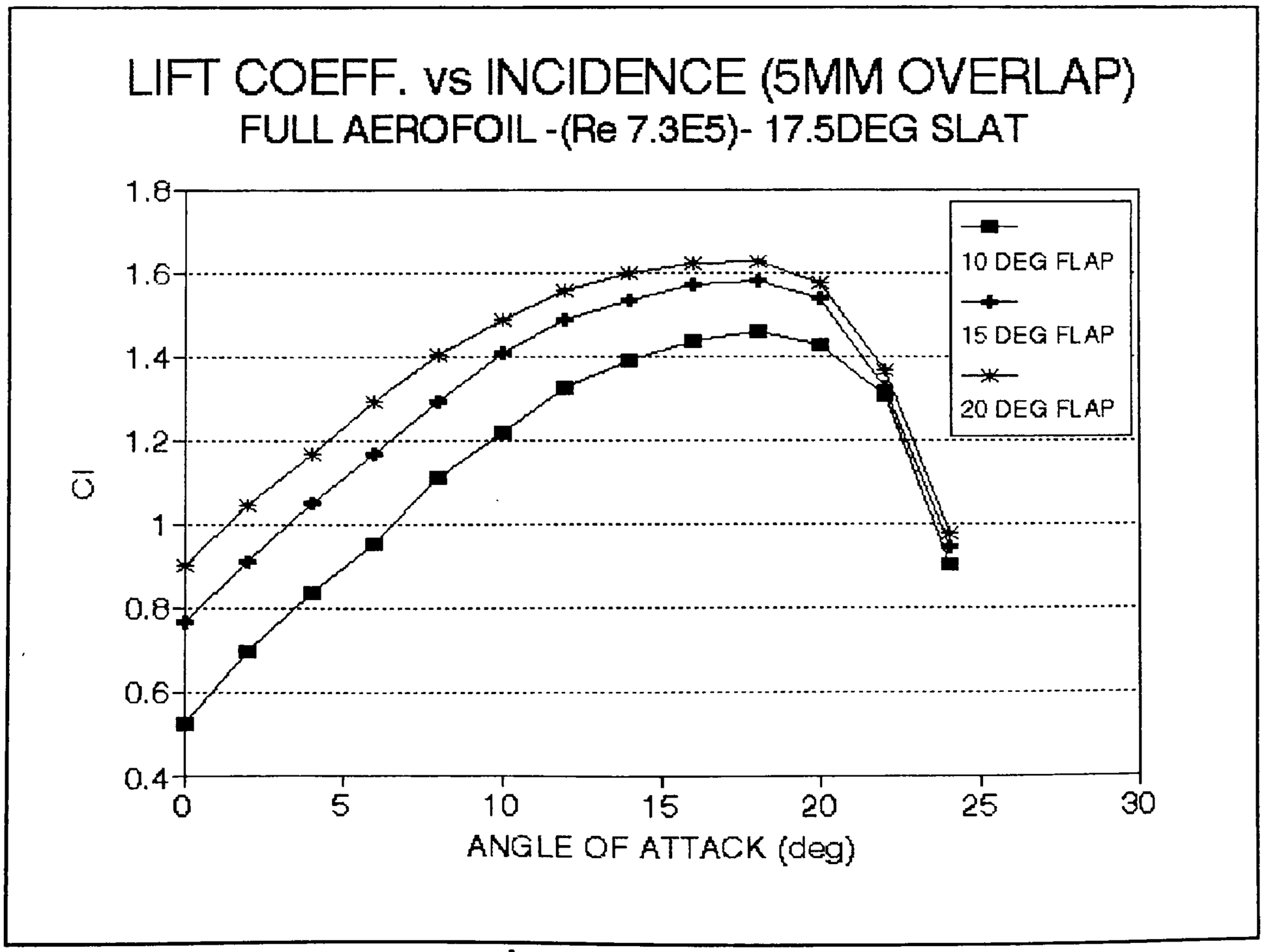

Figure 9:5a:5d

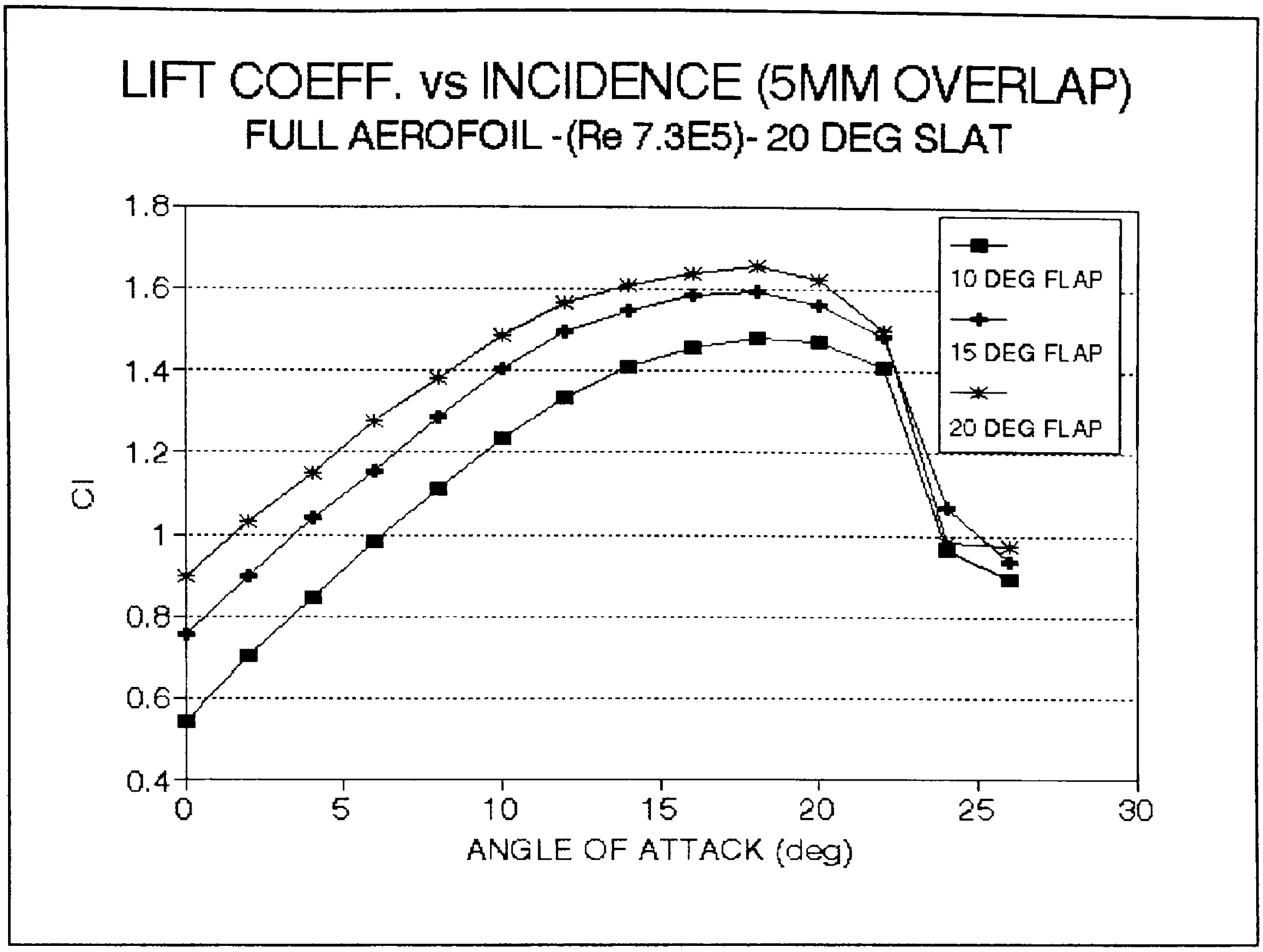

Figure 9:5a:5e

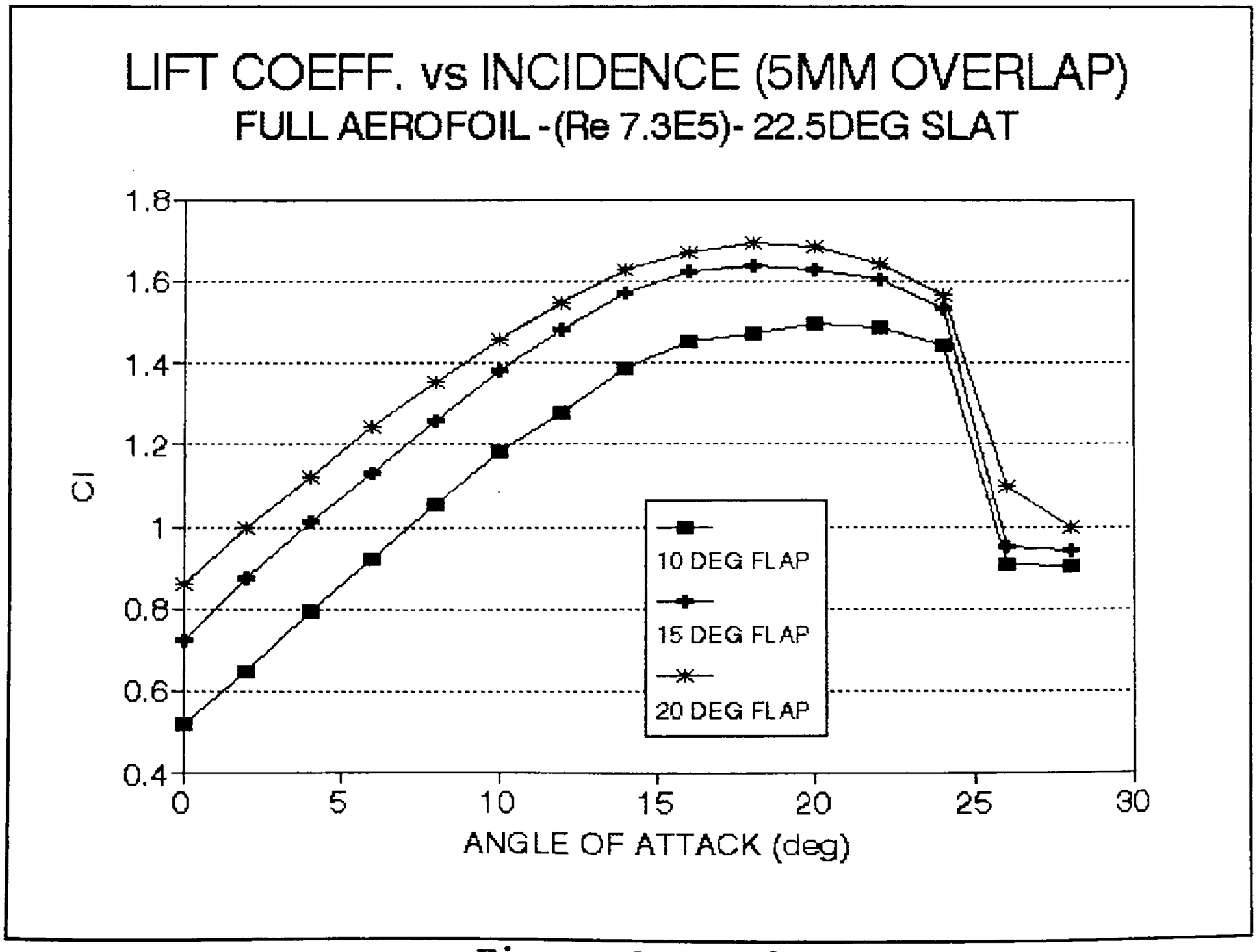

Figure 9:5a:5f

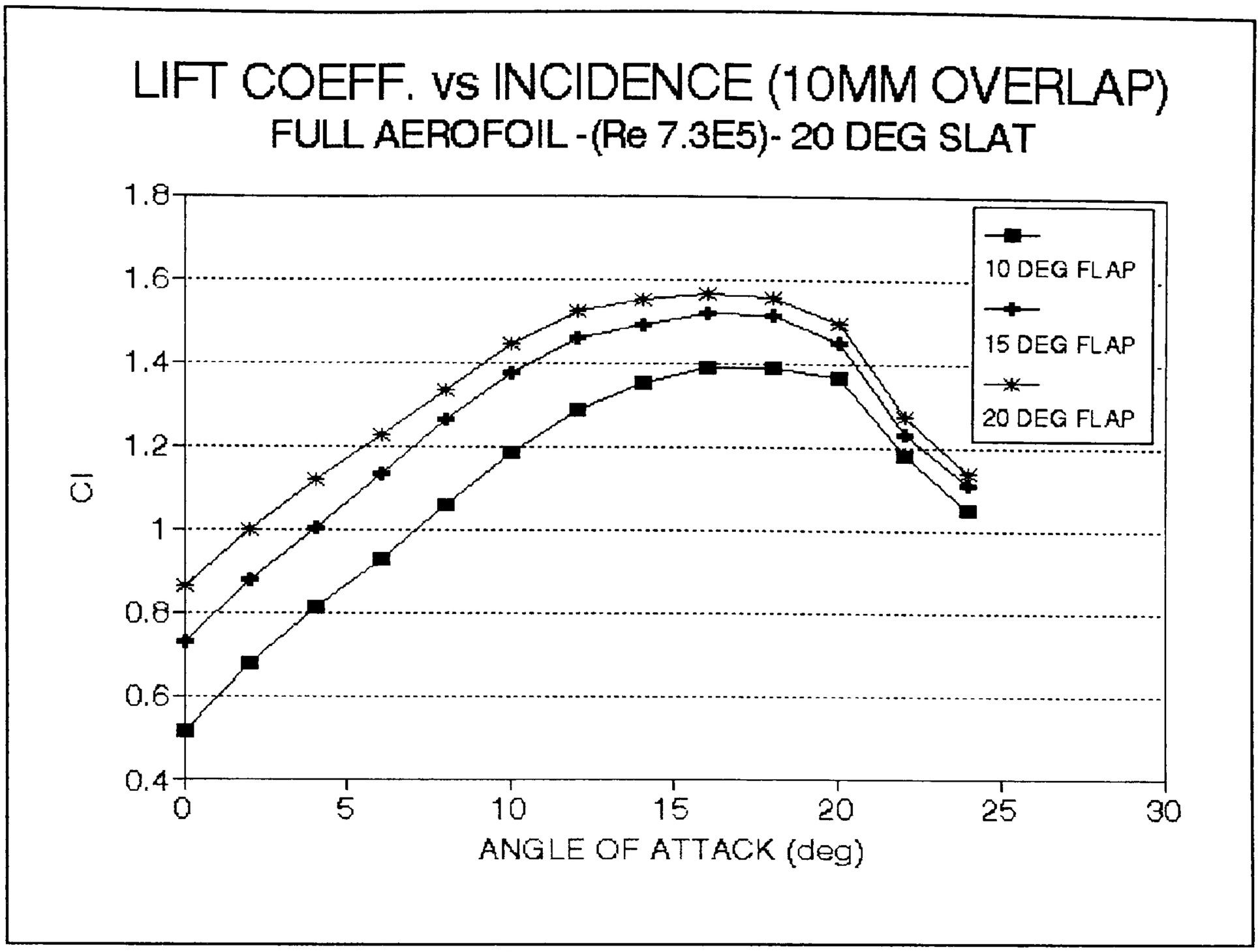

Figure 9:5a:5g

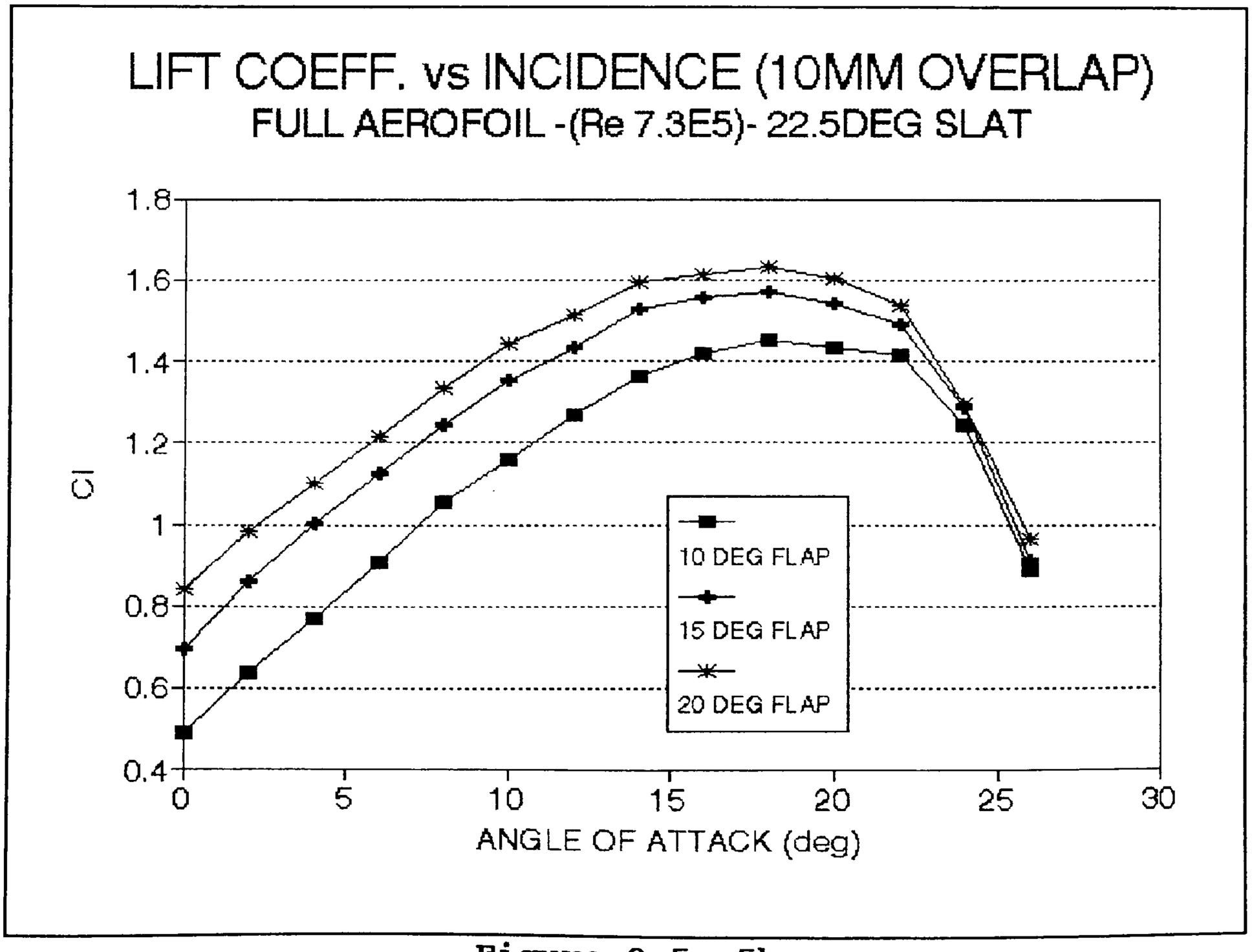

Figure 9:5a:5h

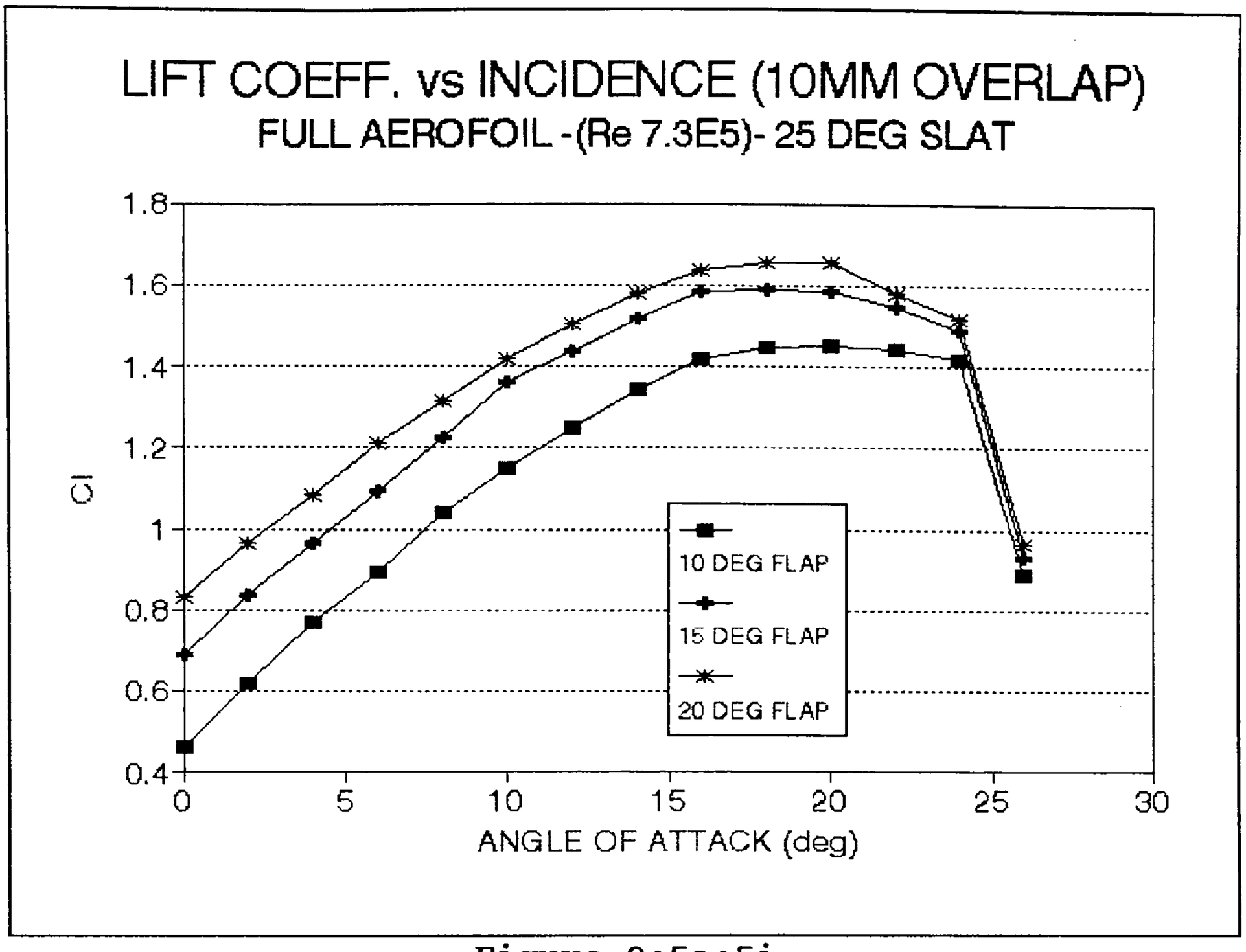

Figure 9:5a:5i

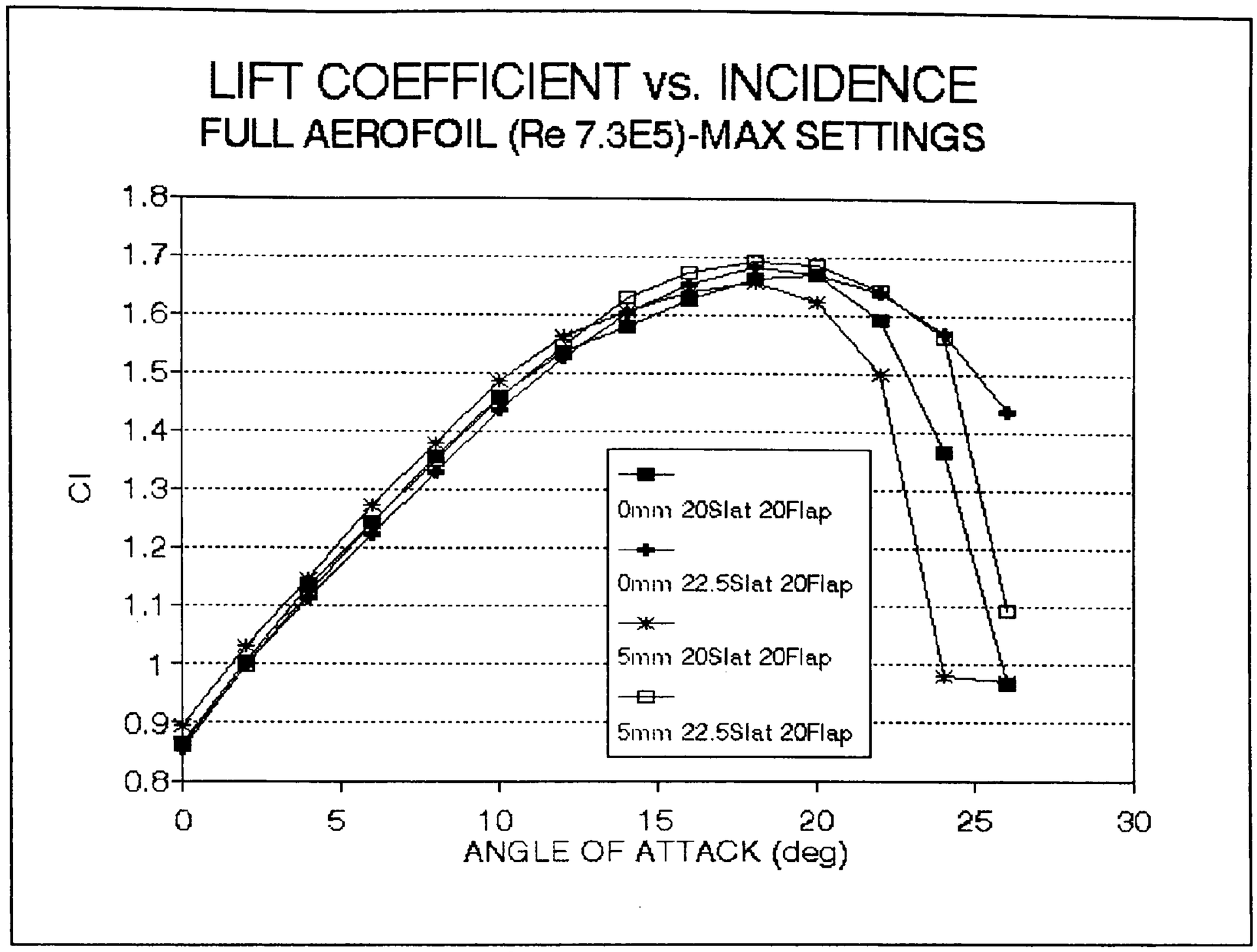

Figure 9:5b:6a

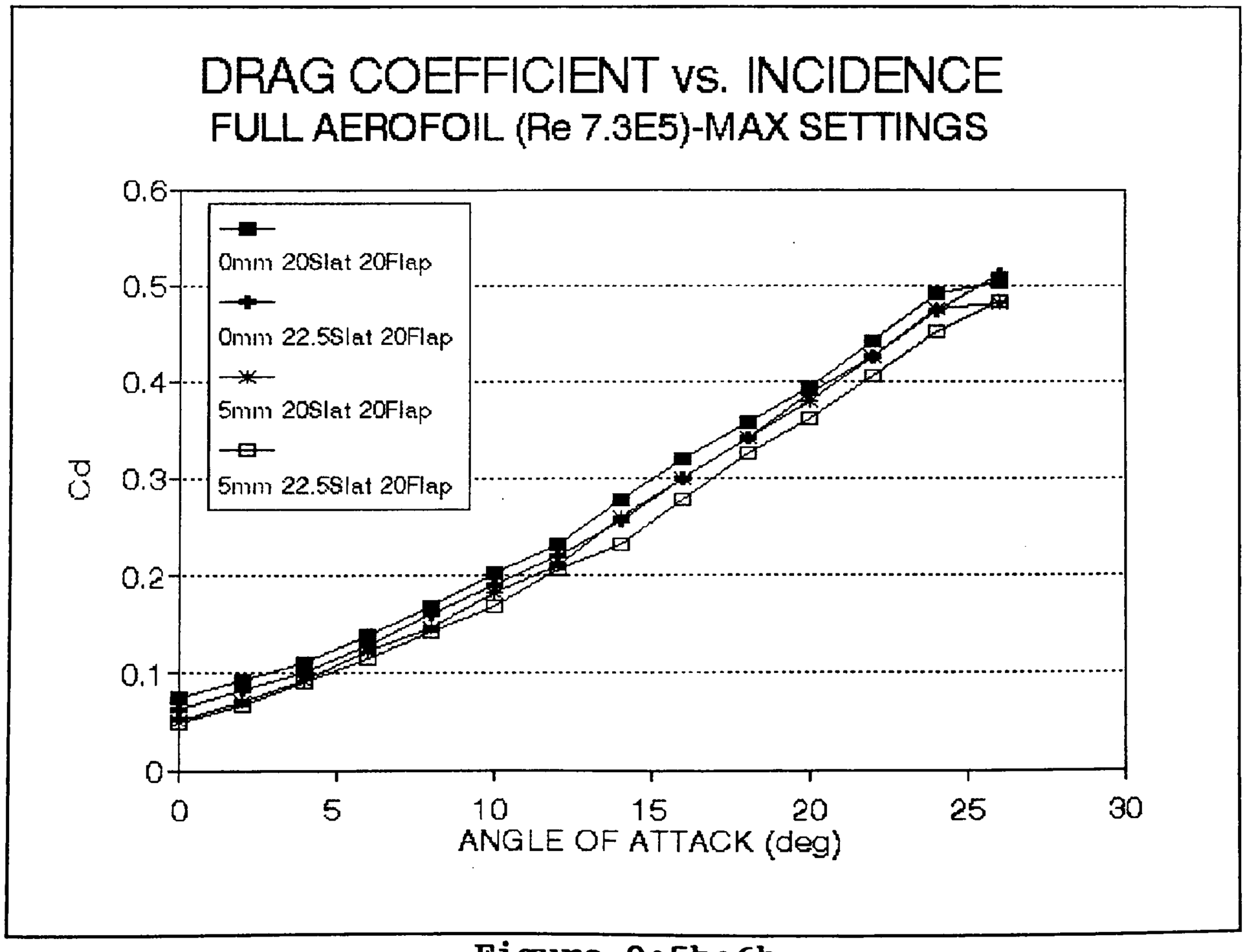

Figure 9:5b:6b

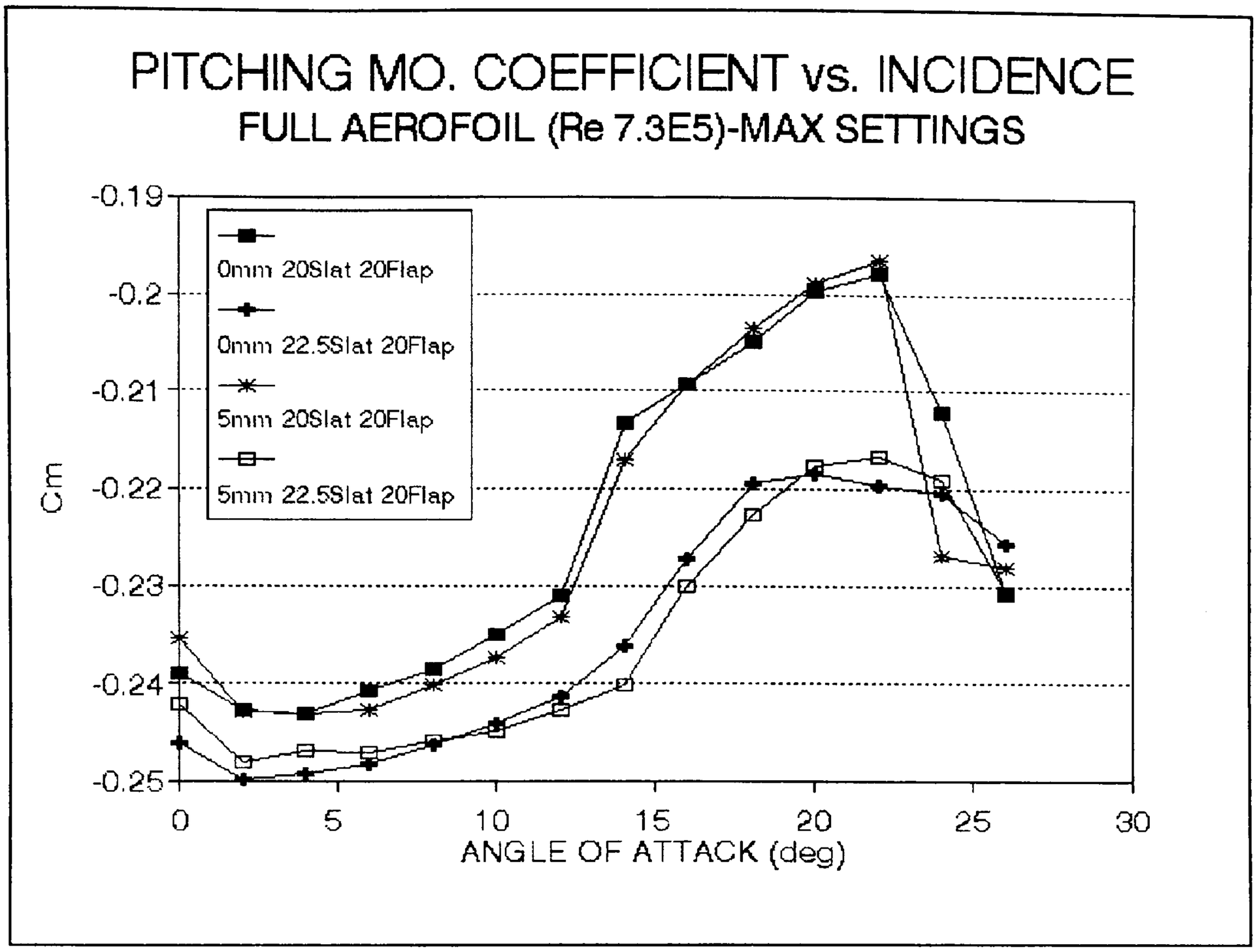

Figure 9:5b:6c

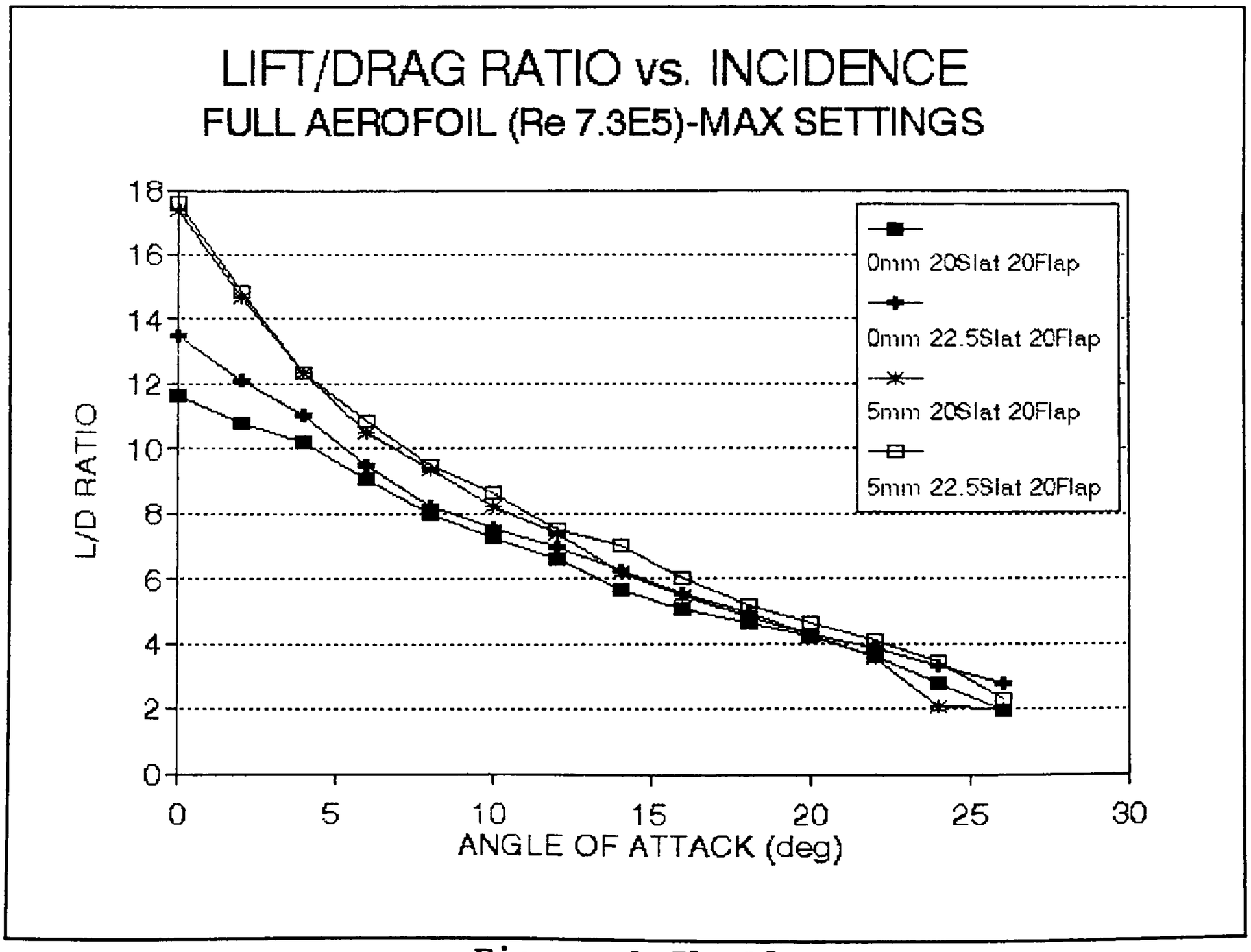

Figure 9:5b:6d

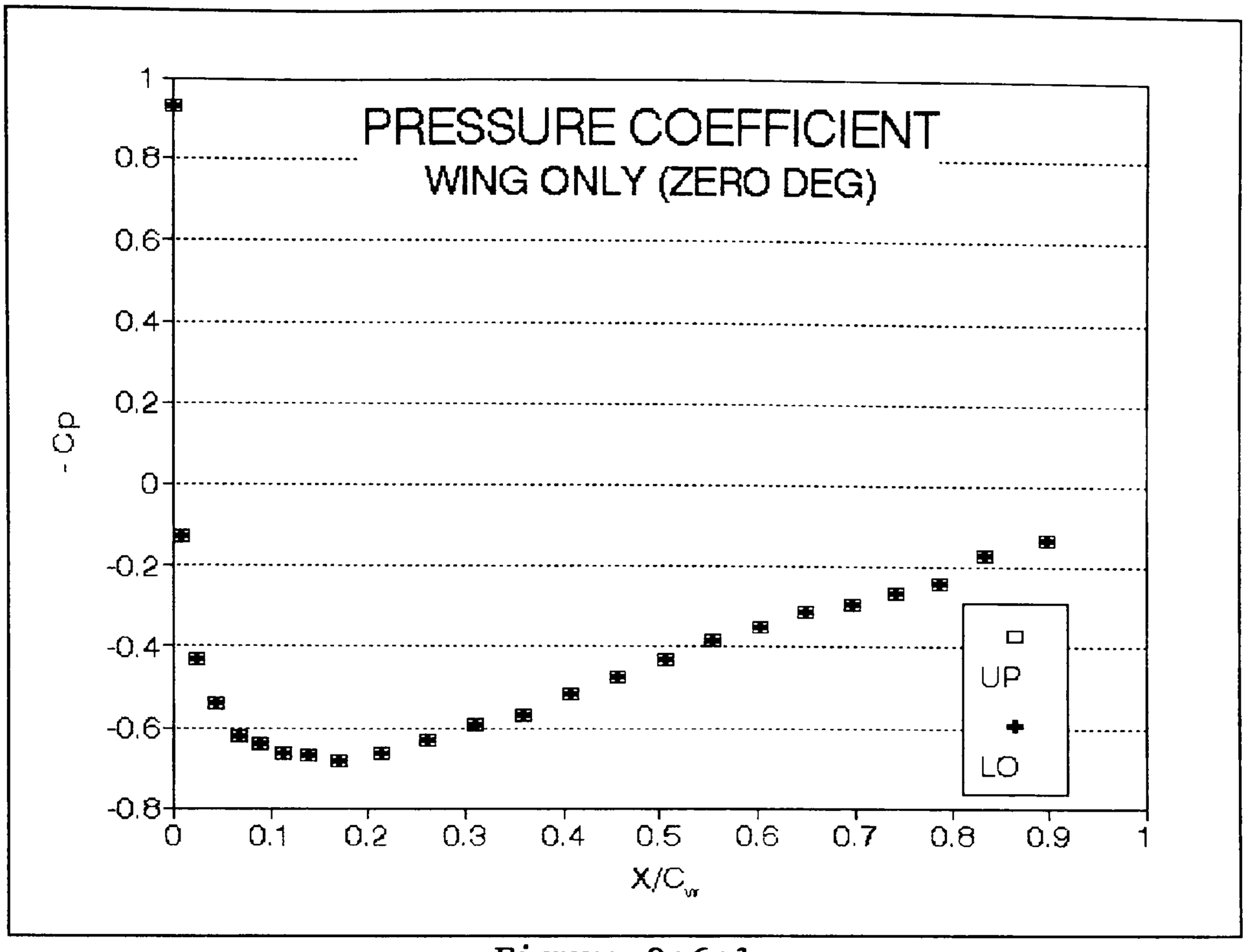

Figure 9:6:1

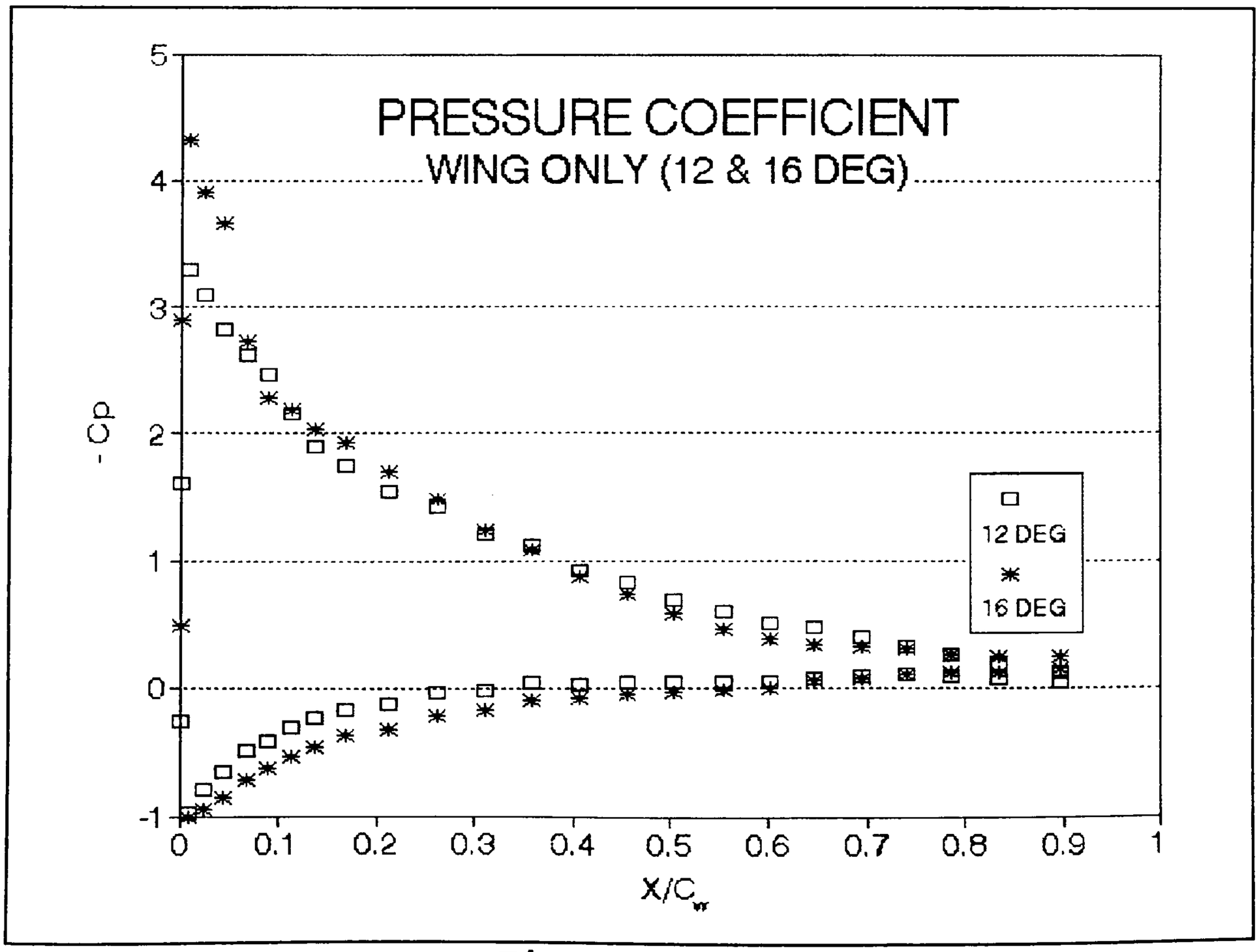

Figure 9:6:2

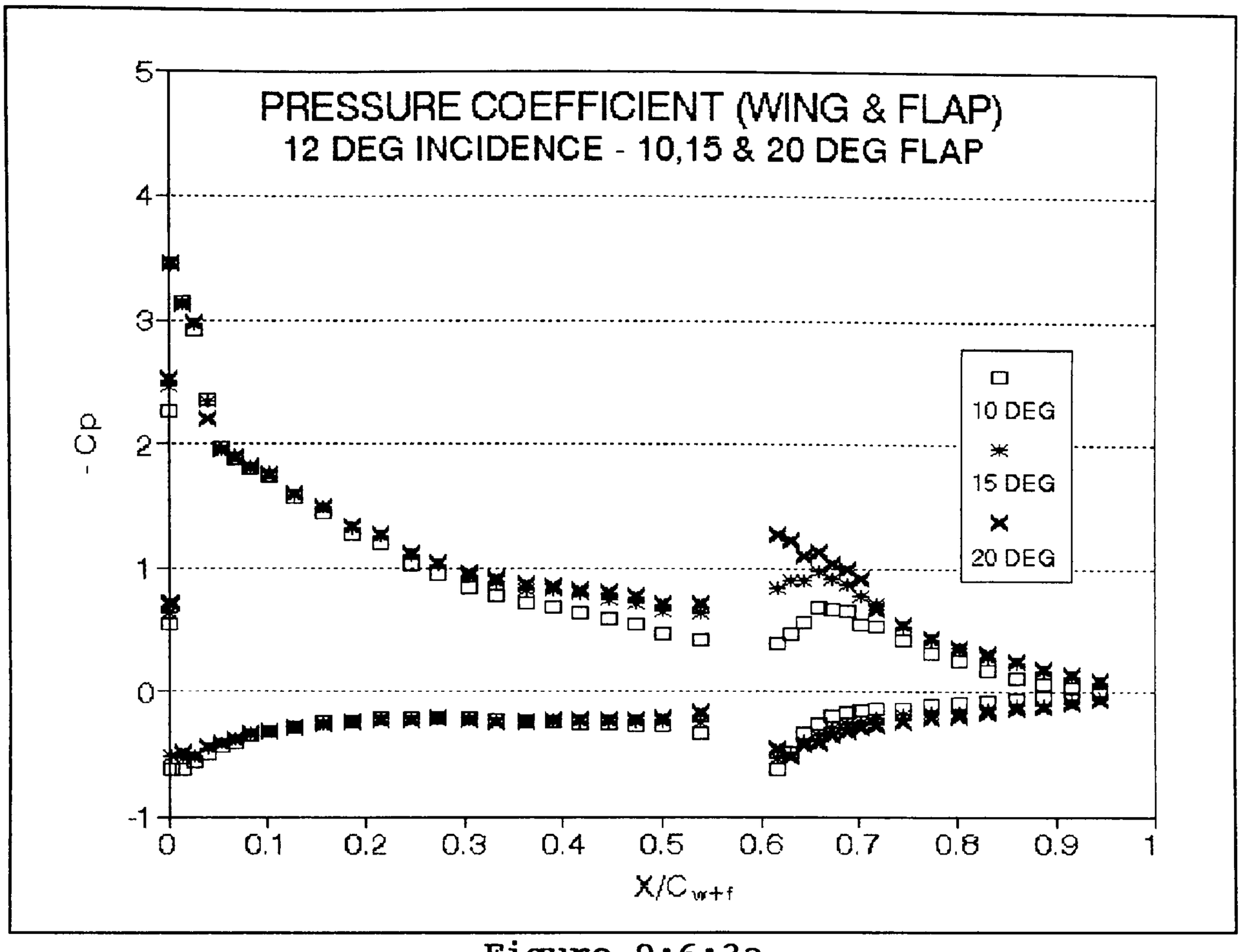

Figure 9:6:3a

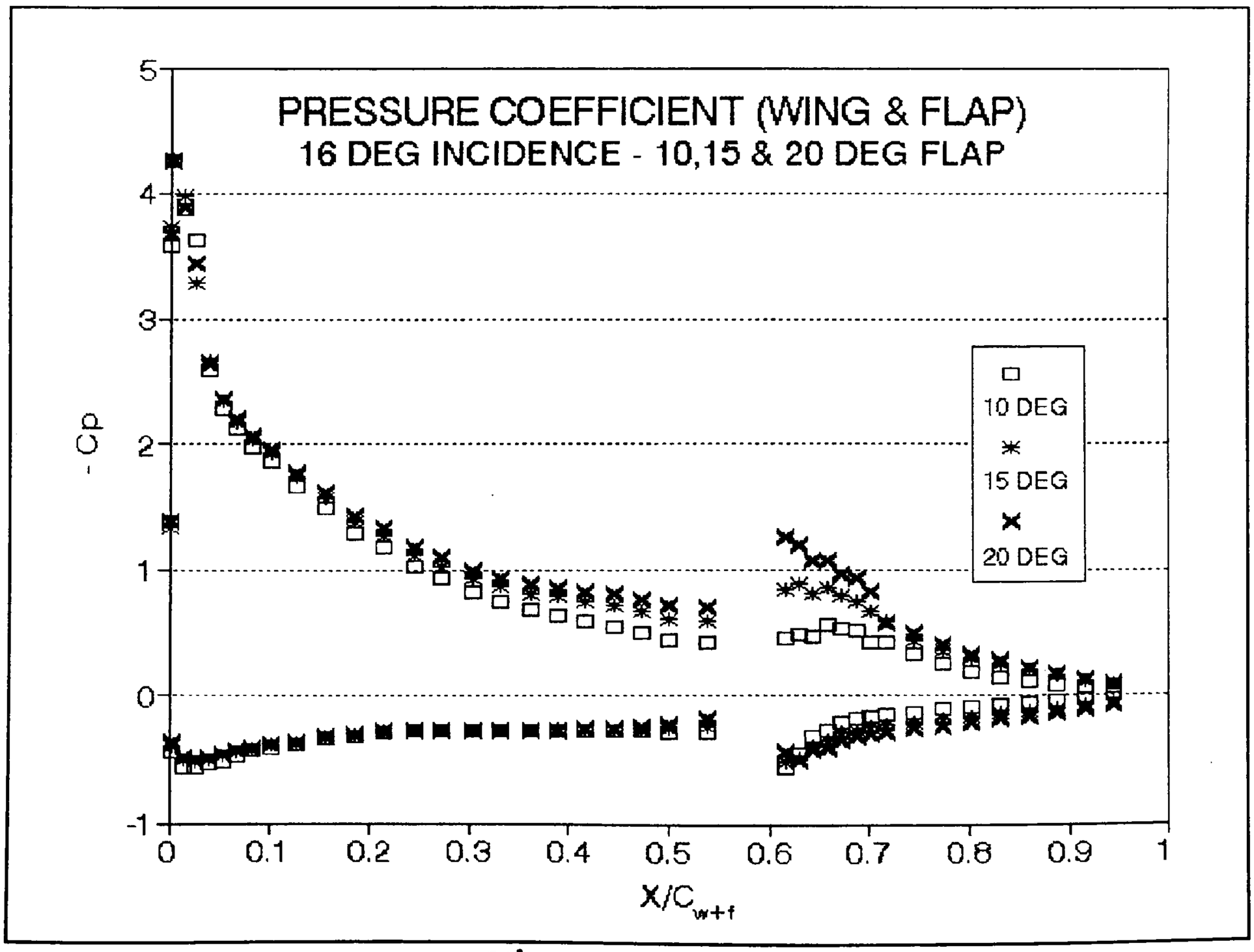

Figure 9:6:3b

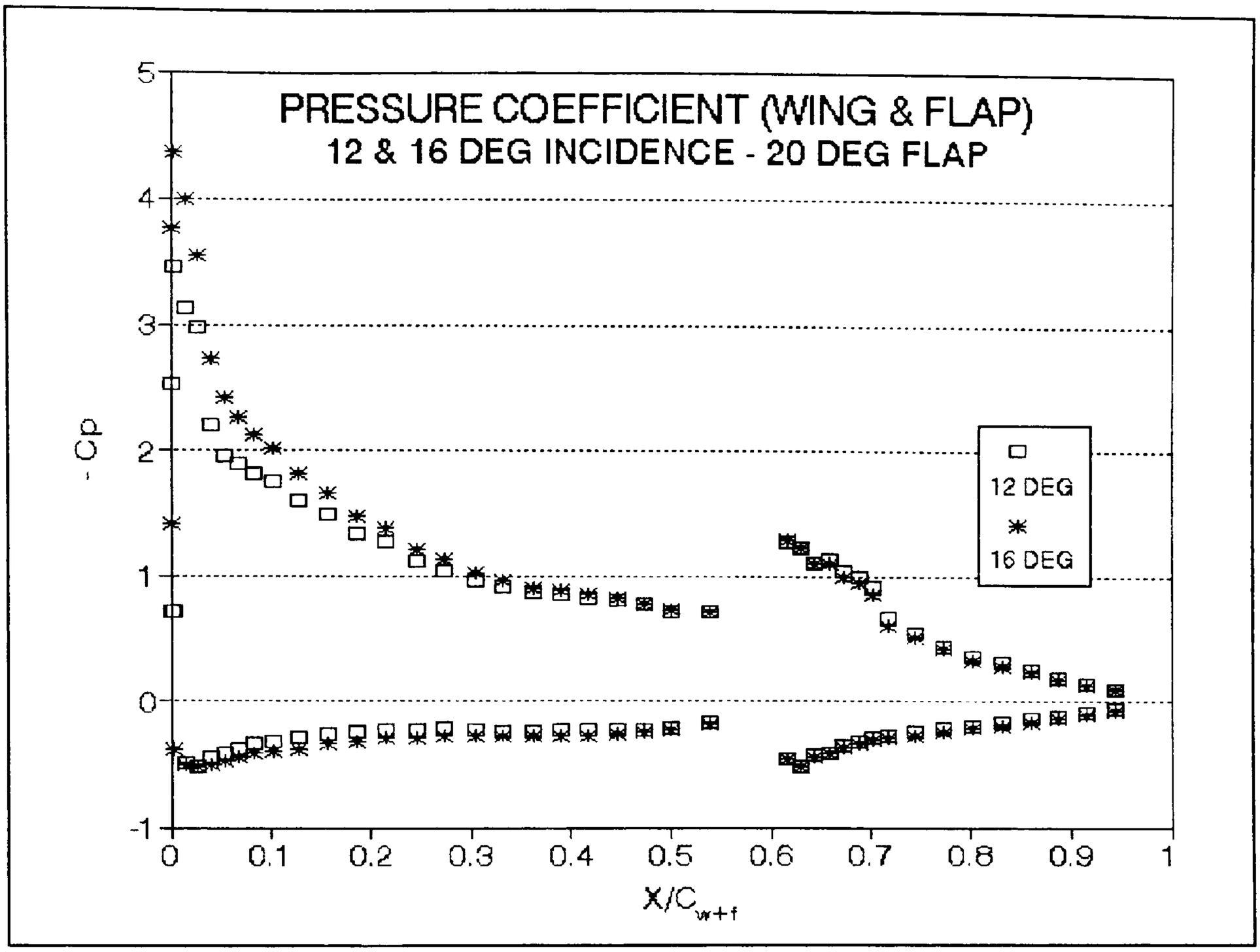

Figure 9:6:4

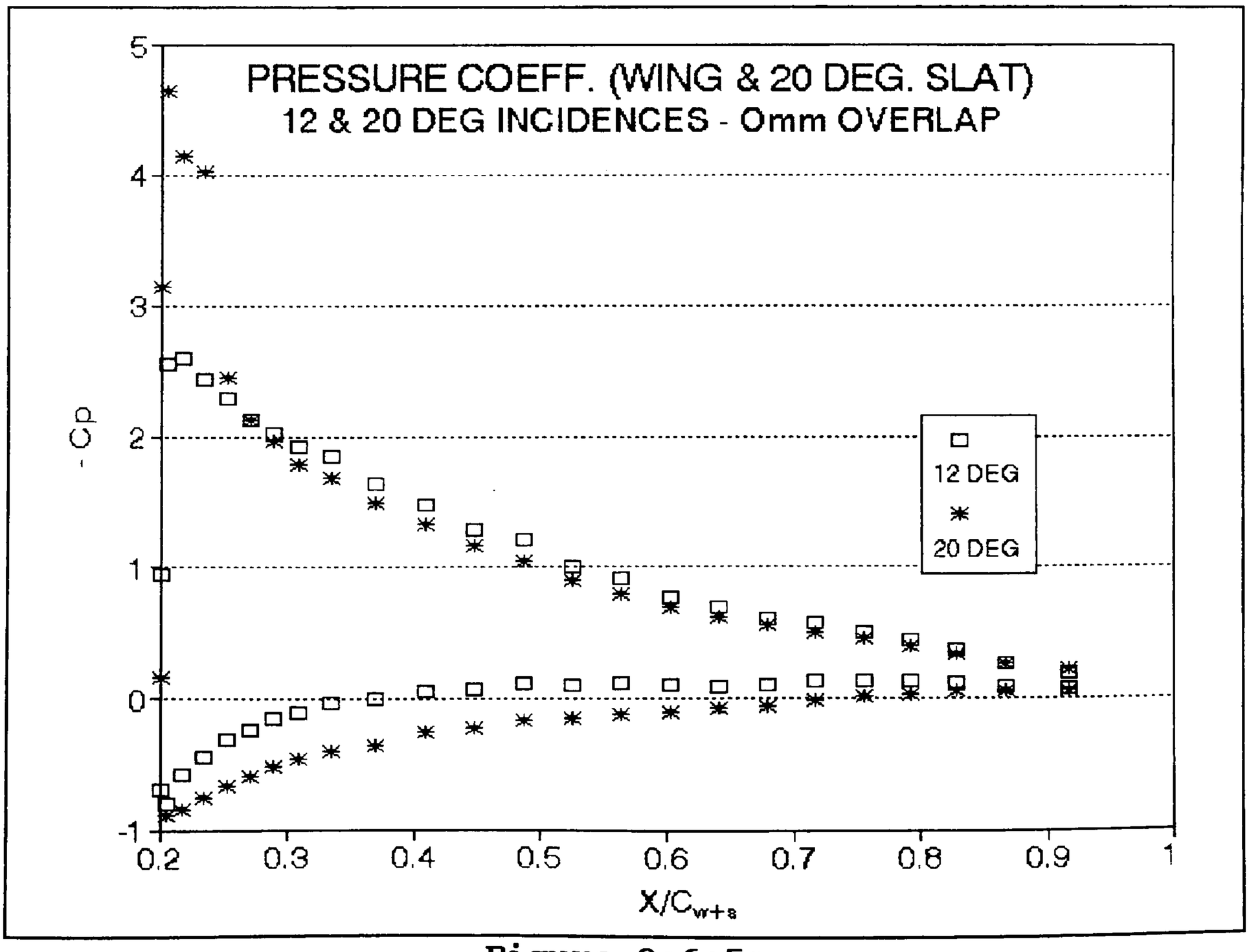

Figure 9:6:5a

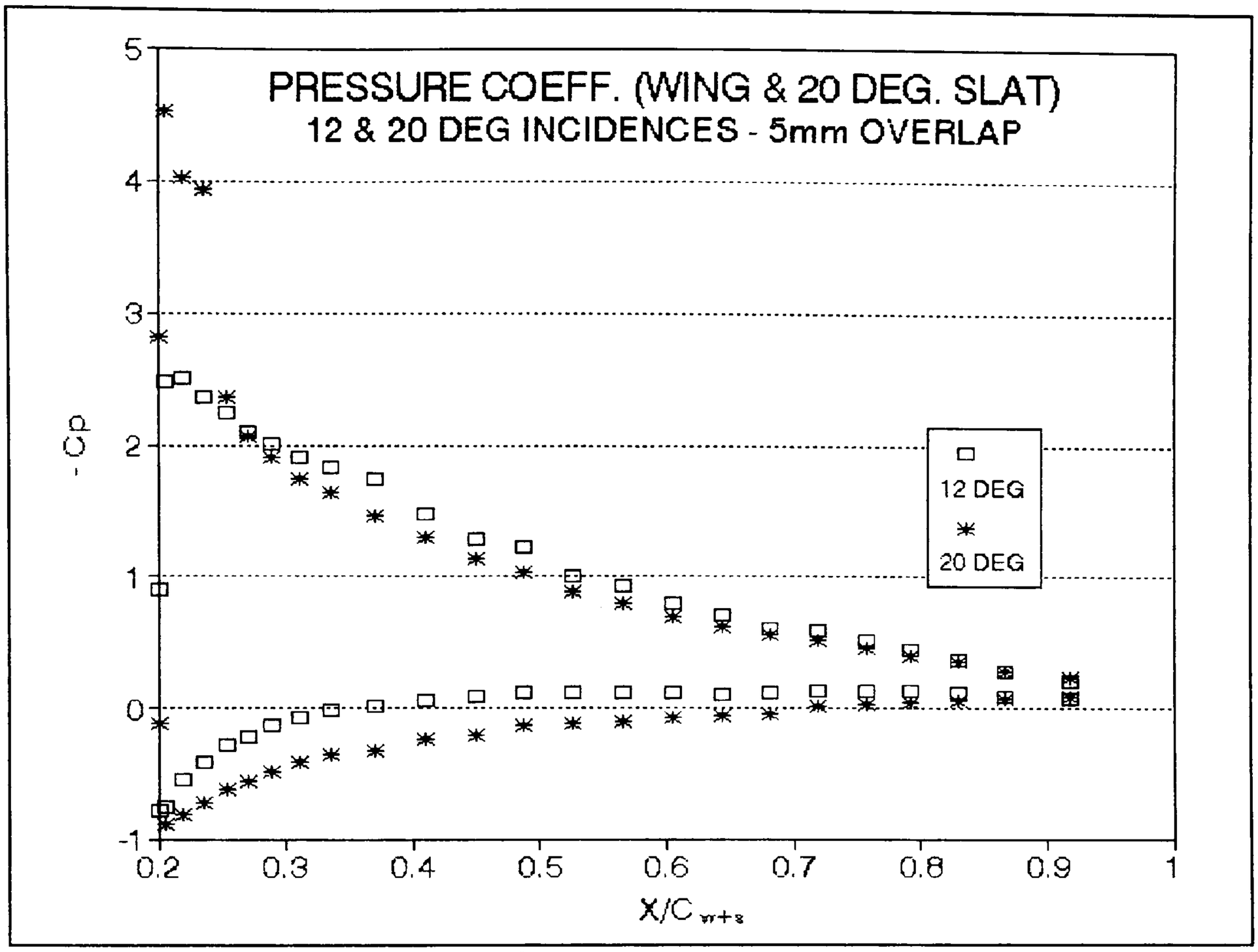

Figure 9:6:5b

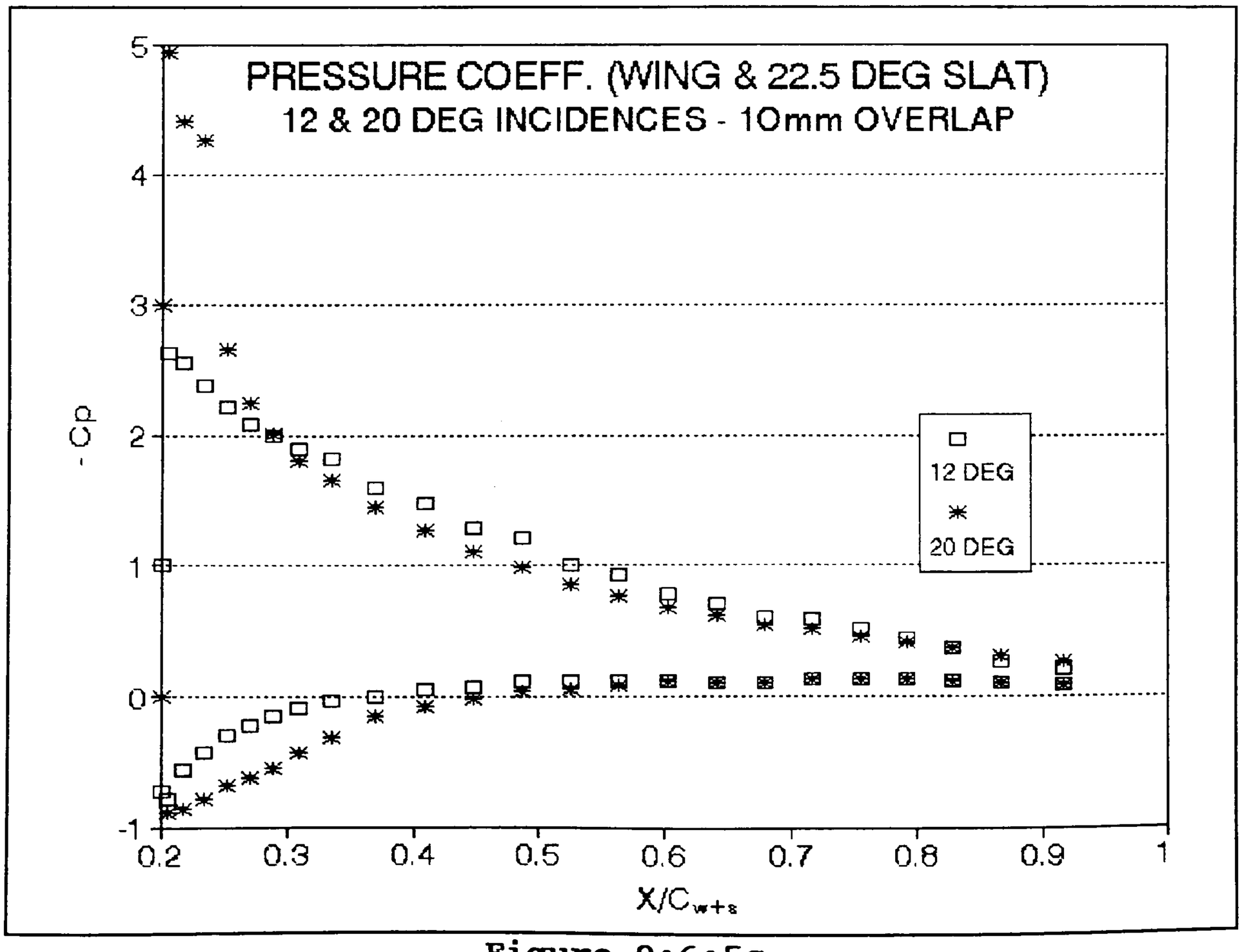

Figure 9:6:5c

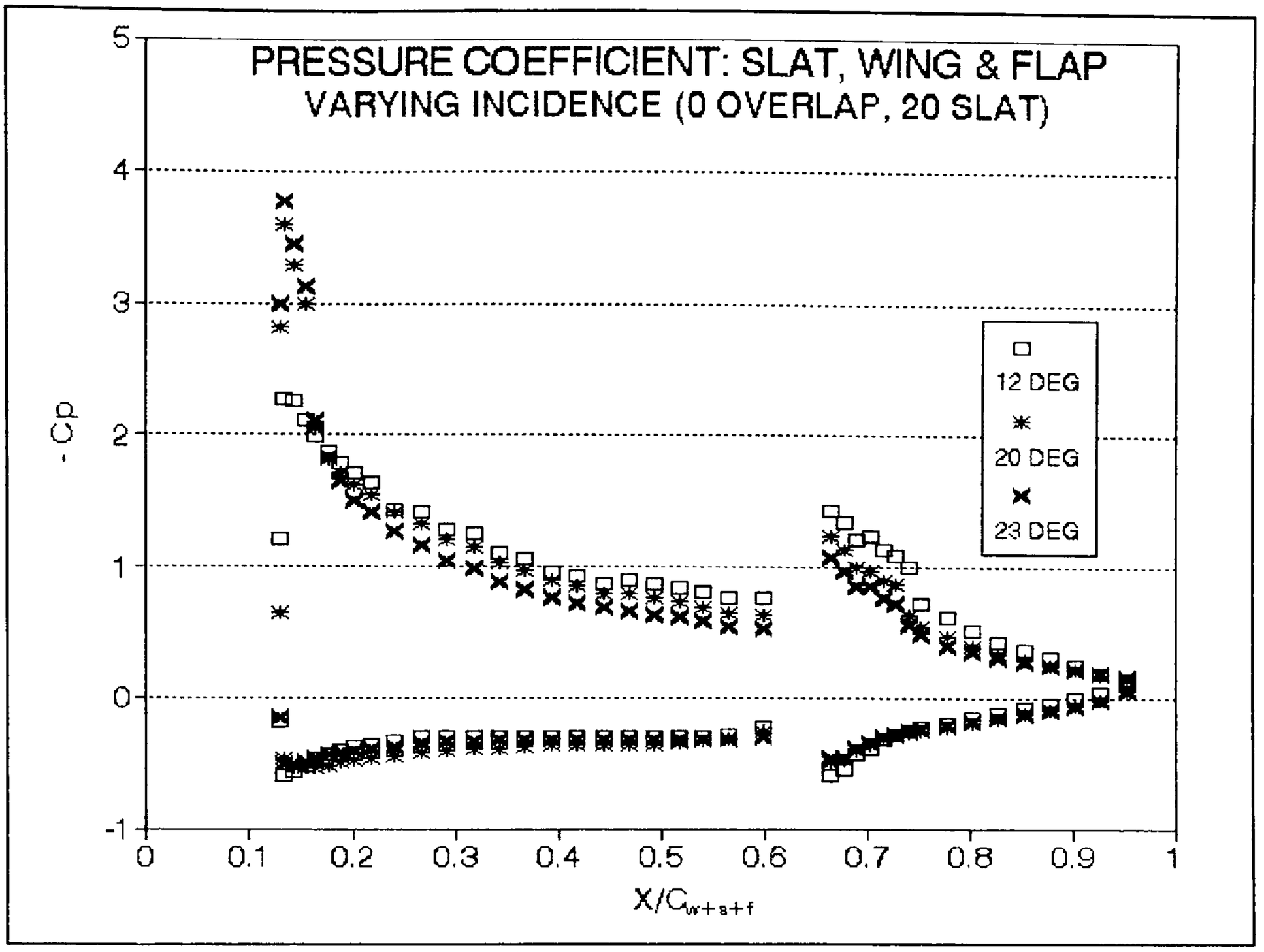

Figure 9:7:6a

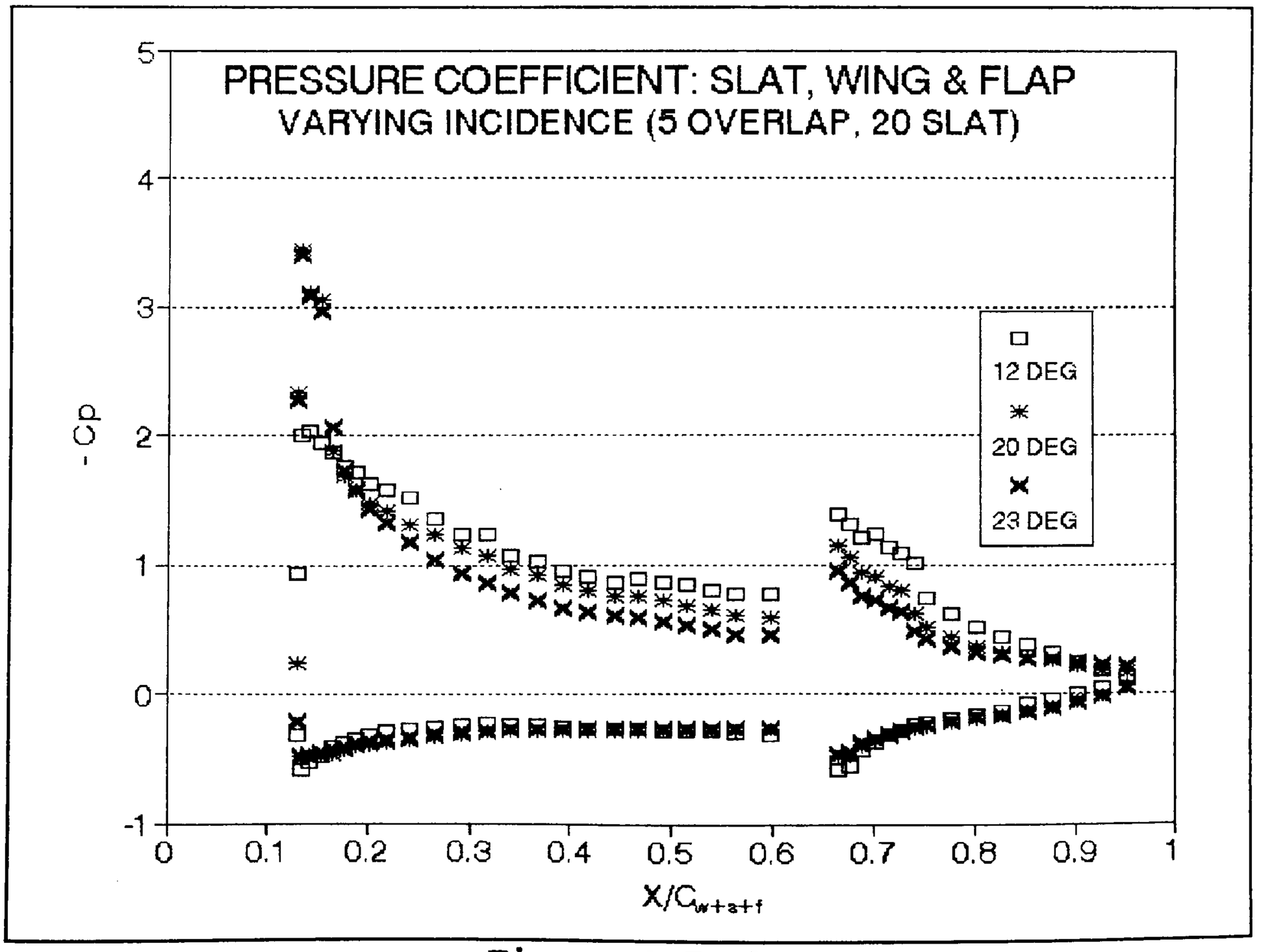

Figure 9:7:6b

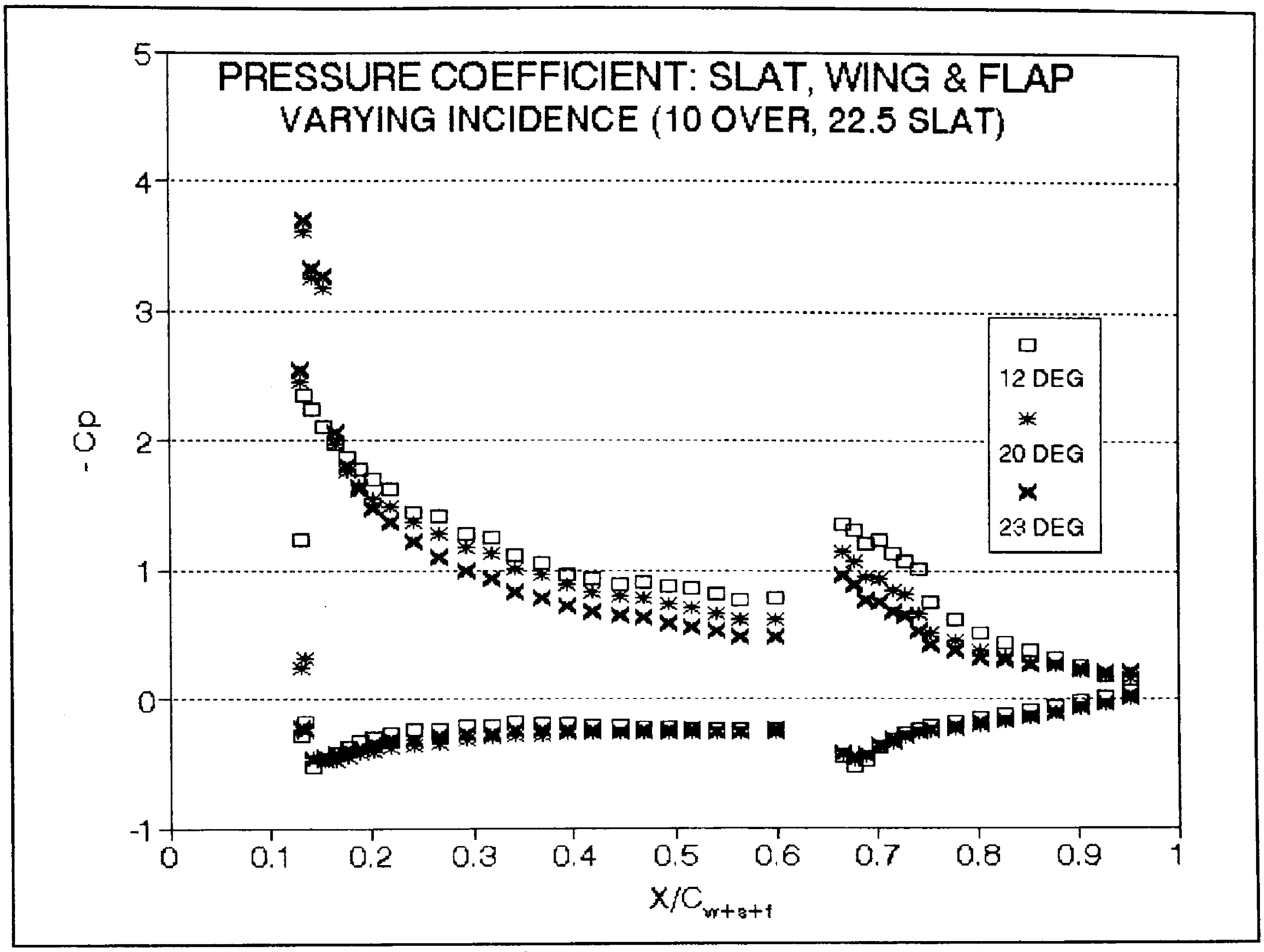
PRESSURE COEFFICIENT: SLAT, WING & FLAP
VARYING INCIDENCE (10 OVER, 22.5 SLAT)
-Cp
X/C w+s+f
12 DEG
20 DEG
23 DEG
5
4
3
2
1
0
-1
0
0.1
0.2
0.3
0.4
0.5
0.6
0.7
0.8
0.9
1

Figure 9:7:6c

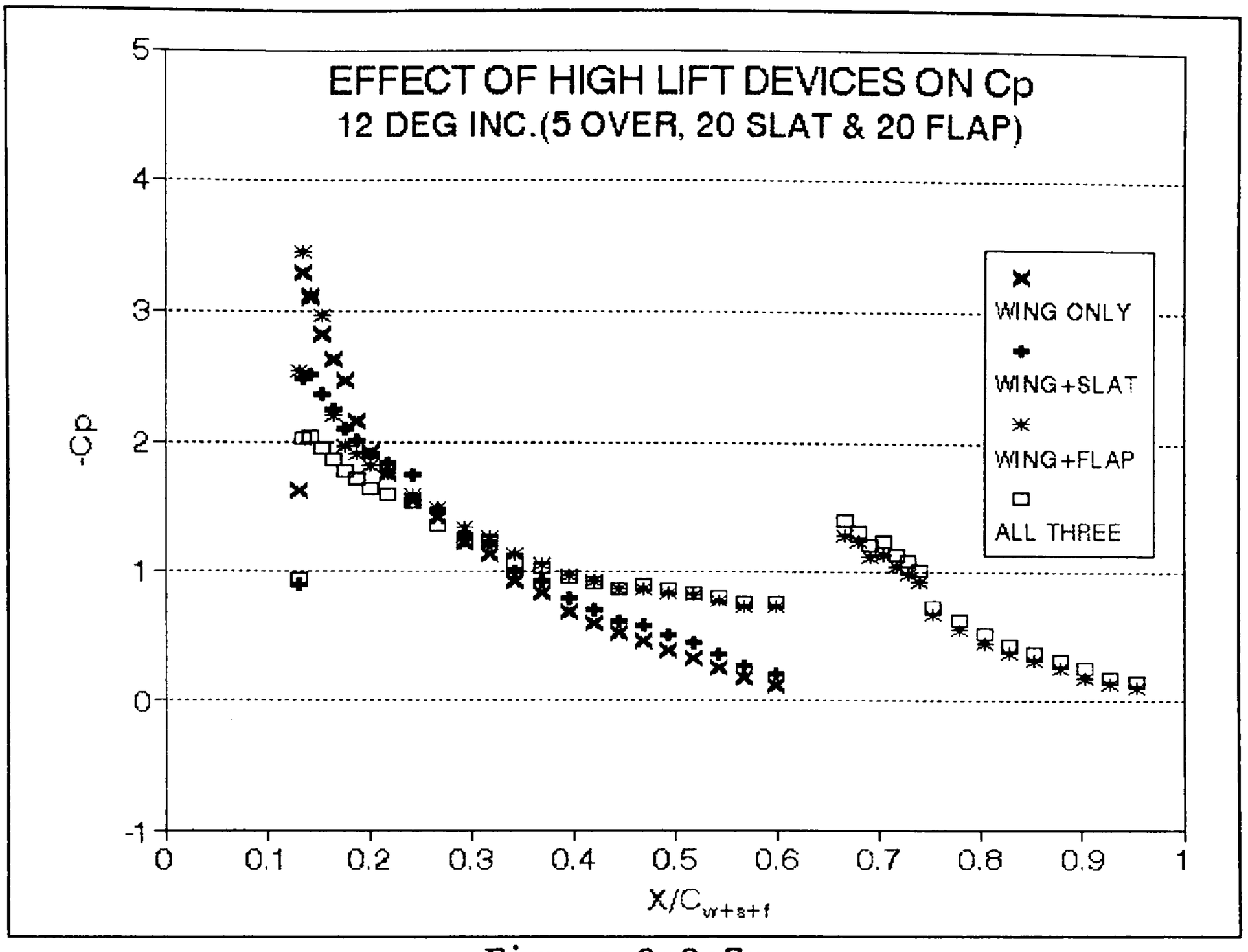

Figure 9:8:7a

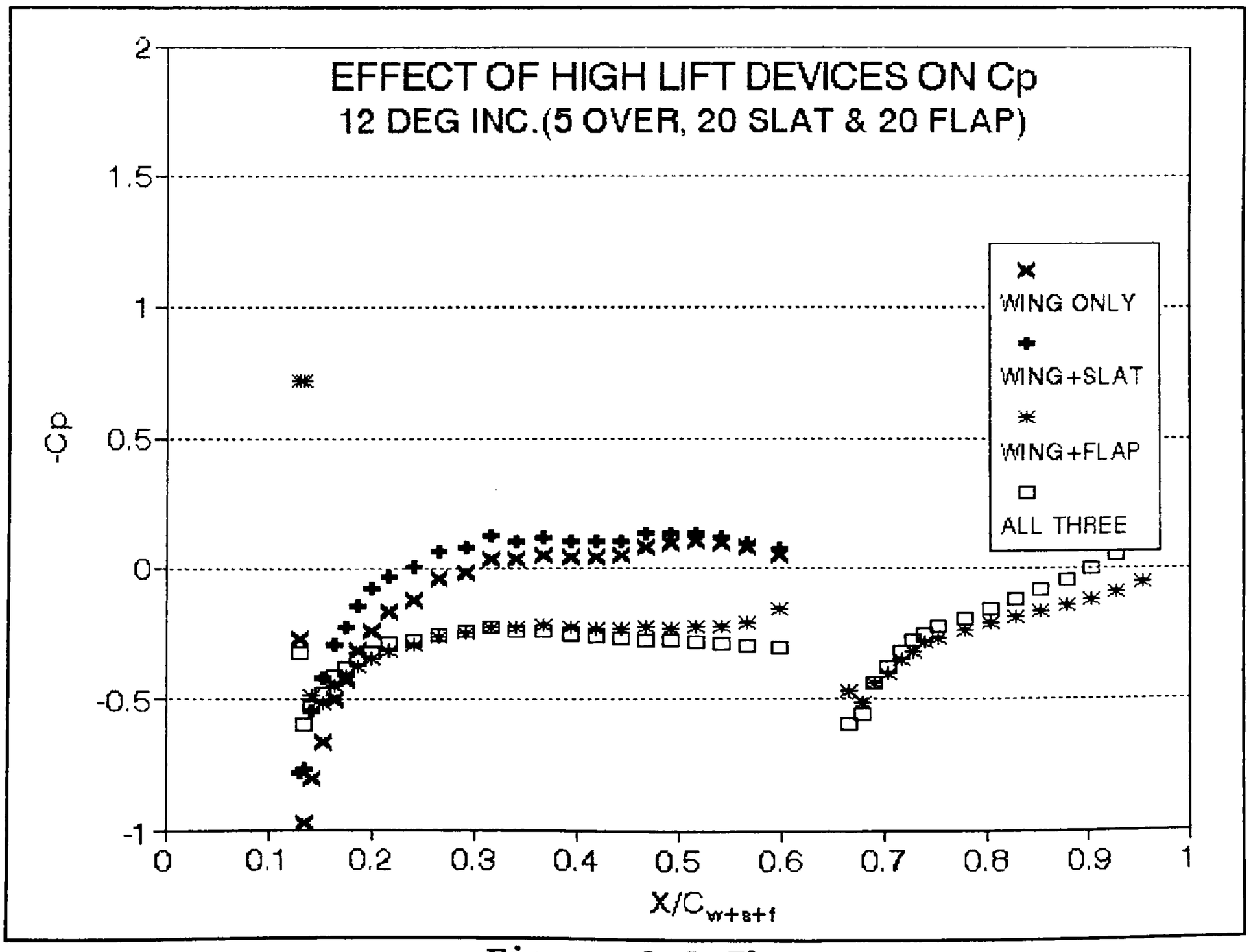

Figure 9:8:7b

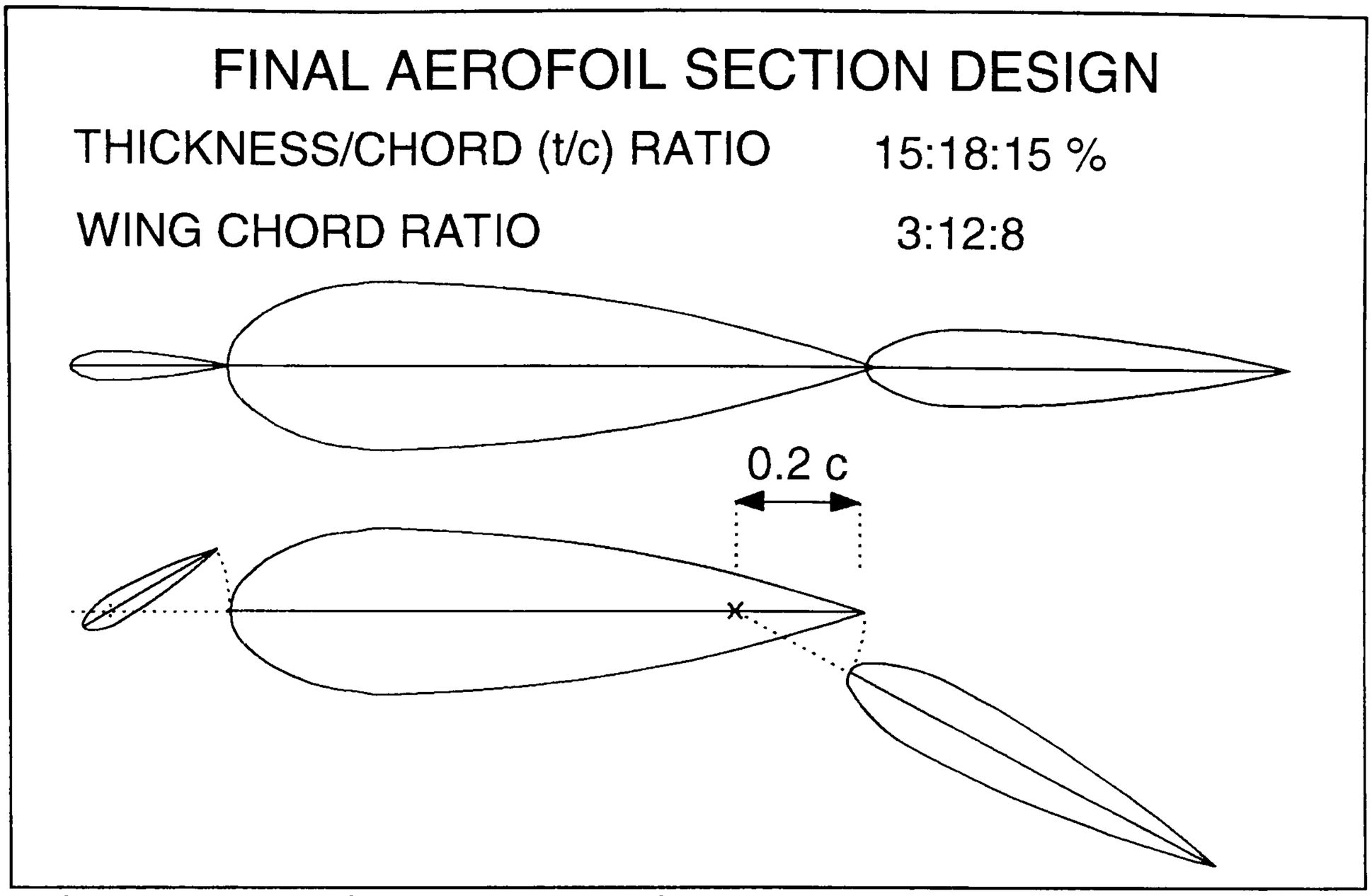

Figure 9:9 Final Model Thickness & Chord Configuration

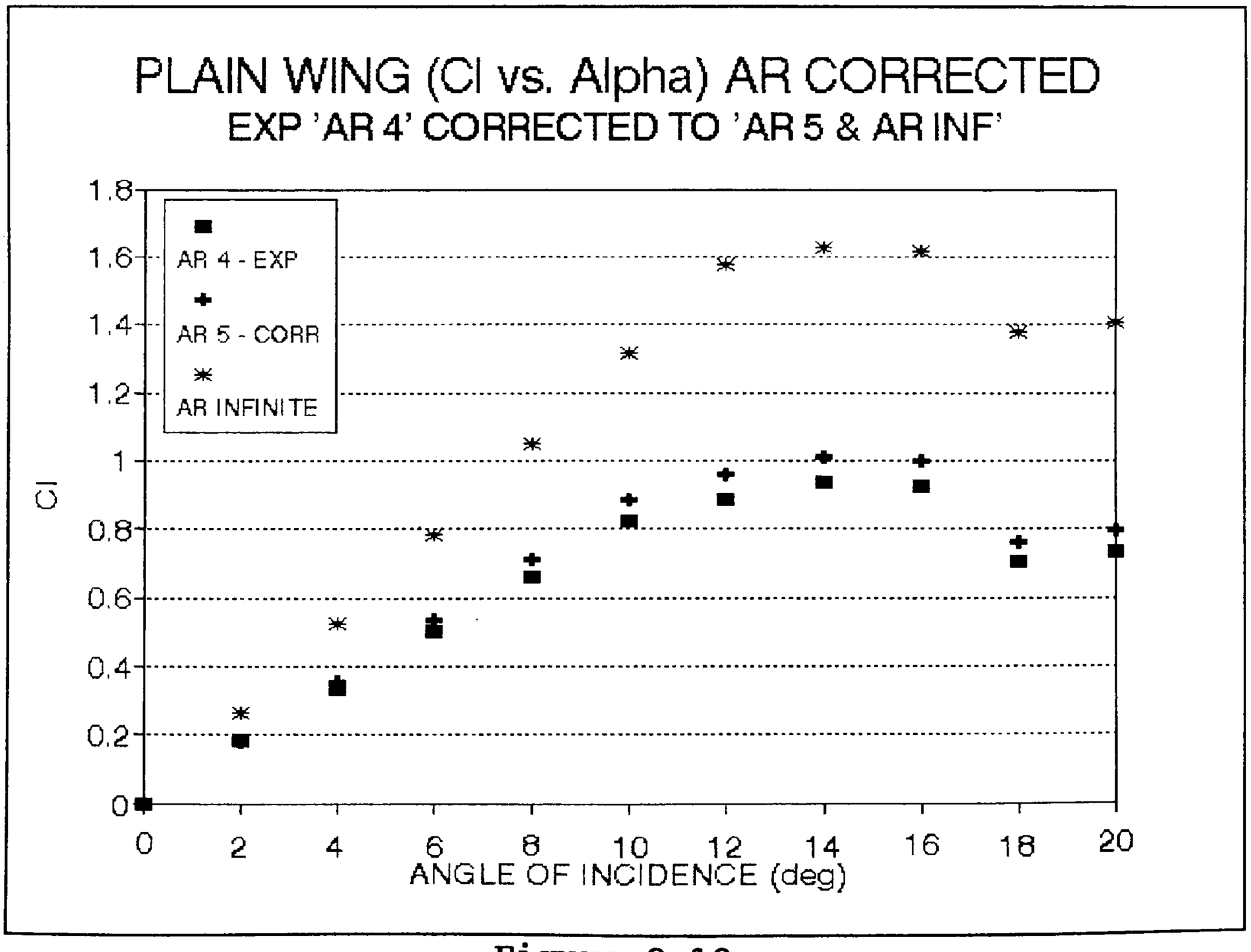

Figure 9:10a

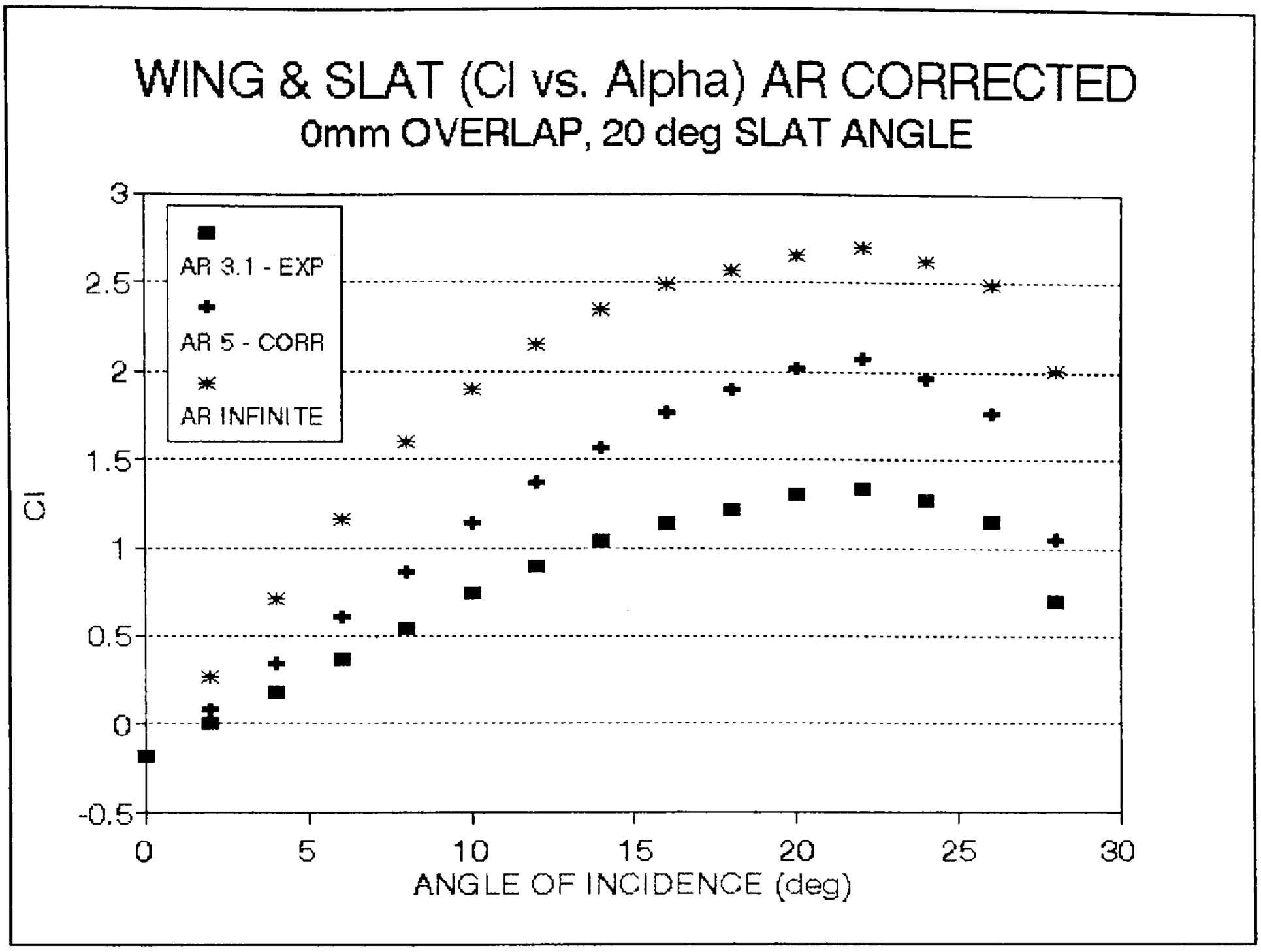

Figure 9:10b

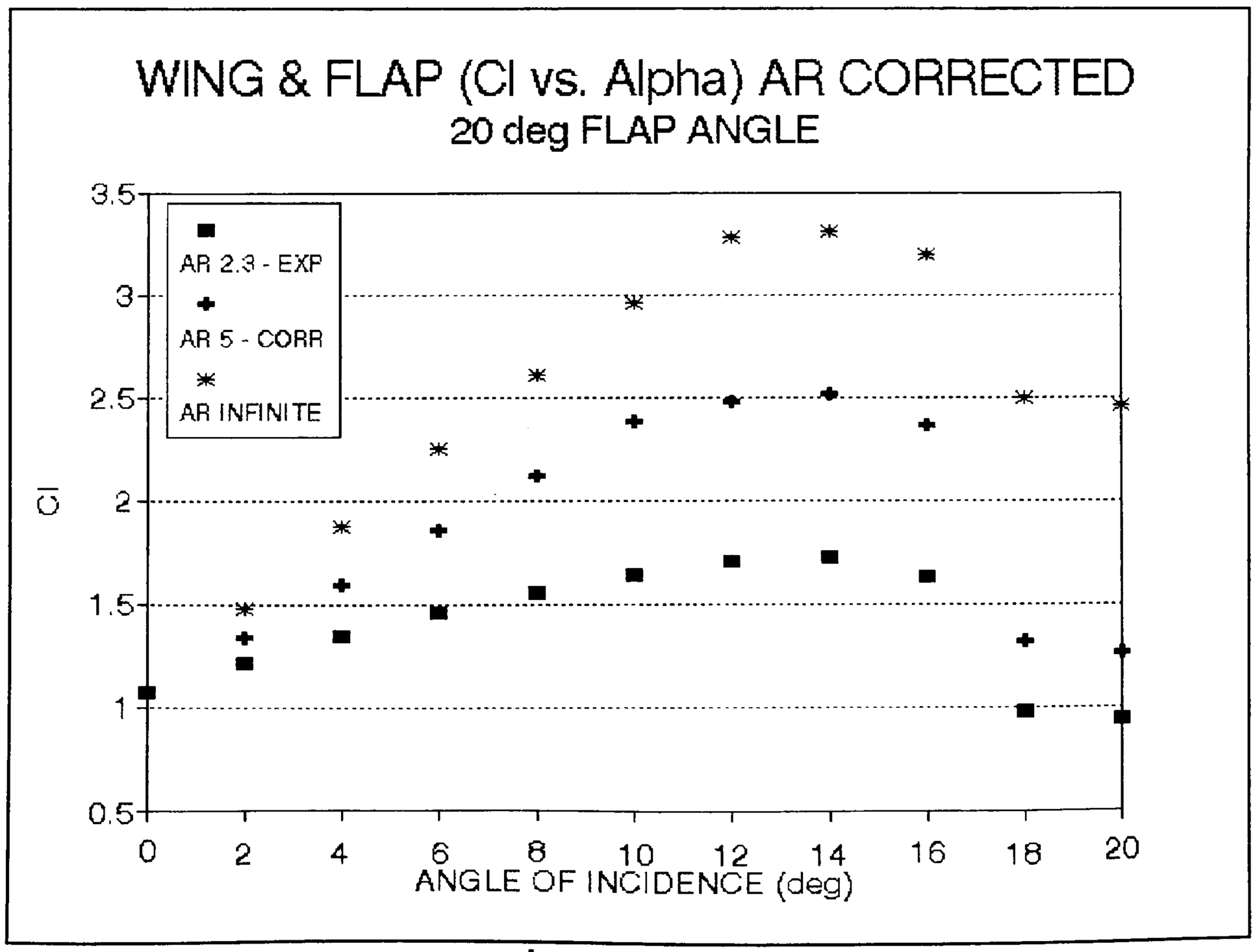

Figure 9:10c

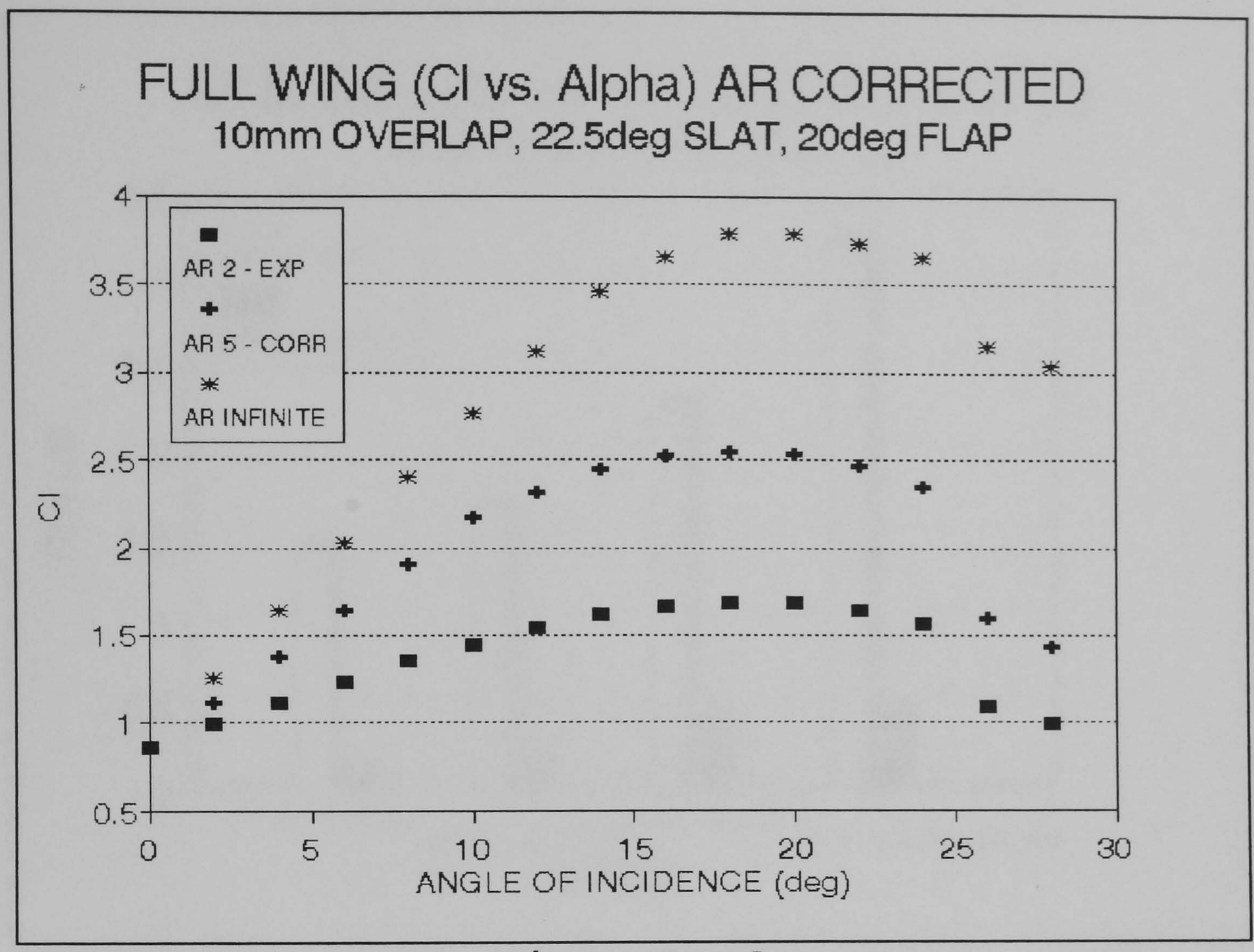

Figure 9:10d

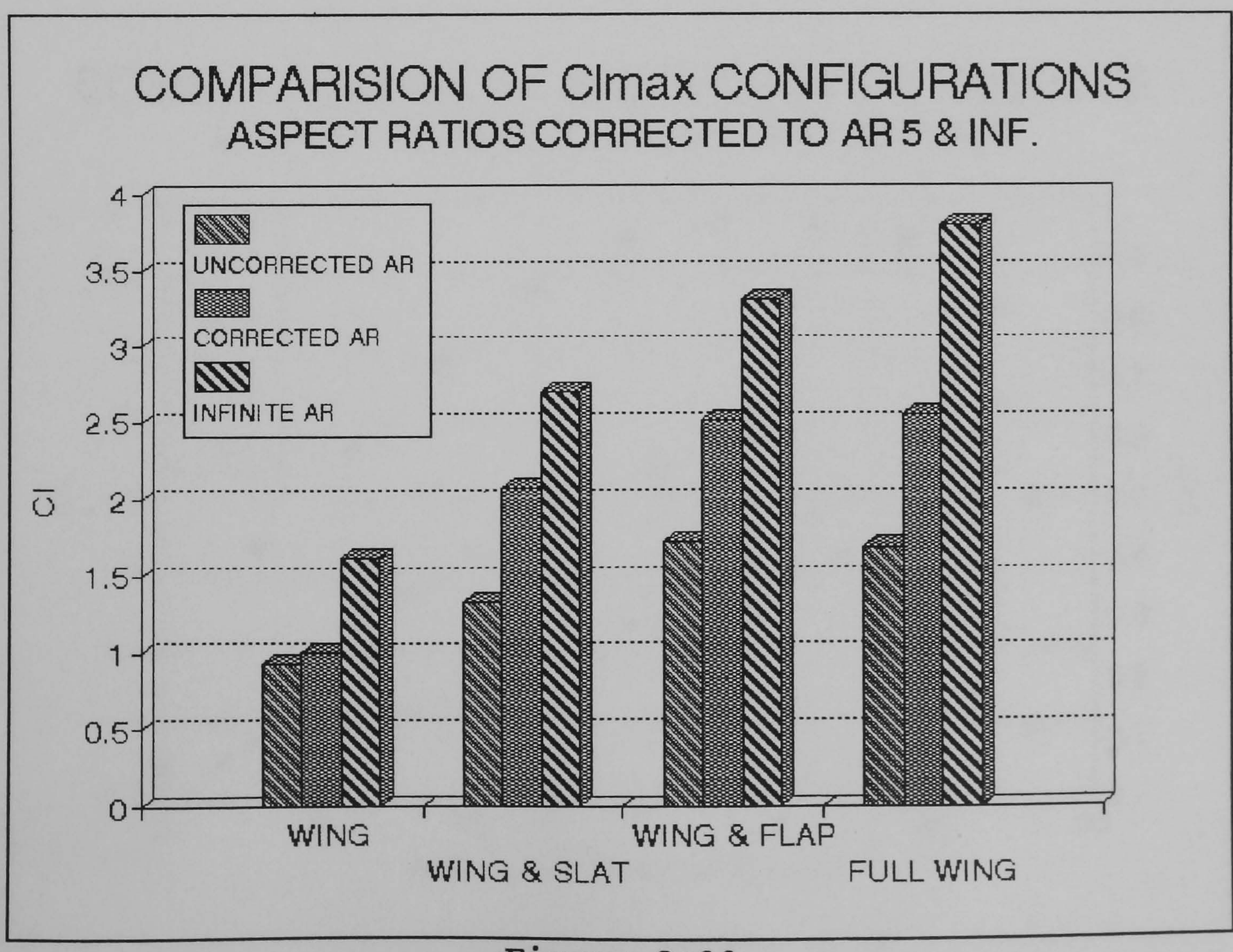

Figure 9:11

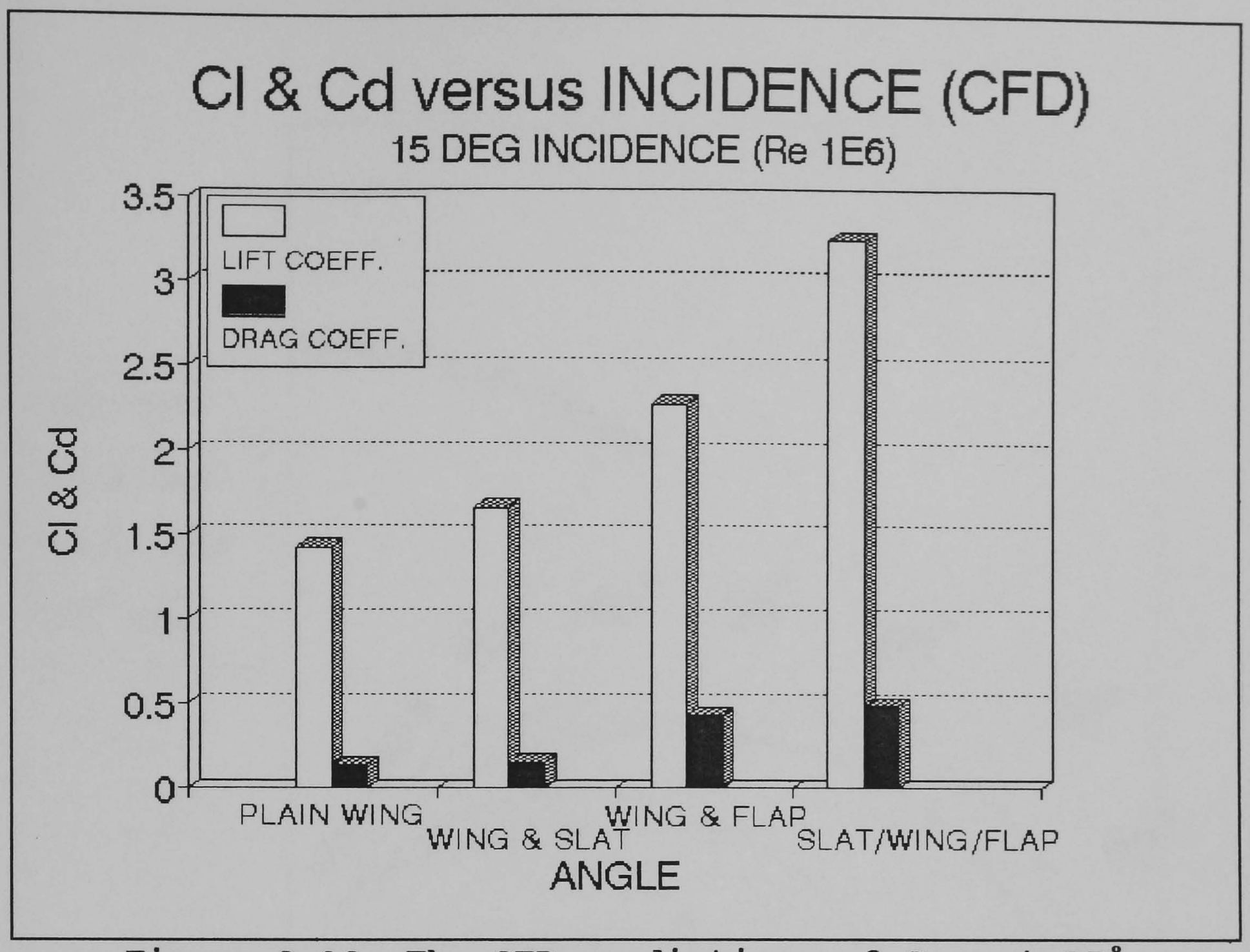

Figure 9:12 The CFD predictions of C_{Lmax} at 15°

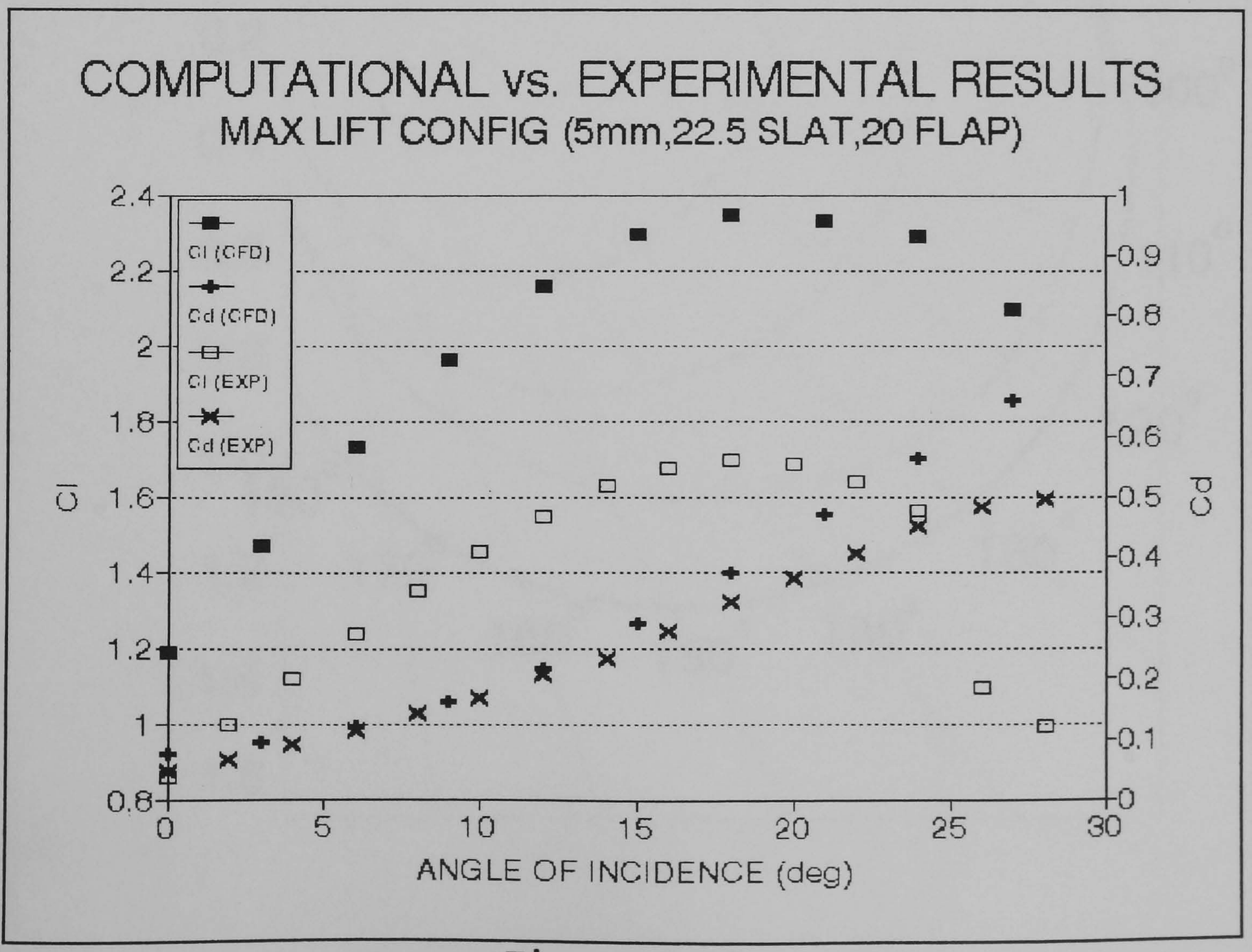

Figure 9:13

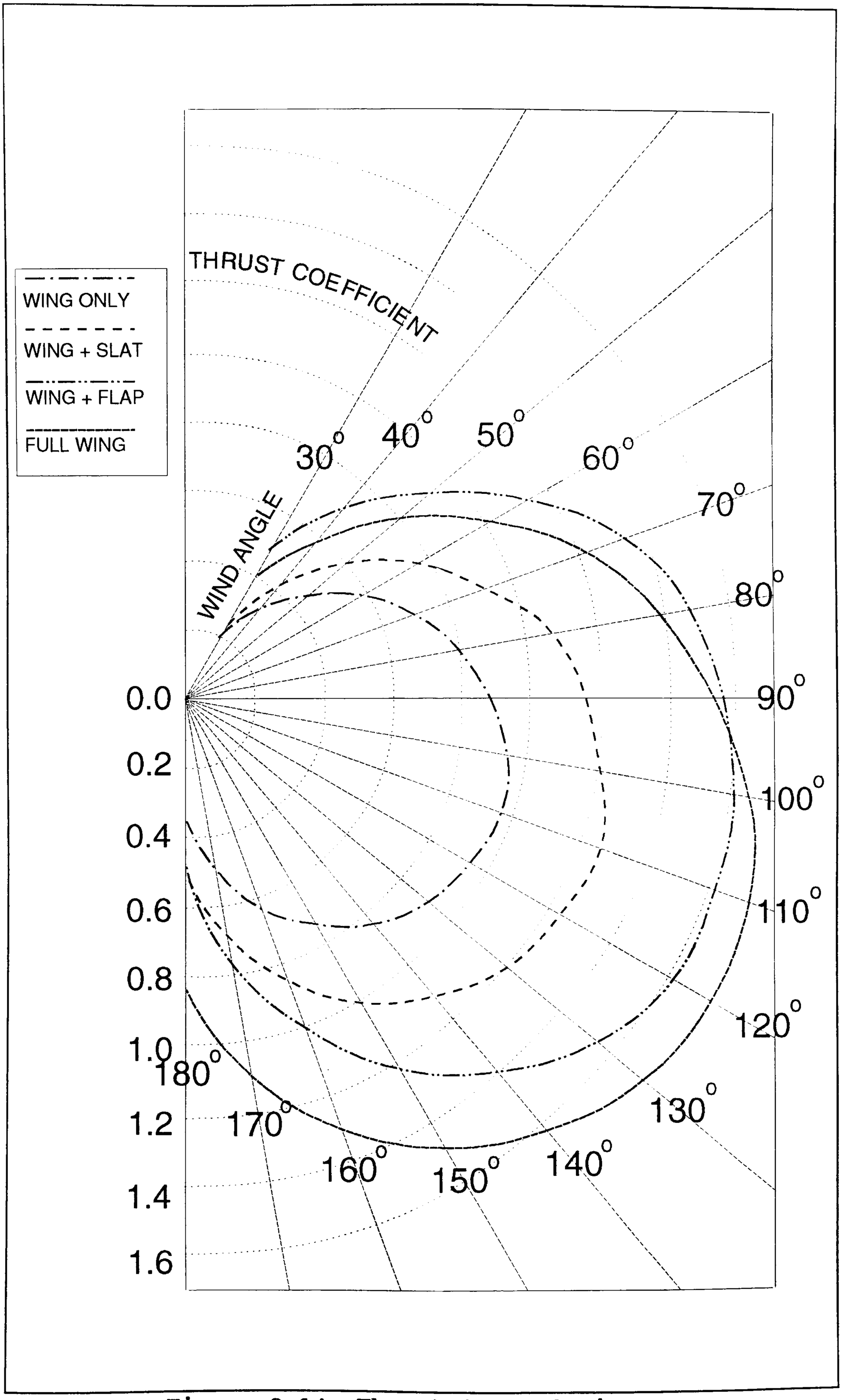

Figure 9:14 Thrust 'Polar' Diagram

Appendix A

WINGSAIL HISTORY

A.1 Wingsail (1922)

It was Anton Flettner who in 1922 developed the first rigid lift-generating devices for use as auxiliary ship propulsion. Flettner, a trained aircraft engineer, had previously developed rudders with trim-tabs intended for use on both aircraft and oceangoing ships. Flettner's first design was the 3-tower Flettner schooner, shown in **Figure A:1**. The aerofoils Flettner used had a thickness/chord ratio of 17% and trim-tab operated flaps of 33% total chord length.

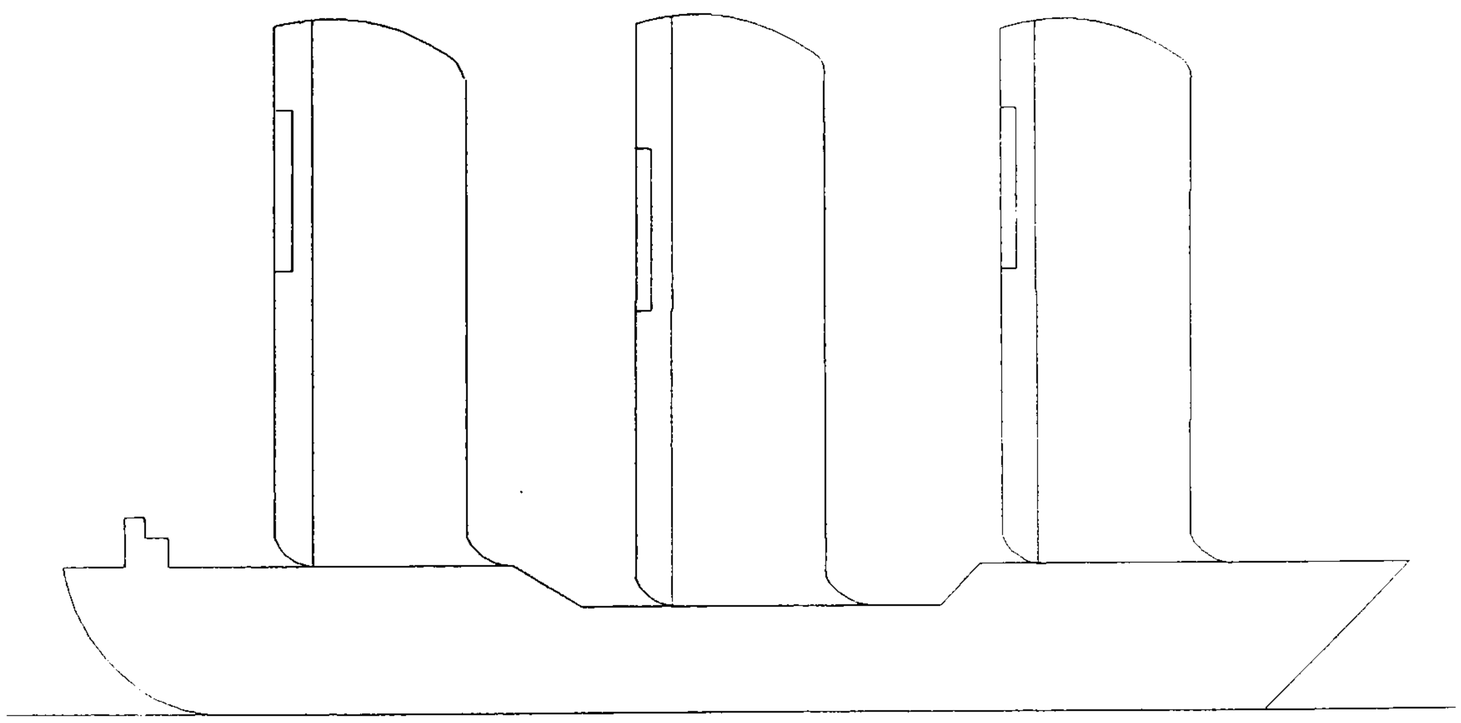

Figure A:1 The 3 Tower Flettner Schooner

For structural reasons Flettner found it necessary to alter the overall configuration of his aerofoils to a tri-plane, thus Flettner is also credited with designing the first 'wingset', shown in **Figure A:2**. The control tab, or auxiliary rudder was placed on a tail behind the central wing. The indicated C_{Lmax} for this system was 1.4, significantly better than soft sails of that era.

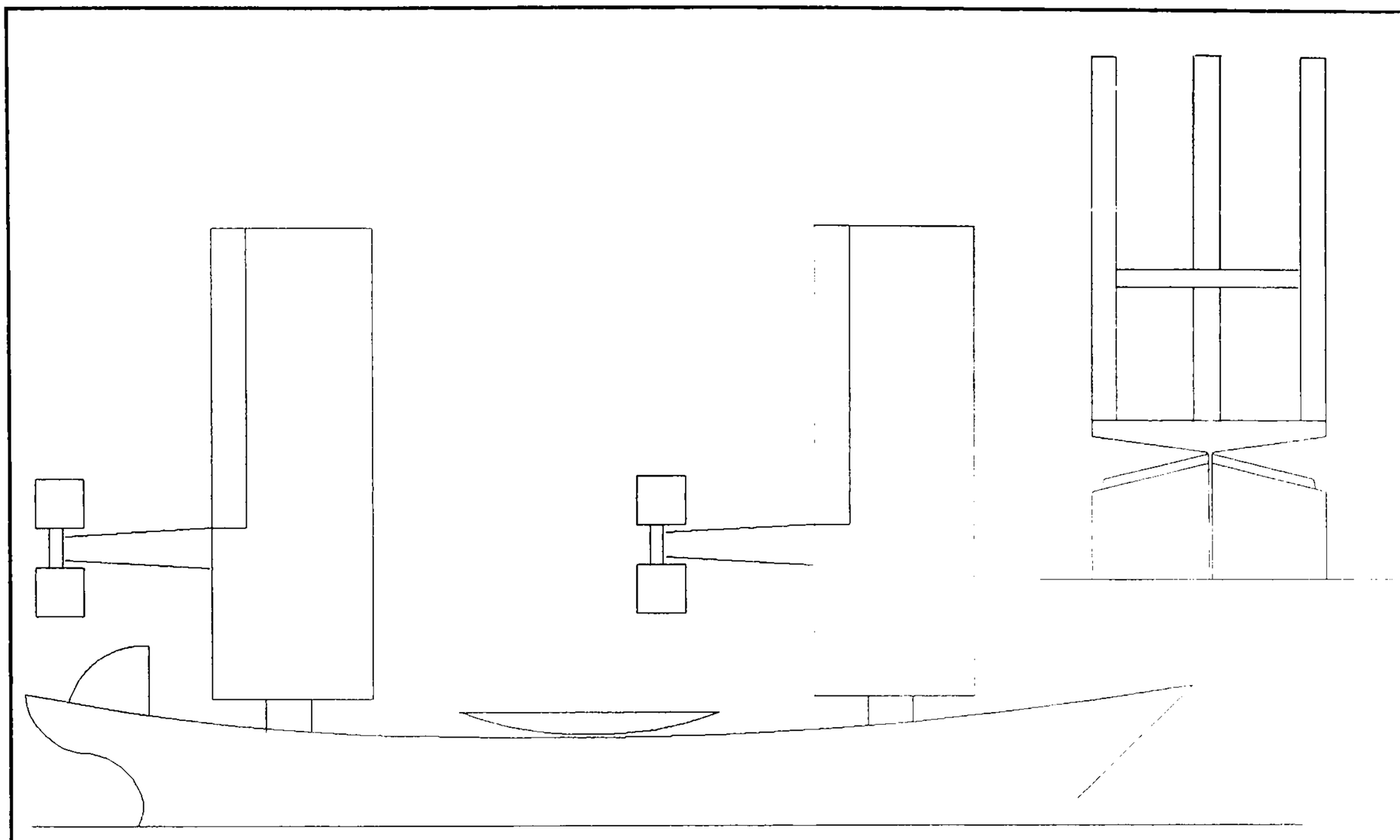

Figure A:2 Flettners' Wingset

Flettner designed his tri-planes to fit two vessels Barbara and Backau, although these were never fitted. Flettner ceased to design wingsails when he became obsessed with his famous rotor project. Flettner did not surface again until he appeared in World War 2 as a leading figure in the German helicopter programme.

A.2 Fin Utne

Fin Utne was working in Norway before the second world war, his excellent design, the little boat 'Flaunder' **Figure A:3** was the first fully working, self-trimming wingsail known. Utne's wingsail was a modified RAF 30 section, with a wing area of 3.7m^2. The wingsail was statically mass balanced about its axis of rotation. Unfortunately, she was sadly destroyed by the German occupying forces, who viewed her as a 'potential weapon of war'.

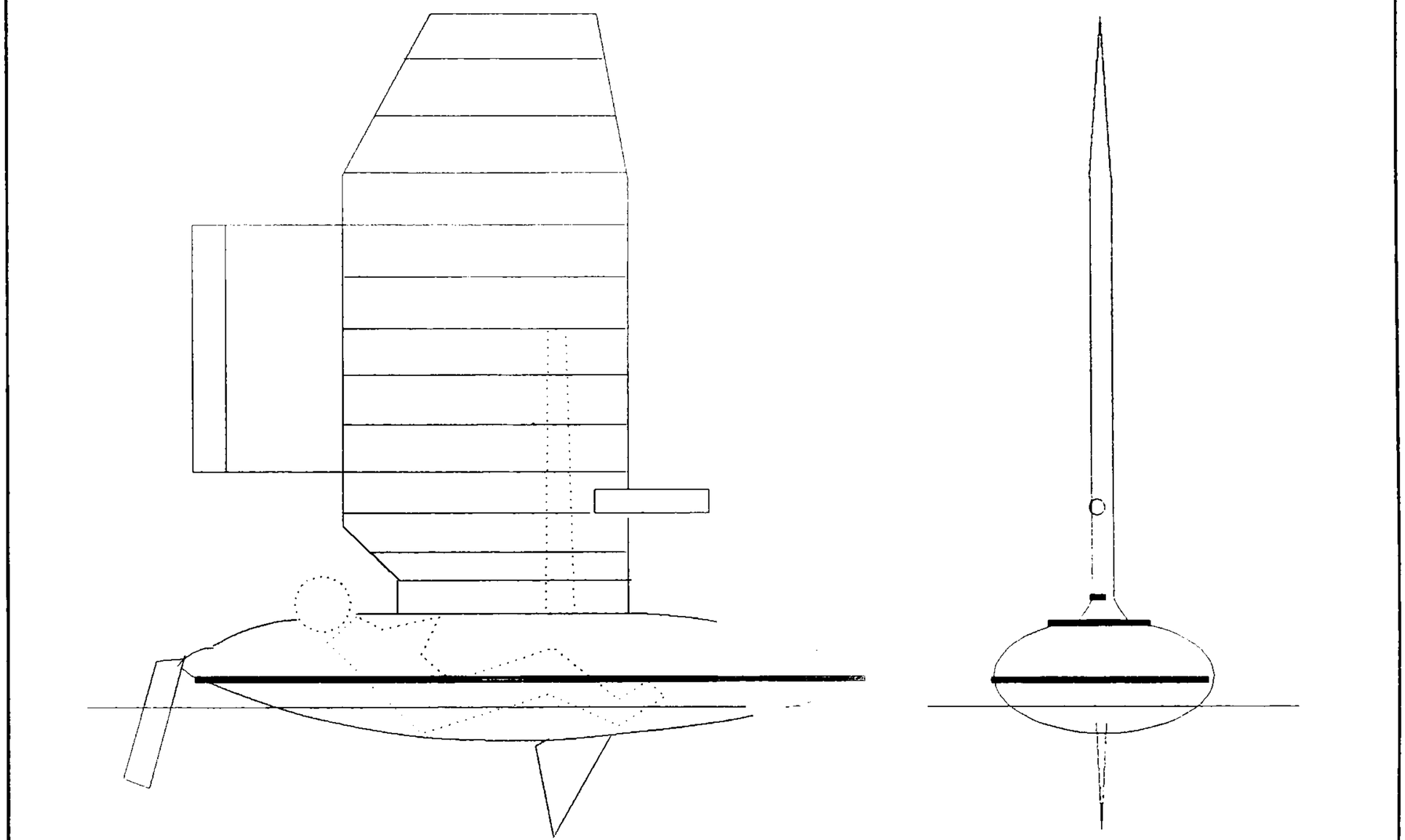

Figure A:3 The Fin Utne 'Flaunder'

A.3 Blackburn Aircraft (1962)

The Blackburn Aircraft yacht, shown in **Figure A:4**, was the second full-scale boat with a self-trimming wingsail. This 5.8m^2 wingsail had a NACA 0015 section, a 25% flap chord and was pivoted 30% of the chord length, aft of the wingsail leading edge. This wing was mounted on a dinghy which frequently developed divergent rolling oscillations and capsized. This unfortunate characteristic was over come by mass-balancing the rig and increasing the area at the tail of the vessel.

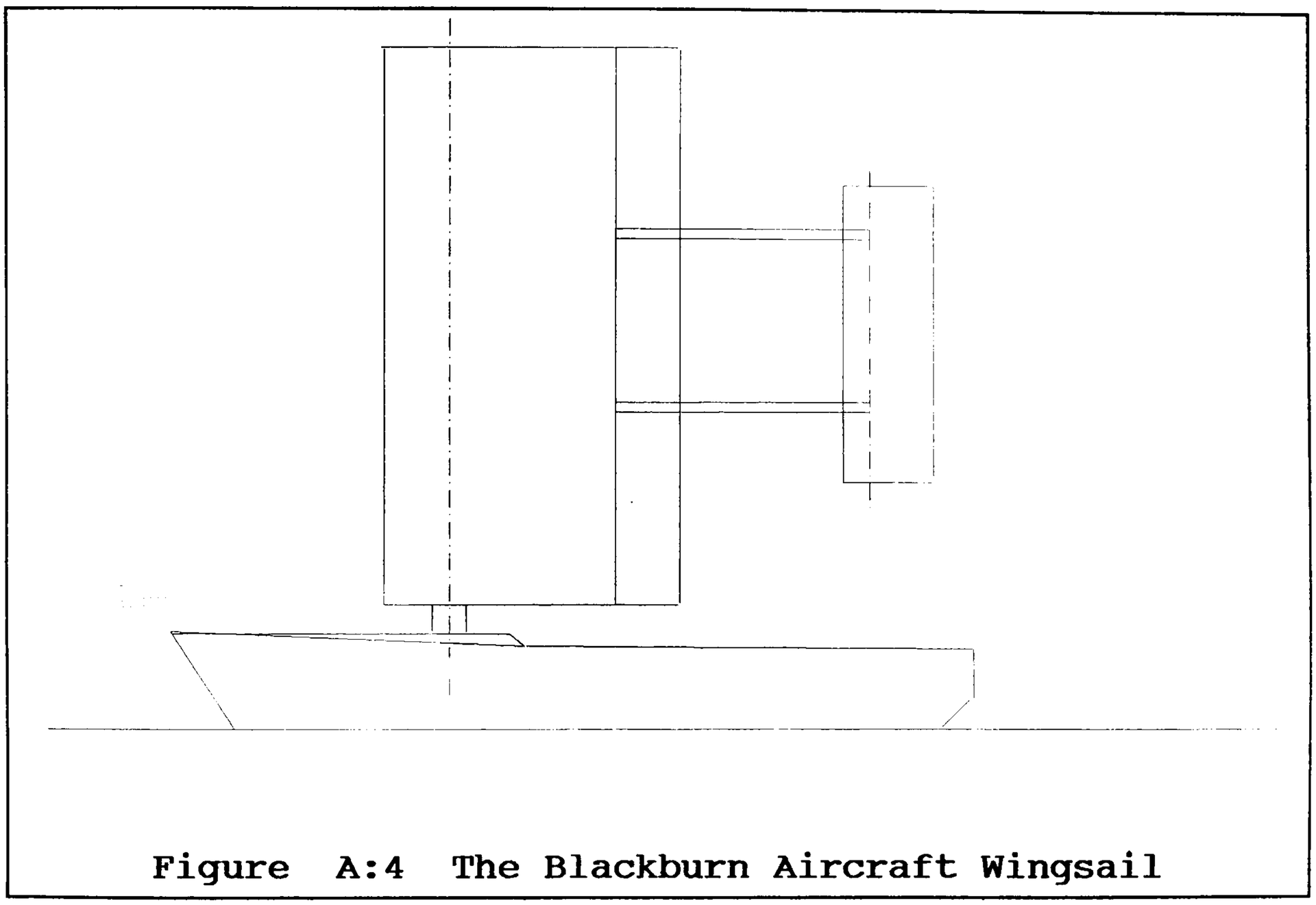

Figure A:4 The Blackburn Aircraft Wingsail

A.4 Planesail (1964)

The first design by J.G.Walker [18] an engineer who is very prominent in this field. 'Planesail' was a 10m long trimaran, propelled by four parallel wingsails. She shared the simple symmetrical NACA 0015 section with 'Flaunder' ,and according to all reports, worked extremely well.

A.5 Flyer (1976)

Another vessel from drawing board of John Walker, a 10m long vessel, equipped with a 7.2m x 2.5m single wingsail. The wingsail is mounted on a slewing ring type bearing, and trimmed by a low aspect ratio tail vane mounted on a single boom, aft of the sail, shown in **Figure A:5**.

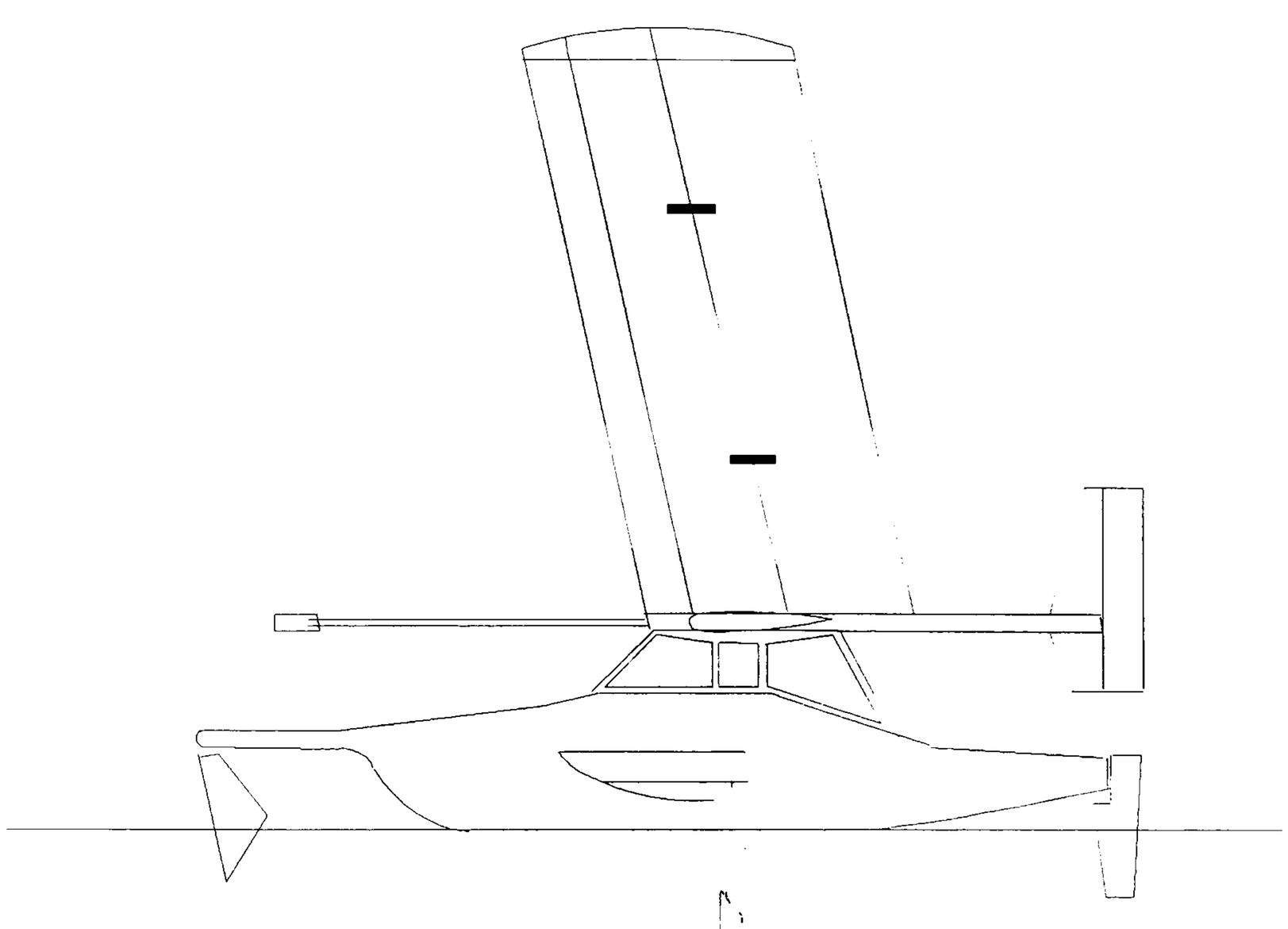

Figure A:5 The Walker Wingsail 'Flyer'

On the water 'Flyer' was a great success, giving controlled thrust exactly as designed. The hydraulic controls were operated by microprocessor, giving progressive thrust availability from zero to maximum. In a force 5 wind, Flyer would either lie quite stationary when desired, or leave a 70hp chase boat standing when switched to 'ahead'.

A.6 Windship Development Corporation (1979)

The commission of the Windship Development Corporation (Headed by Lloyd Bergeson and based in Norwell, Mass.) did not immediately produce a wingsail design, but were influential in wingsail development nevertheless. The U.S. Maritime Administration (MARAD) was the first client of this newly developed company, they commissioned the first study into "Wind propulsion for ships of the American merchant marine". This lead to the design of Mini Lace and Golden Bear, the two best documented sail-assist trials to date. Both vessels proved that the wingsail was the most suitable sail-assist device for the future.

A.7 Shin-Aitoku-Maru (1980)

The Japanese tanker, the Shin-Aitoku-Maru (shown in **Figure A:6)** was launched in 1980. She was the world's first sail-assisted commercial ship, a 1600 dwt tanker. She was a fuel efficient vessel, equipped with a fully automated wingsail control system which required no extra crew.

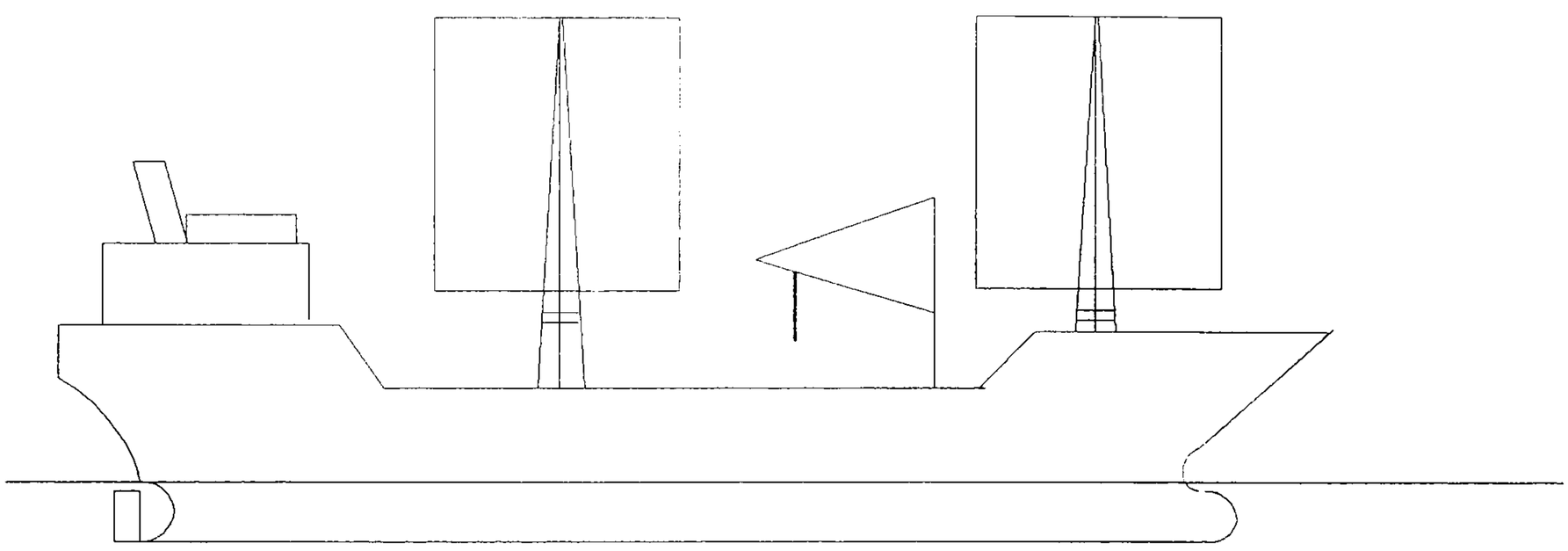

Figure A:6 The Shin-Aitoku-Maru

The Japanese continued with the development of their wind assist programme and by 1987 a total of 15 wind assisted ships had come into service. This included the 26000 dwt bulk carrier 'Usaki Pioneer', chemical tanker 'Shinoku Maru' and the 319g/t tuna long liner 'Yichago Maru no.1'. These ships were not just designed as motor ships with sails, but in fact totally integrated energy saving vessels. Accordingly, the Shin-Aitoku-Maru sail area was small, just 200m^2 compared with 2400m^2 of the famous 'Cutty Sark', despite the fact that both are approximately the same size.

A.8 Mini Lace (1980)

Mini Lace was a 3000 dwt Greek flag ship with a 3000ft^2 Cat rig. The vessel was designed in parallel with an identical sister ship which was to be fitted with a wingsail. After 14 months of service, the owner reported savings of at least 24% and over 30% on favourable routes. Due to a worldwide recession in the shipping industry, the wingsail version was never built. This was unfortunate as simulations had promised even greater fuel savings.

A.9 Ashington (1986)

The Ashington, a carrier vessel, was the first fitment of the module 2 'Walker Wingsail'. The module 2 was the most highly sophisticated wingsail built so far and is similar to the Walker Wingsails in production today. The control system was fully microprocessor controlled and the vessel owners were very satisfied with the performance of the wingsail. When the vessel changed hands, the new vessel owners were not keen to have the wingsail on the vessel and it was removed.

A.10 Blue Nova 1989

Designed and constructed by Walker Wingsails, Blue Nova is a 53ft luxury trimaran. This trimaran has achieved great success and silenced the critics of wingsail design. In 1991/2 Blue Nova sailed from Plymouth to the United States, where it stole the limelight at the national boat shows. The Walker wingsail dispelled any of the fears voiced by sailors and ship operators about the reliability of these devices. During the transatlantic crossing the multihull encountered, and rode out, two huge storms with the sail set to 'feather'.

The Walker wingsails are by far the most sophisticated wingsails built to date, they are light, strong and extremely efficient. The wingsail can produce a C_{Lmax} of over 2.8 and wind tunnel tests have produced C_{Lmax} values greater than three. Walker wingsails are currently altering production to a 40ft trimaran, with similar cabin area as Blue Nova, but powered by one single forward swept wingsail.

Appendix B

COMPUTATIONAL CODE

B.1 Data Aquisition Code (PASCAL)

B.1.1 Windtunnel Force Readings

```
{************************ VARIABLES DEFINED HERE ***********************}
uses crt, dos;
type string_80 = string[80];
var BAAD,
    BAIO                    :word;
    sampleLO,
    sampleHI                :byte;
    ans,
    lift,drag,sforce,
    pitch,roll,yaw,
    catchyn,
    scan,
    tunn,
    ans_scani,
    ans_tunnel,
    corr_scani,
    corr_tunnel             :char;
    regs                    :registers;
    chan,
    stop,
    filter,
    home,
    count,
    porte,
    samples,
    mintapp,
    maxtapp,
    atmos,
    angle,
    cycles                  :integer;
    postive,
    update_tunnel,
    update_scani,
    cont                    :boolean;
    volt_tunnel,
    average,
    check,
    newcheck,
    total,
    newcalib,
    calib                   :array[1..16] of real;
    volt_scani,
    calib_scani,
```

```
    av_volt,
    average_calib          :array[1..50] of real;
    data_tunnel            :array[1..16] of word;
    data_scani             :array[1..50] of word;
    fce                    :array[1..6] of string;
    fce_ans                :array[1..6] of char;
    tunnelfylenom,
    scanifylenom           :text;
    namefiletunnel,
    namefilescani          :string;

{********************** PROCEDURES DEFINED HERE **********************}

procedure beep;
begin
  sound(700);
  delay(100);
  nosound
end;

procedure cursor_off;
begin
with regs do
  begin
  regs.ah:=$01;
  regs.ch:=$20;
  regs.cl:=$20;
  end;
intr($10,regs);
end;

procedure cursor_on;
begin
  with regs do
    begin
      regs.ah:=$01;
      regs.ch:=$0C;
      regs.cl:=$0D;
    end;
  intr($10,regs);
end;

procedure cent(y:integer; writing:string_80);
var x: integer;
begin
  x:=Round((80-length(writing))/2);
  GotoXY(x,y);
  write(writing)
end;

procedure puts(x,y:integer; writing:string_80);
begin
  GotoXY(x,y);
  write(writing);
end;

Procedure init_addr;
begin
  BAAD:=$300;
  BAIO:=$600;
  port[BAIO+3]:=$82;
  port[BAIO+0]:=0;
end;

procedure init_fce;
begin
  fce[1]:='ROLL';
  fce[2]:='PITCH';
  fce[3]:='DRAG';
```

```
  fce[4]:='SIDE FORCE';
  fce[5]:='LIFT';
  fce[6]:='YAW';
end;

procedure convert_to_volts;
begin
  if (data_tunnel[chan] AND 2048)=0 then postive:=true else postive:=false;
  if postive=true then volt_tunnel[chan]:=4*data_tunnel[chan]/4095
             else volt_tunnel[chan]:=-4*(4095-data_tunnel[chan])/4095;
  average[chan]:=average[chan]+volt_tunnel[chan];
end;

procedure tunnel_menu;
begin
  clrscr;
  textcolor(lightblue);
  cursor_off;
  cent(1,'UNIVERSITY OF SALFORD');
  cent(2,'WINDTUNNEL NO.1 DATA AQUISITION');
  cent(3,'SOFTWARE');
  cent(4,'written by: D.Atkins');
  textcolor(white);
  repeat
   { cent(6,'ENTER THE FORCES/MOMENTS YOU WISH TO RECORD:');
   { init_fce;
   { count:=1;
   { repeat
   {   gotoxy(15,7+count);
   {   write(fce[count],' Y/N? ');
   {   repeat
   {     gotoxy(40,7+count);
   {     fce_ans[count]:=readkey;
   {     fce_ans[count]:=upcase(fce_ans[count]);
   {     if (fce_ans[count] = 'Y') or (fce_ans[count] = 'N')
   {     then write(fce_ans[count]);
   {   until (fce_ans[count] = 'Y') or (fce_ans[count] = 'N');
   {   inc(count);
   { until count=7;
   {************** Ph.D ammendment *************}
    init_fce;
    fce_ans[1]:= 'N';
    fce_ans[2]:= 'Y';
    fce_ans[3]:= 'Y';
    fce_ans[4]:= 'N';
    fce_ans[5]:= 'Y';
    fce_ans[6]:= 'N';
    repeat
      puts(5,10,'ENTER INITIAL INCIDENCE ANGLE ..... (deg)');
      gotoxy(62,10);
      readln(angle);
    until angle>=0;
   { ****************************************}
   textcolor(lightred+blink);
   cent(25,'press any key to continue .....');
   repeat until keypressed;
   catchyn:=readkey;
   textcolor(white);
   cent(25,'                                  ');
   beep;
   cursor_on;
   puts(5,16,'ENTER THE FILENAME FOR THE RESULTS TO BE STORED IN ...          ');
   puts(5,17,'(if no path is specified the data will follow the default path)');
   gotoxy(62,16);
   readln(namefiletunnel);
   puts(5,20,'DO YOU WISH TO ADD THE DATA TO AN EXISTING FILE Y/N   ');
   repeat
     gotoxy(62,20);
     ans_tunnel:=readkey;
```

```
    ans_tunnel:=upcase(ans_tunnel);
    if (ans_tunnel='Y') or (ans_tunnel='N') then write(ans_tunnel);
  until (ans_tunnel='Y') or (ans_tunnel='N');
  if ans_tunnel = 'Y' then update_tunnel:=true else update_tunnel:=false;
  cent(22,'ARE THESE ANSWERS CORRECT? ....  Y/N');
  repeat
    gotoxy(62,22);
    corr_tunnel:=readkey;
    corr_tunnel:=upcase(corr_tunnel);
    if (corr_tunnel='Y') or (corr_tunnel='N') then write(corr_tunnel);
  until (corr_tunnel='Y') or (corr_tunnel='N');
until (corr_tunnel='Y');
textcolor(lightred+blink);
cent(25,'PRESS ANY KEY TO CONTINUE .....');
  repeat until keypressed;
  catchyn:=readkey;
  textcolor(white);
  beep;
end;

procedure callibrate;
begin
  if chan=1 then calib[chan]:=(average[chan]+0.03)/-0.1413;
  if chan=2 then calib[chan]:=(average[chan]+0.047)/-0.068066;
  if chan=3 then calib[chan]:=(average[chan])/-0.01149;
  if chan=4 then calib[chan]:=(average[chan]-0.025)/0.00588;
  if chan=5 then calib[chan]:=(average[chan]-1.196)/-0.00349;
  if chan=6 then calib[chan]:=(average[chan]-0.16)/-0.131;
end;

procedure tunnel_to_disk;
begin
  chan:=1;
  assign(tunnelfylenom,namefiletunnel);
  if update_tunnel=true then append(tunnelfylenom) else rewrite(tunnelfylenom);
  repeat
    if fce_ans[chan] <> 'Y' then inc(chan) else
    begin
      write(tunnelfylenom, newcalib[chan]:10:3);
      inc(chan);
    end;
  until chan=7;
  writeln(tunnelfylenom,  angle:4);
  close(tunnelfylenom);
  cursor_on;
end;

procedure scan_port;
begin
  port[BAAD+3]:=8;
  delay(10);
  port[BAAD+2]:=0;
  delay(10);
  sampleLO:=port[BAAD];
  sampleHI:=port[BAAD+1] and $F;
  data_scani[porte]:=256*sampleHI +sampleLO;
  if (data_scani[porte] AND 2048)=0 then postive:=true else postive:=false;
  if postive=true then volt_scani[porte]:=4*data_scani[porte]/4095
                  else volt_scani[porte]:=-4*(4095-data_scani[porte])/4095;
  volt_scani[porte]:=volt_scani[porte];
  calib_scani[porte]:=volt_scani[porte];
  calib_scani[porte]:=((calib_scani[porte]+0.0205)/0.000205);
  av_volt[porte]:=av_volt[porte]+volt_scani[porte];
  average_calib[porte]:=average_calib[porte]+calib_scani[porte];
end;

procedure step_port;
begin
  port[BAIO+0]:=1;
```

```
  delay(1);
  port[BAIO+0]:=0;
end;

procedure scani_menu;
begin
  clrscr;
  mintapp:=0;
  repeat
    textcolor(lightblue);
    cent(4,'**********  SCANIVALVE MENU  **********');
    textcolor(white);
    cent(8,'ENTER THE NUMBER OF PRESSURE TAPPINGS TO BE RECORDED');
    puts(25,9,'zero inclusive (49 max).....');
  repeat
    gotoxy(65,9);
    read(maxtapp);
    until (maxtapp<=48) and (maxtapp>=mintapp);
  puts(5,13,'ENTER THE NUMBER OF SAMPLES TO BE TAKEN AT EACH PORT.... ');
  puts(5,14,'       (100 samples on 49 ports will take 30 seconds)');
  gotoxy(65,13);
  readln(samples);
  puts(5,16,'ENTER THE FILENAME FOR THE RESULTS TO BE STORED IN ... ');
  puts(5,17,'(if no path is specified the data will follow the default path)');
  gotoxy(65,16);
  readln(namefilescani);
  if (namefilescani=namefiletunnel) then
  begin
    update_scani:=true;
  end
  else
  begin
    puts(5,19,'DO YOU WISH TO ADD THE DATA TO AN EXISTING FILE Y/N   ');
    gotoxy(65,19);
      repeat
        ans_scani:=readkey;
        ans_scani:=upcase(ans_scani);
        if (ans_scani='Y') or (ans_scani='N') then write(ans_scani);
      until (ans_scani='Y') or (ans_scani='N');
      if ans_scani = 'Y' then update_scani:=true else update_scani:=false;
    end;
    cent(22,'ARE THESE ANSWERS CORRECT? ....  Y/N');
    repeat
      gotoxy(65,22);
      corr_scani:=readkey;
      corr_scani:=upcase(corr_scani);
      if (corr_scani='Y') or (corr_scani='N') then write(corr_scani);
    until (corr_scani='Y') or (corr_scani='N');
  until (corr_scani='Y');
  delay(500);
  clrscr;
end;

procedure home_port;
begin
cycles:=0;
  repeat
    home:=port[BAIO+1] and $1;
    if home<>1 then
    begin
      port[BAIO+0]:=1;
      delay(5);
      port[BAIO+0]:=0;
    end else begin end;
    inc(cycles);
    delay(100);
  until home=1;
end;
```

```
procedure scani_to_disk;
begin
  count:=mintapp;
  assign(scanifylenom,namefilescani);
  if update_scani=true then append(scanifylenom) else rewrite(scanifylenom);
  writeln(scanifylenom,'');
  repeat
    writeln(scanifylenom, count:4, average_calib[count]:10:3, av_volt[count]:10:3);
    inc(count);
  until count=(maxtapp+1);
  close(scanifylenom);
end;

procedure tunnel;
begin
  clrscr;
  chan:=1;
  cycles:=1;
  repeat
    total[chan]:=0;
    newcalib[chan]:=0;
    check[chan]:=0;
    newcheck[chan]:=0;
    inc(chan);
  until chan=7;
  chan:=1;
  cent(4,'VOLTAGE  NEWTONS  CYCLES  ALLAVERAGE');
  cent(5,'-----------------------------------');
  repeat
    repeat
      if (fce_ans[chan] <> 'Y') then inc(chan);
    until fce_ans[chan] = 'Y';
    port[BAAD+3]:=chan-1;
    average[chan]:=0;
    filter:=1;
    repeat
      port[BAAD+2]:=0;
      delay(1);
      sampleLO:=port[BAAD];
      sampleHI:=port[BAAD+1] AND $F;
      data_tunnel[chan]:=256*sampleHI + sampleLO;
      convert_to_volts;
      filter:=filter+1
    until filter=500;
    filter:=filter-1;
    average[chan]:=(average[chan]/filter);
    check[chan]:=check[chan]+average[chan];
    newcheck[chan]:=check[chan]/cycles;
    callibrate;
    total[chan]:=total[chan]+calib[chan];
    newcalib[chan]:=total[chan]/cycles;
    gotoxy(12,6+chan);
    write(angle:4, fce[chan]:10, average[chan]:9:3, calib[chan]:9:3, cycles:6, newcheck[chan]:9:3, newcalib[chan]:10:3);
    inc(chan);
    if chan>=6 then
    begin
      textcolor(lightred+blink);
      cent(25,'PRESS ANY KEY WHEN SATISFIED WITH READINGS ...');
      textcolor(white);
    end else begin end;
    repeat
      if fce_ans[chan] <> 'Y' then inc(chan);
    until fce_ans[chan] = 'Y';
    if chan >=7 then
    begin
      chan:=1;
      cycles:=cycles+1;
    end else begin end;
    port[BAAD+3]:=  (chan-1) AND $F;
```

```
    delay(5);
  until keypressed;
  catchyn:=readkey;
  beep;
  clrscr;
  if update_tunnel=false then
  begin
    tunnel_to_disk;
    update_tunnel:=true;
  end
  else tunnel_to_disk;
  delay(50);
end;

procedure scani;
begin
  clrscr;
  home_port;
  porte:=mintapp;
  for porte:=0 to 50 do
  begin
    volt_scani[porte]:=0;
    calib_scani[porte]:=0;
    av_volt[porte]:=0;
    average_calib[porte]:=0;
  end;
  porte:=0;
  repeat
    count:=0;
    for count:=1 to samples do
    begin
      scan_port;
    end;
    av_volt[porte]:=av_volt[porte]/samples;
    average_calib[porte]:=average_calib[porte]/samples;
    if porte>24 then gotoxy(30,porte-24) else gotoxy(5,porte+1);
    write(porte:4, average_calib[porte]:10:2, av_volt[porte]:7:4);
    step_port;
    delay(250);
    inc(porte);
until porte=maxtapp;
gotoxy(30,25);
textcolor(lightred+blink);
write('press any key to continue ');
repeat
until keypressed;
textcolor(white);
catchyn:=readkey;
clrscr;
if update_scani=false then
begin
  scani_to_disk;
  update_scani:=true;
end
  else scani_to_disk;
  delay(50);
end;

procedure initial_run;
begin
  if (tunn='Y') and (scan='Y') then
  begin
    tunnel_menu;
    scani_menu;
  end
  else if (tunn='Y') and (scan='N') then
  begin
    tunnel_menu;
  end
```

```
else if (tunn='N') and (scan='Y') then
begin
  scani_menu;
end;
if (tunn='Y') and (scan='Y') then
begin
  tunnel;
  scani;
end
else if (tunn='Y') and (scan='N') then
begin
  tunnel;
end
else if (tunn='N') and (scan='Y') then
  begin
    scani;
  end;
end;

procedure get_angle;
begin
  puts(5,15,'ENTER NEW INCIDENCE ANGLE .... (deg)');
  gotoxy(65,15);
  readln(angle);
end;

procedure balance;
begin
  puts(5,10,'WOULD YOU LIKE ANOTHER SET OF BALANCE READINGS ?      Y/N  ');
  gotoxy(65,10);
  repeat
    tunn:=readkey;
    tunn:=upcase(tunn);
    if (tunn='Y') or (tunn='N') then write(tunn);
  until (tunn='Y') or (tunn='N');
  if (tunn='Y') then
  begin
    get_angle
  end else;
end;

procedure valves;
begin
  puts(5,12,'WOULD YOU LIKE ANOTHER SET PRESSURE OF READINGS ?     Y/N  ');
  gotoxy(65,12);
  repeat
    scan:=readkey;
    scan:=upcase(scan);
    if (scan='Y') or (scan='N') then write(scan);
  until (scan='Y') or (scan='N');
end;

procedure roundabout;
begin
stop:=0;
if (tunn='Y') and (scan='Y') then
begin
  tunnel;
  scani;
end else;
if (tunn='Y') and (scan='N') then
begin
  tunnel;
end else;
if (tunn='N') and (scan='Y') then
begin
  scani;
end else;
if (tunn='N') and (scan='N') then
```

```
  begin
    stop:=1
  end else;
end;
procedure next_runs;
begin
  stop:=0;
  clrscr;
  balance;
  scan:='N';
  {roundabout;}
  if (tunn='Y') then begin tunnel; end else;
  if (tunn='N') and (scan='N') then
  begin
    append(tunnelfylenom);
    writeln(tunnelfylenom,'');
    {writeln(tunnelfylenom,'');}
    close(tunnelfylenom);
    stop:=1
  end else;
end;

procedure phd;
begin
  clrscr;
  textcolor(white);
  cent(10,'PRESS ANY KEY TO CONTINUE .....');
  repeat
  until keypressed;
  catchyn:=readkey;
  tunn:='Y';
  scan:='N';
  delay(500);
  beep;
end;

procedure menu_main;
begin
  clrscr;
  textcolor(white);
  cent(10,'PLEASE INDICATE WHICH READINGS YOU WILL REQUIRE.. ');
  cent(13,'WINDTUNNEL FORCES       Y/N');
  cent(14,'SCANIVALVE PRESSURES    Y/N');
  repeat
    gotoxy(60,13);
    tunn:=readkey;
    tunn:=upcase(tunn);
    if (tunn='Y') or (tunn='N') then write(tunn);
  until (tunn='Y') or (tunn='N');
  repeat
    gotoxy(60,14);
    scan:=readkey;
    scan:=upcase(scan);
    if (scan='Y') or (scan='N') then write(scan);
  until (scan='Y') or (scan='N');
  delay(500);
  beep;
end;

{************************ MAIN PROGRAM STARTS HERE ********************}

Begin
  init_addr;
  phd;
  initial_run;
  repeat
    next_runs;
  until stop=1;
End.
```

B.1.2 Scanivalve Program

```
uses crt,dos;

{********************** Variables defined here **********************}

var sampleLO,
    sampleHI                :byte;
    BAAD,
    BAIO                    :word;
    home,
    count,
    porte,
    samples,
    cycles,
    reset,
    maxtapp                  :integer;
    data                    :array[1..50] of word;
    volt,
    calib,
    avcalib,
    average                  :array[1..50] of real;
    pos,
    update                  :boolean;
    namefile                 :string;
    fylenom                  :text;
    catch_yn,
    answer                  :char;

{********************** Procedures defined here **********************}

Procedure init_addr;
begin
  BAAD:=$300;
  BAIO:=$600;
  port[BAIO+3]:=$82;
  port[BAIO+0]:=0;
end;

procedure scani_menu;
begin
  clrscr;
  textcolor(yellow);
  gotoxy(8,8);
  writeln('ENTER THE NUMBER OF PRESSURE TAPPINGS TO BE RECORDED');
  gotoxy(8,9);
  writeln('(1 - 48) ..... ');
  gotoxy(65,9);
  read(maxtapp);
  gotoxy(8,15);
  writeln('ENTER THE NUMBER OF SAMPLES TO BE TAKEN AT EACH PORT.... ');
  writeln('       (100 samples on 48 ports will take 30 seconds)');
  gotoxy(65,15);
  readln(samples);
  clrscr;
  gotoxy(1,8);
  writeln('ENTER THE FILENAME FOR THE RESULTS TO BE STORED IN ... ');
  writeln('(if no path is specified the data will follow the default path)');
  gotoxy(62,8);
  readln(namefile);
  gotoxy(1,12);
  writeln('DO YOU WISH TO ADD THE DATA TO AN EXISTING FILE Y/N   ');
  gotoxy(62,12);
  repeat
    answer:=readkey;
    answer:=upcase(answer);
  until (answer='Y') or (answer='N');
  if answer = 'Y' then update:=true else update:=false;
  textcolor(white);
```

```
  clrscr;
end;

procedure home_port;
begin
  cycles:=0;
  repeat
    home:=port[BAIO+1] AND $1;
    if home<>1 then
    begin
      port[BAIO+0]:=1;
      delay(1);
      port[BAIO+0]:=0;
    end else begin end;
    inc(cycles);
    delay(100);
  until home=1;
end;

procedure scan_port;
begin
  port[BAAD+3]:=8;
  delay(5);
  port[BAAD+2]:=0;
  delay(10);
  sampleLO:=port[BAAD];
  sampleHI:=port[BAAD+1] and $F;
  data[porte]:=256*sampleHI +sampleLO;
  if (data[porte] and 2048)=0 then pos:=true else pos:=false;
  if pos=true then volt[porte]:=4*data[porte]/4095
              else volt[porte]:=-4*(4095-data[porte])/4095;
  volt[porte]:=volt[porte];
  calib[porte]:=volt[porte];
  calib[porte]:=((calib[porte]+0.0205)/0.000205);
  avcalib[porte]:=avcalib[porte]+calib[porte];
  average[porte]:=average[porte]+volt[porte];
end;

procedure step_port;
begin
  port[BAIO+0]:=1;
  delay(1);
  port[BAIO+0]:=0;
end;

procedure write_to_disk;
begin
  count:=0;
  assign(fylenom,namefile);
  if update=true then append(fylenom) else rewrite(fylenom);
  writeln(fylenom,'');
  repeat
    writeln(fylenom, count:4, average[count]:10:3, avcalib[count]:10:3);
    inc(count);
  until count=(maxtapp+1);
  close(fylenom);
end;

{************************ Main program starts here ******************}

Begin
  init_addr;
  scani_menu;
  home_port;
  repeat
    porte:=1;
    reset:=1;
    repeat
      volt[reset]:=0;
```

```
  average[reset]:=0;
  avcalib[reset]:=0;
  inc(reset);
until reset=49;
repeat
  for count:=1 to samples do
  begin
    scan_port;
  end;
  avcalib[porte]:=avcalib[porte]/samples;
  average[porte]:=average[porte]/samples;
  if porte>24 then gotoxy(30,porte-24) else gotoxy(5,porte);
  write(porte:4, average[porte]:10:3, avcalib[porte]:10:3);
  delay(250);
  step_port;
  inc(porte);
until porte=maxtapp+1;
gotoxy(30,25);
textcolor(lightred+blink);
write('press any key to continue ');
repeat
until keypressed;
textcolor(white);
catch_yn:=readkey;
clrscr;
gotoxy(10,10);
writeln('WOULD YOU LIKE ANOTHER SET OF READINGS ?...  Y/N  ');
gotoxy(62,10);
repeat
  answer:=readkey;
  answer:=upcase(answer);
until (answer='Y') or (answer='N');
if update=false then
begin
    write_to_disk;
    update:=true;
  end
  else write_to_disk;
  clrscr;
  home_port;
until answer='N';
End.
```

B.2 ANSYS (.log) Files

B.2.1 Flat Plate

```
/title,Re. NUMBER 1 MILL flow over a FLAT PLATE

!x- 7.593 (0)

!y- 0.000 (0)

FSX = 36.6
FSY = 0.000                    ! free stream velocity

/PREP7                         ! enter preprocessor
ET,1,55                        ! define element type

! Create Flow Region
!DEFINE MODEL
K,1,0,0,
K,2,1,0,
K,3,10,0,
K,4,10,-.001
K,5,1,-.001

L,1,2
L,2,3
L,3,4
L,4,5
L,5,1

!DEFINE DOMAIN
K,6,10,8
K,7,0,8
K,8,-5,8
K,9,-5,0
K,10,-5,-8
K,11,0,-8
K,12,10,-8

/PNUM,DEFAULT
/PNUM,LINE, 1
/PNUM,KPOI,1
/PBC,ALL,,0
/WIN,ALL,ON
LPLOT

LCOMB,1,2
LCOMB,4,5

L,3,6
L,1,7
L,1,9
L,1,11
L,4,12

L,6,7
L,7,8
L,8,9
L,9,10
L,10,11
L,11,12

LPLOT

ESHAPE,2

LESIZE,1,,,100,100
LESIZE,4,,,100,1/100
```

```
LESIZE,2,,,40,400
LESIZE,5,,,40,400
LESIZE,6,,,40,400
LESIZE,7,,,40,400
LESIZE,8,,,40,400
LESIZE,9,,,100,1/100
LESIZE,10,,,40,1/2
LESIZE,11,,,40,1/32
LESIZE,12,,,40,32
LESIZE,13,,,40,2
LESIZE,14,,,100,100

AL,1,2,9,5
AL,5,10,11,6
AL,6,12,13,7
AL,7,14,8,4

AMESH,ALL

DOF,VX,VY,,PRES,TEMP,ENKE,ENDS

! Name boundaries and generate boundary conditions
LSEL,S,LINE,,11,12,
LSEL,A,LINE,,9,10,
LSEL,A,LINE,,13,14,
CM,INLET,LINE
NSLL,S,1
D,ALL,VX,FSX
D,ALL,VY,FSY

LSEL,S,LINE,,2,8,6
LSEL,A,LINE,,3,
CM,OUTLET,LINE
NSLL,S,1
D,ALL,PRES,0

LSEL,S,LINE,,1,
LSEL,A,LINE,,4,
LSEL,A,LINE,,3,
CM,PLATE,LINE
NSLL,S,1
D,ALL,VX,0,,,,VY

ALLSEL

FLDA,1S,JB,FAST
FLDA,1S,IT,600
FLDA,1S,RS,F
FLDA,1S,TB,T
FLDA,1S,PR,T
!FLWRITE,ALL
SAVE,FAST,db,

FINISH
/EXIT,NOSAV
```

B.2.2 Plain Wing

```
PLAIN WING - LOG FILE
OMESH.LOG


/title,Re 3mil flow over an aerofoil (TWFOUR deg)
!x- 47.840 (0), 47.770 (3), 47.578 (6), 47.250 (9),
    ! 46.795 (12), 46.21  (15), 45.496 (18), 44.662 (21)

!y- 0.000 (0), 2.504 (3), 5.001 (6), 7.484 (9),
    ! 9.9465 (12), 12.382 (15), 14.783 (18), 17.144 (21)

FSX = 40.801
FSY = 18.166                ! free stream velocity

/PREP7                      ! enter preprocessor
ET,1,55                     ! define element type

/com,keypoint definition for wing profile

! Define aerofoil section
K,  1,  .00  , .00000, .0
K,  2,  .0125, .02841, .0
K,  3,  .025 , .03922, .0
K,  4,  .05  , .05332, .0
K,  5,  .075 , .06300, .0
K,  6,  .10  , .07024, .0
K,  7,  .15  , .08018, .0
K,  8,  .20  , .08606, .0
K,  9,  .25  , .08912, .0
K, 10,  .30  , .09003, .0
K, 11,  .40  , .08705, .0
K, 12,  .50  , .07941, .0
K, 13,  .60  , .06845, .0
K, 14,  .70  , .05496, .0
K, 15,  .80  , .03935, .0
K, 16,  .90  , .02172, .0
K, 17,  .95  , .01210, .0
K, 18, 1.00  , .00000, .0 ! Changed from y=.00189
K, 19,  .5   , .00000, .0 ! Centre of circle
K, 20,  .0125, -.02841, .0
K, 21,  .025 , -.03922, .0
K, 22,  .05  , -.05332, .0
K, 23,  .075 , -.06300, .0
K, 24,  .10  , -.07024, .0
K, 25,  .15  , -.08018, .0
K, 26,  .20  , -.08606, .0
K, 27,  .25  , -.08912, .0
K, 28,  .30  , -.09003, .0
K, 29,  .40  , -.08705, .0
K, 30,  .50  , -.07941, .0
K, 31,  .60  , -.06845, .0
K, 32,  .70  , -.05496, .0
K, 33,  .80  , -.03935, .0
K, 34,  .90  , -.02172, .0
K, 35,  .95  , -.01210, .0
K, 36,-1.0   ,  .00000, .0 ! Radius of circle
K, 37, 0.4671E-02, 0.17318E-01, .0 ! TESTFIT OF L.E RADIUS
K, 38, 0.4671E-02, -0.17318E-01, .0 ! TESTFIT OF L.E RADIUS

! Points on inner circle
K,40,0.5,0
K,41,0.5,1.5
K,42,-0.25,1.299
K,43,-0.799,0.75
K,44,-1,0
K,45,-0.799,-0.75
K,46,-0.25,-1.299
```

```
K,47,0.5,-1.5
K,48,1.25,-1.299
K,49,1.799,-0.75
K,50,1.799,0.75
K,51,1.25,1.299

! Create splines for wing surface
BSPLIN,P50X
1
11
  10
KX(37),KY(37),KZ(37)
KX(2),KY(2),KZ(2)
KX(3),KY(3),KZ(3)
KX(4),KY(4),KZ(4)
KX(5),KY(5),KZ(5)
KX(6),KY(6),KZ(6)
KX(7),KY(7),KZ(7)
KX(8),KY(8),KZ(8)
KX(9),KY(9),KZ(9)
KX(10),KY(10),KZ(10)
BSPLIN,P50X
11
18
  6
KX(12),KY(12),KZ(12)
KX(13),KY(13),KZ(13)
KX(14),KY(14),KZ(14)
KX(15),KY(15),KZ(15)
KX(16),KY(16),KZ(16)
KX(17),KY(17),KZ(17)
BSPLIN,P50X
1
29
  10
KX(38),KY(38),KZ(38)
KX(20),KY(20),KZ(20)
KX(21),KY(21),KZ(21)
KX(22),KY(22),KZ(22)
KX(23),KY(23),KZ(23)
KX(24),KY(24),KZ(24)
KX(25),KY(25),KZ(25)
KX(26),KY(26),KZ(26)
KX(27),KY(27),KZ(27)
KX(28),KY(28),KZ(28)
BSPLIN,P50X
29
18
  6
KX(30),KY(30),KZ(30)
KX(31),KY(31),KZ(31)
KX(32),KY(32),KZ(32)
KX(33),KY(33),KZ(33)
KX(34),KY(34),KZ(34)
KX(35),KY(35),KZ(35)

CIRCLE,P50X,,,,,4
       2
KX(19),KY(19),KZ(19)
KX(36),KY(36),KZ(36)

KSLL,S       !Selects all points defining a line
KSEL,INVE    !Unselects these points and selects all others
KDEL,ALL     !Deletes these selected points (i.e. not defining lines)
KSEL,ALL     !Reselects all remaining points

/PNUM,LINE,1
/PNUM,KPOI,1
LPLOT
```

```
LDIV,P50X,P50X
7
   0.4828773
LDIV,P50X,P50X
6
   0.5171227

L,18,3
L,18,2
K,,1.35,0.1
K,,1.35,-.1

L,4,5
L,18,53
LCSL,14,13
LANG,11,5,90
LANG,12,4,90

A,18,8,4,6        !1
A,18,6,5,7        !2
A,6,53,2,8,4      !3
A,18,8,2,54,11    !4
A,11,54,39,1      !5
A,1,39,52,29      !6
A,29,52,3,7,18    !7
A,7,3,53,6,5      !8

ESHAPE,2
M=30
M2=M/2

LESIZE,15,,,M2,4
LESIZE,20,,,M2,4
LESIZE,12,,,M2,4
LESIZE,11,,,M2,4
LESIZE,14,,,M2,4
LESIZE,18,,,M2,4
LESIZE,17,,,M2,1/4
!Wing
LESIZE,1,,,M,3
LESIZE,2,,,20,1/3
LESIZE,3,,,M,3
LESIZE,4,,,20,1/3
!Partitions
LESIZE,21,,,M,1/50
LESIZE,22,,,M,1/50
LESIZE,23,,,M,1/50
LESIZE,13,,,M2,10
LESIZE,19,,,M2,10
LESIZE,16,,,M2,10

NUMC,ALL
AMESH,1,2

LCCAT,12,19
LCCAT,11,13
LCCAT,17,20
LCCAT,14,18

AMESH,ALL
NUMC,ALL

CIRCLE,10,11,,,,12
LCOMB,31,32
LCOMB,31,33
LCOMB,34,35
LCOMB,34,36
LCOMB,28,29
LCOMB,38,39
```

```
NUMC,ALL

A,12,15,18,19
A,12,19,20,13
A,13,20,21,3
A,3,21,16,14
A,14,16,17,2
A,2,17,18,15

LESIZE,34,,,25,30
LESIZE,35,,,25,1/30
LESIZE,39,,,25,1/30
LESIZE,38,,,25,1/30
LESIZE,37,,,25,1/30
LESIZE,36,,,25,1/30

AMESH,ALL
NUMM,ALL
NUMC,ALL

DOF,VX,VY,,PRES,TEMP,ENKE,ENDS

LSEL,S,LINE,,29,32
CM,INLET,LINE
NSLL,S,1
D,ALL,VX,FSX
D,ALL,VY,FSY

LSEL,S,LINE,,28
LSEL,A,LINE,,33
CM,OUTLET,LINE
NSLL,S,1
D,ALL,PRES,0

LSEL,S,LINE,,1,4
CM,AFOIL,LINE
NSLL,S,1
D,ALL,VX,0,,,,VY
ALLSEL

FLDA,1S,JB,TWFOUR
FLDA,1S,IT,600
FLDA,1S,RS,F
FLDA,1S,TB,T
FLDA,1S,PR,T
!FLWRITE,ALL
SAVE,TWFOUR,db,
FINISH
/EXIT,NOSAV
```

B.2.3 Triple Element Aerofoil

```
FULL, TRIPLE ELEMENT AEROFOIL (FINAL CONFIGURATION)
TRIPLE.LOG

/title,Re 1mil flow over a TRIPLE aerofoil (15:18:15%) (15:60:40) VARIOUS deg inc
!x- 15.19 (0), 15.17 (3), 15.10 (6), 15.00 (9),
    ! 14.85 (12), 14.67 (15), 14.44 (18), 14.18 (21)
    ! 13.87 (24), 13.53 (27)

!y- 0.000 (0), 0.795 (3), 1.587 (6), 2.376 (9),
    ! 3.157 (12), 3.931 (15), 4.693 (18), 5.442 (21)
    ! 6.177 (24), 6.895 (27)

FSX = 13.53
FSY = 6.895                 ! free stream velocity

/PREP7                      ! enter preprocessor
ET,1,55                     ! define element type

/com,keypoint definition for wing profile

! Define aerofoil section

! SLAT SECTION
K,  1   ,   -0.13558 ,   0    ,
K,  2   ,   -0.13536 ,   0.004009 ,
K,  3   ,   -0.13422 ,   0.006022 ,
K,  4   ,   -0.13156 ,   0.009193 ,
K,  5   ,   -0.12866 ,   0.011862 ,
K,  6   ,   -0.12563 ,   0.014254 ,
K,  7   ,   -0.11934 ,   0.018523 ,
K,  8   ,   -0.11284 ,   0.022332 ,
K,  9   ,   -0.10619 ,   0.02582  ,
K,  10  ,   -0.09943 ,   0.029063 ,
K,  11  ,   -0.08565 ,   0.035007 ,
K,  12  ,   -0.07163 ,   0.040422 ,
K,  13  ,   -0.05743 ,   0.045459 ,
K,  14  ,   -0.0431  ,   0.050209 ,
K,  15  ,   -0.02867 ,   0.054719 ,
K,  16  ,   -0.01412 ,   0.058999 ,
K,  17  ,   -0.00681 ,   0.061048 ,
K,  18  ,   0.000637 ,   0.062815 ,
!K, 19  ,   ERR ,   0    ,
K,  20  ,   -0.13239 ,   -0.00244 ,
K,  21  ,   -0.13012 ,   -0.00288 ,
K,  22  ,   -0.12598 ,   -0.00291 ,
K,  23  ,   -0.12206 ,   -0.00244 ,
K,  24  ,   -0.11828 ,   -0.00169 ,
K,  25  ,   -0.11095 ,   0.000322 ,
K,  26  ,   -0.10383 ,   0.002794 ,
K,  27  ,   -0.09686 ,   0.005587 ,
K,  28  ,   -0.09    ,   0.008626 ,
K,  29  ,   -0.07653 ,   0.015245 ,
K,  30  ,   -0.06331 ,   0.022393 ,
K,  31  ,   -0.05027 ,   0.02992  ,
K,  32  ,   -0.03735 ,   0.037732 ,
K,  33  ,   -0.02455 ,   0.045786 ,
K,  34  ,   -0.01185 ,   0.054068 ,
K,  35  ,   -0.00554 ,   0.058302 ,
!K, 36  ,   0.000637 ,   0.062815 ,

! MAIN WING SECTION
K,   40 ,      0 ,      0 ,
K,   41 ,   0.0075 ,  0.017046 ,
K,   42 ,   0.015 ,   0.023532 ,
K,   43 ,   0.03 ,    0.031992 ,
K,   44 ,   0.045 ,   0.0378 ,
K,   45 ,   0.06 ,    0.042144 ,
```

```
K,    46 ,     0.09 ,   0.048108 ,
K,    47 ,     0.12 ,   0.051636 ,
K,    48 ,     0.15 ,   0.053472 ,
K,    49 ,     0.18 ,   0.054018 ,
K,    50 ,     0.24 ,    0.05223 ,
K,    51 ,      0.3 ,   0.047646 ,
K,    52 ,     0.36 ,    0.04107 ,
K,    53 ,     0.42 ,   0.032976 ,
K,    54 ,     0.48 ,    0.02361 ,
K,    55 ,     0.54 ,   0.013032 ,
K,    56 ,     0.57 ,    0.00726 ,
K,    57 ,      0.6 ,          0 ,
!K    58 ,        0 ,          0 ,
K,    59 ,   0.0075 ,   -0.01705 ,
K,    60 ,    0.015 ,   -0.02353 ,
K,    61 ,     0.03 ,   -0.03199 ,
K,    62 ,    0.045 ,    -0.0378 ,
K,    63 ,     0.06 ,   -0.04214 ,
K,    64 ,     0.09 ,   -0.04811 ,
K,    65 ,     0.12 ,   -0.05164 ,
K,    66 ,     0.15 ,   -0.05347 ,
K,    67 ,     0.18 ,   -0.05402 ,
K,    68 ,     0.24 ,    -0.05223 ,
K,    69 ,      0.3 ,   -0.04765 ,
K,    70 ,     0.36 ,   -0.04107 ,
K,    71 ,     0.42 ,   -0.03298 ,
K,    72 ,     0.48 ,   -0.02361 ,
K,    73 ,     0.54 ,   -0.01303 ,
K,    74 ,     0.57 ,   -0.00726 ,
!K    75 ,        0 ,          0 ,


! FLAP SECTION
K,    80 ,  0.587939 ,    -0.0684 ,
K,    81 ,  0.595875 ,   -0.06122 ,
K,    82 ,  0.601806 ,   -0.05954 ,
K,    83 ,  0.612811 ,   -0.05854 ,
K,    84 ,  0.623312 ,   -0.05893 ,
K,    85 ,  0.633534 ,   -0.06008 ,
K,    86 ,   0.65346 ,   -0.06381 ,
K,    87 ,  0.672926 ,   -0.06881 ,
K,    88 ,  0.692069 ,   -0.07469 ,
K,    89 ,  0.710965 ,   -0.08125 ,
K,    90 ,  0.748213 ,   -0.09586 ,
K,    91 ,  0.784931 ,   -0.11193 ,
K,    92 ,  0.821268 ,   -0.12905 ,
K,    93 ,  0.857318 ,   -0.14695 ,
K,    94 ,  0.893126 ,   -0.16553 ,
K,    95 ,  0.928704 ,   -0.18473 ,
K,    96 ,  0.946401 ,   -0.19458 ,
K,    97 ,  0.963816 ,   -0.20521 ,
!K,   98 ,  0.587939 ,    -0.0684 ,
K,    99 ,  0.589399 ,   -0.07901 ,
K,   100 ,  0.592865 ,   -0.08411 ,
K,   101 ,  0.600654 ,   -0.09194 ,
K,   102 ,  0.608947 ,    -0.0984 ,
K,   103 ,  0.617519 ,   -0.10408 ,
K,   104 ,   0.63518 ,   -0.11404 ,
K,   105 ,  0.653302 ,   -0.12272 ,
K,   106 ,  0.671747 ,   -0.13052 ,
K,   107 ,  0.690438 ,   -0.13764 ,
K,   108 ,  0.728365 ,   -0.15039 ,
K,   109 ,  0.766823 ,   -0.16168 ,
K,   110 ,  0.805661 ,   -0.17193 ,
K,   111 ,  0.844787 ,   -0.18138 ,
K,   112 ,  0.884154 ,   -0.19018 ,
K,   113 ,  0.923752 ,   -0.19833 ,
K,   114 ,  0.943643 ,   -0.20216 ,
!K,  115 ,  0.963816 ,   -0.20521 ,
```

```
K,    89  ,  0.710965  ,  -0.08125  ,
K,    90  ,  0.748213  ,  -0.09586  ,
K,    91  ,  0.784931  ,  -0.11193  ,
K,    92  ,  0.821268  ,  -0.12905  ,
K,    93  ,  0.857318  ,  -0.14695  ,
K,    94  ,  0.893126  ,  -0.16553  ,
K,    95  ,  0.928704  ,  -0.18473  ,
K,    96  ,  0.946401  ,  -0.19458  ,
K,    97  ,  0.963816  ,  -0.20521  ,
!K,   98  ,  0.587939  ,   -0.0684  ,
K,    99  ,  0.589399  ,  -0.07901  ,
K,   100  ,  0.592865  ,  -0.08411  ,
K,   101  ,  0.600654  ,  -0.09194  ,
K,   102  ,  0.608947  ,   -0.0984  ,
K,   103  ,  0.617519  ,  -0.10408  ,
K,   104  ,   0.63518  ,  -0.11404  ,
K,   105  ,  0.653302  ,  -0.12272  ,
K,   106  ,  0.671747  ,  -0.13052  ,
K,   107  ,  0.690438  ,  -0.13764  ,
K,   108  ,  0.728365  ,  -0.15039  ,
K,   109  ,  0.766823  ,  -0.16168  ,
K,   110  ,  0.805661  ,  -0.17193  ,
K,   111  ,  0.844787  ,  -0.18138  ,
K,   112  ,  0.884154  ,  -0.19018  ,
K,   113  ,  0.923752  ,  -0.19833  ,
K,   114  ,  0.943643  ,  -0.20216  ,
!K,  115  ,  0.963816  ,  -0.20521  ,

K, 19,  .5   , .00000, .0 ! Centre of circle
K, 36,-1.2   ,  .00000, .0 ! Radius of circle

! Create splines for wing surface
! SLAT BSPLINES  ************************************
BSPLIN,P50X
1
11
 9
KX(2),KY(2),KZ(2)
KX(3),KY(3),KZ(3)
KX(4),KY(4),KZ(4)
KX(5),KY(5),KZ(5)
KX(6),KY(6),KZ(6)
KX(7),KY(7),KZ(7)
KX(8),KY(8),KZ(8)
KX(9),KY(9),KZ(9)
KX(10),KY(10),KZ(10)
BSPLIN,P50X
11
18
 6
KX(12),KY(12),KZ(12)
KX(13),KY(13),KZ(13)
KX(14),KY(14),KZ(14)
KX(15),KY(15),KZ(15)
KX(16),KY(16),KZ(16)
KX(17),KY(17),KZ(17)
BSPLIN,P50X
1
29
 9
KX(20),KY(20),KZ(20)
KX(21),KY(21),KZ(21)
KX(22),KY(22),KZ(22)
KX(23),KY(23),KZ(23)
KX(24),KY(24),KZ(24)
KX(25),KY(25),KZ(25)
KX(26),KY(26),KZ(26)
KX(27),KY(27),KZ(27)
KX(28),KY(28),KZ(28)
```

```
BSPLIN,P50X
29
18
  6
KX(30),KY(30),KZ(30)
KX(31),KY(31),KZ(31)
KX(32),KY(32),KZ(32)
KX(33),KY(33),KZ(33)
KX(34),KY(34),KZ(34)
KX(35),KY(35),KZ(35)


! MAIN WING BSPLINES ********************************************
BSPLIN,P50X
40
51
  10
KX(41),KY(41),KZ(41)
KX(42),KY(42),KZ(42)
KX(43),KY(43),KZ(43)
KX(44),KY(44),KZ(44)
KX(45),KY(45),KZ(45)
KX(46),KY(46),KZ(46)
KX(47),KY(47),KZ(47)
KX(48),KY(48),KZ(48)
KX(49),KY(49),KZ(49)
KX(50),KY(50),KZ(50)
BSPLIN,P50X
51
57
  5
KX(52),KY(52),KZ(52)
KX(53),KY(53),KZ(53)
KX(54),KY(54),KZ(54)
KX(55),KY(55),KZ(55)
KX(56),KY(56),KZ(56)
BSPLIN,P50X
40
69
  10
KX(59),KY(59),KZ(59)
KX(60),KY(60),KZ(60)
KX(61),KY(61),KZ(61)
KX(62),KY(62),KZ(62)
KX(63),KY(63),KZ(63)
KX(64),KY(64),KZ(64)
KX(65),KY(65),KZ(65)
KX(66),KY(66),KZ(66)
KX(67),KY(67),KZ(67)
KX(68),KY(68),KZ(68)
BSPLIN,P50X
69
57
  5
KX(70),KY(70),KZ(70)
KX(71),KY(71),KZ(71)
KX(72),KY(72),KZ(72)
KX(73),KY(73),KZ(73)
KX(74),KY(74),KZ(74)


! FLAP BSPLINES *************************************************

BSPLIN,P50X
80
91
  10
KX(81),KY(81),KZ(81)
```

```
KX(82),KY(82),KZ(82)
KX(83),KY(83),KZ(83)
KX(84),KY(84),KZ(84)
KX(85),KY(85),KZ(85)
KX(86),KY(86),KZ(86)
KX(87),KY(87),KZ(87)
KX(88),KY(88),KZ(88)
KX(89),KY(89),KZ(89)
KX(90),KY(90),KZ(90)
BSPLIN,P50X
91
97
  5
KX(92),KY(92),KZ(92)
KX(93),KY(93),KZ(93)
KX(94),KY(94),KZ(94)
KX(95),KY(95),KZ(95)
KX(96),KY(96),KZ(96)
BSPLIN,P50X
80
109
  10
KX(99),KY(99),KZ(99)
KX(100),KY(100),KZ(100)
KX(101),KY(101),KZ(101)
KX(102),KY(102),KZ(102)
KX(103),KY(103),KZ(103)
KX(104),KY(104),KZ(104)
KX(105),KY(105),KZ(105)
KX(106),KY(106),KZ(106)
KX(107),KY(107),KZ(107)
KX(108),KY(108),KZ(108)
BSPLIN,P50X
109
97
  5
KX(110),KY(110),KZ(110)
KX(111),KY(111),KZ(111)
KX(112),KY(112),KZ(112)
KX(113),KY(113),KZ(113)
KX(114),KY(114),KZ(114)


CIRCLE,P50X,,,,,4
       2
KX(19),KY(19),KZ(19)
KX(36),KY(36),KZ(36)

KSLL,S       !Selects all points defining a line
KSEL,INVE    !Unselects these points and selects all others
KDEL,ALL     !Deletes these selected points (i.e. not defining lines)
KSEL,ALL     !Reselects all remaining points

/PNUM,LINE, 1
/PNUM,KPOI,1
LPLOT

/ZOOM,  1,-0.40985E-01, 0.25856E-01, 0.00000E+00, 0.16089

LDIV,5,0.6661562E-01
LDIV,4,0.6861636

LCOMB,5,7

LDIV,17,0.9421589E-01
LDIV,13
LDIV,16
LDIV,5,0.1216955
```

```
L,4,18
L,18,6
L,7,5
L,2,3

LDIV,3,0.6367167E-01

LCOMB,1,3
L,8,37
K,,P50X
-.150685863     ,-.940827916E-01,0.000000000E+00
L,8,1

LDIV,24,0.1131132

/ZOOM,  1,-0.78244E-01, 0.18441E-02, 0.00000E+00, 0.29275

L,1,9
LCOMB,4,26
LDIV,4,0.4970721
L,7,10

NUMMRG,ALL
NUMCMP,ALL

!MESH INSIDE SLAT
AL,17,22,18,25
AL,5,25,4,30
AL,24,30,26,27,29

LESIZE,22,,,15
LESIZE,25,,,15
LESIZE,30,,,15
LESIZE,24,,,15,6
LESIZE,27,,,15,4
LESIZE,29,,,15
LESIZE,29,,,30
LESIZE,26,,,15
LESIZE,4,,,15
LESIZE,5,,,15
LESIZE,17,,,15
LESIZE,18,,,15
LCCAT,26,30
ESHAPE,2
AMESH,ALL

! MESH OUTSIDE SLAT
/ZOOM,  1,-0.11278     , 0.17600E-01, 0.00000E+00, 0.34977

K,,P50X
-.321850739     ,0.201208257     ,0.000000000E+00
K,,P50X
-.321850739     ,-.187400686     ,0.000000000E+00

L,24,25
LANG,23,24,90
LANG,28,25,90
LCSL,32,3
LCOMB,1,2

AL,1,23,34,37,39
AL,39,38,36,28,29,27

LESIZE,23,,,15,10
LESIZE,34,,,15
LESIZE,37,,,15
LESIZE,1,,,30,3
LESIZE,39,,,15,4
LESIZE,28,,,15
```

```
LESIZE,38,,,15
LESIZE,36,,,15
LESIZE,38,,,22
LESIZE,36,,,23

LCCAT,34,37
LCCAT,38,36
LCCAT,27,29

AMESH,ALL

!TRAILING EDGE MESH

LDIV,14,
LDIV,15,0.4333616

L,17,18
L,22,15
L,22,29
L,22,11

LDIV,9,0.2198859
LDIV,8,0.6457440

L,17,30
L,20,31
LCOMB,10,47
LCOMB,11,12
LCOMB,6,7
LCOMB,8,21
L,31,14

/ZOOM,  1,  1.2361     ,-0.17273     , 0.00000E+00, 0.42233
K,,P50X
 1.44544718     ,0.102207337     ,0.000000000E+00
K,,P50X
 1.44544718     ,-.393380722     ,0.000000000E+00

L,16,19
LANG,45,16,90
LANG,46,19,90
LCSL,12,44

LESIZE,45,,,20,5
LESIZE,46,,,20,5
LESIZE,55,,,20,4
LESIZE,47,,,20
LESIZE,53,,,20
LESIZE,54,,,20
LESIZE,52,,,20
LESIZE,51,,,30,3
LESIZE,56,,,30,3
LESIZE,21,,,30,3

AL,55,53,47,45
AL,55,46,52,54

AMESH,ALL

AL,54,52,51,41,56
AL,56,15,21,47,53
LCCAT,47,53
LCCAT,54,52

AMESH,ALL

! MESH INSERT BETWEEN WING T.E. AND FLAP
/ZOOM,  1, 0.57240     ,-0.23791E-01, 0.00000E+00, 0.27150
```

```
LDIV,11,P50X
   0.3009076E-01
L,33,31
LDELE,50
LCOMB,9,11

LESIZE,49,,,10
LESIZE,58,,,10,1/5
LESIZE,9,,,15,4
LESIZE,48,,,15,1/3

AL,9,49,48,58

AMESH,ALL

! MESH THE REST
/ZOOM,1,OFF

LESIZE,10,,,20,1/3
LESIZE,57,,,20,3/2
LESIZE,43,,,50,10
LESIZE,6,,,35,1/2
LESIZE,33,,,20,3
LESIZE,40,,,20,3
LESIZE,35,,,20,3
LESIZE,7,,,50,10
LESIZE,8,,,35,1/2

AL,49,10,45,21,42,43
AL,6,43,16,33,23,22
AL,37,34,33,20,40
AL,40,13,35,36,38
AL,8,24,28,35,19,7
AL,58,7,14,51,46,57

LCCAT,45,21
LCCAT,49,10
AMESH,11

LCCAT,P50X,,33
     3
22
23
33
AMESH,12

LCCAT,34,37
LCCAT,36,38

AMESH,13,14

LCCAT,P50X
     3
24
28
35

AMESH,15

LCCAT,57,58
LCCAT,46,51

AMESH,16

!!!!!!!!!

! OUTER CIRCLE
/ZOOM,1,OFF
```

```
CIRCLE,17,10,,,,12
LPLOT

LCOMB,68,69
LCOMB,70,71
LCOMB,64,65
LCOMB,64,66
LDIV,64
LCOMB,73,74
LCOMB,73,75
LDIV,73

L,15,20
L,29,34
L,18,36
L,6,37
L,13,39
L,5,41
L,14,42
L,11,35

AL,15,69,64,71
AL,42,71,65,74
AL,16,74,67,75
AL,20,75,68,76
AL,13,76,70,77
AL,19,77,72,78
AL,14,78,73,79
AL,41,79,66,69

LESIZE,69,,,20,20
LESIZE,71,,,20,20
LESIZE,74,,,20,20
LESIZE,75,,,20,20
LESIZE,76,,,20,20
LESIZE,77,,,20,20
LESIZE,78,,,20,20
LESIZE,79,,,20,20

AMESH,ALL

DOF,VX,VY,,PRES,TEMP,ENKE,ENDS

LSEL,S,LINE,,65,
LSEL,A,LINE,,67,68
LSEL,A,LINE,,70,
LSEL,A,LINE,,72,73
CM,INLET,LINE
NSLL,S,1
D,ALL,VX,FSX
D,ALL,VY,FSY

LSEL,S,LINE,,64,66,2
CM,OUTLET,LINE
NSLL,S,1
D,ALL,PRES,0

LSEL,S,LINE,,4,6,
LSEL,A,LINE,,1,
LSEL,A,LINE,,8,10,
LSEL,A,LINE,,17,18,
LSEL,A,LINE,,26,
LSEL,A,LINE,,48,
LSEL,A,LINE,,57,
CM,AFOIL,LINE
NSLL,S,1
D,ALL,VX,0,,,,VY
ALLSEL
```

```
NUMMRG,ALL
NUMCMP,ALL

FLDA,1S,JB,TWENTSEV
FLDA,1S,IT,600
FLDA,1S,RS,F
FLDA,1S,TB,T
FLDA,1S,PR,T
FLWRITE,ALL
!SAVE,NINE,DB,
FINISH
/EXIT,NOSAV
```

Appendix C

TECHNICAL DRAWINGS

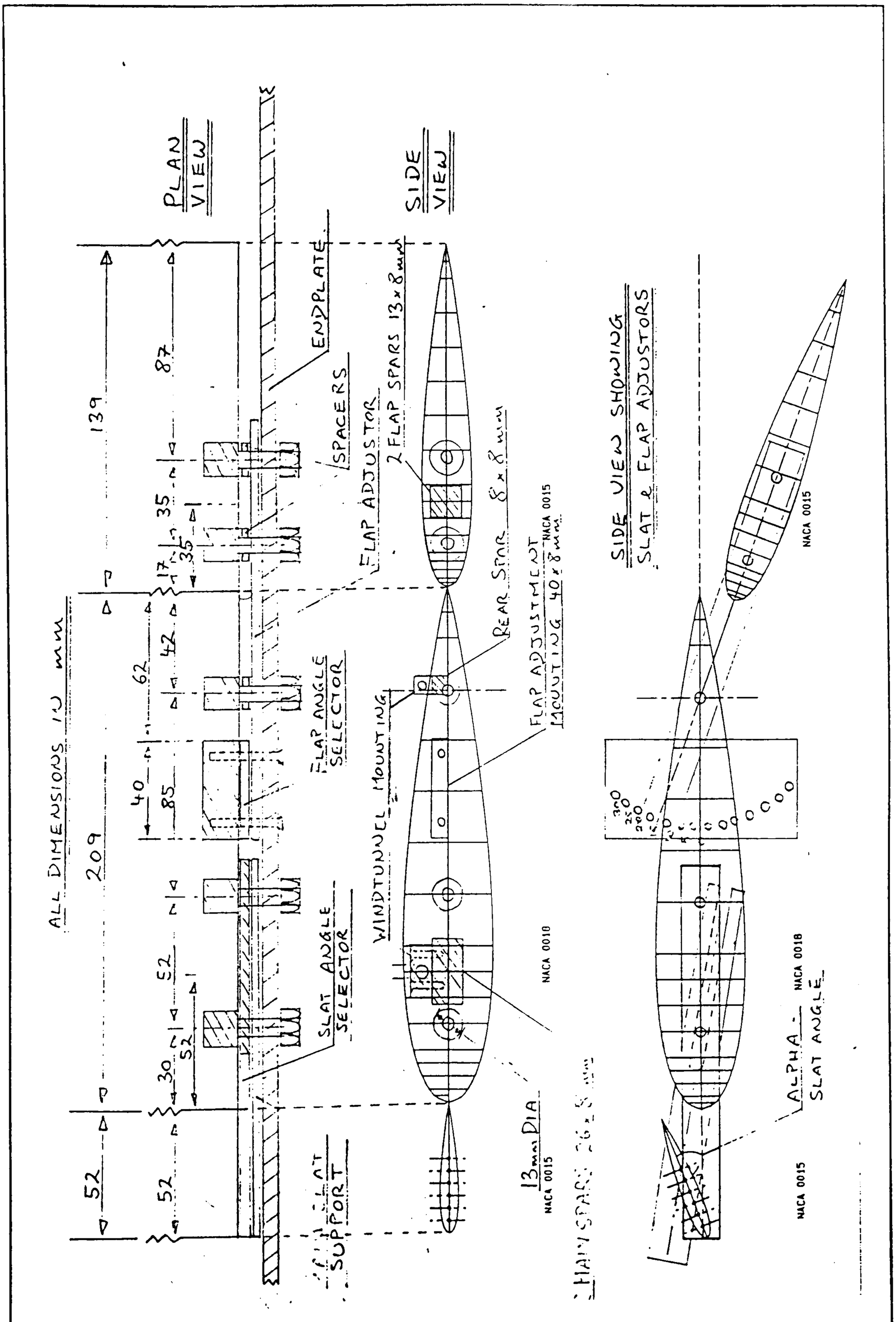

Figure C:1 Model III - Construction

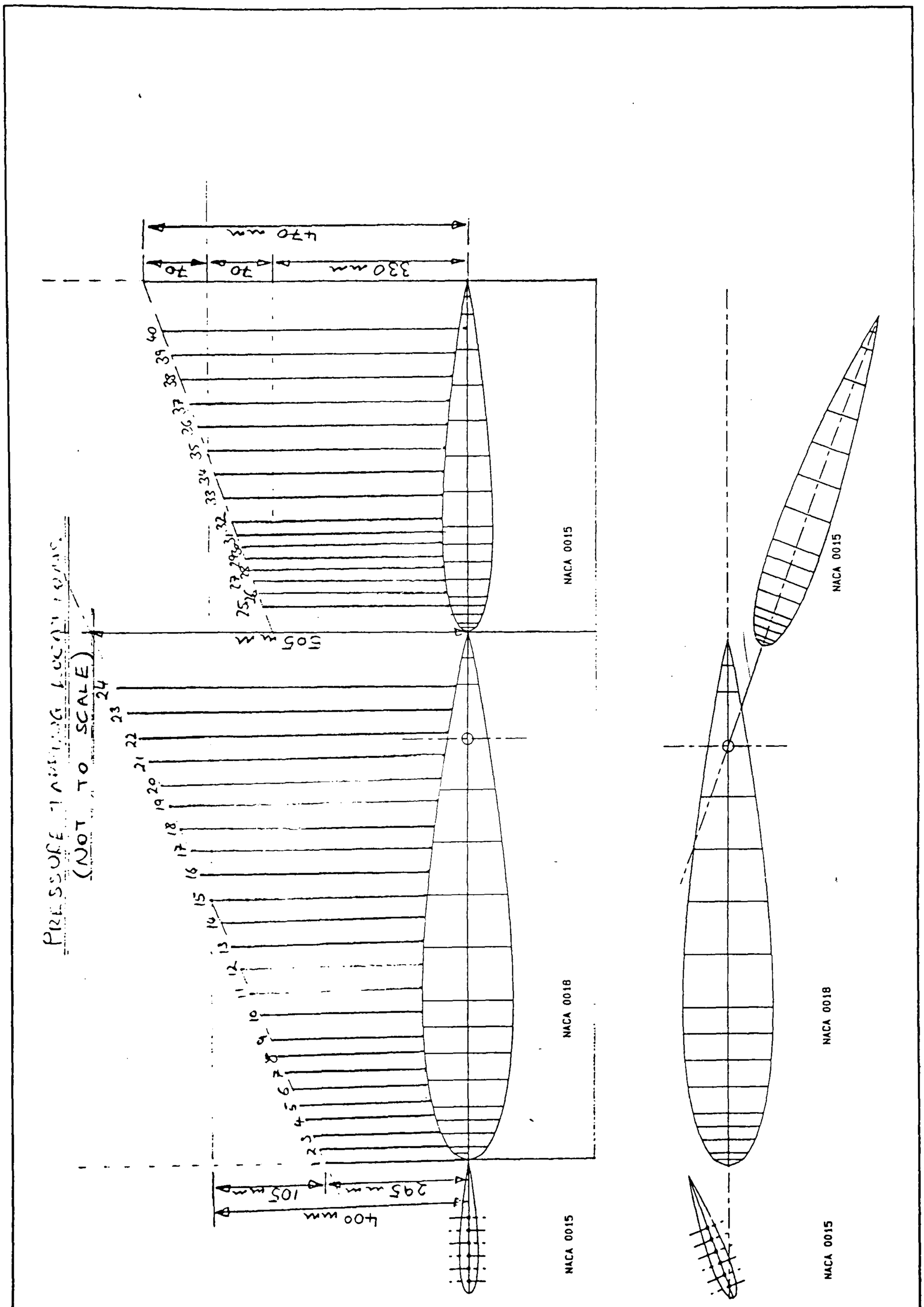

Figure C:2 Pressure Tapping Position

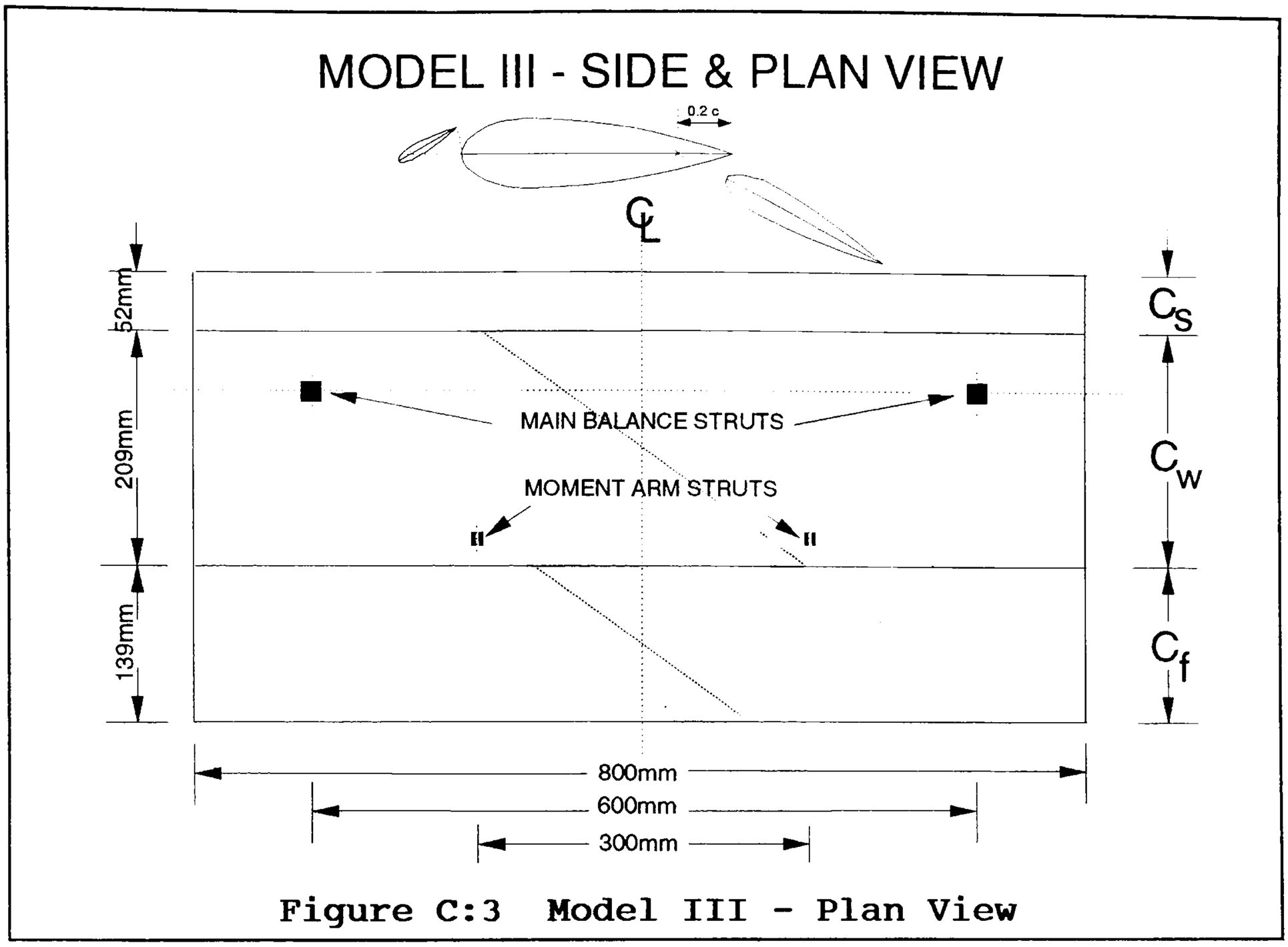

Figure C:3 Model III - Plan View

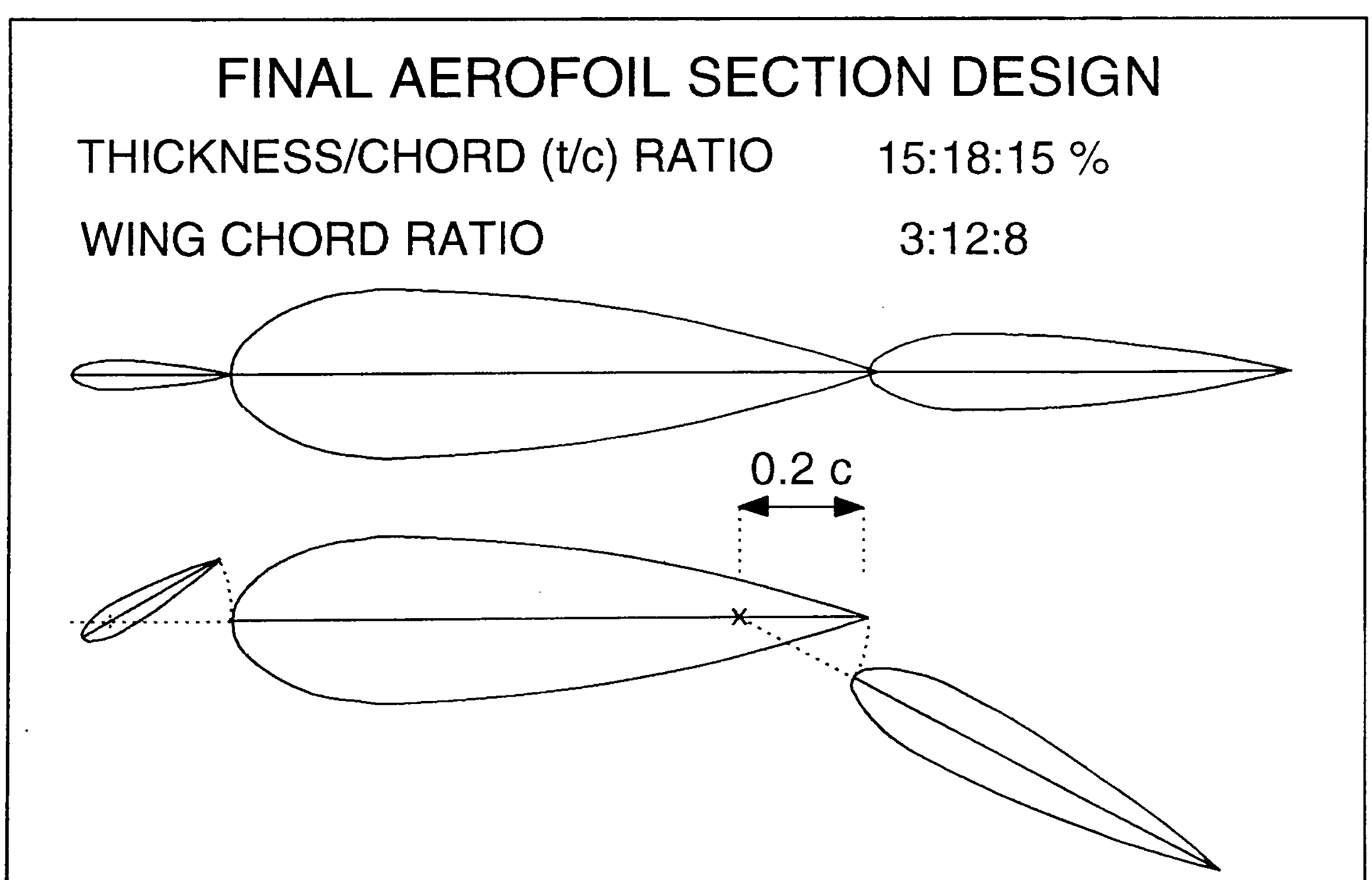

Figure C:4 Model III - Final Configuration

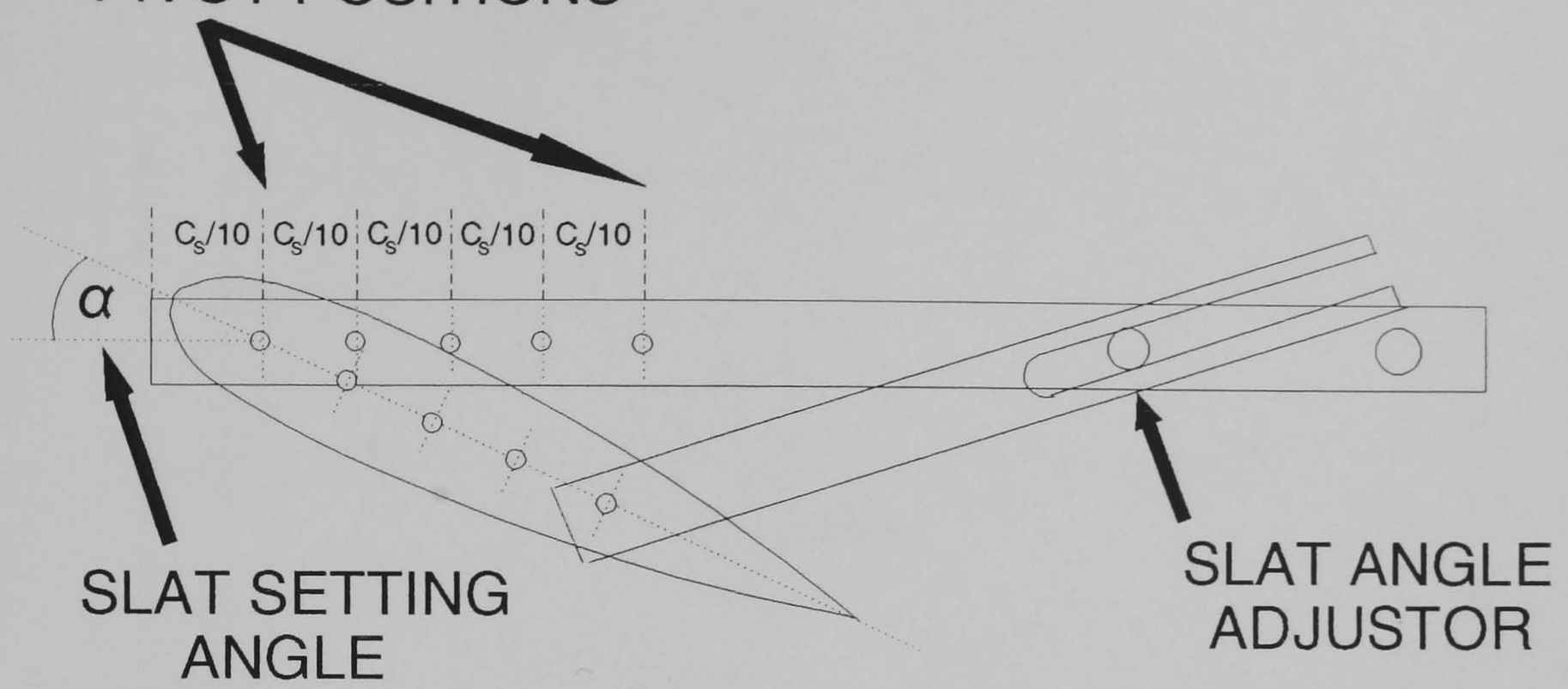

Figure C:5 Model III - Slat Adjustment Mechanism

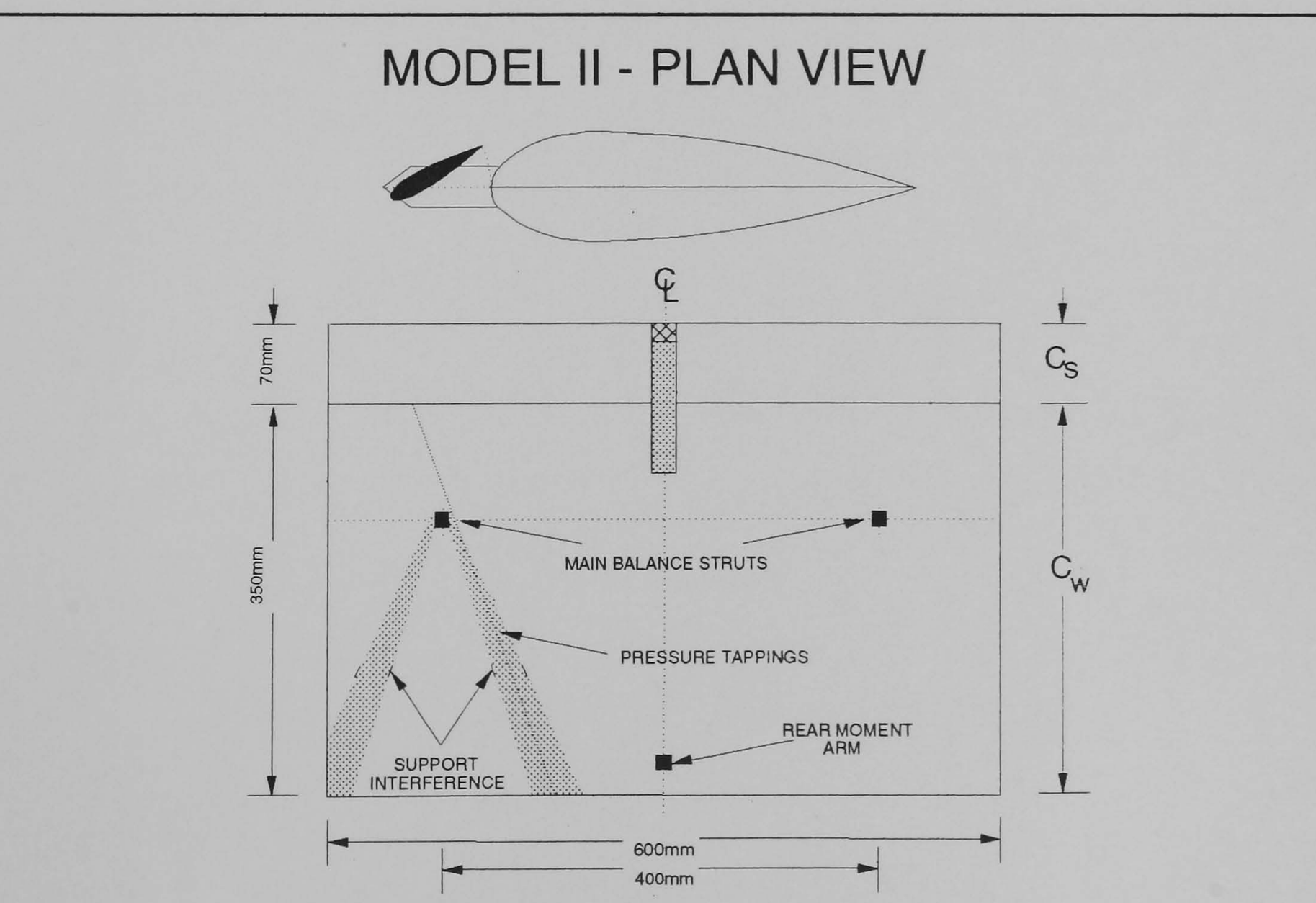

Figure C:6 Model II - Plan View

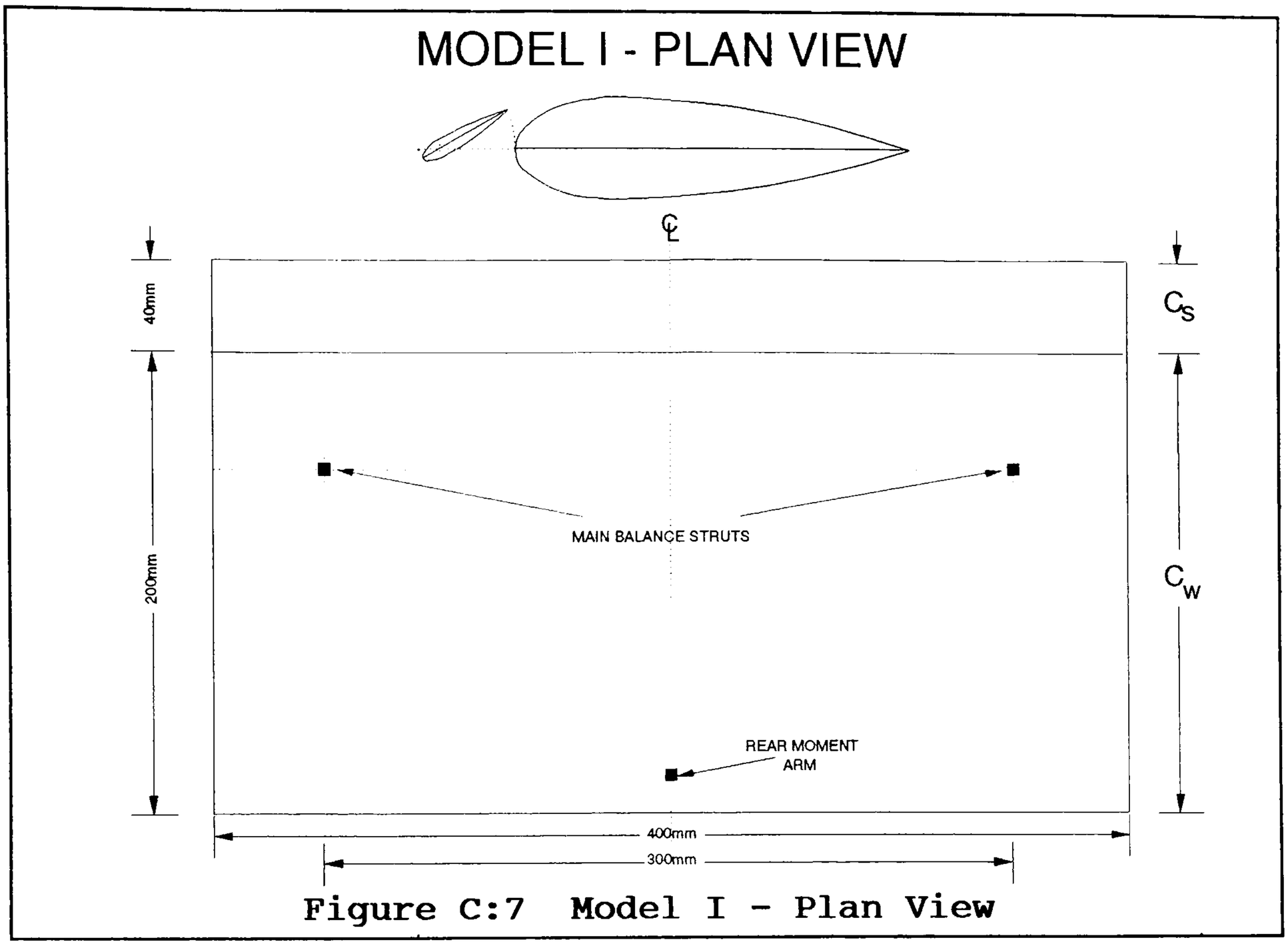

Figure C:7 Model I - Plan View

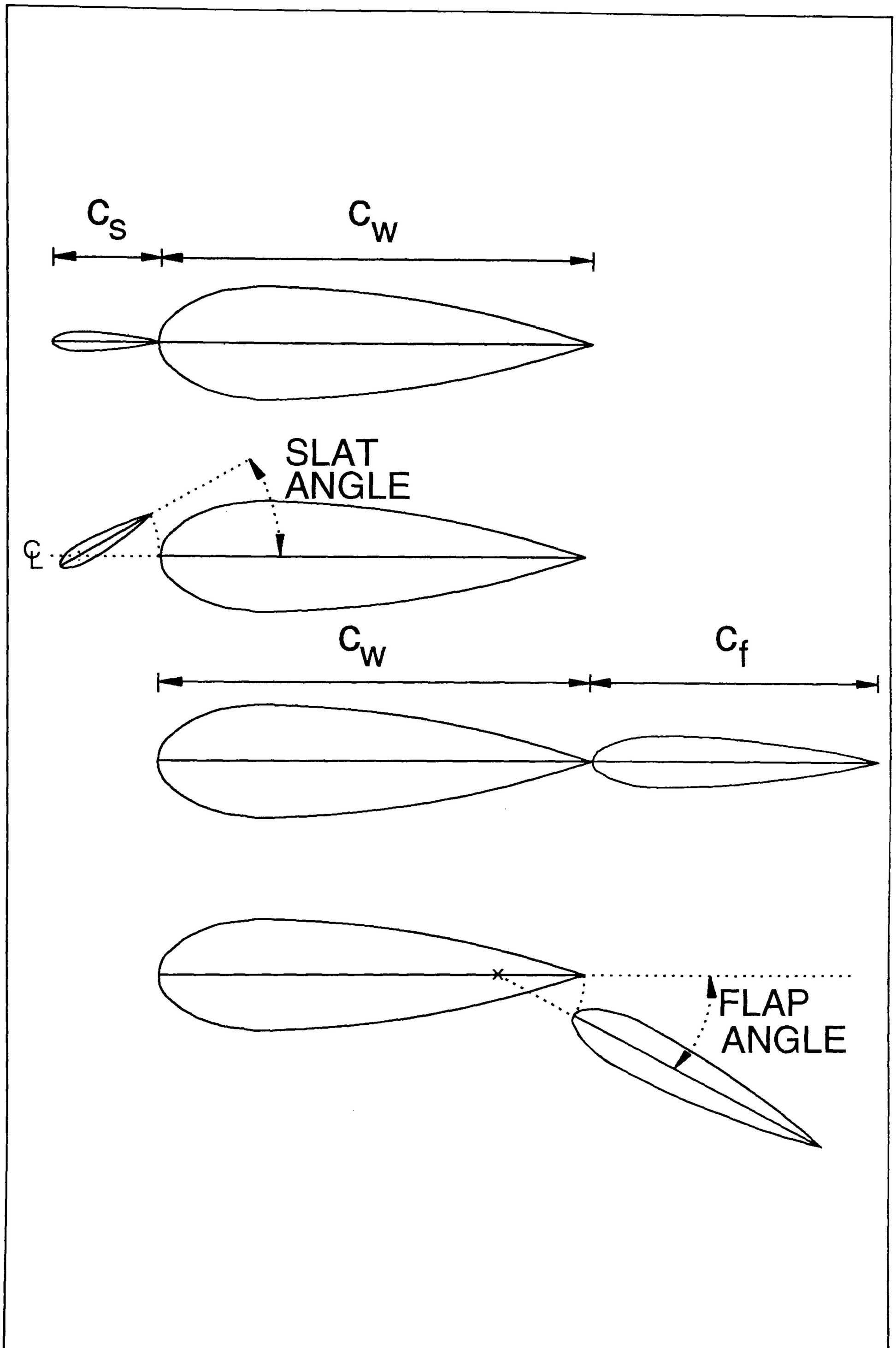

Figure C:8 High Lift Device Configuration Positions